



Interactions et dynamique optique non linéaire pour les applications dans le domaine des télécoms et des lasers

Min Lee

► To cite this version:

Min Lee. Interactions et dynamique optique non linéaire pour les applications dans le domaine des télécoms et des lasers. Optique / photonique. Université Paris 13, Sorbonne Paris Cité, 2018. tel-01963175

HAL Id: tel-01963175

<https://hal.science/tel-01963175>

Submitted on 21 Dec 2018

HAL is a multi-disciplinary open access archive for the deposit and dissemination of scientific research documents, whether they are published or not. The documents may come from teaching and research institutions in France or abroad, or from public or private research centers.

Public Domain

L'archive ouverte pluridisciplinaire **HAL**, est destinée au dépôt et à la diffusion de documents scientifiques de niveau recherche, publiés ou non, émanant des établissements d'enseignement et de recherche français ou étrangers, des laboratoires publics ou privés.

**BUREAU DE LA RECHERCHE
ET DES ETUDES DOCTORALES**

HABILITATION À DIRIGER DES RECHERCHES

**INTERACTIONS ET DYNAMIQUE OPTIQUE NON LINÉAIRE
POUR LES APPLICATIONS DANS LE DOMAINE
DES TÉLÉCOMS ET DES LASERS**

Présenté par Min W. LEE

Maître de Conférence à l'Université Paris 13

a soutenu le 7 décembre 2018 devant la commission d'examen :

| | | |
|---------------------|--------------------|--|
| Président | Benoît BOULANGER | Professeur à l'Université Grenobles Alpes |
| Rapporteurs | Giuseppe LEO | Professeur à l'Université Paris Diderot |
| | Abderrahim RAMDANE | CNRS Directeur de Recherche au Centre de Nanoscience et Nanotechnologie (C2N) |
| | Daniel BLOCH | CNRS Directeur de Recherche à l'Université Paris 13 |
| Examinateurs | Thibaut SYLVESTRE | CNRS Directeur de Recherche à l'Université de Bourgogne Franche-Comté |
| | Esidor NTSOENZOK | Professeur à l'Université d'Orléans |
| | Azzedine BOUDRIOUA | Professeur à l'Université Paris 13 |

Laboratoire de Physique des Lasers

À mes parents en Corée

À ma famille

Remerciements

La soutenance d'HDR a eu lieu au Laboratoire de Physiques des Lasers de l'Institut Galilée. Je remercie d'abord les rapporteurs d'être venus à la soutenance de mon HDR.

J'adresse mes remerciements à Messieurs Abderrahim RAMDANE, directeur de recherche du CNRS au Centre de Nanoscience et Nanotechnologie, Giuseppe LEO, professeur au Laboratoire Matériaux et Phénomènes Quantiques de l'Université Paris Diderot, et Daniel BLOCH, directeur de recherche du CNRS au Laboratoire de Physiques des Lasers de l'Université Paris 13 pour avoir accepté d'être rapporteurs de cette HDR. Je remercie également Messieurs Benoît BOULANGER, professeur à l'Institut Néel de l'Université Grenoble-Alpes, Esidor NTSOENZOK, professeur au CEMHTI de l'Université d'Orléans et Thibaut SYLVESTRE, directeur de recherche du CNRS à l'Institut FEMTO-ST de l'Université Bourgogne Franche-Comté d'avoir accepté d'être jurys de mon HDR.

Les travaux que je présente dans ce manuscrit ont été réalisés avec des collègues et des doctarrants,tes. Je remercie particulièrement Azzedine BOUDRIOUA, responsable de l'équipe PON (Photonique Organique Nanostructure), de son soutien, encouragement et conseil pour le manuscrit et la soutenance de mon HDR. Je remercie également les autres membres de l'équipe, Alexis FISCHER, Homère NKAWO, Mahmoud CHAKAROUN et Jeanne SOLARD. Je tiens aussi à exprimer mes plus sincères remerciements à Safia, Zohra, Alex, Gabriella, Amadou, Sarra, Quentin, Fadwa, Lei, Hocine et Mohamed pour leurs gentillesses et aides.

Je remercie à l'occasion le directeur du LPL, Olivier GORCEIX pour son soutien de mon HDR. Je ne saurai oublier l'équipe administrative, Maryse, Carole et Sylvie, y compris celles qui sont parties : Solène, Martine et Diouldé. Je dois également remercier les personnels du LPL, Albert, Haniff, Thierry, Loïc, Fabrice, Stéphane, Marc et Dejan pour leurs aides lors des besoins. Je remercie également tous les membres du LPL, plus particulièrement Vincent pour ses aides et amitiés. Je tiens à remercier collègues de l'IUT de Villetaneuse, plus particulièrement Rushed pour son encouragement.

Je remercie également M. Lung-Han PENG de la National Taiwan University et M. Ignacio ZALDIVAR de l'INAOE (Instituto Nacional de Astrofísica, Optica y Electrónica) du Mexique en collaboration.

Enfin, J'adresse un remerciement à mes parents en Corée et ma famille qui m'a soutenu et encouragé.

Je remercie toutes les personnes que je n'ai pas citées par manque de place mais qui m'ont apporté soutiens et aides.

Merci encore à toutes et à tous.

A Villetaneuse, le 10 décembre 2018.



TABLE DES MATIÈRES

| | |
|---|-----------|
| I Curriculum Vitæ | 3 |
| I.1 Faits marquants | 4 |
| I.2 Expériences professionnelles | 4 |
| I.3 Diplômes | 4 |
| I.4 Activités pédagogiques | 5 |
| I.5 Direction, animation, montage de formations | 7 |
| I.6 Participation au jury de thèse | 7 |
| I.7 Responsabilités scientifiques | 8 |
| I.8 Responsabilités administratives | 8 |
| I.9 Participation à l'encadrement de thèse | 8 |
| I.10 Encadrement de master de recherche | 11 |
| I.11 Liste des publications | 11 |
| Articles dans des revues internationales à comité de lecture | 11 |
| I.12 Conférences invitées | 15 |
| I.13 Conférences internationales | 15 |
| I.14 Brevet | 22 |
| II Activités de recherche avant UP13 | 23 |
| II.1 Thèse de doctorat | 24 |
| II.2 Activités de recherche à l'Université de Bangor | 25 |
| 2.1 Synchronisation des diodes lasers soumises à un retour optique et communications sécurisées par chaos | 25 |
| 2.2 Synchronisation et communications chaotiques utilisant des VCSELs | 31 |
| 2.3 Système de trois diodes lasers en cascade | 32 |
| II.3 Activités de recherche à l'Institut FEMTO-ST | 35 |
| 3.1 Effets non linéaires dans une fibre optique | 35 |
| 3.2 Amplificateur paramétrique à fibre optique | 37 |
| 3.3 Rétrodiffusion Brillouin stimulée et ses applications aux capteurs distribués à fibre optique | 40 |

TABLE DES MATIÈRES

| | | |
|------------|--|-----------|
| 3.3.1 | BOTDA et BEDS | 40 |
| 3.3.2 | Etudes de PCF | 42 |
| 3.3.3 | DPSK-BEDS | 44 |
| 3.4 | Génération de continuum dans la bande UV dans une PCF | 45 |
| II.4 | Résumé | 46 |
| | Bibliographies | 47 |
| III | Activités de recherche à UP13 | 51 |
| III.1 | Optique non linéaire dans un cristal photonique non linéaire | 52 |
| 1.1 | SHG dans un guide de PPLN-2D | 54 |
| 1.2 | OPG dans un PPLT-2D | 57 |
| 1.2.1 | Génération multi-longueur d'onde | 60 |
| 1.2.2 | Dégénérescence multi-longueur d'onde | 62 |
| III.2 | Dynamique non linéaire d'une diode laser soumise à un retour optique | 66 |
| 2.1 | Retour optique filtré par FBG | 66 |
| 2.2 | Observation des ondes scélérates | 69 |
| 2.3 | Etude d'une diode laser soumise à une SBS | 72 |
| III.3 | Autres activités de recherche | 74 |
| III.4 | Résumé | 75 |
| | Bibliographies | 76 |
| IV | Conclusion et perspectives | 83 |
| IV.1 | Conclusion générale | 83 |
| IV.2 | Perspectives | 83 |
| V | Publications significatives | 85 |
| V.1 | Opt. Lett., 28 , pp. 2168 (2003) | 86 |
| V.2 | Electron. Lett., 40 , pp. 614 (2004) | 89 |
| V.3 | Opt. Lett., 29 , pp. 2497 (2004) | 91 |
| V.4 | Opt. Lett., 29 , pp. 1215 (2004) | 94 |
| V.5 | Phot. Tech. Lett., 16 , pp. 2392 (2004) | 97 |
| V.6 | J. Opt. Soc. Am. B, 23 , pp. 846 (2006) | 100 |
| V.7 | Phot. Tech. Lett., 18 , pp. 169 (2006) | 106 |
| V.8 | IEE Proceeding on Optoelectronics, 152 , pp. 97 (2005) | 109 |

TABLE DES MATIÈRES

| | | |
|-----------------------|--|------------|
| V.9 | J. Lightwave Technol., 28 , pp. 2173 (2010) | 115 |
| V.10 | Opt. Express, 18 , pp. 20136 (2010) | 121 |
| V.11 | Phot. Tech. Lett., 24 , pp. 667 (2012) | 128 |
| V.12 | Phot. Tech. Lett., 24 , pp. 79 (2012) | 131 |
| V.13 | Phot. Tech. Lett., 25 , pp. 94 (2013) | 134 |
| V.14 | Opt. Lett., 37 , pp. 130 (2012) | 137 |
| V.15 | Opt. Express, 21 , pp. 7202 (2013) | 140 |
| V.16 | Opt. Express, 25 , pp. 30253 (2017) | 147 |
| V.17 | Opt. Lett., 41 , pp. 2950 (2016) | 153 |
| V.18 | Opt. Lett., 41 , pp. 4476 (2016) | 157 |
| V.19 | Org. Electron., 56 , pp. 284 (2018) | 161 |
| Glossaires | | 168 |
| Résumé | | 171 |
| en français | | 171 |
| en anglais | | 171 |

INTRODUCTION

Ce rapport d'Habilitation à Diriger des Recherches comprend quatre parties :

1 LA PREMIÈRE PARTIE est un C.V. détaillé qui présente également les projets de recherche dans lesquels j'ai participés, mes activités d'encadrement doctoral et la liste de mes publications et mes communications.

2 LA DEUXIÈME PARTIE est un résumé de mes activités de recherche menés avant mon arrivé au LPL de l'Université Paris 13. Elle commence par les activités dans les domaines des communications sécurisées par chaos et de la synchronisation de chaos utilisant une diode laser soumise à un retour optique, menées à l'Université de Bangor (Royaume Uni). Le deuxième volet de cette partie comporte mes activités, dans le domaine de l'optique non linéaire dans des fibres optiques, effectuées à l'Université de Franche-Comté. Durant cette période, mes travaux se situent au tour de l'amplification paramétrique à fibre et du capteur distribué Brillouin à fibre. Je commencerai dans chaque partie par une introduction avec l'état de l'art ou un historique afin de faciliter la compréhension de mes activités avec une bonne bibliographie.

3 LA TROISIÈME PARTIE est un résumé de mes activités de recherche menées au seins du LPL. Cette partie se divise en deux : l'optique non linéaire dans un cristal photonique non linéaire et les comportements dynamiques des diodes lasers soumises à un retour optique. Ces activités concernent principalement les travaux de thèse que j'ai co-encadrés. Dans l'optique non linéaire, je décrirai mes travaux sur la [SHG](#) et l'[OPG](#) dans des cristaux photoniques non linéaires. Dans l'étude des comportements dynamiques, je présenterai les comportements dynamiques d'une diode laser soumise à un retour optique filtré et d'une diode laser soumise à une rétrodiffusion Brillouin stimulée, ainsi que les ondes scélérates. Je commencerai également dans chaque partie par une introduction avec l'état de l'art ou un historique afin de faciliter la bonne compréhension de mes activités avec une bonne bibliographie.

4 LA QUATRIÈME PARTIE consiste en une compilation des publications significatives.

CURRICULUM VITÆ

Sommaire

| | | |
|------|--|----|
| I.1 | Faits marquants | 4 |
| I.2 | Expériences professionnelles | 4 |
| I.3 | Diplômes | 4 |
| I.4 | Activités pédagogiques | 5 |
| I.5 | Direction, animation, montage de formations | 7 |
| I.6 | Participation au jury de thèse | 7 |
| I.7 | Responsabilités scientifiques | 8 |
| I.8 | Responsabilités administratives | 8 |
| I.9 | Participation à l'encadrement de thèse | 8 |
| I.10 | Encadrement de master de recherche | 11 |
| I.11 | Liste des publications | 11 |
| | Articles dans des revues internationales à comité de lecture | 11 |
| I.12 | Conférences invitées | 15 |
| I.13 | Conférences internationales | 15 |
| I.14 | Brevet | 22 |

MIN W. LEE

né à Séoul (Corée du Sud), marié, de nationalité Britannique, 48 ans
Laboratoire de Physique des Lasers CNRS UMR 7538
Université Paris 13, Sorbonne Paris Cité
99, Avenue Jean-Baptiste Clément
93430 Villetaneuse – France
Courier électronique : min.lee@univ-paris13.fr

I.1 FAITS MARQUANTS

- 2018 : Promotion en hors classe du CNU 63^{ième}
- 2017 – 2018 : Obtention d'un congé de recherche (CRCT) d'un semestre
Décharge de service de 96 h

I.2 EXPÉRIENCES PROFESSIONNELLES

- Depuis septembre 2011 : Maître de conférences à l'IUT de Villetaneuse, attaché au Laboratoire de Physique des Lasers, Université Paris 13
- 2009 – 2011 : Post-doc à l'Institut FEMTO-ST, Université de Franche-Comté
- 2002 – 2008 : Post-doc à l'Université de Bangor (Pays de Galles, Royaume Uni)
- 1998 : Ingénieur d'étude à l'université Ajou (Suwon, Corée du Sud)

I.3 DIPLÔMES

- 1998 – 2002 : Doctorat de Sciences pour l'Ingénieur (Thèse soutenue le 19 février 2002) Laboratoire d'Optique P. M. Duffieux, Université de Franche-Comté (Besançon)
« Étude des comportements chaotiques en modulation de cohérence et application à la cryptographie »
- 1996 – 1998 : Master en Physique, Université Ajou (Suwon, Corée du Sud)
- 1990 – 1996 : Licence en Physique, Université Ajou (Suwon, Corée du Sud) (incluant 2 ans de service militaire)

I.4 ACTIVITÉS PÉDAGOGIQUES

1. Présentation synthétique des enseignements

Service annuel (H eq. TD) :

| | Niveau | FI/FC | Nature | Effectifs | Volume | Discipline |
|--|--------------|-------|-------------|-----------|--------|---------------------|
| Principe de transmission radio | DUT 1 | FI | Cours/TD/TP | 52 | 30 h | Elec. |
| Mesures de signaux | DUT 1 | FI | TP | 12 | 12 h | Elec. |
| Transmission hyperfréquence et optique | DUT 2 | FI | Cours/TD/TP | 42 | 30 h | Elec. |
| Transmission hyperfréquence et optique | DUT 2 | APP | Cours/TD/TP | 12 | 30 h | Elec. |
| Fibres optiques | DUT 2 | FI | TP | 12 | 12 h | Opt. |
| Projets tutorés | DUT 2 | FI | projet | 6 | 22 h | Elec. |
| Electronique micro-onde | Licence pro. | FI/FC | Cours/TD/TP | 14 | 30 h | Elec. |
| Instrumentation par LabVIEW | Licence pro. | FI/FC | Cours/TD/TP | 14 | 20 h | Elec. |
| Salle blanche | Licence pro. | FI/FC | TP | 14 | 30 h | Phys. |
| Projets tutorés | Licence pro. | FI/FC | projet | 3 | 11 h | Elec. |
| Introduction à la nanotechnologie | Master | FI | Cours/TD/TP | 12 | 30 h | Phys. |
| Instrumentation d'expérience par LabVIEW | Doctorat | | Cours/TD/TP | 6 | 20 | Formation doctorale |

2. Présentation des activités d'enseignement

- **M2107 Principe de transmission radio** : Depuis 2013, je suis responsable de ce module qui est destiné à environ 52 étudiants de première année de DUT. Il s'agit d'un module sur la transmission radio en électronique. Avec le changement de PPN, j'ai été emmené à créer l'enseignement pour ce module. Il est composé de 6h de cours, de 12h de TD et de 12h de TP. Dans ce module, nous abordons la modulation d'amplitude, la modulation de fréquence et les structures des émetteurs et des récepteurs, notamment talkie-walkie. J'ai également monté 4 TP : TP 1 - modulation d'amplitude avec la radio AM, TP 2 - modulation de fréquence, TP 3 - transposition de fréquence et TP 4 - talkie-walkie. J'ai monté plus particulièrement un TP sur la réalisation d'un émetteur de talkie-walkie avec le principe de transmission radio abordé dans le cours. Ce TP est très attractif pour les étudiants.
- **M3205 Transmission hyperfréquence et optique** : Depuis 2012, je suis responsable de ce module qui est destiné à environ 42 étudiants de deuxième année de DUT. Il s'agit d'un module sur la transmission radio en électronique. Il est composé de 6h de cours, de 12h de TD et de

12h de TP. L'objectif de ce module est de comprendre les phénomènes de la propagation d'ondes dans un câble, le coefficient de réflexion, l'onde stationnaire, l'impulsion de tension, l'abaque de Smith, l'adaptation d'impédance. J'ai également monté 4 TP : TP 1 – impulsion de tension, TP 2 – caractérisation de câbles, TP 3 – adaptation d'impédance et TP 4 – onde stationnaire.

- **M8 Electronique Micro-ondes** : En 2011 – 2015, j'ai été responsable de ce module qui est destiné à environ 14 étudiants de Licence professionnelle Electronique, Optique et Nanotechnologie. Il est composé de 6h de cours, de 9h de TD et de 15h de TP. Dans ce module, nous abordons la propagation d'ondes dans un câble, le coefficient de réflexion, l'onde stationnaire, l'impulsion de tension, l'abaque Smith, l'adaptation d'impédance. J'ai également monté 4 TPs : TP 1 – impulsion de tension, TP 2 – caractérisation de câbles, TP 3 – adaptation d'impédance, TP 4 – onde stationnaire et TP 5 – définition de l'impédance quelconque.
- **M9 Instrumentation par LabVIEW** : Depuis 2011, je suis responsable de ce module qui est destiné à environ 14 étudiants de Licence professionnelle Electronique, Optique et Nanotechnologie. Il est composé de 6h de cours et de 14h de TP. Dans ce module, nous abordons la programmation graphique et le pilotage des instruments tels que GBF, oscilloscope, multimètre, carte NI-DAQ. J'ai également monté 6 TP : TP 1 – Introduction à LabVIEW, TP 2 – pilotage d'un multimètre par RS232, TP 3 – pilotage d'un GBF par GPIB, TP 4 – acquisition de données d'un oscilloscope par USB, TP 5 – caractérisation de LEDs par une carte NI-DAQ et TP 6 – caractérisation d'un circuit RLC par l'automatisation de banc.
- **Instrumentation d'expérience par LabVIEW** : Depuis 2017, j'anime une formation pour les doctorants. C'est une formation volontaire pour aider les doctorants à pouvoir mener leurs expériences pilotées par un ordinateur à l'aide du logiciel LabVIEW. La formation est faite pour 6 doctorants qui font leurs thèses soit au Laboratoire de Physique des Lasers (LPL) soit au Laboratoire des Science des Procédés et Matériaux (LSPM). Elle est composée de cours/TP de 20 h.
- **Création de Fablab** : En 2017, j'ai porté un projet pour monter un Fablab au sein de l'IUT de Villetaneuse. Ce dernier est un atelier de fabrication qui est essentiel aux étudiants ou aux enseignants qui veulent réaliser des projets de valorisation ou des projets pédagogiques.

Je participe également à l'enseignement d'autres modules en électronique et en optique. J'ai également participé à l'enseignement au département GEII et à l'institut Galilée. J'ai aussi enseigné un module « Introduction à la nanotechnologie » en master. J'ai effectué un enseignement de 298 HETD pour l'année 2013/2014, 288 HETD pour l'année 2014/2015, 253 HETD pour l'année 2015/2016 et 239 HETD pour l'année 2016/2017.

Pour l'année 2017-2018, j'ai obtenu un congé de recherche (CRCT) d'un semestre, ce qui m'a permis d'effectuer un enseignement de 96 HETD et de consacrer davantage de temps pour la recherche.

I.5 DIRECTION, ANIMATION, MONTAGE DE FORMATIONS

- **Responsable de la Licence Professionnelle Electronique, Optique et Nanotechnologie**
2013 – 2017

C'est une formation avec un effectif de 15 étudiants en formation initiale et formation continue.
Organisation de la formation, suivi des étudiants
Recrutement, suivi de stages

- **Animation de la Journée Porte Ouverte** (2013 – 2016)

Accueil des élèves, Organisation de la visite de la salle blanche et des salles de TPs d'électronique et d'optique

- **Animation du stand de Salon APB** (2013 – 2016)

Accueil des élèves

- **Visite des Lycées** (2013 – 2016)

Démonstration de téléphonie sur IP

- **Création de Fablab** (2017)

Porteur de projet de la création de Fablab au sein de l'IUT de Villetaneuse

Budget, organisation, achat de matériels

- **Animation Stand « Réseaux et Télécoms »** (2015 – 2016)

Dans le cadre de Savante Banlieue, j'ai animé un stand pour la démonstration de téléphonie sur IP et de transmissions par fibres optiques. Cet événement est organisé pour des élèves de collèges, de lycées et des adultes par Plaine Commune Seine Saint-Denis et a lieu tous les ans pendant deux jours au mois d'octobre sur le campus de Villetaneuse.

I.6 PARTICIPATION AU JURY DE THÈSE

- Birgit STILLER : Thèse « Brillouin scattering in photonic crystal fiber : from fundamentals to fiber optic sensors » soutenue le 12 décembre 2011 à l'Institut FEMTO-ST à Besançon, invité.
- Quentin RIPAULT : Thèse « Second-Harmonic Generation in Helium-implanted Nonlinear Photonic Crystal (2D-PPLN) waveguide » soutenue le 16 juillet 2013 au Laboratoire de Physique des Lasers, membre de jury encadrant.
- Fadwa BALADI : Thèse « Comportement dynamique de diodes laser de puissance multimodes à 980 nm soumises à un retour optique sélectif en fréquence provenant d'un réseau de Bragg photoinscrit » soutenue le 17 décembre 2015 au Laboratoire de Physique des Lasers, membre de jury encadrant.
- Ana Gabriela CORREA-MENA : Thèse « Use of a microwave photonic architecture for simultaneous transmission of analog and digital signals » soutenue le 13 septembre 2018 à l'INAOE au Mexique, examinateur.

I.7 RESPONSABILITÉS SCIENTIFIQUES

- **Porteur principal d'un projet CNRS PICS (2017 – 2019)**

« Cristaux photoniques non linéaires pour l'optique quantique et la mise au point de nouvelles sources »

Collaborateur : Prof. L.-H. Peng à l'Université National de Taïwan

Budget : 21 000,00 euros sur 3 ans

Dans ce projet, nous travaillons en collaboration avec le Prof. L. H. Peng sur la génération paramétrique optique de large bande dans les PPLT-2D et PPLN-2D.

- **Porteur principal d'un projet BQR (2017)**

« Développement du procédé smart-cut pour la fabrication de guide d'onde **CPNL** et de cristaux photoniques 3D »

Budget : 11 700,00 euros

Ce projet porte sur le développement d'un nouveau procédé pour réaliser des systèmes compacts de conversion de fréquence en utilisant des cristaux photoniques non linéaires.

- **Participation au projet de collaboration industrielle avec 3S Photonics (2013 – 2014)**

« Vertically integrated Enhanced pRoduCTs for Industrial Chain using Amplifier Lasers »

Budget : 104 328,00 euros

Ce projet a permis de comprendre le comportement dynamique d'une diode laser utilisée dans un amplificateur optique pour une liaison sous-marine.

- **Editeur de « Journal of Chaos »**

2013 – 2016

Hindawi Publishing Corporation

<http://www.hindawi.com/journals/jcha/>

Attribution d'articles, décision d'acceptation

I.8 RESPONSABILITÉS ADMINISTRATIVES

- **Membre de conseil du Laboratoire de Physique des Lasers (2014 – à jour)**

Attribution de bourse de thèse, classement de projets, etc

- **Membre de conseil du Département réseaux et télécoms (2014 – 2018)**

- **Membre de commission pédagogique de l'IUT de Villetaneuse (2014 – 2017)**

Définition de la modalité de contrôles et des examens et des absences

I.9 PARTICIPATION À L'ENCADREMENT DE THÈSE

Cette section est un bref descriptif de mon expérience de participation à l'encadrement de thèse. Depuis mon arrivée en septembre 2011, j'ai participé à l'encadrement de cinq thèses. J'ai également encadré une étudiante en master 2.

- Quentin RIPAUT : Thèse « Second-Harmonic Generation in Helium-implanted Nonlinear Photonic Crystal (2D-PPLN) waveguide » soutenue le 16 juillet 2013.

Thèse cotutelle avec l'Université National de Taïwan

Directeurs de thèse : Prof. A. Boudrioua, Prof. L.-H. Peng à Taïwan

Cette thèse nous a permis d'effectuer une étude approfondie sur la conversion de fréquences de laser dans un cristal photonique non linéaire. De plus, nous avons réalisé un guide d'onde par l'implantation d'hélium, ce qui a permis une augmentation de l'efficacité de conversion par rapport à un cristal massif. A l'issue de cette thèse, nous avons publié les résultats dans Optics Express [ACL I.35]. Grâce à cette thèse, nous avons également établi une solide collaboration avec l'Université National de Taïwan.

- Fadwa BALADI : Thèse « Comportement dynamique de diodes laser de puissance multimodes à 980 nm soumises à un retour optique sélectif en fréquence provenant d'un réseau de Bragg photoinscrit » soutenue le 17 décembre 2015.

Thèse CIFRE avec l'entreprise 3SP Technologies

Co-encadrant : M. M. Bettati (3SP Technologies)

Directeurs de thèse : Prof. A. Fischer

Dans cette thèse, nous avons étudié le comportement dynamique d'une diode laser à 980 nm. Cette dernière joue un rôle clé dans les transmissions optiques comme une pompe laser, notamment à longue distance. La pompe laser est composée d'une cavité fibrée avec un réseau de Bragg fibré pour un retour optique. A cause de la réinjection de l'émission laser par un retour optique, le comportement dynamique de la pompe montre un régime stable ou un régime instable, notamment le régime chaotique. Dans cette thèse, nous avons établi une cartographie des comportements dynamiques de la pompe laser à 980 nm en fonction du courant de la pompe et le taux de retour optique. Cette étude permet de développer une pompe laser fiable pour assurer des liaisons sous-marines fiables. A l'issue de cette thèse, nous avons publié les résultats dans Optics Letters [ACL I.39]. Cette thèse nous a permis d'obtenir un financement industriel OSEO dans le cadre du projet VERTICAL. Durant cette thèse, nous avons aussi démontré pour la première fois l'existence des ondes scélérates optiques dans ce type de diode laser. Ces résultats ont également été publiés dans Optics Letter [ACL I.40]. Grâce à cette démonstration, nous avons été invités à une conférence internationale « EECOS » qui a eu lieu à Buenos Aires en Argentine au mois de décembre 2015.

- Alex CHIME : Thèse « Etude théorique et expérimentale de micro-OLEDs rapides sur électrodes coplanaires en régime d'impulsions à haute densité de courante » soutenue le 21 décembre 2017.

Co-encadrant : Mr. M. Chakaroun

Directeurs de thèse : Prof. A. Fischer, Mr. H. Nkwawo

Dans cette thèse, nous avons travaillé sur la démonstration d'une diode laser organique à base d'une OLED pompée par des impulsions électriques nanosecondes. Une diode laser organique n'a jamais été démontrée malgré ses grandes applications potentielles. C'est un défi scientifique,

mais aussi technologique. Nous avons travaillé sur la réalisation d'un circuit et d'un banc de caractérisation pour des impulsions électriques (nanosecondes). Nous avons également travaillé sur l'aspect physique du comportement d'une OLED sous le régime impulsifnanoseconde. Avec ces travaux, nous avons déposé deux brevets à l'Office Européen des Brevets et un article a été accepté dans *Organic Electronics* [ACL I.46].

- Ana Gabriela CORREA-MENA : Thèse mexicaine en collaboration « Use of a microwave photonic architecture for simultaneous transmission of analog and digital signals » soutenue le 14 septembre 2018

Thèse en collaboration avec l'INAOE au Mexique

Directeurs de thèse : Mr. I. Zaldivar au Mexique

Dans le cadre de cette thèse, nous avons étudié les dynamiques non linéaires d'une diode laser soumise à une rétrodiffusion Brillouin stimulée. La fréquence de la rétrodiffusion Brillouin est décalée de 10,7 GHz dans une fibre monomode standard par rapport à la fréquence de laser. La rétrodiffusion est réinjectée à la diode laser afin de perturber son comportement dynamique. Ainsi nous avons étudié son comportement dynamique non linéaire et comparons avec celui d'une diode laser soumise à un retour optique simple. Mme. Correa-Mena a séjourné au LPL pendant 8 mois pour finir ces travaux.

- Zohra YELLAS : Thèse algérienne en collaboration « Génération paramétrique optique large bande dans les cristaux photoniques non linéaires (2D PPLT et 2D PPLN) » soutenue le 14 septembre 2018.

Thèse à l'Université de Jijel en Algérie

Co-encadrant : M. R. Beghoul (Algérie)

Directeurs de thèse : Prof. A. Boudrioua et Prof. H. Bouridah en Algérie

Dans le cadre de cette thèse, nous avons travaillé sur la génération de multi-longueur d'onde dans un cristal photonique non linéaire (2D-PPLT). Grâce au réseau du cristal, nous avons démontré la génération multi-longueurs d'onde en cascade à partir d'une source laser à 532 nm par les processus de génération paramétrique optique, de génération de somme de fréquences et de génération de second-harmonique. Nous avons publié un article sur ces résultats dans *Optics Express* [ACL I.45].

Thèse en cours

- Safia MOHAND OUSAID : octobre 2017 – « Etude de la génération paramétrique optique dans des cristaux photoniques non linéaires et la fabrication de cristaux photoniques non linéaires 3D » thèse en deuxième année.

Directeur de thèse : Prof. A. Boudrioua

Dans ses travaux de thèse, nous nous intéressons au contrôle des mécanismes de conversion de fréquences dans les PPLT-2D dans l'objectif de mettre au point un système compact de source

cohérente accordable et large bande.

I.10 ENCADREMENT DE MASTER DE RECHERCHE

- Safia MOHAND OUSAID : Master 2, « Etude de la génération paramétrique optique dans les cristaux photoniques non linéaires » Il s'agit de la suite de la thèse de Mlle. Z. Yellas. Dans sa thèse, la simulation montre une possibilité de la génération d'un spectre large bande dans un PPLT-2D grâce aux vecteurs de réseau réciproques. Dans ce stage de master, nous avons donc travaillé sur la démonstration d'un spectre large bande par le processus de la génération paramétrique optique. J'ai encadré ce stage entièrement et la soutenance a eu lieu septembre 2017. Elle est actuellement en thèse que je co-encadre avec Mr. Boudrioua.

I.11 LISTE DES PUBLICATIONS

ARTICLES DANS DES REVUES INTERNATIONALES À COMITÉ DE LECTURE

- [I.1] S. H. Lee, C. K. Kim, O P. Kwon, M. W. Lee et Y. H. Won, « Investigation of dipole alignments by swelling in poled thin films of a side-group polymer using second harmonic generation », *J. Polym. Sci., Part B, Polym. Phys.*, **37**(21), pp. 3108–3114 (1999), [http://onlinelibrary.wiley.com/doi/10.1002/\(SICI\)1099-0488\(19991101\)37:21%3C3108::AID-POLB19%3E3.0.CO;2-L/abstract](http://onlinelibrary.wiley.com/doi/10.1002/(SICI)1099-0488(19991101)37:21%3C3108::AID-POLB19%3E3.0.CO;2-L/abstract).
- [I.2] S. Y. Kim, M. W. Lee, Y. H. Won, Y. K. Kim et H. G. Lee, « Simple polarimetric method for electro-optic coefficients », *J. Opt. Soc. Korea*, **3**(1), pp. 23–26 (1999), <https://www.osapublishing.org/josk/abstract.cfm?uri=josk-3-1-23>.
- [I.3] L. Larger, M. W. Lee, J.-P. Goedgebuer, W. Elflein et T. Erneux, « Chaos in coherence modulation : bifurcations of an oscillator generating fluctuations of optical delay », *J. Opt. Soc. Am. B*, **18**(8), pp. 1063–1068, (août 2001), <https://www.osapublishing.org/josab/abstract.cfm?uri=josab-18-8-1063>.
- [I.4] V. S. Udal'tsov, L. Larger, J.-P. Goedgebuer, M. W. Lee, E. Genin et W. T. Rhodes, « Band-pass chaotic dynamics of electronic oscillator operating with delayed non-linear feedback », *IEEE Trans. Circuits and Syst. I*, **49**(7), pp. 1006–1009, (juillet 2002), <http://ieeexplore.ieee.org/document/1016833/>.
- [I.5] M. W. Lee, L. Larger et J.-P. Goedgebuer, « Transmission system using chaotic delays between lightwaves », *IEEE J. Quantum Electron.*, **39**(7), pp. 931–935 (juillet 2003), <http://ieeexplore.ieee.org/document/1206838/>.
- [I.6] M. W. Lee, J. Paul, S. Sivaprakasam et K. A. Shore, « Comparison of closed- and open-loop feedback schemes of message decoding using chaotic laser diodes », *Opt. Lett.*, **28**(22), pp. 2168–2170 (novembre 2003), <https://www.osapublishing.org/ol/abstract.cfm?uri=ol-28-22-2168> (voir la page 86, Chapitre IV).
- [I.7] M. W. Lee, L. Larger, V. Udal'tsov, E. Genin et J.-P. Goedgebuer, « Demonstration of a chaos generator using two time delays », *Opt. Lett.*, **29**(4), pp. 325–327 (février 2004), <https://www.osapublishing.org/ol/abstract.cfm?uri=ol-29-4-325>.

- [I.8] E. Genin, L. Larger, J.-P. Goedgebuer, M. W. Lee, R. Ferrière et X. Bavard, « Chaotic oscillations of the optical phase for multigigahertz-bandwidth secure communications », IEEE J. Quantum Electron., **40**(3), pp. 294–298 (mars 2004), <http://ieeexplore.ieee.org/document/1271362/>.
- [I.9] M. W. Lee et K. A. Shore, « Chaotic message broadcasting using DFB laser diodes », Electron. Lett., **40**(10), pp. 614–615 (mai 2004), <http://ieeexplore.ieee.org/document/1300295/?arnumber=1300295&pageNumber%3D13%26rowsPerPage%3D75> (voir la page 89, Chapitre IV).
- [I.10] Y. Hong, M. W. Lee, P. S. Spencer et K. A. Shore, « Synchronization of chaos in unidirectionally coupled vertical-cavity surface-emitting lasers », Opt. Lett., **29**(11), pp. 1215–1217 (juin 2004), <https://www.osapublishing.org/ol/abstract.cfm?uri=ol-29-11-1215> (voir la page 94, Chapitre IV).
- [I.11] T. Erneux, L. Larger, M. W. Lee et J.-P. Goedgebuer, « Ikeda Hopf bifurcation revisited », Physica D, **194**, pp. 49–64 (juillet 2004), <http://www.sciencedirect.com/science/article/pii/S0167278904000673>.
- [I.12] M. W. Lee, Y. Hong et K. A. Shore, « Experimental demonstration of VCSEL-based chaotic optical communications », IEEE Photon. Technol. Lett., **16**(10), pp. 2392–2394 (octobre 2004), <http://ieeexplore.ieee.org/document/1336940/> (voir la page 97, Chapitre IV).
- [I.13] J. Paul, M. W. Lee et K. A. Shore, « Effect of chaos pass filtering on message decoding quality using chaotic external-cavity laser diodes », Opt. Lett., **29**(21), pp. 2497–2499 (novembre 2004), <https://www.osapublishing.org/ol/abstract.cfm?uri=ol-29-21-2497> (voir la page 91, Chapitre IV).
- [I.14] M. W. Lee et K. A. Shore, « Two-mode chaos synchronisation using a multi-mode external-cavity laser diode and two single-mode laser diodes », J. Lightwave Technol., **23**, (1), pp. 1068–1073, (mars 2005), <http://ieeexplore.ieee.org/document/1417001/?reload=true&arnumber=1417001>.
- [I.15] M. W. Lee, J. Paul, I. Pierce et K. A. Shore, « Frequency-detuned synchronisation-switching in chaotic DFB laser diodes », IEEE J. Quantum Electron., **41**(3), pp. 302–307, (mars 2005), <http://ieeexplore.ieee.org/document/1397876/>.
- [I.16] J. Paul, M. W. Lee et K. A. Shore, « 3.5 GHz message transmission in an all-optical chaotic communication system using 1550 nm diode lasers », IEEE Photon. Technol. Lett., **17**(4), pp. 920–922, (avril 2005), <http://ieeexplore.ieee.org/document/1411921/>.
- [I.17] M. W. Lee, P. Rees, K. A. Shore, S. Ortín, L. Pesquera et A. Valle, « Dynamical characterisation of a laser diode subject to double optical feedback for chaotic optical communications », IEE Proceedings on Optoelectronics, **152**(2), pp. 97–102, (avril 2005), <http://ieeexplore.ieee.org/document/1425779/> (voir la page 109, Chapitre IV).
- [I.18] M. W. Lee et K. A. Shore, « Demonstration of a chaotic optical message relay using DFB laser diodes », IEEE Photon. Technol. Lett., **18**(1), pp. 169–171, (janvier 2006), <http://ieeexplore.ieee.org/document/1561321/> (voir la page 106, Chapitre IV).
- [I.19] D. M. Kane, J. P. Toomey, M. W. Lee et K. A. Shore, « Correlation dimension signature of wide-band chaos synchronization of semiconductor lasers », Opt. Lett., **31**(1), pp. 20–22, (janvier 2006), <https://www.osapublishing.org/ol/abstract.cfm?uri=ol-31-1-20>.
- [I.20] M. W. Lee, J. Paul, C. Masoller et K. A. Shore, « Observation of cascade complete chaos synchronisation with zero time lag in laser diodes », J. Opt. Soc. Am. B, **23**(5), pp. 846–851, (mai 2006), <https://www.osapublishing.org/josab/abstract.cfm?uri=josab-23-5-846> (voir la page 100, Chapitre IV).

- [I.21] Y. Hong, M. W. Lee, J. Paul, P. S. Spencer et K. A. Shore, « Enhanced chaos synchronization in unidirectionally coupled VCSELs with polarization-preserved injection », Opt. Lett., **33**(6), pp. 587–589, (mars 2008), <https://www.osapublishing.org/ol/abstract.cfm?uri=ol-33-6-587>.
- [I.22] Y. Hong, M. W. Lee, J. Paul, P. S. Spencer et K. A. Shore, « GHz bandwidth message transmission using chaotic vertical-cavity surface-emitting lasers », J. Lightwave Technol., **27**(22), pp. 5099–5105, (novembre 2009), <https://www.osapublishing.org/jlt/abstract.cfm?uri=jlt-27-22-5099>.
- [I.23] Y. Hong, M. W. Lee et K. A. Shore, « Optimised message extraction in laser diode based optical chaos communications », IEEE J. Quantum Electron., **46**(2), pp. 253–257 (février 2010), <http://ieeexplore.ieee.org/document/5361383/>.
- [I.24] M. W. Lee, T. Sylvestre, M. Delqué, A. Kudlinski, A. Mussot, J.-F. Gleyze, A. Jolly et H. Maillotte, « Demonstration of an all-fibre broadband optical parametric amplifier at 1 μm », J. Lightwave Technol., **28**(15), pp. 2173–2178 (août 2010), <http://ieeexplore.ieee.org/document/5491052/> (voir la page 115, Chapitre IV).
- [I.25] J. P. Toomey, D. M. Kane, M. W. Lee et K. A. Shore, « Nonlinear dynamics of semiconductor lasers with feedback and modulation », Opt. Express, **18**(16), pp. 16955–16972 (août 2010), <https://www.osapublishing.org/oe/abstract.cfm?URI=oe-18-16-16955>.
- [I.26] B. Stiller, S. M. Foaleng, J.-C. Beugnot, M. W. Lee, M. Delqué, G. Bouwmans, A. Kudlinski, L. Thévenaz, H. Maillotte et T. Sylvestre, « Photonic crystal fiber mapping using Brillouin echoes distributed sensing », Opt. Express, **18**(19), pp. 20136–20142 (septembre 2010), <https://www.osapublishing.org/oe/abstract.cfm?uri=oe-18-19-20136> (voir la page 121, Chapitre IV).
- [I.27] B. Stiller, M. Delqué, J.-C. Beugnot, M. W. Lee, G. Mélin, H. Maillotte, V. Laude et T. Sylvestre, « Frequency-selective excitation of guided acoustic modes in a photonic crystal fiber », Opt. Express, **19**(8), pp. 7689–7694 (avril 2011), <https://www.osapublishing.org/oe/abstract.cfm?uri=oe-19-8-7689>.
- [I.28] Emile Carry, Jean-Charles Beugnot, Birgit Stiller, Min W. Lee, Hervé Maillotte, and Thibaut Sylvestre, « Temperature coefficient of the high-frequency guided acoustic mode in a photonic crystal fiber », Appl. Opt., **50**(35), pp. 6543–6547 (2011), <https://www.osapublishing.org/ao/abstract.cfm?uri=ao-50-35-6543>.
- [I.29] M. W. Lee, B. Stiller, J. Hauden, H. Maillotte, C. Roch, L. Thévenaz et T. Sylvestre, « Differential phase-shift keying-based Brillouin echo distributed sensing », IEEE Photon. Technol. Lett., **24**(1), pp. 79–81 (janvier 2012), <http://ieeexplore.ieee.org/document/6046098/> (voir la page 131, Chapitre IV).
- [I.30] T. Sylvestre, A. R. Ragueh, M. W. Lee, B. Stiller, G. Fanjoux, B. Barviau, A. Mussot, and A. Kudlinski, « Black-light continuum generation in a silica-core photonic crystal fiber », Opt. Lett. **37**(2), pp. 130–132 (janvier 2012), <https://www.osapublishing.org/ol/abstract.cfm?uri=ol-37-2-130> (voir la page 137, Chapitre IV).
- [I.31] A. Boucon, B. Barviau, J. Fatome, C. Finot, T. Sylvestre, M. W. Lee, G. Millot et P. Grelu, « Noise-like pulses generated at high-harmonics in a partially-mode-locked km-long Raman fiber laser », App. Phys. B, **106**(2), pp. 283–287 (2012), <https://link.springer.com/article/10.1007/s00340-011-4816-5>.
- [I.32] B. Stiller, A. Kudlinski, M. W. Lee, G. Bouwmans, M. Delqué, J.-C. Beugnot, H. Maillotte et T. Sylvestre, « SBS Mitigation in a microstructured optical fiber by periodically varying the core

- diameter », IEEE Photon. Technol. Lett., **24**(8), pp. 667–669 (2012), <http://ieeexplore.ieee.org/document/6142012/> (voir la page 128, Chapitre IV).
- [I.33] A. Mussot, A. Kudlinski, R. Habert, I. Dahman, G. Mélin, L. Galkovsky, A. Fleureau, S. Lemperiere, L. Lago, D. Bigourd, T. Sylvestre, M. W. Lee et E. Hugonnot, « 20 THz-bandwidth continuous-wave fiber optical parametric amplifier operating at 1 μm using a dispersion-stabilized photonic crystal fiber », Opt. Express, **20**(27), pp. 28906–28911 (décembre 2012), <https://www.osapublishing.org/oe/abstract.cfm?uri=oe-20-27-28906>.
- [I.34] A. Coens, M. Chakaroun, A. P. A. Fischer, M. W. Lee, A. Boudrioua, B. Geffroy et G. Vemuri, « Experimental optimization of the optical and electrical properties of a half-wavelength-thick organic hetero-structure in a Micro-cavity », Opt. Express, **20**(28), pp. 29252–29259 (décembre 2012), <https://www.osapublishing.org/oe/abstract.cfm?uri=oe-20-28-29252>.
- [I.35] D. M. Nguyen, B. Stiller, M. W. Lee, J. C. Beugnot, H. Maillette, A. Mottet, J. Hauden, et T. Sylvestre, « Distributed Brillouin fiber sensor with enhanced sensitivity based on anti-Stokes single-sideband carrier-suppressed modulation », IEEE Photon. Technol. Lett., **25**(1), pp. 94–96 (Janvier 2013), <http://ieeexplore.ieee.org/document/6359757/> (voir la page 134, Chapitre IV).
- [I.36] Q. Ripault, M. W. Lee, F. Meriche, T. Touam, B. Courtois, E. Ntsoenzok, L.-H. Peng, A. Fischer et A. Boudrioua, « Investigation of a planar optical waveguide in 2D PPLN using Helium implantation technique », Opt. Express, **21**(6), pp. 7202–7208 (mars 2013), <https://www.osapublishing.org/oe/abstract.cfm?uri=oe-21-6-7202> (voir la page 140, Chapitre IV).
- [I.37] M. Chakaroun, A. Coens, A. P. A. Fischer, B. Ratier, A. Moliton, M. W. Lee et A. Boudrioua, « Enhanced electron injection and stability in organic light-emitting devices using an ion beam assisted cathode », Solid State Sciences, **15**, pp. 84–90 (2013), <http://www.sciencedirect.com/science/article/pii/S1293255812003056>.
- [I.38] M. W. Lee, S. Chicot, C.-C. Chen, M. Chakaroun, G. Ayenew, A. P. A. Fischer et A. Boudrioua, « Study of the light coupling efficiency of OLEDs using a nanostructured glass substrate », J. Nanoscience, 2014, pp. 258937 (2014), <https://www.hindawi.com/journals/jns/2014/258937/>.
- [I.39] Y. Souidi, F. Taleb, J. Zheng, M. W. Lee, F. Du Burck et V. Roncin, « Low-noise and high-gain Brillouin optical amplifier for narrowband active optical filtering based on a pump-to-signal optoelectronic tracking », App. Opt., **55**, pp. 248 (2016), <https://www.osapublishing.org/ao/abstract.cfm?uri=ao-55-2-248>.
- [I.40] F. Baladi, M. W. Lee, J.-R. Burie, M. A. Bettati, A. P. A. Fischer and A. Boudrioua, « High-resolution low frequency fluctuation map of a multimode laser diode subject to filtered optical feedback via a fibre Bragg grating », Opt. Lett., **41**, 2950–2953 (2016), <https://www.osapublishing.org/ol/abstract.cfm?uri=ol-41-13-2950> (voir la page 153, Chapitre IV).
- [I.41] M. W. Lee, F. Baladi, A. P. A. Fischer, M. Bettati, J.-R. Burie et A. Boudrioua, « Demonstration of optical rogue waves using a laser diode emitting at 980 nm and a fibre Bragg grating », Opt. Lett., **41**, pp. (2016), <https://www.osapublishing.org/ol/abstract.cfm?uri=ol-41-19-4476> (voir la page 157, Chapitre IV).
- [I.42] I. E. Zaldívar-Huerta, A. G. Correa-Mena, P. Hernández-Nava, A. García-Juárez, J. Rodríguez-Asomoza, M. W. Lee, « Demonstration and experimental evaluation of a bi-directional 10-GHz mi-

- crowave photonic filter », Opt. Laser Technol., **83**, pp. 76–80 (2016), <http://www.sciencedirect.com/science/article/pii/S0030399216300433>.
- [I.43] H. Chikh-Touami, R. Kremer, H-J. Lee, M. Lee, A. P. A. Fischer, L-H. Peng et A. Boudrioua, « Experimental demonstration of substantial gain enhancement of optical parametric generation in square lattice nonlinear photonic crystal », J. Opt., **19**(6), pp. 065503 (2017), <http://iopscience.iop.org/article/10.1088/2040-8986/aa67b8/pdf>.
- [I.44] H. Chikh-Touami, R. Kremer, H-J. Lee, M. Lee, L-H. Peng et A. Boudrioua, « Shared optical parametric generation interactions in square lattice nonlinear photonic crystals », App. Phys. B, **123** pp. 113 (2017), <https://link.springer.com/article/10.1007/s00340-017-6702-2>.
- [I.45] A. G. Correa-Mena, I. E. Zaldívar-Huerta, M. W. Lee, A. García-Juárez et L. A. García-Delgado, « Performance evaluation of an optoelectronic oscillator based on a band-pass microwave photonic filter architecture », Radioengineering, **26**(3), pp. 642–646 (2017), http://www.radioeng.cz/fulltexts/2017/17_03_0642_0646.pdf.
- [I.46] Z. Yellas, M. W. Lee, R. Kremer, K.-H. Chang, M. R. Beghoul, L.-H. Peng et A. Boudrioua, « Multiwavelength generation from multi-nonlinear optical process in a 2D PPLT », Opt. Express, **25**, pp. 30253–30258 (2017), <https://www.osapublishing.org/oe/abstract.cfm?uri=oe-25-24-30253> (voir la page 147, Chapitre IV).
- [I.47] A. C. Chime, S. Bensmida, M. Chakaroun, M. W. Lee, H. Nkwawo et A. P. A. Fischer, « Electrical modelling and design of ultra-fast micro-OLED with coplanar wave-guided electrodes in ON-OFF regime », Org. Electron., **56**, pp. 284–290 (2018), <https://www.sciencedirect.com/science/article/pii/S1566119917306225>.
- [I.48] A. G. Correa-Mena, M. W. Lee, I. E. Zaldívar-Huerta, Y. Hong et A. Boudrioua, « Study of the dynamical behaviour of a high-power laser diode subject to stimulated Brillouin scattering optical feedback », **en préparation**, (2018), .

I.12 CONFÉRENCES INVITÉES

- M. W. Lee et K. A. Shore, Demonstration of dual wavelength synchronisation for multiplexed optical chaos communication, **Security and Defence 2004** (SPIE European Symposium on Optics/Photonics in Security & Defence), Londres, Royaume Uni (25–28 octobre 2004).
- M. W. Lee, J. Paul, Y. Hong, I. Pierce, P. S. Spencer et K. A. Shore, Chaos communications for cryptography in external-cavity laser diodes, **ICED 2006** (International Conference on Electronic Design), Plenary Paper, Veracruz, Mexique (21–23 novembre 2006).
- M. W. Lee, F. Baladi, J.-R. Burie, M. A. Bettati, A. Boudrioua et A. P. A. Fischer, Observation of rogue waves in a 980nm-laser diode subject to filtered optical feedback, **ECCOS**, Buenos Aires, Argentine, (Décembre 2015).

I.13 CONFÉRENCES INTERNATIONALES

- [1] M. W. Lee, Y. H. Won, Y. K. Kim et H. G. Lee, The measurement of electro-optic coefficient of corona poled polymer thin film using polarimetric method, **Conference of Korean Physical Society**, Suwon, Corée du Sud (octobre 1997).

- [2] M. W. Lee, L. Larger, J.-P. Goedgebuer et W. Elflein, Dynamique chaotique sur un retard optique dans un schéma de modulation de cohérence, **3^{ième} rencontre du non-linéaire**, pp. 117–122, Paris, France (9–10 mars 2000).
- [3] M. W. Lee, L. Larger et J.-P. Goedgebuer, Mise en œuvre à des fins de cryptage d'un générateur de retard optique chaotique, **JNOG 2000**, pp. 125–127, Toulouse, France (19–22 novembre 2000).
- [4] M. W. Lee, L. Larger et J.-P. Goedgebuer, Etudes des comportements dynamiques d'un système différentiel non-linéaire du 1er ordre à 2 retards, **4^{ième} rencontre du non-linéaire**, pp. 159–164, Paris, France (9–10 mars 2001).
- [5] L. Larger, M. W. Lee et J.-P. Goedgebuer, Bifurcations de Hopf super- et sous-critique des systèmes dynamiques non-linéaires à retard : expériences et analyse perturbative, **4^{ième} rencontre du non-linéaire**, pp. 153–158, Paris, France (9–10 mars 2001).
- [6] M. W. Lee, L. Larger et J.-P. Goedgebuer, Secure optical communication using chaotic coherence modulation, **CLEO/Europe-EQEC 2001**, oral, pp. 184, Munique, Allemagne (19–22 juin 2001).
- [7] M. W. Lee, L. Larger, V. Udal'tsov, É. Genin et J.-P. Goedgebuer, New nonlinear dynamical system with 2 time delays, **CLEO/Europe-EQEC 2001**, poster, pp. 241, Munique, Allemagne (19–22 juin 2001).
- [8] M. W. Lee et K. A. Shore, Laser diode chaos generation with double optical feedback, **SIOE' 2003** (Semiconductor and Integrated OptoElectronics), orale, Cardiff, Royaume Uni (14–16 avril 2003).
- [9] M. W. Lee, J. Paul, S. Sivaprakasam et K. A. Shore, Experimental determination of message decoding quality in optical chaos communications using laser diode transmitters, **CLEO/Europe-EQEC 2003**, post-deadline paper, Munique, Allemagne (23–27 juin 2003).
- [10] M. W. Lee, J. Paul, S. Sivaprakasam et K. A. Shore, Experimental determination of message decoding quality in optical chaos communications using laser diode transmitters, **APHYS-2003**, poster, Badajoz, Espagne (13–18 octobre 2003).
- [11] M. W. Lee, J. Paul et K. A. Shore, Chaotic message broadcasting using DFB laser diodes, « First Rio de la Plata » **Workshop on Noise, Chaos and Complexity in Lasers and Nonlinear Optics**, poster, Colonia del Sacramento, Uruguay (1–5 décembre 2003).
- [12] K. A. Shore, M. W. Lee, Y. Hong, J. Paul, R. Ju, I. Pierce, P. S. Spencer, P. Rees et S. Sivaprakasam Synchronisation of chaotic external cavity laser diodes for secure optical communication networks, « First Rio de la Plata » **Workshop on Noise, Chaos and Complexity in Lasers and Nonlinear Optics**, invited, Colonia del Sacramento, Uruguay (1–5 décembre 2003).
- [13] M. W. Lee, Y. Hong et K. A. Shore, Synchronisation and message encoding using chaotic external-cavity VCSELs, **SIOE' 2004**, oral, Cardiff, Royaume Uni (5–7 avril 2004).
- [14] M. W. Lee et K. A. Shore, Dual wavelength synchronisation for multiplexed optical chaos communication, **SIOE' 2004**, poster, Cardiff, Royaume Uni (5–7 avril 2004).
- [15] M. W. Lee, Y. Hong et K. A. Shore, Synchronisation and message encoding using chaotic external-

- cavity VCSELs, **ECC8** (The 8th Experimental Chaos Conference 2004), poster, Florence, Italie (14–17 juin 2004).
- [16] S. Ortin, M. W. Lee, L. Pesquesra, K. A. Shore et A. Valle, Estimation of delay times from an external double cavity laser experiment, **ECC8** (The 8th Experimental Chaos Conference 2004), Florence, Italie (14–17 juin 2004).
 - [17] M. W. Lee et K. A. Shore, Demonstration of dual wavelength synchronisation for multiplexed optical chaos communication, **Security and Defence 2004** (SPIE European Symposium on Optics/Photonics in Security & Defence), invité, Londres, Royaume Uni (25–28 octobre 2004).
 - [18] M. W. Lee et K. A. Shore, Demonstration of network capabilities using chaotic message broadcasting with DFB laser diodes, **Security and Defence 2004**, poster, Londres, Royaume Uni (25–28 octobre 2004).
 - [19] Y. Hong, M. W. Lee et K. A. Shore, Experimental demonstration of chaos synchronisation and message encoding using chaotic VCSELs, **Security and Defence 2004**, orale, Londres, Royaume Uni (25–28 octobre 2004).
 - [20] M. W. Lee, I. Pierce et K. A. Shore, Characterisation of chaotic self-pulsating laser diodes subject to optical feedback, **SIOE' 2005**, poster, Cardiff, Royaume Uni (21–23 mars 2005).
 - [21] S. Sivaprakasam, M. W. Lee, J. Paul, P. S. Spencer et K. A. Shore, Partial bi-directional coupling of chaotic diode lasers for secure optical communication, **SIOE' 2005**, poster, Cardiff, Royaume Uni (21–23 mars 2005).
 - [22] M. W. Lee et K. A. Shore, Demonstration of chaotic message relay for secure optical communication networks, **PhAST/CLEO**, orale, Baltimore, USA (23–26 mai 2005).
 - [23] M. W. Lee, J. Paul, I. Pierce et K. A. Shore, Demonstration of synchronisation-switching via frequency-detuning for secure optical communications, **OECC 2005** (OptoElectronics and Communications Conference), poster, Séoul, Corée du Sud (4–8 juillet 2005).
 - [24] J. Paul, M. W. Lee et K. A. Shore, Effect of chaos pass filtering on multi-GHz message transmission using chaotic DFB laser diodes, **OECC 2005**, poster, Séoul, Corée du Sud (4–8 juillet 2005).
 - [25] K. A. Shore, M. W. Lee, J. Paul, Y. Hong, R. Ju et P. S. Spencer, Network technologies for chaotic optical communications, **ISMOT-2005** (10th International Symposium on Microwave and Optical Technology), invité, Fukuoka, Japon (22–25 août 2005).
 - [26] J. P. Toomey, D. M. Kane, M. W. Lee et K. A. Shore, Chaotic semiconductor laser (CSL) and synchronised CSL - chaos analysis and noise, **2005 IEEE LEOS**, orale, Sydney, Australie, 22-28 October, 2005(22 – 28 octobre 2005)
 - [27] M. W. Lee, J. Paul, C. Masoller et K. A. Shore, Demonstration of contemporaneous cascade chaos synchronisation in laser diodes, **SIOE' 2006**, poster, Cardiff, Royaume Uni (10–12 avril 2006).
 - [28] M. W. Lee, I. Pierce et K. A. Shore, Synchronisation of chaotic pulse-sequences in self-pulsating laser diodes, **Workshop on the Transmission of Chaotic Signals**, orale, Bristol, Royaume Uni (1–3 août 2006).

- [29] M. W. Lee, J. Paul, C. Masoller et K. A. Shore, Demonstration of contemporaneous chaos synchronisation using three-unidirectionally coupled laser diodes, **Workshop on the Transmission of Chaotic Signals**, poster, Bristol, Royaume Uni (1–3 août 2006).
- [30] K. A. Shore, S. Sivaprakasam, P. S. Spencer, Y. Hong, I. Pierce, J. Paul, M.W. Lee, R. Ju, S. Peters-Flynn et P. Rees, Chaos synchronisation and communication in lasers diodes, **Workshop on the Transmission of Chaotic Signals**, orale, Bristol, Royaume Uni (1–3 août 2006).
- [31] K. A. Shore, M. W. Lee, J. Paul, Y. Hong, I. Pierce et P. S. Spencer, Networked Chaotic Optical Communications, **Photonics Conference 2006**, Plenary Paper, Sorak, Corée du Sud (8–10 novembre 2006).
- [32] M. W. Lee, J. Paul, Y. Hong, I. Pierce, P. S. Spencer et K. A. Shore, Chaos communications for cryptography in external-cavity laser diodes, **ICED 2006** (International Conference on Electronic Design), Plenary Paper, Veracruz, Mexique (21–23 novembre 2006).
- [33] K. A. Shore, Y. Hong, M. W. Lee, J. Paul, A. Murakami, I. Pierce et P. S. Spencer, Chaos synchronization and message extraction in optical chaos communications, **XVI Conference on Nonequilibrium Statistical Mechanics and Nonlinear Physics** (Medyfinol '06), invité, Mar dela Plata, Argentine, (décembre 2006).
- [34] M. W. Lee et I. Pierce, Chaos synchronisation of self-pulsating laser diodes, **SIOE' 2007**, oral, Cardiff, Royaume Uni (2–4 avril 2007).
- [35] M. W. Lee et I. Pierce, Routes to chaos in a self-pulsating laser diode driven by external modulation, **SIOE' 2007**, poster, Cardiff, Royaume Uni (2–4 avril 2007).
- [36] M. W. Lee et I. Pierce, Chaos synchronisation of self-pulsating laser diodes, **CLEO/Europe-IQEC 2007**, poster, Munique, Allemagne (17–22 juin 2007).
- [37] K. A. Shore, M. W. Lee, J. Paul, Y. Hong, I. Pierce et P. S. Spencer, Application of external cavity semiconductor lasers in optical chaos communications, **CLEO/Pacific Rim 2007**, invité, Séoul, Corée du Sud (26–31 août 2007).
- [38] B. Stiller, M. Delqué, M. W. Lee, T. Sylvestre, J.-C. Beugnot, A. Kudlinski et H. Maillotte, Characterization of backward and forward Brillouin scattering in photonic crystal fibers, **COST 299 Meeting**, Wroclaw, Pologne (9–11 septembre 2009).
- [39] B. Stiller, M. Delqué, M. W. Lee, S. F. Mafang, J.-C. Beugnot, A. Kudlinski, L. Thévenaz, H. Maillotte et T. Sylvestre, Effect of inhomogeneities on backward and forward Brillouin scattering in photonic crystal fibers, **SPIE 2010**, orale, Bruxelles, Belgique (12–16 avril 2010).
- [40] J-C. Beugnot, M. Delqué, B. Stiller, M. W. Lee, H. Maillotte, V. Laude, Gilles Mélin et T. Sylvestre, Guided acoustic wave Brillouin scattering in a nanostructure core fiber, **Nonlinear Photonics 2010**, orale, Karlsruhe, Allemagne (21 – 24 juin 2010).
- [41] M. W. Lee, T. Sylvestre, M. Delqué, A. Kudlinski, A. Mussot, J.-F. Gleyze, A. Jolly et H. Maillotte, All-fibre optical parametric amplifier at 1 ?m using a microstructured fibre, **NFO2010**, orale, Cancun, Mexique (19 – 21 juillet 2010).
- [42] B. Stiller, J-C. Beugnot, S. Foaleng Mafang, M. W. Lee, M. Delqué, A. Kudlinski, H. Maillotte, V. Laude, L. Thévenaz et T. Sylvestre, Observation of Brillouin linewidth broadening and decay

- time in photonic crystal fiber, **NFO2010**, poster, Cancun, Mexique (19 – 21 juillet 2010).
- [43] J.-C. Beugnot, B. Stiller, S. Foaleng Mafang, M. W. Lee, M. Delqué, A. Kudlinski, H. Maillotte, V. Laude, L. Thévenaz et T. Sylvestre, Experimental observation of Brillouin linewidth broadening and decay time in photonic crystal fiber, **ECOC2010**, orale, Turin, Italie (19 – 23 septembre 2010).
- [44] M. W. Lee, T. Sylvestre, M. Delqué, A. Kudlinski, A. Mussot, J.-F. Gleyze, A. Jolly et H. Maillotte, Demonstration of an all-fibre broadband optical parametric amplifier at 1 μm , **JNOG 2010**, poster, Besançon, France (20 – 22 octobre 2010).
- [45] B. Stiller, S. Foaleng Mafang, J.-C. Beugnot, M. Delqué, M. W. Lee, A. Kudlinski, L. Thévenaz, H. Maillotte et T. Sylvestre, Cartographie des fibres optiques microstructurées par détection des échos Brillouin, **JNOG2010**, poster, Besançon, France (20 – 22 octobre 2010).
- [46] A. Boucon, J. Fatome, C. Finot, G. Millot, T. Sylvestre, M. W. Lee et P. Grelu, Laser impulsif Raman à verrouillage de mode passif fonctionnant à 1 GHz, **JNOG2010**, orale, Besançon, France (20 – 22 octobre 2010).
- [47] J. P. Toomey, D. M. Kane, M. W. Lee et K. A. Shore, Instabilities in semiconductor laser with optical feedback and modulation, **COMMAD2010**, orale, Canberra, Australie (12 – 15 décembre 2010)
- [48] B. Stiller, M. W. Lee, M. Delqué, G. Bouwmans, A. Kudlinski, J.-C. Beugnot, H. Maillotte et T. Sylvestre, Suppression of SBS in a photonic crystal fiber with periodically-varied core diameter, **OFC2011**, orale, Los Angeles, USA, (6 – 10 mars 2011).
- [49] A. Boucon, B. Barviau, J. Fatome, C. Finot, T. Sylvestre, M. W. Lee, P. Grelu et G. Millot, High-harmonic km-long self-pulsed Raman fiber laser, **CLEO/Europe 2011**, orale, Munich, Allemagne (22 – 26 mai 2011).
- [50] M. W. Lee, B. Stiller, J. Hauden, H. Maillotte, L. Thévenaz et T. Sylvestre, Capteur distribué à fibre optique à haute résolution utilisant l'effet Brillouin et la technique DPSK, **JNOG2011**, orale, Marseille, France (4 – 7 juillet 2011).
- [51] B. Stiller, M. W. Lee, M. Delqué, G. Bouwmans, A. Kudlinski, J.-C. Beugnot, H. Maillotte et T. Sylvestre, Suppression de l'effet Brillouin dans une fibre optique microstructurée périodique, **JNOG2011**, poster, Marseille, France (4 – 7 juillet 2011).
- [52] A. R. Ragueh, M. W. Lee, B. Stiller, B. Barviau, A. Mussot, A. Kudlinski et T. Sylvestre, Génération d'un continuum de lumière noire dans une fibre optique microstructurée avec un laser ultraviolet, **JNOG2011**, poster, Marseille, France (4 – 7 juillet 2011).
- [53] M. W. Lee, B. Stiller, J. Hauden, H. Maillotte, L. Thévenaz et T. Sylvestre, Brillouin echo-distributed sensing based on differential phase-shift keying technique, **ECOC2011**, orale, Genève, Suisse (18 – 22 septembre 2011).
- [54] B. Stiller, M. W. Lee, J. Hauden, A. Mottet, D. M. Nguyen, H. Maillotte et T. Sylvestre, Fiber optic Brillouin distributed sensing using phase-shift keying modulation techniques, **2012 Photonics Europe/SPIE**, orale, Bruxelles, Belgique (16 – 19 avril 2012).
- [55] T. Sylvestre, A.-I. Robleh Ragueh, M. W. Lee, B. Stiller, G. Fanjoux, B. Barviau, A. Mussot

- et A. Kudlinski, Supercontinuum generation in the black light region by pumping at 355 nm a silica photonic crystal fiber, **2012 Photonics Europe/SPIE**, orale, Bruxelles, Belgique (16 – 19 avril 2012).
- [56] A. Coens, A. P. Fischer, M. W. Lee, M. Chakaroun, A. Boudrioua, J. Solard, B. Geffroy, D. Tondelier, M. Lequime, Experimental and theoretical study of the optical and electrical properties optimization of an OLED in a microcavity, **2012 Photonics Europe/SPIE**, orale, Bruxelles, Belgique (16 – 19 avril 2012).
- [57] T. Sylvestre, M. W. Lee, A.-I. Robleh Ragueh, B. Stiller, G. Fanjoux, B. Barviau, A. Mussot et A. Kudlinski, Supercontinuum generation with picosecond ultraviolet pulses in a solid-core photonic crystal fiber, **Nonlinear Photonics**, orale, Colorado, Etats-Unis (17 – 21 juin 2012).
- [58] A. Mussot, A. Kudlinski, L. Lago, D. Bigourd, T. Sylvestre, M. W. Lee et E. Hugonnot, Experimental demonstration of all-fiber continuous wave optical parametric amplifier operating at 1 μm , **Nonlinear Photonics**, orale, Colorado, Etats-Unis (17 – 21 juin 2012).
- [59] H. Maillotte, J.-C. Beugnot, B. Stiller, M. W. Lee, D. M. Nguyen, M. Delqué, S. Benchabane, V. Laude, S. Foaleng Mafang, L. Thévenaz, G. Bouwmans, A. Kudlinski, G. Mélin, J. Hauden et T. Sylvestre, Opto-acoustic coupling and Brillouin phenomena in microstructure optical fibers, **IEEE OECC 2012**, invité, Busan, Corée du Sud (2 – 6 juillet 2012).
- [60] Q. Ripault, M. W. Lee, F. Meriche, T. Touam, A. Boudrioua, E. Ntsoenzok, L. H. Peng et A. Fischer, Guides d'ondes optiques par implantation d'hélium (He+) dans les cristaux photoniques non linéaire (PPLN 2D), **JNOG2012**, orale, Lyon, France (10 – 12 juillet 2012).
- [61] F. Baladi, M. W. Lee, A. Fischer, A. Boudrioua, J.-R. Burie et M. Bettiati, Etude du comportement dynamique de diodes laser de puissance soumises à un retour optique sélectif en fréquence au voisinage du régime cohérence collapse, **JNOG2012**, poster, Lyon, France (10 – 12 juillet 2012).
- [62] C. C. Chen, S. Chicot, M. W. Lee, A. Fischer et A. Boudrioua, Amélioration de l'extraction lumineuse d'OLED en utilisant des substrat de verre nanostructurés dans le volume, **JNOG2012**, poster, Lyon, France (10 – 12 juillet 2012).
- [63] A. Coens, M. Chakaroun, A. P. Fischer, M. W. Lee, J. Solard, B. Geffroy et A. Boudrioua, Etude expérimentale et théorique sur l'optimisation des propriétés optiques et électriques d'OLED en microcavité, **JNOG2012**, poster, Lyon, France (10 – 12 juillet 2012).
- [64] D. M. Nguyen, B. Stiller, M. W. Lee, J.-C. Beugnot, H. Maillotte, T. Sylvestre, A. Mottet et J. Hauden, Capteur Brillouin reparti à fibre optique utilisant la modulation à bande latérale unique, **JNOG2012**, orale, Lyon, France (10 – 12 juillet 2012).
- [65] F. Baladi, A. P. A. Fischer, M. W. Lee, J.-R. Burie, A. Boudrioua et M. A. Bettiati, Diagramme des instabilités basses fréquences de diode laser 974nm soumise à un retour optique sélectif en fréquence provenant d'un FBG , **JNOG2013**, Poster, Lyon, France France (juillet 2013).
- [66] F. Baladi, M. W. Lee, A. P. A. Fischer, J.-R. Burie, A. Boudrioua et M. A. Bettiati, Map of the low frequency fluctuations in a high power diode laser subject to filtered optical feedback viaa fiber bragg grating, **ISPALD**, orale, France, Paris, (Octobre 2013).
- [67] M. W. Lee, F. Baladi , M. Morali, A. Boudrioua, J.-R. Burie, M. Bettiati et A. Fischer, Etude de

- l’élargissement spectral d’une diode laser soumise à un retour optique sélectif en fréquence issu d’un FBG », Poster, **JNOG2014**, Nice, France (Octobre 2014).
- [68] M. W. Lee, F. Baladi, J.-R. Burie, M. A. Bettiati, A. Boudrioua et A. P. A. Fischer, Cartographie de l’apparition d’ondes spectrales dans une diode laser à 980 nm soumise à un retour optique filtre spectralement, **JNOG2015**, Poster, Rennes, France (Juillet 2015).
- [69] M. W. Lee, F. Baladi, J.-R. Burie, M. A. Bettiati, A. Boudrioua et A. P. A. Fischer, Observation of rogue waves in a 980nm-laserdiode subject to filtered optical feedback, **CLEO Pacific RIM**, orale, Busan, Corée du Sud (Aout 2015).
- [70] F. Baladi, M. W. Lee, J.-R. Burie, M. A. Bettiati, A. Boudrioua et A. P. A. Fischer, Revisiting low frequency fluctuations in high power multi-mode laser diodes subject to filtered optical feedback, **CLEO Pacific RIM**, poster, Busan, Corée du Sud (Aout 2015).
- [71] M. W. Lee, F. Baladi, J.-R. Burie, M. A. Bettiati, A. Boudrioua et A. P. A. Fischer, Observation of rogue waves in a high-power laser diode subject to optical feedback via a fibre Bragg grating, **ISPALD**, orale, Metz, France (Octobre 2015).
- [72] F. Baladi, M. W. Lee, J.-R. Burie, M. A. Bettiati, A. Boudrioua et A. P. A. Fischer, Low frequency fluctuation mapping of a high power laser diode emitting at 980 nm subject to filtered optical feedback, **ISPALD**, poster, Metz, France (Octobre 2015).
- [73] M. W. Lee, F. Baladi, J.-R. Burie, M. A. Bettiati, A. Boudrioua et A. P. A. Fischer, Observation of rogue waves in a 980nm-laserdiode subject to filtered optical feedback, **ECCOS**, Invité, Buenos Aires, Argentine, (Décembre 2015).
- [74] A. Chime, A. P. A. Fischer, L. Zeng, M. Chakaroun, M. W. Lee, S. Bensmida, H. Nkwawo, et A. Boudrioua, Réponse impulsionale de micro-OLEDs soumises à des impulsions électriques nanoseconde à haute densité de courant, **JNPO2016**, oral, Bordeaux, France (Juillet 2016).
- [75] Z. Illas, M. W. Lee, R. Kremer, K.-H. Chang, M. R. Beghoul, L.-H. Peng et A. Boudrioua, Simultaneous frequency conversions in nonlinear photonic crystals of lithium tantalate with a square lattice and multiwavelength generation from multi-nonlinear optical process in a 2D PPLT, **CLEO/Europe 2017**, poster, Munique, Allemagne (25 – 29 juin 2017).
- [76] Z. Illas, M. W. Lee, R. Kremer, K.-H. Chang, M. R. Beghoul, L.-H. Peng et A. Boudrioua, Conversion de fréquences en cascade dans les cristaux photoniques non-linéaires de PPLT 2D, **JNOG-JCOM2017**, poster, Bordeaux, France (4 – 6 juillet 2017).
- [77] A. G. Correa-Mena, M. W. Lee, I. E. Zaldívar-Huerta, Y. Hong et A. Boudrioua, Study of the dynamical behaviour of a high-power laser diode subject to stimulated Brillouin scattering optical feedback, **Optique2018**, poster, Toulouse, France (3 – 5 juillet 2018).
- [78] L. J. Quintero-Rodríguez, M. W. Lee, A. G. Correa-Mena et I. E. Zaldívar-Huerta, Simulation of the Brillouin effect in an optical feedback, **Frontiers in Optics/Laser Science 2018**, poster, Washington, Etats-Unis (16 – 20 septembre 2018).

I.14 BREVET

- H. Nkwawo, A. P. A. Fischer, A. Chime, L. Zeng, M. W. Lee, M. Chakaroun et A. Boudrioua, Micro organic opto-électronic device configured for high current density, Déposé à l'Office européen des brevets, (septembre 2017).

ACTIVITÉS DE RECHERCHE AVANT UP13

Sommaire

| | |
|---|-----------|
| II.1 Thèse de doctorat | 24 |
| II.2 Activités de recherche à l’Université de Bangor | 25 |
| 2.1 Synchronisation des diodes lasers soumises à un retour optique et communications sécurisées par chaos | 25 |
| 2.2 Synchronisation et communications chaotiques utilisant des VCSELs | 31 |
| 2.3 Système de trois diodes lasers en cascade | 32 |
| II.3 Activités de recherche à l’Institut FEMTO-ST | 35 |
| 3.1 Effets non linéaires dans une fibre optique | 35 |
| 3.2 Amplificateur paramétrique à fibre optique | 37 |
| 3.3 Rétrodiffusion Brillouin stimulée et ses applications aux capteurs distribués à fibre optique | 40 |
| 3.3.1 BOTDA et BEDS | 40 |
| 3.3.2 Etudes de PCF | 42 |
| 3.3.3 DPSK-BEDS | 44 |
| 3.4 Génération de continuum dans la bande UV dans une PCF | 45 |
| II.4 Résumé | 46 |
| Bibliographies | 47 |

J'ai soutenu ma thèse de doctorat le 19 février 2002 au sein du Laboratoire d'Optique P. M. Duffieux à Besançon. Après ma thèse, je suis parti au Royaume Uni pour faire des recherches post-doctorales. Par la suite je suis revenu au laboratoire de Besançon. Lors de mes travaux post-doctoraux, j'ai pu enrichir mes connaissances et expertises dans diverses thématiques de recherche : la théorie du chaos, la synchronisation de chaos, et les communications optiques chaotiques, d'une part, l'étude des fibres microstructurées, l'amplificateur paramétrique à fibre et les capteurs distribués à fibre microstructurées, d'autre part. De solides compétences dans les trois premières thématiques de recherche ont été développées lors de mon travail post-doctoral à l'université de Bangor (Royaume Uni). Les trois dernières thématiques de recherche correspondent à mes axes de recherche développés au sein de l'institut FEMTO-ST UMR 6174 à Besançon. Dans ce chapitre, je vais décrire rapidement les travaux que j'ai réalisés durant les années avant mon arrivée à l'Université Paris 13.

II.1 THÈSE DE DOCTORAT

J'ai effectué ma thèse de doctorat dans le domaine de la théorie du chaos pour l'application aux communications sécurisées dans le groupe *Optoélectronique* sous la direction de M. Jean-Pierre Goedgebuer et de M. Laurent Larger. Grâce aux travaux de thèse, j'ai acquis des compétences dans les domaines du chaos et de l'optoélectronique. Ma principale contribution dans ces travaux a été la mise en œuvre expérimentale d'un système de communications sécurisées par chaos en modulation de cohérence. Dans la partie suivante, je présenterai un résumé de mes travaux de thèse.

Titre : Étude des comportements chaotiques en modulation de cohérence et application à la cryptographie.

- Dates : octobre 1998 – février 2002
- Résumé : Ce travail de thèse concerne la démonstration théorique et expérimentale d'un système de communication optique sécurisé. Il exploite principalement deux principes physiques, la modulation de cohérence optique d'une source à large spectre, et les fluctuations chaotiques du retard optique produit par un modulateur électro-optique de Mach-Zehnder intégré. Ces fluctuations chaotiques de très grande dimension sont générées par un oscillateur non-linéaire à simple ou double retard temporel, dont la non-linéarité est produite par la fonction de transfert de modulation de cohérence. L'association de la modulation de cohérence et du chaos permet un double niveau de sécurité. Une information est ainsi noyée dans une dynamique chaotique, elle-même masquée par la modulation de cohérence qui ne génère quasiment aucune variation d'intensité optique. Le décodage est obtenu par la soustraction optique entre le faisceau reçu et un chaos local synchronisé, avec un rapport signal-à-bruit de 33dB.
- Directeurs de thèse : M. Jean-Pierre Goedgebuer et M. Laurent Larger
- Soutenue le 19 février 2002

- Lieu : Laboratoire d'Optique P. M. Duffieux UMR 6603 (actuellement, devenu FEMTO-ST UMR 6174), Université de Franche-Comté
- Composition du jury :
 - Président : M. Daniel Van Labeke, Professeur à l'Université de Franche-Comté
 - Rapporteurs : M. Thomas Erneux, Directeur de Recherche à l'Université Libre de Bruxelles
 - Rapporteurs M. Alain Brun, Professeur à l'Institut d'Optique Théorique et Appliquée, Université de Paris-Sud-Orsay
 - Examinateurs : M. Jean-Pierre Goedgebuer, Professeur à l'Université de Franche-Comté
 - Examinateurs : M. Laurent Larger, Maître de conférences à l'Université de Franche-Comté

Mots clés : Télécommunications optiques, Cryptage par chaos, Optique intégrée

II.2 ACTIVITÉS DE RECHERCHE À L'UNIVERSITÉ DE BANGOR

LES COMMUNICATIONS SÉCURISÉES PAR CHAOS était une des principales activités de recherche que j'ai menée à Bangor. C'était également la thématique de ma thèse. Durant mes travaux à Bangor j'ai travaillé dans l'équipe Optoélectronique avec K. Alan Shore (responsable d'équipe), Sivaraman Sivaprakasam, Yanhua Hong et Jon Paul, un doctorant que j'ai co-encadré. Les projets de recherche portaient sur la mise en œuvre expérimentale des communications optiques chaotiques utilisant des diodes lasers à cavité externe. Ces travaux ont été financés par deux projets européens OCCULT (Optical Chaos Communication Using Laser Transmitters, IST-2000-29683) et PICASSO (Photonic Integrated Components Applied to Secure chaoS encoded Optical communications systems, FP6-2006-IST-2.5.1), et par un projet britannique EPSRC (Engineering and Physical Sciences Research Council, GR/S22936/01). Ces travaux ont donné lieu à de nombreuses publications et des collaborations avec des équipes espagnoles et une équipe australienne. Durant ces années, j'ai principalement contribué au développement de différents systèmes de communications optiques chaotiques utilisant des diodes lasers, au co-encadrement d'un doctorant, Jon Paul, et à la participation aux différentes activités des projets. Dans cette section, je vais décrire principalement les travaux sur la synchronisation de chaos et les communications optiques chaotiques utilisant différents types de lasers dans des configurations variées.

2.1 Synchronisation des diodes lasers soumises à un retour optique et communications sécurisées par chaos

La synchronisation de chaos est une thématique qui s'appuie sur la théorie du chaos. Cette dernière a été énoncée pour la première fois par Henri Poincaré dans son livre mentionnant une sensibilité aux conditions initiales dans un système solaire à trois corps [II.1]. Une poignée de scientifique russe a également travaillé sur le même phénomène. La théorie du chaos est cependant considérée comme un

nouveau phénomène à partir de 1963, lorsque E. Lorenz, un météorologue américain, l'a redécouvert et appelé ce phénomène le fameux « effet papillon » [II.2]. Depuis, de nombreux scientifiques ont commencé à travailler sur ce phénomène dans divers domaines y compris en optique. Le signal chaotique est très sensible aux conditions initiales et a une allure d'un comportement dynamique complexe, mais déterministe. De ce fait, il est considéré pseudo-aléatoire. Malgré le comportement dynamique complexe, Pecora et Carroll ont proposé une méthode pour synchroniser deux oscillateurs chaotiques en transmettant une des variables dont le degré de complexité est le plus élevé [II.3]. A partir de leur première démonstration de synchronisation de chaos, d'autres techniques ont été proposées dans différents systèmes, notamment dans des systèmes de laser chaotiques [II.4, II.5, II.6].

Le système chaotique sur lequel j'ai travaillé durant mon post-doc est une diode laser soumise à un retour optique (optical feedback) par un miroir externe comme montré sur la figure II.1. Sur celle-ci, la diode laser a une émission continue et le miroir externe renvoie l'émission. L'atténuateur permet de varier le taux de retour optique. Ce retour optique modifie les propriétés de la diode laser introduisant l'élargissement spectrale, la diminution du seuil de laser et les comportements dynamiques chaotiques [II.4, II.7, II.8].



FIGURE II.1 – Diode laser soumise à un retour optique par un miroir externe.

Plus particulièrement, les comportements dynamiques d'une diode laser changent radicalement avec le taux de retour optique. Les comportements se classent en cinq régimes [II.9] :

- **Régime I** : Taux de retour [-90 à -52 dB]. En fonction de la phase de l'onde réinjectée la raie laser peut être soit affinée ou élargie en comparaison avec celle d'un laser isolée (non soumis à une rétro injection optique).
- **Régime II** : Taux de retour [-52 à -45 dB]. Ce régime se caractérise par l'apparition d'un phénomène de saut de modes entre les différents modes de cavité externe.
- **Régime III** : Taux de retour [-45 à -39 dB]. L'émission de laser est stable et monomode sur le mode de plus faible largeur de raie (K. Petermann, 1988).
- **Régime IV** : Taux de retour [-39 à -9 dB]. Des harmoniques de la fréquence d'oscillation de relaxation apparaissent, ce qui provoque un élargissement du spectre d'émission pouvant conduire une perte de cohérence (coherence collapse) [II.10]. Il s'agit d'un régime où la diode laser perd toute ses caractéristiques de mono-chromatique, son spectre d'émission est d'allure chaotique avec une largeur de raie considérablement augmentée. Certains systèmes de télécommunication optique utilisent des diodes lasers fonctionnant dans ce régime pour obtenir une émission large spectre.
- **Régime V** : Taux de retour [> -10 dB]. C'est le « régime de stabilisation » où la diode laser

retrouve sa cohérence et l'émission se stabilise sur un mode de cavité externe avec une très faible largeur de raie.

Une grande attention a été portée particulièrement au régime IV. Ce dernier correspond à un régime où la diode laser peut manifester un comportement dynamique chaotique. De ce fait, on assimile un laser dans ce régime à un *laser chaotique*.

Le comportement chaotique est un comportement complexe, mais déterministe avec une très grande sensibilité aux conditions initiales. Afin de synchroniser un laser chaotique comme celui de la figure II.1, il faut une autre diode laser dont les caractéristiques sont identiques ou similaires pour construire un système maître-esclave comme montré sur la figure II.2.

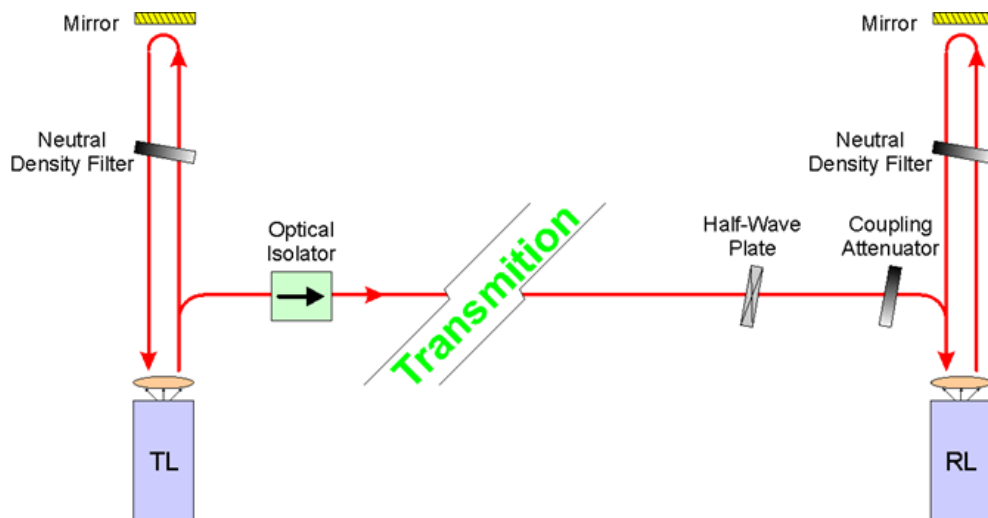


FIGURE II.2 – Deux diodes lasers en maître-esclave dans une configuration de boucle-fermée.

Dans ce système, une partie du signal optique chaotique du maître est envoyé à l'esclave. L'esclave est progressivement entraîné par le maître et fini par émettre le même signal chaotique ; ce que l'on appelle la *synchronisation de chaos*. Cette procédure de synchronisation est illustré sur la figure II.3(a).

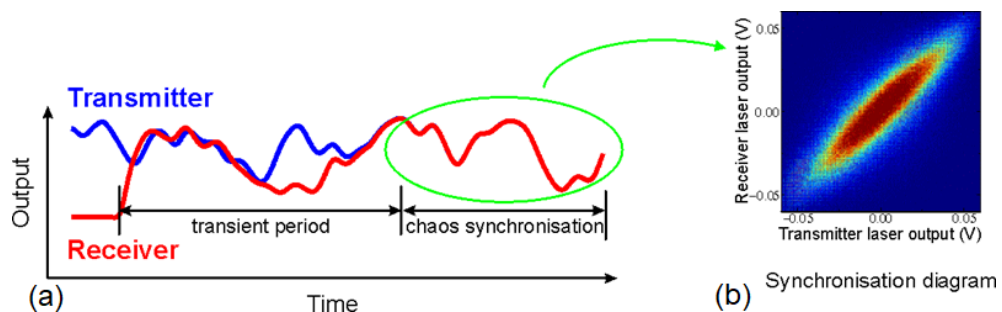


FIGURE II.3 – (a) Synchronisation de deux signaux chaotiques. (b) Diagramme de synchronisation

En synchronisation de chaos, les deux lasers émettent les mêmes signaux chaotiques avec un retard temporel dû au temps de vol entre le maître et l'esclave. En tenant compte de ce retard temporel, un diagramme de synchronisation peut être construit avec une représentation qualitative de l'intensité des

deux signaux maître-esclave comme montré sur la figure II.3(b). Beaucoup de démonstrations ont été rapportées suivant cette configuration [II.11, II.12, II.13, II.14].

Jusqu'en 1993, la synchronisation de chaos a fait l'objet de recherche fondamentale. A partir de cette date, des applications commencent à apparaître particulièrement dans la sécurisation des communications. De nos jours, les télécommunications sont partout, soit par les ondes hertziennes, soit par la lumière. Dans ces communications, une énorme quantité de données est transférée à chaque instant. Cependant, une faille de sécurité de données peut produire un dégât économique considérable. La demande de la sécurisation de communication devient de plus en plus forte.

En 1993, Hayes et ses collègues ont rapporté qu'il était possible de masquer un message par le chaos dans le contexte d'une communication sécurisée [II.15]. Le chaos possède un caractère de bruit. Ce dernier n'est pas aléatoire, mais correspond à un bruit pseudo-aléatoire qui est déterministe et reproductible. Ces caractéristiques du chaos permettent de masquer une information en la mélangeant à un bruit chaotique (la porteuse chaotique) dans un émetteur. L'information est donc protégée par le chaos contre un espionnage pendant la transmission. Afin de pouvoir extraire l'information, le récepteur doit effectuer une synchronisation afin de reproduire le même chaos que celui de l'émetteur suivant l'ajustement délicat des paramètres dynamiques (clés de décodage) entre l'émetteur et le récepteur. Grâce à la synchronisation de chaos, le message peut alors être décodé par une soustraction entre le chaos mélangé avec le message et le chaos reproduit au niveau du récepteur.

En optique, les communications chaotiques sont une des applications de laser chaotique qui a déjà donné naissance à plusieurs démonstrateurs dans des systèmes optoélectroniques [II.16, II.17], dans des systèmes laser en anneau dopé erbium [II.18], des lasers à retour électrique [II.19], des lasers microchip Nd:YVO₄ [II.20] ou encore des laser à cavité externe [II.21, II.22, II.23]. C'est une nouvelle technique de sécurisation de message qui possède un grand potentiel d'application dans les télécommunications optiques. Beaucoup de projets dans ce thème de recherche ont été globalement lancés, dont les deux projets européens OCCULT et PICASSO. De nombreux travaux ont été publiés avec des résultats remarquables. Ce thème de recherche m'a donc motivé pour effectuer une thèse en France et un post-doctorat au Royaume Uni.

Nous allons regarder comment fonctionnent les communications optiques chaotiques avec deux lasers à cavité externe. Dans une configuration de deux diodes lasers, un message peut être ajouté au laser émetteur par une modulation directe comme montré sur la figure II.4(a). Sur la figure, le message est un signal sinusoïdal à 1 GHz. Le message est donc dissimulé par un signal chaotique émis par la diode laser à cavité externe comme montré sur le tracé rouge de la figure II.4(b). Le message crypté (caché par le signal chaotique) est ensuite envoyé au récepteur. Sur la figure II.4(b), il est possible de remarquer une petite différence d'amplitude entre les tracés de l'émetteur et du récepteur. Alors que la sortie de l'émetteur (le tracé rouge) contient du signal chaotique et le message, la sortie du récepteur (le tracé bleu) ne contient que du signal chaotique qui est le même que celui de l'émetteur grâce à la synchronisation de chaos. Une soustraction entre les deux signaux peut donc être effectuée afin de

récupérer le message d'origine. Cette technique est appelé *filtrage de passe chaotique*.

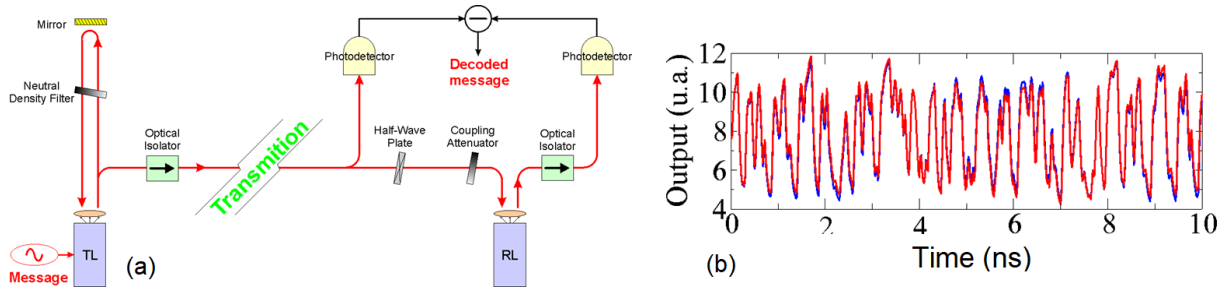


FIGURE II.4 – (a) Banc expérimental de communications sécurisées par chaos utilisant deux diodes lasers. (b) Tracés de l'émetteur (courbe rouge) et du récepteur (courbe bleue).

Dans ce contexte, j'ai travaillé sur la synchronisation de chaos et les communications sécurisées par chaos suivant une configuration présentée sur la figure II.2. Dans un premier temps, nous avons effectué une étude comparative de deux configurations : une boucle ouverte et une boucle fermée. Si le récepteur a la même cavité que celle de l'émetteur comme la figure II.2, c'est une configuration de boucle fermée. En revanche, quand le récepteur est une simple diode laser sans cavité comme la figure II.4(a), c'est une configuration de boucle ouverte. De nombreuses études ont été faites avec les deux configurations, mais sans comparaison des deux configurations. Nous avons menée pour la première fois une étude comparative et notre étude comparative a indiqué que la configuration de la boucle ouverte a de meilleures performances de l'extraction de messages [ACL I.6] (voir la page 86, Chapitre IV).

Nous avons aussi travaillé sur la diffusion d'un message à deux récepteurs. Le message est un signal sinusoïdal de 1 GHz dissimulé par un signal chaotique. Ce message codé est envoyé à deux récepteurs simultanément. La synchronisation est ainsi obtenue entre l'émetteur et les deux récepteurs. Ceci est une première démonstration de communication chaotique montrant qu'un émetteur peut envoyer le message à plusieurs récepteurs. Le message est récupéré à chaque récepteur avec un rapport signal-surface de 14 dB comme montré sur la figure II.5 [ACL I.9] (voir la page 89, Chapitre IV).

Nous avons également étudié l'effet de filtrage de passe chaotique avec la configuration de la figure II.4(a). Une diode laser possède intrinsèquement une oscillation de relaxation. Il s'agit d'une oscillation au début de l'émission laser avant d'arriver à une émission constante et stable. Sa fréquence est généralement de l'ordre de GHz. Cette oscillation de relaxation impacte les performances du filtrage de passe chaotique. Afin d'extraire le message du signal chaotique, le récepteur ne doit que reproduire le signal chaotique sans le message. La figure II.6 montre les amplitudes du message de l'émetteur, du récepteur et du message récupéré au récepteur. La fréquence d'oscillation de relaxation est de 6,58 GHz. En augmentant la fréquence du message, son amplitude de message codé à l'émetteur ne varie pas beaucoup alors que celle du récepteur augmente. Cela signifie que vers la fréquence d'oscillation de relaxation le récepteur est entraîné à reproduire aussi le message de l'émetteur. Cette synchronisation ne permet pas d'extraire le message par une soustraction. Par conséquent, l'amplitude du message

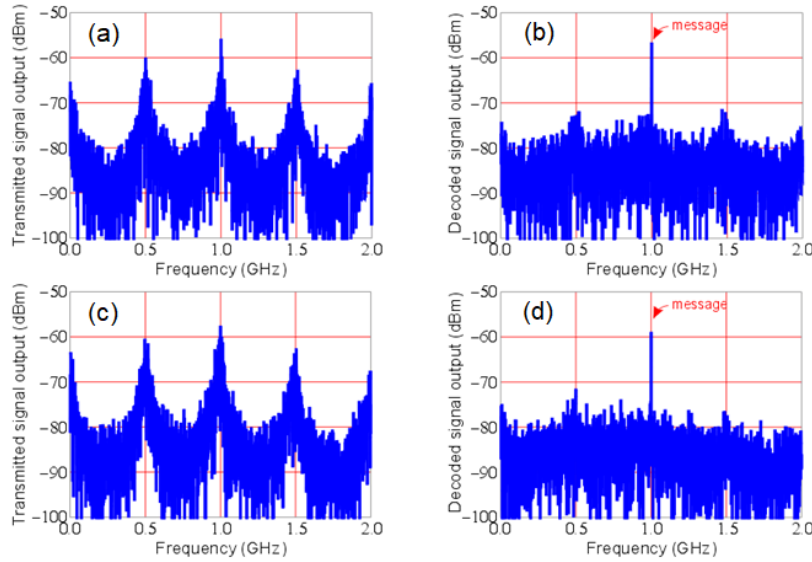


FIGURE II.5 – Spectres RF (a) d'un message codé reçu par le récepteur 1, (b) d'un message récupéré au récepteur 1, (c) d'un message reçu par le récepteur 2 et (d) d'un message récupéré au récepteur 2. Source : Réf. [ACL I.9].

extrait du récepteur diminue en augmentant la fréquence du message vers la fréquence d'oscillation de relaxation [ACL I.13] (voir la page 91, Chapitre IV). Ce travail a renseigné pour la première fois la bande passante d'un tel système de communications sécurisées par chaos. D'après la figure, la bande passante de notre système est de 3,5 GHz à -3 dB. Par la suite, nous avons démontré une transmission d'un message à 3,5 GHz, ce qui est la transmission de message dont la fréquence est la plus haute à l'époque [ACL I.16].

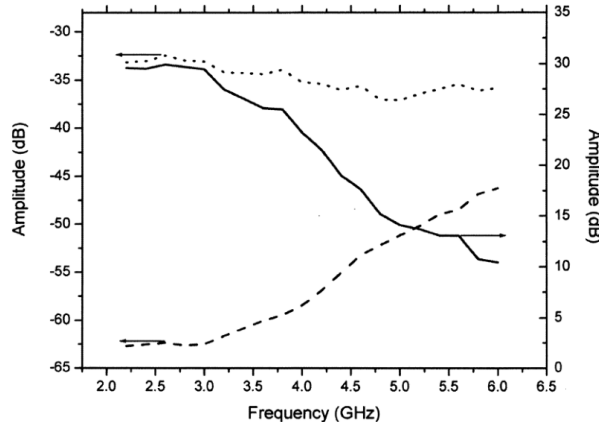


FIGURE II.6 – Amplitudes du message de l'émetteur (courbe pointillée), du récepteur (courbe discontinue) et du message récupéré (courbe solide). Source : Réf. [ACL I.13].

Nous avons aussi démontré une synchronisation entre une diode laser multimode et deux diodes lasers monomodes dont les longueurs d'onde sont différentes. Chaque diode laser esclave est synchronisée aux différents modes de la diode laser multimode maître [ACL I.14].

2.2 Synchronisation et communications chaotiques utilisant des VCSELs

J'ai également travaillé avec des VCSELs. Les lasers VCSELs (Vertical-cavity surface-emmiting laser) sont connus pour un bas seuil de courant, une émission monomode et un profil de faisceau circulaire. Pour ces caractéristiques avantageuses, il y a un grand intérêt à utiliser ce type de diodes lasers dans les télécommunications optiques. Dans ce contexte, j'ai proposé une démonstration expérimentale de la synchronisation de chaos avec deux VCSELs. L'expérience avec deux VCSELs à une émission de 850 nm est schématisée sur la figure II.7. Il y a deux VCSELs : l'un maître et l'autre esclave. Le VCSEL maître est une source chaotique en établissant une cavité externe par un miroir. Une partie de l'émission chaotique est envoyée à l'esclave à travers une série de composants optiques et plus particulièrement des polariseurs. Les VCSELs peuvent changer l'état de leurs polarisation (x ou y) suivant le courant [II.24]. Pour cette raison, l'utilisation de polariseurs est primordiale dans cette expérience.

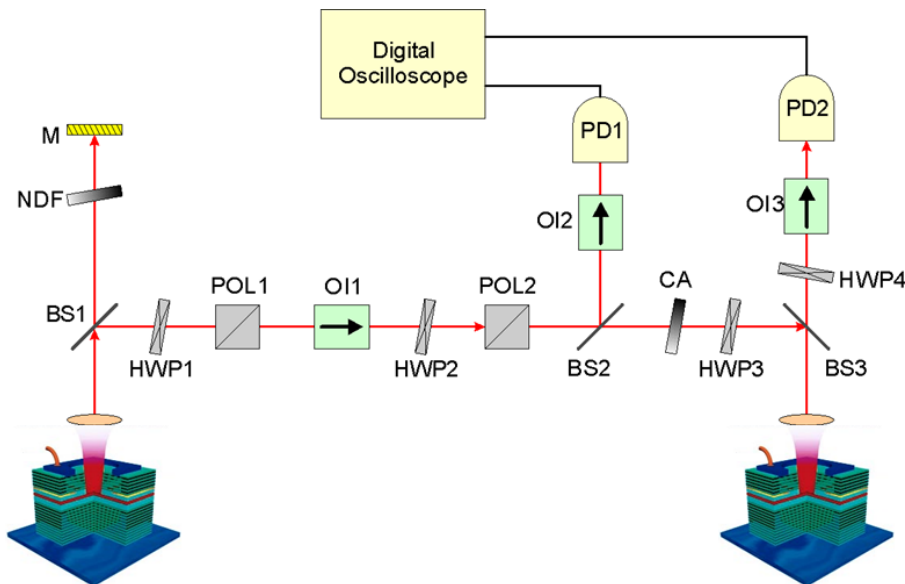


FIGURE II.7 – Banc expérimental de synchronisation de deux VCSELs. OI : isolateur optique, HWP : lame demi-onde, POL : polariseur, ATT : atténuateur, BS : lame séparatrice, NDF : filtre de densité neutre, atténuateur de couplage, M : miroir, PD : photodétecteur.

La figure II.8(a) représente un diagramme de synchronisation entre la dynamique du maître en polarisation- y et celle de l'esclave en polarisation- y tandis que la figure II.8(b) montre un diagramme de la dynamique du maître en polarisation- y et celle de l'esclave en polarisation- x . Comme on peut voir, la synchronisation de la figure II.8(b) est effectuée avec une pente opposée, ce qu'on appelle *synchronisation en anti-phase*.

Dans ces travaux, nous avons réussi pour la première fois la démonstration de la synchronisation de deux VCSELs et aussi une synchronisation en anti-phase en tenant compte de l'état de leurs polarisation [ACL I.10] (voir la page 94, Chapitre IV).

Avec le même système, nous avons aussi travaillé sur la démonstration de communications sécu-

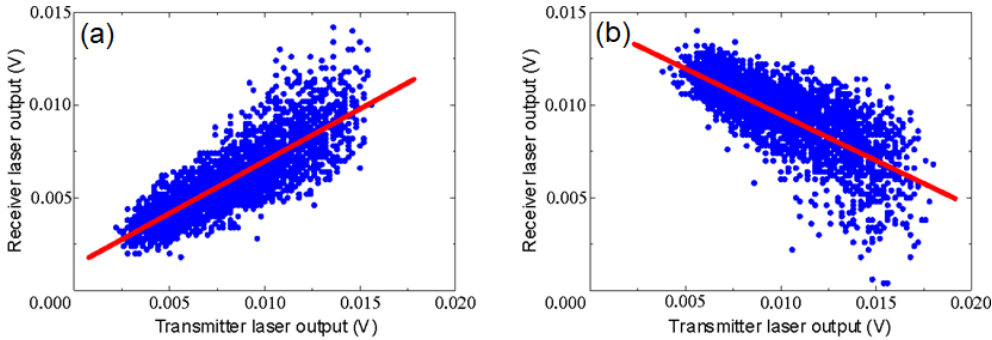


FIGURE II.8 – Diagrammes de synchronisation (a) de la dynamique- y du maître et de la dynamique- y de l'esclave, et (b) de la dynamique- y du maître et de la dynamique- x de l'esclave.

risées par chaos. La particularité de ce système est la polarisation des VCSELs. Comme indiqué sur la figure II.8, il faut ajuster la polarisation pour obtenir une synchronisation conventionnelle de la figure II.8(a). La figure II.9 montre un signal sinusoïdal de 200 MHz qui est récupéré par le récepteur avec un rapport signal-sur-bruit de 9 dB [ACL I.12] (voir la page 97, Chapitre IV).

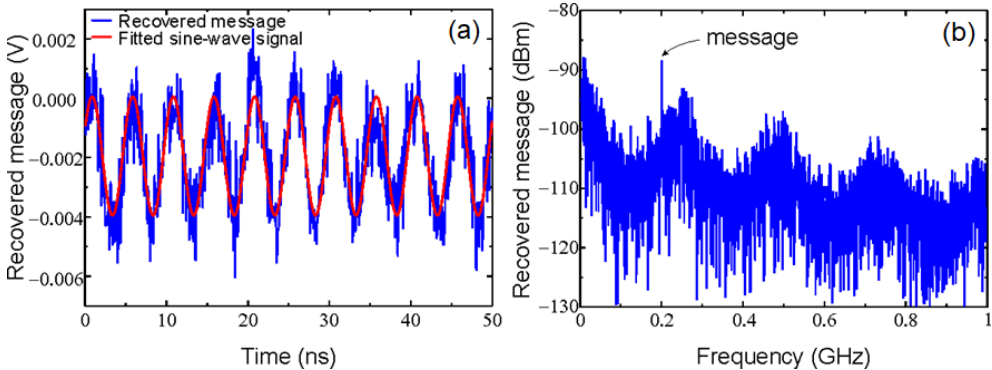


FIGURE II.9 – Message décodé (a) dans le domaine temporel et (b) dans le domaine fréquentiel.

La synchronisation a été améliorée en injectant au récepteur les dynamiques de deux polarisations de l'émetteur [ACL I.21] et la bande passante de message de ce système est également augmentée [ACL I.22].

2.3 Système de trois diodes lasers en cascade

Jusqu'à présent, nous avons travaillé sur une configuration maître-esclave. J'ai proposé une configuration maître-intermédiaire-esclave avec trois diodes laser en cascade. Une synchronisation de trois diodes lasers cascades avait déjà été démontrée [II.25]. Ce qui est nouveau dans ma proposition est une synchronisation simultanée de trois lasers. Il existe deux méthodes de synchronisation : la synchronisation généralisée et la synchronisation complète. La première méthode consiste à forcer l'esclave à se synchroniser par une injection-locking et la seconde méthode consiste à envoyer les conditions initiales à l'esclave qui est identique au maître. Il s'agit de la construction d'une copie d'un système maître et la synchronisation peut être obtenue sans retard sous certaines conditions. Dans ce régime

de synchronisation, il est même possible de synchroniser en anticipation, c'est-à-dire l'esclave émet un signal chaotique avant que le maître émette le même signal en dépit de la distance séparant les deux systèmes [II.26, II.27, II.28, II.29]. Cela est possible si le temps de vol entre les deux systèmes est plus court que le temps d'aller-retour de la cavité externe, c'est-à-dire le retard temporel. Dans ce contexte, nous avons travaillé sur une configuration de trois lasers en cascade comme montré sur la figure II.10. Cette configuration comporte trois lasers (laser DFB à 1550 nm) : le laser maître (ML), le laser intermédiaire (IL) et le laser esclave (SL). Leurs caractéristiques sont similaires entre eux. Le comportement dynamique du ML est entraîné chaotique par une cavité dont le temps d'aller-retour est de $\tau = 2,8$ ns, équivalent à une longueur de cavité de 42 cm. L'IL et le SL sont placés pour que les temps de vol τ_{c1} et τ_{c2} correspondent au temps d'aller-retour τ . Afin d'obtenir une synchronisation complète, les taux de couplage entre le ML et l'IL, et entre l'IL et le SL ont été ajustés au taux de retour optique du ML.

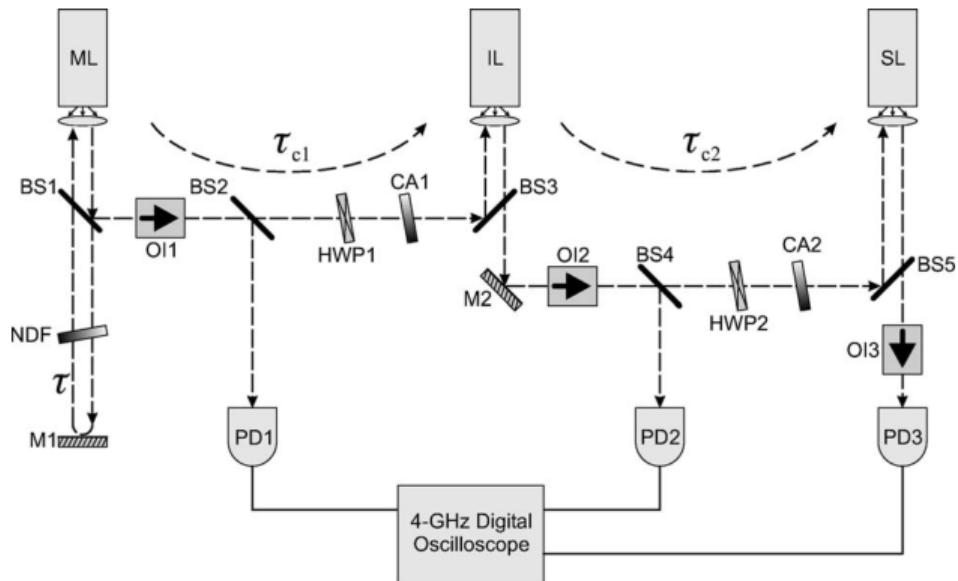


FIGURE II.10 – Banc expérimental de synchronisation de trois diodes lasers en cascade. Source : Réf. [ACL I.20].

Après les ajustements soignés, nous avons obtenu une synchronisation sans retard sur les trois lasers. La figure II.11 montre clairement que les trois lasers sont synchronisés simultanément. Afin d'évaluer la qualité de synchronisation, les corrélations croisées ont également été calculées entre les trois lasers.

Dans ces travaux, nous avons démontré, pour la première fois, la synchronisation simultanée de trois lasers dans une configuration cascadée. Nous avons également effectué une simulation de cette configuration et les résultats confirment ceux obtenus expérimentalement [ACL I.20] (voir la page 100, Chapitre IV). Cette première démonstration indique qu'il est possible en théorie de synchroniser un nombre infini des diodes lasers en cascade simultanément.

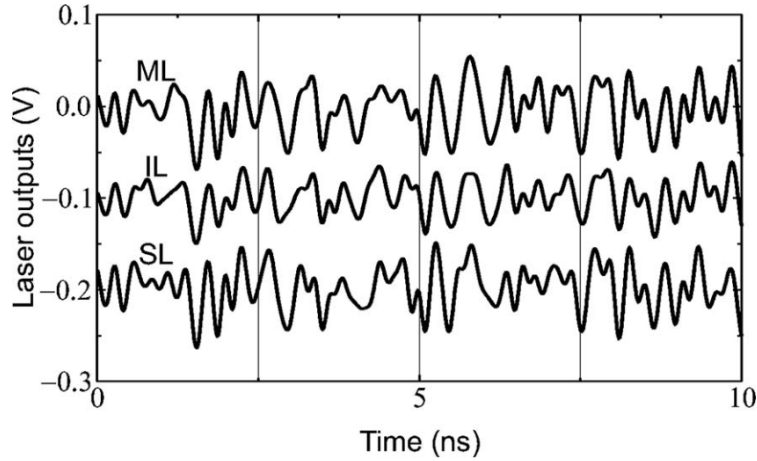


FIGURE II.11 – Tracés temporels de ML, IL et SL. Source : Réf. [ACL I.20].

Nous avons également démontré le cryptage et le décryptage de message à 1 GHz avec ce même système. Le message caché au ML est décrypté à l'IL qui renvoie le message au SL par la suite. L'IL joue un rôle d'extraction du message et de relai du message. Le SL synchronisé décode également le message [ACL I.18] (voir la page 106, Chapitre IV).

En outre, j'ai travaillé sur le comportement dynamique d'une diode laser à double cavité externe. L'objectif de ce travail était, d'une part, d'augmenter le degré de complexité de comportement chaotique, et d'autre part, de réduire la signature de retard temporel due à la cavité externe [ACL I.17] (voir la page 109, Chapitre IV).

II.3 ACTIVITÉS DE RECHERCHE À L’INSTITUT FEMTO-ST

L’OPTIQUE NON LINÉAIRE DANS DES FIBRES OPTIQUES était ma deuxième thématique dans laquelle j’ai mené des recherches post-doctorales à Besançon. Après quelques années post-doctorales à Bangor, je suis revenu à Besançon au sein du Département d’Optique de l’institut FEMTO-ST. J’ai travaillé dans l’équipe *Optique non linéaire* avec Hervé Maillotte, Thibaut Sylvestre et Birgit Stiller qui était une doctorante que j’ai co-encadrée. Les travaux de recherche durant ces années étaient le développement d’un amplificateur paramétrique à fibre optique microstructurée, ainsi que la réalisation de capteurs distribués à fibre optique microstructurée utilisant la diffusion Brillouin stimulée. Ces thématiques ont été financées par les projets CEA MULO (échantillonnage Monocoup Ultra Large-bande Optique) et CDFOM (Capteurs Distribués à Fibre Optique Microstructurée) de l’INTERREG IV. Ces projets m’ont permis des publications et des collaborations avec le CEA/CESTA à Bordeaux, l’IRCICA à Lille, l’EPFL à Lausanne et Photline Technologies à Besançon. Etant expérimentaliste habile, ma principale contribution au sein de l’équipe a été la mise en œuvre expérimentale de l’amplificateur et des différents capteurs distribués. J’ai également apporté mes compétences en optoélectronique dans l’équipe optique non linéaire plus particulièrement pour la démonstration des capteurs distribués qui nécessitent des compétences optoélectroniques. Dans cette section, je vais décrire principalement ces travaux effectués au sein de l’Institut FEMTO-ST.

3.1 Effets non linéaires dans une fibre optique

Les cristaux non linéaires tels que le niobate de lithium (LiNbO_3) et le tantalate de lithium (LiTaO_3) peuvent montrer des effets non linéaires lorsqu’un faisceau laser intense se propagent dans les cristaux. Ils sont en général non-centrosymétriques, ce qui produit des effets non linéaires associés à la susceptibilité de second ordre $\chi^{(2)}$. Ces derniers sont la génération de second-harmonique (SHG : second-harmonic generation), la génération de différence de fréquence (DFG : difference-frequency generation), la génération de somme de fréquenc (SFG : sum-frequency generation) et la génération paramétrique optique (OPG : optical parametric generation) [II.30]. Nous en parlerons un peu plus dans le chapitre suivant.

Dans cette section, nous nous sommes plutôt intéressés aux effets non linéaires dans les fibres. Les fibres optiques peuvent également montrer des effets non linéaires lorsque un faisceau intense s’y propagent. Les fibres monomodes (SMF : single-mode fibre) pour les télécoms standard sont faites en silice (SiO_2) fondue. Les fibres sont considérées isotropiques et les molécules de la silice dans les fibres ont la symétrie d’inversion. Les effets non linéaires se manifestent donc dans les fibres optiques en associant la susceptibilité de troisième ordre $\chi^{(3)}$, ce qui est différent du cas dans les cristaux non linéaires. Les effets associés à $\chi^{(3)}$ sont le mélange à quatre-ondes (FWM : four-wave mixing), l’effet Kerr, la diffusion Raman stimulée (SRS : stimulated Raman scattering) et la diffusion Brillouin stimulée (SBS : stimulated Brillouin scattering) [II.31, II.32].

Le processus **FWM** résulte de l'interaction de quatre ondes différemment que l'interaction de trois ondes dans les processus cités pour les cristaux non linéaires à $\chi^{(2)}$. Dans ce processus, deux ondes avec deux fréquences différentes peuvent interagir pour générer deux nouvelles ondes avec les fréquences différentes. Au total, quatre ondes avec quatre différentes fréquences se trouvent à la sortie de fibre d'où le nom de **FWM**.

L'effet Kerr se caractérise par une variation d'indice de réfraction qui est dépendante de l'intensité locale de la lumière. Il est responsable de différents effets tels que l'auto-modulation de phase (**SPM** : self-phase modulation) et la modulation de phase croisée (**XPM** : cross-phase modulation). Pour le cas de la **SPM**, quand une impulsion courte avec une puissance très forte se propage dans une fibre, l'indice de réfraction varient par l'effet Kerr. Cette variation d'indice impacte sur l'impulsion pompe elle-même introduisant une modulation de phase. Par conséquent, le spectre de la pompe s'élargit. Dans le cas de la **XPM**, la modulation de phase se fait par la présence d'une deuxième onde.

L'effet Kerr permet aussi d'effectuer l'amplification paramétrique optique à fibre (**FOPA** : fibre optical parametric amplification) d'un signal en injectant la pompe dont la longueur d'onde se situe près de la dispersion nulle de la fibre (**ZDW** : zero-dispersion wavelength). Dans une fibre standard télécoms, la **ZDW** se trouve à 1,3 µm où la vitesse de groupe est constante, c'est-à-dire, une impulsion lumineuse se propage en gardant sa forme initiale. En dessous de cette longueur d'onde, c'est le régime de la dispersion normale où l'impulsion s'élargit en se propageant. Au delà de la **ZDW**, c'est le régime de la dispersion anormale où l'impulsion raccourcit. La **FOPA** génère un signal et un idler suivant la condition d'un accord de phase avec la pompe. En l'absence du signal à amplifier, la variation d'indice due à l'onde de pompe module l'onde elle-même et ce phénomène est connu sous le nom de l'*instabilité modulationnelle*. Cette modulation est initiée par la **SPM** et donne une bande latérale dans le spectre qui sont *Stokes* et *anti-Stokes*. Ce spectre est une émission spontanée amplifiée (**ASE** : amplified spontaneous emmission) d'une **FOPA**.

La **SRS** et la **SBS** sont les diffusions apparues fréquemment dans les fibres. Nous comparons ces diffusions avec celle Rayleigh sur la figure II.12. La diffusion Rayleigh est un processus élastique où la fréquence de la lumière diffusée reste la même que celle de la pompe. Par contre, dans les cas de la **SRS** et de la **SBS** la fréquence de la lumière diffusée est décalée par rapport à celle de la pompe. Il s'agit des processus inélastiques. Les ondes diffusées en basses fréquences par rapport à la pompe sont les ondes *Stokes* et celles en hautes fréquences sont les ondes *anti-Stokes*. Les ondes anti-Stokes ne sont pas observées parce qu'elles sont absorbées par la pompe. Seules les ondes Stokes peuvent donc être observées en général. La **SBS** est due à l'interaction de l'onde optique et de l'onde acoustique créée par l'électrostriction. Le décalage de fréquence Brillouin (**BFS** : Brillouin frequency shift) est typiquement au tour de 11 GHz dans une **SMF** à une pompe de 1,55 µm. En revanche, la **SRS** est due à la vibration des molécules, par exemple des molécules de silice dans la fibre. Le décalage de fréquence Raman est beaucoup plus important que celui de **SBS**, ce qui est de 13 THz dans une **SMF**. Si le faisceau laser est suffisamment intense dans une fibre, plusieurs **SRS** peuvent manifester en cascade en décalant chaque

fois à -13 THz, ce qu’on appelle le *cascade Raman*.

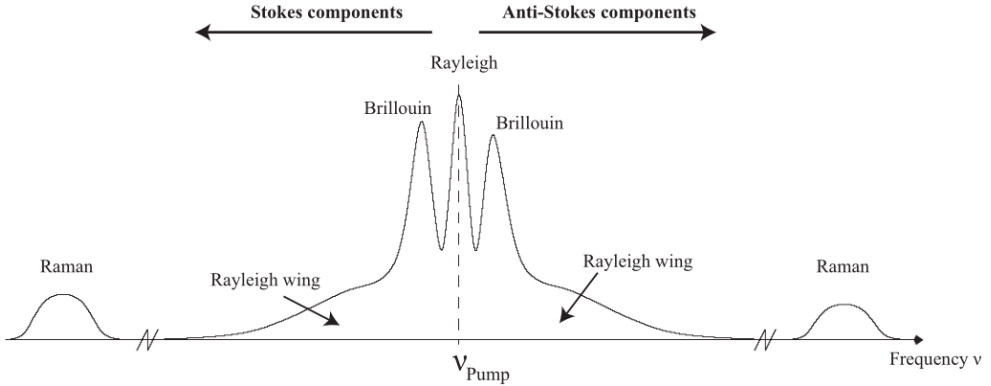


FIGURE II.12 – Spectre des diffusions Rayleigh, Raman et Brillouin. Source : Réf. [II.33]

Nous avons abordé différents effets non linéaires. Quand plusieurs effets sont combinés, le spectre de l’onde pompe s’élargit progressivement en se propageant dans une fibre sur une plage de quelques centaines de nanomètre, voire quelques micromètres. Ceci est la génération de supercontinuum.

Pour une compréhension approfondie de ces effets non linéaires, j’invite les lecteurs à se référer aux livres [II.31, II.32].

Nous venons de voir différents effets non linéaires dans une **SMF** standard pour télécoms. Il existe différents types de fibres, notamment les fibres à cristal photonique (**PCF** : photonic crystal fibre). Ces dernières ont récemment conduit de nombreuses études sur les effets non linéaires. Elles ont une microstructure périodique avec des trous d’air comme montré sur la petite image de la figure II.13. De ce fait, on appelle également les fibres microstructurées. En variant la structure, la période de trou et/ou le diamètre du trou d’air, la **ZDW** de fibre peut être manipulée plus facilement que les fibres standards. Les **PCFs** ont aussi un fort contraste d’indice qui fournit une forte non linéarité de fibre. Il est également possible de fabriquer des fibres monomodes sans fin (endlessly single-mode fiber) avec des microstructures [II.34]. La **PCF** sur l’image a un cœur solide. Il existe aussi des **PCFs** avec un cœur creux (grand trou d’air au cœur) qui permet un guidage par une bande interdite photonique. La lumière est donc piégée et se propage dans le cœur creux [II.35]. Les **PCFs** que j’ai utilisées pour mes travaux au sein de l’Institut FEMTO-ST sont des **PCFs** à cœur solide comme montré sur l’image.

3.2 Amplificateur paramétrique à fibre optique

Ce travail a pour but la réalisation d’un amplificateur paramétrique tout fibré à $1\text{ }\mu\text{m}$ dédié à la mesure des impulsions du laser mégajoule. Cette étude a été financée par le projet MULO. L’amplificateur paramétrique à fibre optique exploite l’effet Kerr dans un milieu non linéaire. Récemment, la **FOPA** a particulièrement attiré l’attention sur un gain de conversion très élevé, une large bande passante et l’aspect de bas bruit [II.36, II.37, II.38]. Il a été rapporté qu’un gain de 70 dB peut être obtenu

pour une application dans les télécoms à 1,55 µm. La **FOPA** peut être utilisée dans des applications telles que l'**OPCPA** (optical parametric chirped-pulse amplification) [II.39, II.40] et l'échantillonnage optique ultra-rapide pour des oscilloscopes optiques [II.41]. Encore plus récemment, des **PCFs** ont été utilisées dans divers systèmes paramétriques [II.42, II.43, II.44, II.45]. Ces caractéristiques permettent, entre autre, de construire une **FOPA** dans la bande à 1 micron. Cette dernière a un intérêt pour l'amplification des lasers à fibre dopés ytterbium.

Dans ce travail, nous avons démontré un **FOPA** entièrement fibré et en utilisant une **PCF**. Un **FOPA** utilisant une fibre microstructurée a été démontré en espace libre [II.46], mais pas dans un système tout-fibré. Une pompe à 1065 nm est injectée dans la fibre pour amplifier un signal à 1053 nm. Cette dernière située dans la bande anti-Stokes, a un besoin spécifique dans un système laser pour la fusion de confinement d'inertie (ICF : Inertial Confinement Fusion) [II.47, II.48]. Le banc expérimental du **FOPA** est illustré sur la figure II.13. Un laser accordable avec une émission continue est utilisé pour la pompe. L'émission continue est transformée en émission pulsée via un modulateur électro-optique (Photline Technologies) et un générateur d'impulsion. La pompe impulsionale est amplifiée par un **YDFA**, filtrée à 1065,8 nm et injectée dans une fibre microstructurée de 400 m de longueur avec la structure d'un réseau triangulaire comme montrée sur la petite image de la figure II.13. La période et le diamètre de trou sont 4,14 µm et 2,61 µm, respectivement. Ces paramètres permettent d'obtenir une **ZDW** à 1065 nm. Un signal à 1053 nm est aussi injecté dans la fibre à travers du port-1% d'un coupleur 99/1. La sortie de la fibre est envoyée à un **OSA** et à une photodiode connectée à un oscilloscope numérique après un filtrage à 1053 nm.

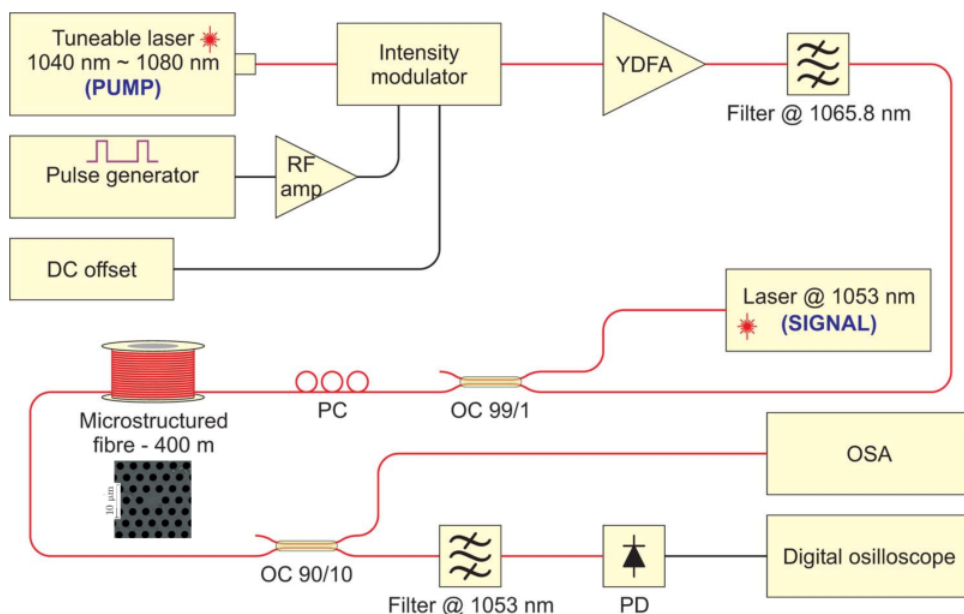


FIGURE II.13 – Banc expérimental d'une **FOPA**. RF amp : amplificateur RF, **YDFA** : amplificateur à fibre dopée ytterbium, OC : coupleur optique, PC : contrôleur de polarisation, PD : photodiode, **OSA** : analyseur de spectre optique. Source : Réf. [ACL I.24].

Dans un premier temps, nous avons effectué une cartographie de l’ASE du **FOPA** en variant la longueur d’onde de la pompe. La carte de l’ASE est montrée sur la figure II.14. Comme on peut voir sur la figure, l’ASE commence à apparaître à 1064,8 nm avec la présence de deux bandes latérales. La carte révèle que la puissance de l’ASE à 1053 nm est maximale lors que la pompe est à 1065,8 nm. La longueur d’onde de pompe du **FOPA** sera donc 1065,8 nm. Nous pouvons remarquer que le spectre n’est pas symétrique entre l’aire gauche et l’aire droite par rapport à la longueur d’onde de la pompe. La diffusion Raman est à l’origine de cette asymétrie spectrale avec l’aire droite (partie Stokes) plus élevée que l’aire gauche (partie anti-Stokes) [II.49, II.50, II.51].

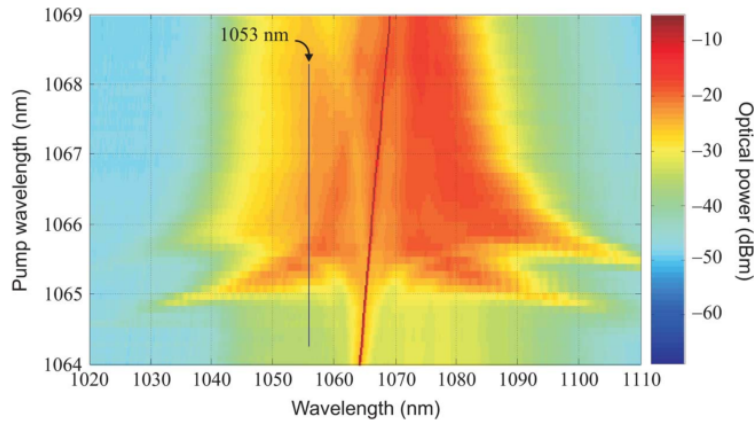


FIGURE II.14 – Cartographie de l’ASE de **FOPA** sans signaux. Source : Réf. [ACL I.24].

Après l’étude de l’ASE du **FOPA**, la pompe d’une puissance moyenne de 2,4 W est envoyée avec un signal à 1053 nm. Sur la figure II.15, nous pouvons voir deux spectres mesurés à l’entrée et à la sortie de l’amplificateur. À l’entrée la puissance de signal est de $-25,4$ dBm alors qu’à la sortie elle augmente à -9 dBm. Le signal est donc amplifié de $16,4$ dB. Il faut en revanche tenir compte du rapport cyclique de $1/16$, ce qui donne $11,1$ dB de gain supplémentaire. Au total, un gain de $27,5$ dB est obtenu.

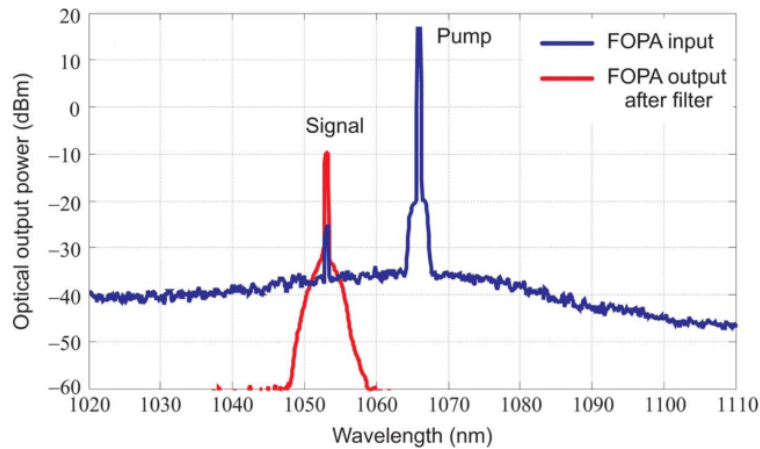


FIGURE II.15 – Spectres du signal mesurés à l’entrée et à la sortie de **FOPA**. Source : Réf. [ACL I.24].

En augmentant la puissance à $3,8$ W, nous avons atteint un gain de 35 dB. Le travail a été effectué

en collaboration avec l'IRCICA à Lille et le CEA/CESTA à Bordeaux [ACL I.24] (voir la page 115, Chapitre IV).

3.3 Rétrodiffusion Brillouin stimulée et ses applications aux capteurs distribués à fibre optique

Nous avons vu au début de la section que la **SBS** est due à l'interaction entre les ondes acoustique et optique dans une fibre. L'onde acoustique crée un réseau de Bragg qui se déplace à la vitesse du son et l'onde optique diffusée par ce réseau est donc décalée en fréquence (effet Doppler). Nous nous rappelons que pour la silice fondu de la **SMF**, ce décalage correspond à environ 11 GHz de **BFS** pour une pompe de 1,55 µm [II.32]. Ce **BFS** peut évoluer via une modification de l'indice de réfraction due à une variation de température ou de contrainte mécanique sur la fibre. Ce phénomène permet alors d'utiliser la fibre optique comme un capteur distribué de température ou de contrainte en mesurant le spectre de gain Brillouin (**BGS** : Brillouin gain spectrum) [II.52, II.53, II.54]. Il existe principalement deux techniques d'analyse pour des applications de capteurs distribués : le **BOCDA** (Brillouin Optical Correlation-Domain Analysis) et le **BOTDA** (Brillouin Optical Time-Domain Analysis). Le **BOCDA** permet d'avoir une distribution spatiale des modifications locales de température ou d'indice de réfraction avec une résolution spatiale de 1 mm [II.55, II.56]. Malgré ces avantages, il est difficile d'appliquer cette technique sur une grande longueur de fibre. En revanche, le **BOTDA** peut fournir des mesures rapides de contraintes et de températures sur une très longue distance en mesurant le **BFS** le long d'une fibre optique [II.57, II.58, II.59]. Cette particularité a suscité un grand intérêt dans le domaine de capteurs distribués.

3.3.1 BOTDA et BEDS

La figure II.16(a) illustre le principe de fonctionnement de **BOTDA**. Une impulsion de forte amplitude est injectée pour la pompe dans un sens. Pour la sonde une émission continue est injectée dans l'autre sens. La pompe et la sonde se propagent donc en contre-propagation. La fréquence de la sonde est décalée de la fréquence de Brillouin par rapport à celle de la pompe. Lorsque la pompe traverse un endroit où se trouve une contrainte ou une variation de température, la pompe laisse du gain Brillouin qui permet d'amplifier la sonde à cet endroit par la rétrodiffusion Brillouin (ou une chute de gain).

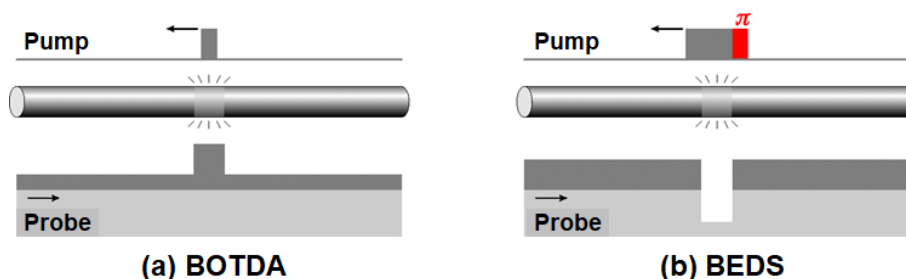


FIGURE II.16 – Le principe de fonctionnement de (a) **BOTDA** et de (b) **BEDS**.

C'est ainsi que l'on peut effectuer une cartographie longitudinale de la variation d'indice de réfraction dans une fibre optique.

Dans le système **BOTDA**, la durée d'impulsion est limitée à 10 ns qui correspond à une résolution de 1 m en tenant compte de la vitesse de propagation de $2/3c$ (où c est la vitesse de lumière dans le vide). En effet, c'est la limite de **BOTDA** due à la durée de vie de **SBS** [II.32]. Afin d'améliorer la résolution, il existe une autre technique : **BEDS** (Brillouin echoes distributed sensing). Dans un système **BEDS** sur la figure II.16(b), un déphasage de π est présent sur une impulsion longue qui donne du gain Brillouin le long de la fibre. Lorsqu'elle rencontre la contrainte, le gain chute à cause du déphasage de π contrairement au **BOTDA**. La durée de déphasage de π peut descendre en dessous de 10 ns, ce qui permet d'améliorer la résolution spatiale à quelques centimètres [II.60, II.61].

La figure II.17(a) représente le schéma expérimental du **BOTDA** que nous avons réalisé. L'émission continue d'un laser **DFB** à 1,55 µm est divisée en deux pour la pompe et la sonde et injectée dans un modulateur Mach-Zehnder sur chaque bras. Pour le côté pompe, un générateur d'impulsion pilote le modulateur (Photline Technologies) sur une durée d'impulsion de 10 ns. La pompe pulsée est amplifiée par un **EDFA**, puis injectée dans une fibre à tester à travers un brouilleur de polarisation et un circulateur optique. Pour le côté sonde, l'émission continue est modulée aux alentours de 11 GHz par un générateur de RF et le modulateur (Photline Technologies). La sonde modulée à 11 GHz est amplifiée avant d'être injectée dans la fibre. La sonde se propage donc en contre sens de la pompe et peut être amplifiée par du gain Brillouin le long de la fibre. En général, le Stokes est exploité pour la sonde. La sonde est donc filtrée par un filtre de Bragg pour enlever l'anti-Stokes et la pompe résiduelle, puis détectée par un photodetecteur et enregistrée sur un oscilloscope numérique. En tenant compte de la vitesse de la lumière dans la fibre, les tracés temporels de l'oscilloscope sont convertis en tracés spatiales. En variant la fréquence de la sonde, le **BGS** est mesuré le long de la fibre pour une construction cartographiée de la fibre. Pour cela, le banc expérimental est entièrement automatisé.

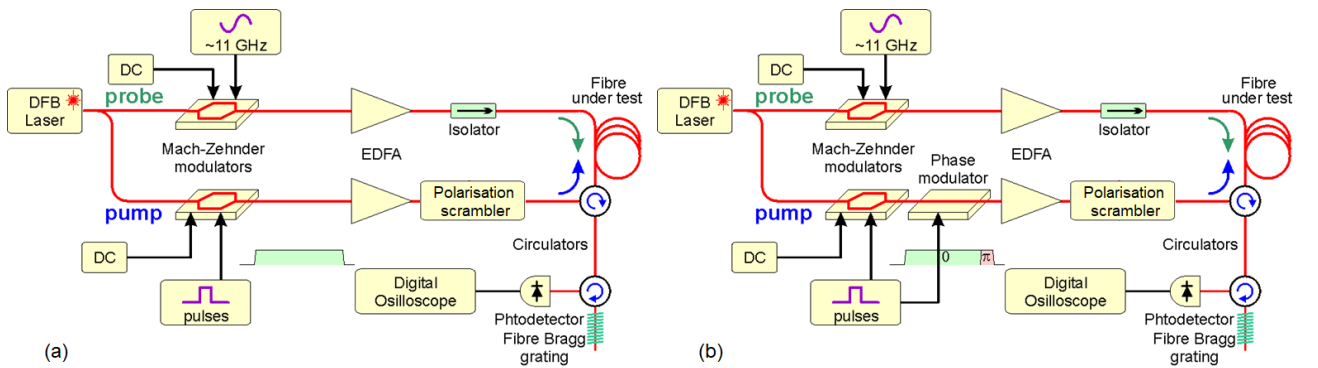


FIGURE II.17 – Banc expérimental (a) de **BOTDA** et (b) de **BEDS**. **DFB** : Distributed feedback, **EDFA** : Erbium-doped fibre amplifier

Pour le système **BEDS**, le banc expérimental est illustré sur la figure II.17(b) qui est presque identique à celui de **BOTDA**. Pour un déphasage de π , il est nécessaire de rajouter un modulateur de phase (Photline Technologies) sur le côté pompe. Ces deux systèmes ont été développés en collaboration

avec Luc Thévenaz à l'EPFL de Lausanne dans le cadre du projet INTERREG IV CDFOM. Ces travaux ont également été menés dans le cadre de la thèse de Mlle. Birgit Stiller que j'ai participé à co-encadrer [II.33].

3.3.2 Etudes de PCF

Dans un premier temps, nous avons étudié des PCFs fournies par l'IRCICA. La figure II.18 montre une image MEB (microscopie électronique à balayage) d'une PCF que nous avons étudiée. Les PCFs ont attiré un intérêt particulière dans le domaine de capteurs distribués grâce à leur forte non linéarité [II.62, II.63, II.64]. Mais il est difficile de les fabriquer sur une grande longueur avec une structure identique. L'IRCICA souhaite développer des techniques pour réduire l'inhomogénéité le long des fibres pendant la fabrication. Nous avons donc étudié l'inhomogénéité et les caractéristiques de la fibre avec le système BEDS.

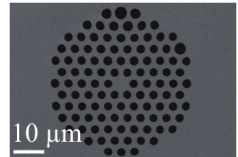


FIGURE II.18 – Image MEB d'une PCF.

La figure II.19 présente une mesure de cartographie de la PCF effectuée par le système BEDS décrit sur la figure II.17(b). La durée d'impulsion de π est de 3 ns, ce qui donne une résolution spatiale de 30 cm. On peut remarquer sur la figure que le BFS est environ 11,07 GHz. Ce qui est remarquable c'est que l'on peut obtenir la variation de BFS en mesurant le BGS tous les 30 cm grâce à la cartographie par le BEDS en variant la fréquence de la sonde de 10,98 GHz à 11,22 GHz. Cette étude a permis de caractériser des PCFs le long de la fibre avec une haute résolution et à l'IRCICA d'améliorer la technique pour réduire l'inhomogénéité [ACL I.26] (voir la page 121, Chapitre IV).

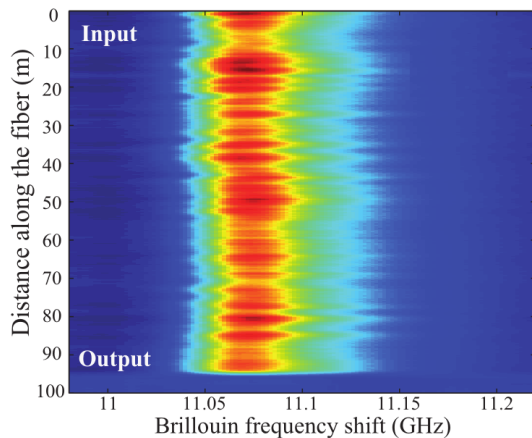


FIGURE II.19 – Cartographie de la PCF avec le BEDS. Source : Réf. [ACL I.26].

Dans un second temps, l'IRCICA a développé une PCF dont le diamètre varie de façon sinusoïdale comme on peut voir sur la figure II.20(a). Cette fibre a été développée afin de réduire la SBS qui est indésirable pour des lasers fibrés à haute-puissance ou des amplificateurs à haute-puissance [II.65, II.66, II.67]. Sur la figure II.20(b), l'image MEB de la fibre montre un diamètre de cœur de 6,4 μm .

Le seuil de **SBS** est obtenu à 26,5 dBm dans cette fibre. En comparant avec une autre **PCF** dont les paramètres sont identiques sans modulation de diamètre, le seuil de **SBS** est 4 dB plus haut que la **PCF** sans modulation.

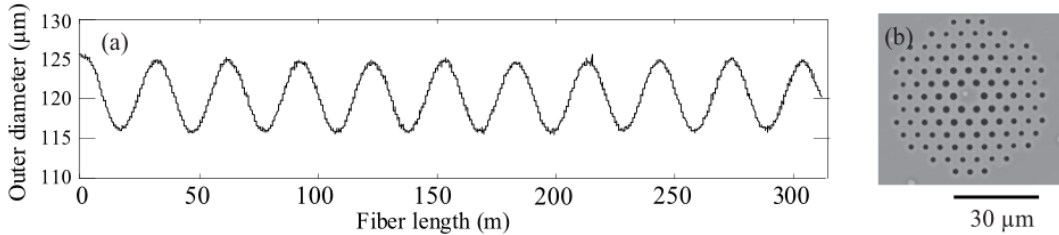


FIGURE II.20 – (a) Fibre dont le diamètre de cœur varie. (b) Image MEB de la fibre microstructurée. Source : Réf. [ACL I.32].

D’après la cartographie d’une résolution de 30 cm comme montré sur la figure II.21(a), le **BFS** est autour de 11,08 GHz et la modulation de diamètre de la fibre de la figure II.20(a) est transférée à la **BFS**. Comme cette dernière est proportionnelle à l’indice de réfraction effectif, on peut déduire la fluctuation d’indice effectif comme montré sur la figure II.21(b). On peut savoir sur la figure qu’une variation du diamètre de fibre de 125 µm à 116 µm produit une variation d’indice entre 1,4337 et 1,4353. Les fluctuations rapides de l’indice sont dues à l’irrégularité structurale de la fibre.

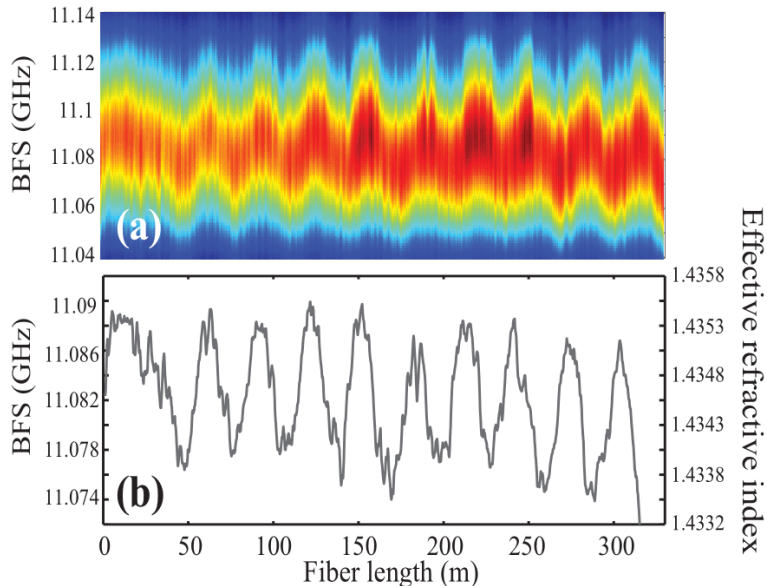


FIGURE II.21 – (a) Cartographie et (b) **BFS** de la **PCF** avec modulation. Source : Réf. [ACL I.32].

Comme on peut voir sur ces résultats, la technique **BEDS** fournit des mesures précises sur des variations structurales ou d’indice en mesurant la **BFS** le long de la fibre [ACL I.32] (voir la page 128, Chapitre IV).

3.3.3 DPSK-BEDS

Malgré une meilleure résolution, le système **BEDS** emploie trois modulateurs (Photline Technologies) : deux modulateurs d'intensité et un modulateur de phase. Mais dans ce travail, nous avons implémenté un système **BEDS** en utilisant seulement deux modulateurs d'intensité. Pour cela, nous avons exploité la technique **DPSK** (differential phase-shift keying) pour générer un déphasage de π comme montré sur la figure II.22(a). Un déphasage de π est généré entre une impulsion positive et une impulsion négative à la fin [II.68]. En pratique, il est difficile d'obtenir une telle impulsion par un seul générateur d'impulsion. En effet, j'ai proposé une solution d'utiliser deux générateurs d'impulsion sur un seul modulateur : l'entrée DC pour l'impulsion positive longue et l'entrée RF pour l'impulsion négative courte comme montré sur la figure II.22(b). Récemment, la technologie de fabrication des modulateurs d'intensité a bien été développée pour le haut débit. Grâce à la technologie, même l'entrée DC d'un modulateur peut recevoir des impulsions électriques de ~ 10 ns. La figure II.22(c) montre la sortie optique du modulateur piloté par deux impulsions sur la figure II.22(b). L'impulsion optique courte qui se trouve à la fin sur la figure est déphasé de π par rapport à l'impulsion longue.

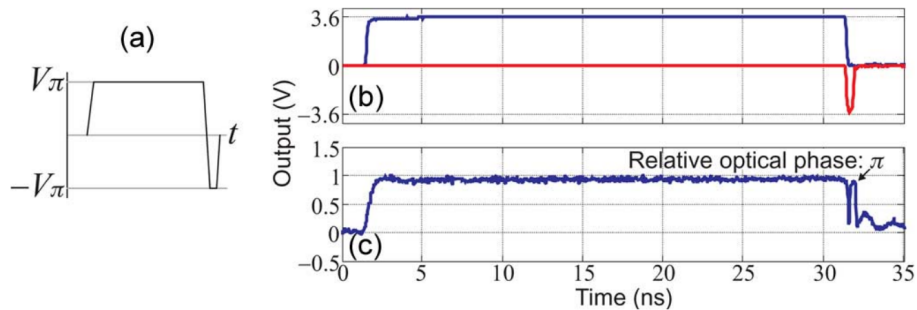


FIGURE II.22 – (a) Impulsion électrique pour la pompe. (b) Deux impulsions positive et négative. (c) Sortie optique du modulateur. Source : Réf. [ACL I.29].

Afin d'appliquer cette technique, nous utilisons le système **BOTDA**, mais avec deux générateurs d'impulsion comme montré sur la figure II.23.

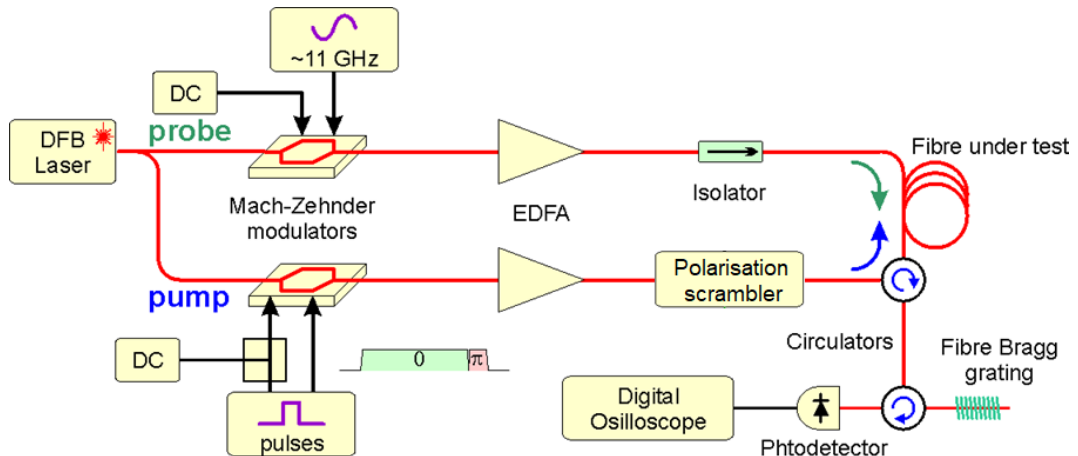


FIGURE II.23 – Banc expérimental de **BEDS** basé sur une technique **DPSK**. Source : Réf. [ACL I.29].

La performance de ce système est comparée avec celle du système **BEDS** conventionnel. La figure II.24 présente deux cartographies sur le point de soudure de fibres **HNA** (high numerical aperture) et **SMF** avec une résolution de 5 cm en utilisant une impulsion de 500 ps. Nous pouvons remarquer que les **BFS** de la **HNA** et de la **SMF** sont mesurés à 10,67 GHz et 10,85 GHz, respectivement. La section de soudure est bien visible sur 5 cm à un **BFS** de 10,55 GHz. Les deux cartographies sont presque identiques, ce qui indique que le **DPSK-BEDS** est une technique aussi performante que le **BEDS** sans modulateur de phase [ACL I.29] (voir la page 131, Chapitre IV).

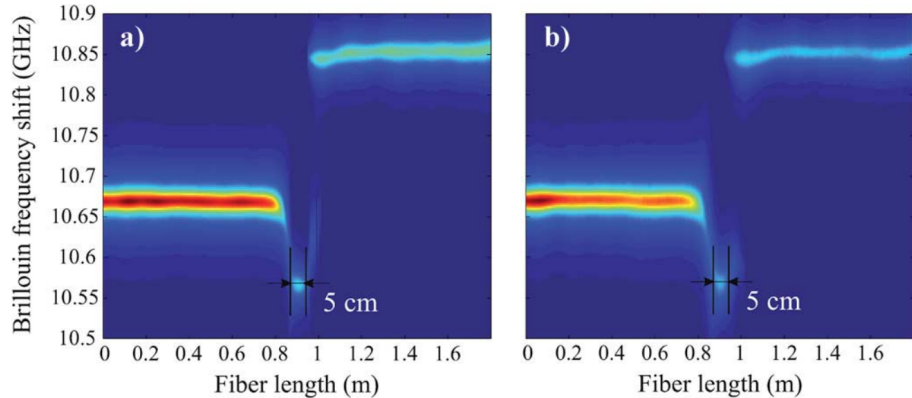


FIGURE II.24 – Cartographie de point de soudure entre deux fibres **HNA** et **SMF** par (a) le **BEDS** et par (b) le **DPSK-BEDS**. Source : Réf. [ACL I.29].

Le système **BOTDA** a également été amélioré pour des mesures de fibres de très grande longueur (>30 km). A cause de la perte intrinsèque provenant de la fibre et la déplétion de la pompe, le contraste sur des mesures diminue considérablement au delà de 10 km de fibre. Afin d’augmenter la longueur de mesure, il est possible d’utiliser l’anti-Stokes au lieu du Stokes pour la sonde. En utilisant un modulateur I/Q qui peut générer une mono-bande latérale sur l’anti-Stokes, la dynamique de mesure a été nettement améliorée sur une fibre de 50 km [ACL I.35] (voir la page 134, Chapitre IV).

3.4 Génération de continuum dans la bande UV dans une PCF

J’ai également travaillé sur la génération de supercontinuum dans une **PCF**. Grâce aux propriétés polyvalentes de **PCF**, la génération de supercontinuum a récemment attiré une attention particulière pour générer de la lumière spatialement cohérente sur un spectre ultra-large [II.69, II.70]. Il existe aussi des démonstrations de la génération de supercontinuum dans la bande UV [II.71, II.72, II.73]. Cependant, aucune démonstration n’a été faite avec une pompe UV. Dans ce contexte, nous avons travaillé sur la génération de supercontinuum en injectant une pompe à 355 nm dans une **PCF**. L’ensemble doit surmonter trois obstacles liés à la pompe UV : une forte absorption, une forte dispersion et une solarisation de fibre. L’IRCICA nous a fournie pour cette démonstration une **PCF** avec une atténuation de 0,5 dB/m et une **ZDW** de 1044 nm. En injectant une pompe de 300 ps à 355 nm dans une **PCF** de 30 m avec une puissance crête de 70 kW, nous avons obtenu des spectres de continuum comme montré sur la figure II.25. En variant la puissance, le spectre s’étale progressivement de l’UV

au bleu vers 470 nm. L'image dans la figure affiche des modes transversaux du continuum de la courbe bleue.

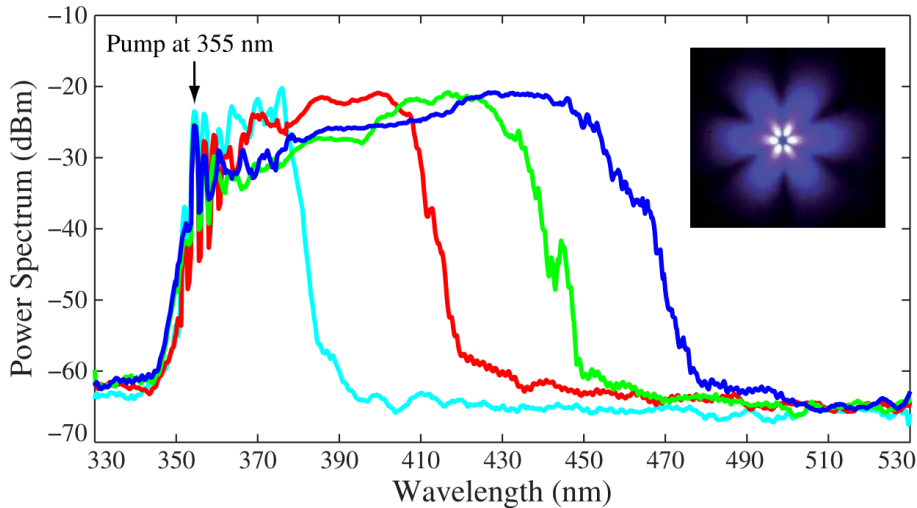


FIGURE II.25 – Spectres de continuum et une image de mode transversal du continuum de la courbe bleue. Source : Réf. [ACL I.30].

Ces continuums sont dus principalement aux cascades Raman. Les limites de cette démonstration sont la forte atténuation, la solarisation de PCF et la durée d'impulsion. La PCF ne résiste pas longtemps à l'UV et est détruite au bout de quelques dizaines de minutes à cause de la solarisation. La courte durée de l'impulsion du laser (300 ps) que nous avons utilisé est aussi la limite à cause du walk-off entre la pompe et des cascades Raman générées. A cause du walk-off temporel, l'interaction ne se fait plus au delà de 30 m de fibre. Les résultats expérimentaux ont été confirmés par les simulations numériques [ACL I.30] (voir la page 137, Chapitre IV).

II.4 RÉSUMÉ

Mes activités de recherche durant mes travaux post-doctoraux au Royaume Uni et à Besançon sont basées sur les domaines de recherche suivants : la théorie du chaos, la synchronisation de chaos, les communications optiques chaotiques, l'amplificateur paramétrique à fibre, les capteurs distribués à fibre utilisant les diffusions Brillouin et la génération de supercontinuum. Grâce à ces travaux, j'ai enrichi mes domaines de recherche. Grâce à ces travaux avec mes collègues et doctorants et aux différentes collaborations, j'ai publiés 26 articles dans les journaux internationaux [ACL I.6,I.9–I.10,I.12–I.33,I.35]. Les projets européen OCCULT, PICASSO et CDFOM m'ont permis de faire connaissance avec des équipes européennes.

BIBLIOGRAPHIES

- [II.1] H. Poincaré, *Sciences et méthodes*, Ernest Flammarion, Paris (1908), Chap. IV Le hasard.
- [II.2] E. N. Lorenz, « Deterministic nonperiodic flow », *J. Atmos. Sci.*, **20**, pp. 130–141 (1963).
- [II.3] L. M. Pecora et T. L. Carroll, « Synchronization in chaotic systems », *Phys. Rev. Lett.*, **64**(8), pp. 821–824 (novembre 1990).
- [II.4] J. Mørk, B. Tromborg et J. Mark, « Chaos in semiconductor lasers with optical feedback : theory and experiment », *IEEE J. Quantum Electron.*, **28**(1), pp. 93–108 (janvier 1992).
- [II.5] J.-P. Goedgebuer, L. Larger, H. Porte et F. Delorme, « Chaos in wavelength with a feedback tunable laser diode », *Phys. Rev. E*, **57**(3), pp. 2795–2798 (mars 1998).
- [II.6] L. Larger, M. W. Lee, J.-P. Goedgebuer, W. Elflein et T. Erneux, « Chaos in coherence modulation : bifurcations of an oscillator generating optical delay fluctuations. », *J. Opt. Soc. Am. B*, **18**(8), pp. 1063–1068 (août 2001).
- [II.7] R. Lang et K. Kobayashi, « External optical feedback effects on semiconductor injection laser properties », *IEEE J. Quantum Electron.*, **16**(3), pp. 347–355 (mars 1980).
- [II.8] J. Ohtsubo, *Semiconductor Lasers : Stability, Instability and Chaos*, Springer Series in Optical Sciences, Springer-Verlag, Berlin Heidelberg, <http://link.springer.com/10.1007/978-3-540-72650-0> (2008).
- [II.9] R. Tkach et A. Chraplyvy, « Regimes of feedback effects in 1.5- μm distributed feedback lasers », *J. Lightwave Technol.*, **4**(11), pp. 1655–1661 (novembre 1986), <https://ieeexplore.ieee.org/document/1074666/>.
- [II.10] D. Lenstra, B. Verbeek et A. D. Boef, « Coherence collapse in single-mode semiconductor lasers due to optical feedback », *IEEE Journal of Quantum Electronics*, **21**(6), pp. 674–679 (juin 1985).
- [II.11] S. Sivaprakasam et K. A. Shore, « Demonstration of optical synchronization of chaotic external-cavity laser diodes », *Opt. Lett.*, **24**(7), pp. 466–468 (avril 1999).
- [II.12] H. Fujino et J. Ohtsubo, « Experimental synchronization of chaotic oscillations in external-cavity semiconductor lasers », *Opt. Lett.*, **25**(9), pp. 625–627 (mai 2000).
- [II.13] T. Heil, I. Fischer, W. Elsäßer, J. Mulet et C. R. Mirasso, « Chaos synchronization and spontaneous symmetry-breaking in symmetrically delay-coupled semiconductor lasers », *Phys. Rev. Lett.*, **86**(5), pp. 795–798 (janvier 2001).
- [II.14] R. J. Jones, P. Rees, P. S. Spencer et K. A. Shore, « Chaos and synchronization of self-pulsating laser diodes », *J. Opt. Soc. Am. B*, **18**(2), pp. 166–172 (février 2001).
- [II.15] S. Hayes, C. Grebogi et E. Ott, « Communicating with chaos », *Phys. Rev. Lett.*, **70**(20), pp. 3031–3034 (mai 1993).
- [II.16] J.-P. Goedgebuer, L. Larger et H. Porte, « Optical cryptosystem based on synchronization of hyperchaos generated by a delayed feedback tunable laserdiode », *Phys. Rev. Lett.*, **80**(10), pp. 2249–2252 (juin 1998).
- [II.17] M. W. Lee, L. Larger et J.-P. Goedgebuer, « Transmission system using chaotic delays between light-waves », *IEEE J. Quantum Electron.*, **39**(7), pp. 931–935 (juillet 2003).
- [II.18] G. D. VanWiggeren et R. Roy, « Optical communication with chaotic waveforms », *Phys. Rev. Lett.*, **81**(16), pp. 3547–3550 (octobre 1998).
- [II.19] J.-M. Liu, H.-f. Chen et S. Tang, « Synchronized chaotic optical communications at high bit rates », *IEEE J. Quantum Electron.*, **38**(9), pp. 1184–1196 (septembre 2002).
- [II.20] A. Uchida, S. Yoshimori, M. Shinozuka, T. Ogawa et F. Kannari, « Chaotic on-off keying for secure communications », *Opt. Lett.*, **26**(12), pp. 866–868 (juin 2001).
- [II.21] S. Sivaprakasam et K. A. Shore, « Signal masking for chaotic optical communication using external-cavity diode lasers », *Opt. Lett.*, **24**(17), pp. 1200–1202 (septembre 1999).
- [II.22] T. Heil, J. Mulet, I. Fischer, C. R. Mirasso, M. Peil, P. Colet et W. Elsäßer, « ON/OFF phase shift keying for chaos-encrypted communication using external-cavity semiconductor lasers », *IEEE J. Quantum Electron.*, **38**(9), pp. 1162–1170 (septembre 2002).
- [II.23] A. Argyris, D. Syvridis, L. Larger, V. Annovazzi-Lodi, P. Colet, I. Fischer, J. García-Ojalvo, C. R. Mirasso, L. Pesquera et K. A. Shore, « Chaos-based communications at high bit rates using commercial fibre-optic links », *Nature*, **438**(7066), pp. 343–346 (novembre 2005), <https://www.nature.com/articles/nature04275>.

- [II.24] Y. Hong, K. A. Shore, A. Larsson, M. Ghisoni et J. Halonen, « Polarisation switching in a vertical cavity surface emitting semiconductor laser by frequency detuning », *IEE Proc. Optoelectron.*, **148**(1), pp. 31–34 (2001).
- [II.25] S. Sivaprakasam et K. A. Shore, « Cascaded synchronization of external-cavity laser diodes », *Opt. Lett.*, **26**(5), pp. 253–255 (mars 2001).
- [II.26] H. U. Voss, « Anticipating chaotic synchronization », *Phys. Rev. E*, **61**(5), pp. 5115–5119 (2000).
- [II.27] C. Masoller, « Anticipation in the synchronization of chaotic semiconductor lasers with optical feedback », *Phys. Rev. Lett.*, **86**(13), pp. 2782–2785 (2001).
- [II.28] S. Sivaprakasam, E. M. Shahverdiev, P. S. Spencer et K. A. Shore, « Experimental demonstration of anticipating synchronization in chaotic semiconductor lasers with optical feedback », *Phys. Rev. Lett.*, **87**(15), pp. 154101–1–3 (octobre 2001).
- [II.29] S. Tang et J.-M. Liu, « Experimental verification of anticipated and retarded synchronization in chaotic semiconductor lasers », *Phys. Rev. Lett.*, **90**(19), pp. 194101–1–4 (mai 2003).
- [II.30] R. W. Boyd, *Nonlinear Optics*, Elsevier, <https://linkinghub.elsevier.com/retrieve/pii/B97801216825X50007>, 3^e édition (2003).
- [II.31] M. Gonzalez-Herraez et T. Sylvestre, *Advanced fiber optics : concepts and technology, Chapter 5 : Nonlinear effects in optical fibers*, EPFL Press, Lausanne, Editor : Luc Thévenaz, also distributed by CRS Press, Taylor and Francis, Lausanne, <http://dx.doi.org/10.1201/b16404> (2011).
- [II.32] G. Agrawal, « Chapter 9 - Stimulated Brillouin Scattering », dans *Nonlinear Fiber Optics (Third Edition)* (Réd. G. Agrawal), Optics and Photonics, pp. 355 – 388, Academic Press, Boston, third edition édition (2001), <http://www.sciencedirect.com/science/article/pii/B9780123970237000097>.
- [II.33] B. Stiller, *Brillouin scattering in photonic crystal fiber : from fundamentals to fiber optic sensors*, Thèse de doctorat, Besançon (décembre 2011), <http://www.theses.fr/2011BESA2019>.
- [II.34] T. A. Birks, J. C. Knight et P. S. J. Russell, « Endlessly single-mode photonic crystal fiber », *Opt. Lett.*, **22**(13), pp. 961–963 (juillet 1997), <https://www.osapublishing.org/ol/abstract.cfm?uri=ol-22-13-961>.
- [II.35] P. Russell, « Photonic Crystal Fibers », *Science*, **299**(5605), pp. 358–362 (janvier 2003), <http://science.sciencemag.org/content/299/5605/358>.
- [II.36] R. Stolen et J. Bjorkholm, « Parametric amplification and frequency conversion in optical fibers », *IEEE Journal of Quantum Electronics*, **18**(7), pp. 1062–1072 (juillet 1982), <https://protect.kern+.2222em\relax//ieeexplore.ieee.org/document/1071660/>.
- [II.37] J. Hansryd, P. A. Andrekson, M. Westlund, J. Li et P. O. Hedekvist, « Fiber-based optical parametric amplifiers and their applications », *IEEE J. Sel. Topics Quantum Electron.*, **8**(3), pp. 506–520 (May 2002), <https://ieeexplore.ieee.org/document/1016354>.
- [II.38] M. E. Marhic, *Fiber Optical Parametric Amplifiers, Oscillators and Related Devices by Michel E. Marhic*, Cambridge University Press, <https://www.cambridge.org/core/books/fiber-optical-parametric-amplifiers-oscillators-and-related-devices/0D196103820EEF65BA AFC4B355C0EAE3> (novembre 2007).
- [II.39] M. Hanna, F. Druon et P. Georges, « Fiber optical parametric chirped-pulse amplification in the femtosecond regime », *Optics Express*, **14**(7), pp. 2783–2790 (avril 2006), <https://www.osapublishing.org/oe/abstract.cfm?uri=oe-14-7-2783>.
- [II.40] C. Caucheteur, D. Bigourd, E. Hugonnot, P. Sriftgiser, A. Kudlinski, M. Gonzalez-Herraez et A. Mussoft, « Experimental demonstration of optical parametric chirped pulse amplification in optical fiber », *Opt. Lett.*, **35**(11), pp. 1786–1788 (juin 2010), <https://www.osapublishing.org/ol/abstract.cfm?uri=ol-35-11-1786>.
- [II.41] A. Jolly, J.-F. Gleyze, P. D. Bin et V. Kermène, « Demonstration of a true single-shot 100 GHzbandwidth optical oscilloscope at 1053-1064 nm », *Opt. Express*, **17**(14), pp. 12109–12120 (juillet 2009), <https://www.osapublishing.org/oe/abstract.cfm?uri=oe-17-14-12109>.
- [II.42] J. Fan, A. Dogariu et L. J. Wang, « Parametric amplification in a microstructure fiber », *Appl. Phys. B*, **81**(6), pp. 801 (octobre 2005), <https://link.springer.com/article/10.1007/s00340-005-1991-2>.
- [II.43] J. E. Sharping, M. Fiorentino, P. Kumar et R. S. Windeler, « Optical parametric oscillator based on four-wave mixing in microstructure fiber », *Opt. Lett.*, **27**(19), pp. 1675–1677 (octobre 2002), <https://www.osapublishing.org/ol/abstract.cfm?uri=ol-27-19-1675>.

- [II.44] A. Y. H. Chen, G. K. L. Wong, S. G. Murdoch, R. Leonhardt, J. D. Harvey, J. C. Knight, W. J. Wadsworth et P. S. J. Russell, « Widely tunable optical parametric generation in a photonic crystal fiber », *Optics Letters*, **30**(7), pp. 762–764 (avril 2005), <https://www.osapublishing.org/ol/abstract.cfm?uri=ol-30-7-762>.
- [II.45] J. E. Sharping, « Microstructure Fiber Based Optical Parametric Oscillators », *J. Lightwave Technol.*, **26**(14), pp. 2184–2191 (juillet 2008), <https://www.osapublishing.org/jlt/abstract.cfm?uri=jlt-26-14-2184>.
- [II.46] T. Sylvestre, A. Kudlinski, A. Mussot, J. F. Gleyze, A. Jolly et H. Maillotte, « Parametric amplification and wavelength conversion in the 1040–1090 nm band by use of a photonic crystal fiber », *Appl. Phys. Lett.*, **94**(11), pp. 111104 (2009), <https://doi.org/10.1063/1.3100192>.
- [II.47] D. Besnard, « The megajoule laser program – ignition at hand », *Eur. Phys. J. D*, **44**(2), pp. 207–213 (août 2007), <https://link.springer.com/article/10.1140/epjd/e2006-00165-4>.
- [II.48] C. A. Haynam, P. J. Wegner, J. M. Auerbach, M. W. Bowers, S. N. Dixit, G. V. Erbert, G. M. Heestand, M. A. Henesian, M. R. Hermann, K. S. Jancaitis, K. R. Manes, C. D. Marshall, N. C. Mehta, J. Menapace, E. Moses, J. R. Murray, M. C. Nostrand, C. D. Orth, R. Patterson, R. A. Sacks, M. J. Shaw, M. Spaeth, S. B. Sutton, W. H. Williams, C. C. Widmayer, R. K. White, S. T. Yang et B. M. V. Wonterghem, « National Ignition Facility laser performance status », *Applied Optics*, **46**(16), pp. 3276–3303 (juin 2007), <https://www.osapublishing.org/ao/abstract.cfm?uri=ao-46-16-3276>.
- [II.49] D. A. Chestnut, C. J. S. d. Matos et J. R. Taylor, « Raman-assisted fiber optical parametric amplifier and wavelength converter in highly nonlinear fiber », *JOSA B*, **19**(8), pp. 1901–1904 (août 2002), <https://www.osapublishing.org/josab/abstract.cfm?uri=josab-19-8-1901>.
- [II.50] T. Sylvestre, H. Maillotte, E. Lantz et P. T. Dinda, « Raman-assisted parametric frequency conversion in a normally dispersive single-mode fiber », *Opt. Lett.*, **24**(22), pp. 1561–1563 (novembre 1999), <https://www.osapublishing.org/ol/abstract.cfm?uri=ol-24-22-1561>.
- [II.51] A. S. Y. Hsieh, G. K. L. Wong, S. G. Murdoch, S. Coen, F. Vanholsbeeck, R. Leonhardt et J. D. Harvey, « Combined effect of Raman and parametric gain on single-pump parametric amplifiers. », *Optics Express*, **15**(13), pp. 8104–8114 (juin 2007), <https://www.osapublishing.org/oe/abstract.cfm?uri=oe-15-13-8104>.
- [II.52] T. Kurashima, T. Horiguchi et M. Tateda, « Distributed-temperature sensing using stimulated Brillouin scattering in optical silica fibers », *Optics Letters*, **15**(18), pp. 1038–1040 (septembre 1990), <https://www.osapublishing.org/ol/abstract.cfm?uri=ol-15-18-1038>.
- [II.53] X. Bao, D. J. Webb et D. A. Jackson, « Combined distributed temperature and strain sensor based on Brillouin loss in an optical fiber », *Opt. Lett.*, **19**(2), pp. 141–143 (janvier 1994), <https://www.osapublishing.org/ol/abstract.cfm?uri=ol-19-2-141>.
- [II.54] K. Y. Song et H. J. Yoon, « High-resolution Brillouin optical time domain analysis based on Brillouin dynamic grating », *Optics Letters*, **35**(1), pp. 52–54 (janvier 2010), <https://www.osapublishing.org/ol/abstract.cfm?uri=ol-35-1-52>.
- [II.55] K. Hotate et M. Tanaka, « Distributed fiber Brillouin strain sensing with 1-cm spatial resolution by correlation-based continuous-wave technique », *IEEE Photon. Technol. Lett.*, **14**(2), pp. 179–181 (février 2002).
- [II.56] K. Y. Song, Z. He et K. Hotate, « Distributed strain measurement with millimeter-order spatial resolution based on Brillouin optical correlation domain analysis », *Opt. Lett.*, **31**(17), pp. 2526–2528 (septembre 2006), <https://www.osapublishing.org/ol/abstract.cfm?uri=ol-31-17-2526>.
- [II.57] M. Niklès, L. Thévenaz et P. A. Robert, « Simple distributed fiber sensor based on Brillouin gain spectrum analysis », *Opt. Lett.*, **21**(10), pp. 758–760 (mai 1996), <https://www.osapublishing.org/ol/abstract.cfm?uri=ol-21-10-758>.
- [II.58] F. Rodríguez-Barrios, S. Martín-López, A. Carrasco-Sanz, P. Corredera, J. D. Ania-Castañón, L. Thévenaz et M. González-Herráez, « Distributed Brillouin Fiber Sensor Assisted by First-Order Raman Amplification », *J. Lightwave Technol.*, **28**(15), pp. 2162–2172 (août 2010), <https://www.osapublishing.org/jlt/abstract.cfm?uri=jlt-28-15-2162>.
- [II.59] M. A. Soto, G. Bolognini et F. D. Pasquale, « Long-range simplex-coded BOTDA sensor over 120km distance employing optical preamplification », *Opt. Lett.*, **36**(2), pp. 232–234 (janvier 2011), <https://www.osapublishing.org/ol/abstract.cfm?uri=ol-36-2-232>.

- [II.60] L. Thévenaz, « Brillouin distributed time-domain sensing in optical fibers : state of the art and perspectives », *Frontiers Optoelectron. China*, **3**(1), pp. 13–21 (mars 2010), <https://link.springer.com/article/10.1007/s12200-009-0086-9>.
- [II.61] S. M. Foaleng, M. Tur, J.-C. Beugnot et L. Thévenaz, « High Spatial and Spectral Resolution Long-Range Sensing Using Brillouin Echoes », *J. Lightwave Technol.*, **28**(20), pp. 2993–3003 (octobre 2010), <https://www.osapublishing.org/jlt/abstract.cfm?uri=jlt-28-20-2993>.
- [II.62] L. Zou, X. Bao et L. Chen, « Distributed Brillouin temperature sensing in photonic crystal fiber », *Smart Mater. Struct.*, **14**(3), pp. S8 (2005), <http://stacks.iop.org/0964-1726/14/i=3/a=002>.
- [II.63] P. Dainese, P. S. J. Russell, N. Joly, J. C. Knight, G. S. Wiederhecker, H. L. Fragnito, V. Laude et A. Khelif, « Stimulated Brillouin scattering from multi-GHz-guided acoustic phonons in nanostructured photonic crystal fibres », *Nat. Phys.*, **2**(6), pp. 388–392 (juin 2006), <https://www.nature.com/articles/nphys315>.
- [II.64] J.-C. Beugnot, T. Sylvestre, D. Alasia, H. Maillotte, V. Laude, A. Monteville, L. Provino, N. Traynor, S. F. Mafang et L. Thévenaz, « Complete experimental characterization of stimulated Brillouin scattering in photonic crystal fiber », *Opt. Express*, **15**(23), pp. 15517–15522 (novembre 2007), <https://www.osapublishing.org/oe/abstract.cfm?uri=oe-15-23-15517>.
- [II.65] J. Hansryd, F. Dross, M. Westlund, P. A. Andrekson et S. N. Knudsen, « Increase of the SBS Threshold in a Short Highly Nonlinear Fiber by Applying a Temperature Distribution », *J. Lightwave Technol.*, **19**(11), pp. 1691 (novembre 2001), <https://www.osapublishing.org/jlt/abstract.cfm?uri=jlt-19-11-1691>.
- [II.66] J. M. C. Boggio, J. D. Marconi et H. L. Fragnito, « Experimental and numerical investigation of the SBS-threshold increase in an optical fiber by applying strain distributions », *J. Lightwave Technol.*, **23**(11), pp. 3808–3814 (novembre 2005).
- [II.67] K. Shiraki, M. Ohashi et M. Tateda, « Suppression of stimulated Brillouin scattering in a fibre by changing the core radius », *Electron. Lett.*, **31**(8), pp. 668–669 (avril 1995).
- [II.68] G. Charlet, « Progress in optical modulation formats for high-bit rate WDM transmissions », *IEEE J. Sel. Topics Quantum Electron.*, **12**(4), pp. 469–483 (juillet 2006).
- [II.69] J. M. Dudley, G. Genty et S. Coen, « Supercontinuum generation in photonic crystal fiber », *Rev. Mod. Phys.*, **78**(4), pp. 1135–1184 (octobre 2006), <https://link.aps.org/doi/10.1103/RevModPhys.78.1135>.
- [II.70] A. Boucon, D. Alasia, J. C. Beugnot, G. Melin, S. Lempereur, A. Fleureau, H. Maillotte, J. M. Dudley et T. Sylvestre, « Supercontinuum Generation From 1.35 to 1.7 μm by Nanosecond Pumping Near the Second Zero- Dispersion Wavelength of a Microstructured Fiber », *IEEE Photon. Technol. Lett.*, **20**(10), pp. 842–844 (mai 2008).
- [II.71] A. Kudlinski, A. K. George, J. C. Knight, J. C. Travers, A. B. Rulkov, S. V. Popov et J. R. Taylor, « Zero-dispersion wavelength decreasing photonic crystal fibers for ultraviolet-extended supercontinuum generation », *Opt. Express*, **14**(12), pp. 5715–5722 (juin 2006), <https://www.osapublishing.org/oe/abstract.cfm?uri=oe-14-12-5715>.
- [II.72] J. M. Stone et J. C. Knight, « Visibly “white” light generation in uniform photonic crystal fiber using a microchip laser », *Opt. Express*, **16**(4), pp. 2670–2675 (février 2008), <https://www.osapublishing.org/oe/abstract.cfm?uri=oe-16-4-2670>.
- [II.73] S. P. Stark, A. Podlipensky, N. Y. Joly et P. S. J. Russell, « Ultraviolet-enhanced supercontinuum generation in tapered photonic crystal fiber », *J. Opt. Soc. Am. B*, **27**(3), pp. 592–598 (mars 2010), <https://www.osapublishing.org/josab/abstract.cfm?uri=josab-27-3-592>.

ACTIVITÉS DE RECHERCHE À UP13

Sommaire

| | |
|---|-----------|
| III.1 Optique non linéaire dans un cristal photonique non linéaire | 52 |
| 1.1 SHG dans un guide de PPLN-2D | 54 |
| 1.2 OPG dans un PPLT-2D | 57 |
| 1.2.1 Génération multi-longueur d'onde | 60 |
| 1.2.2 Dégénérescence multi-longueur d'onde | 62 |
| III.2 Dynamique non linéaire d'une diode laser soumise à un retour optique . . | 66 |
| 2.1 Retour optique filtré par FBG | 66 |
| 2.2 Observation des ondes scélérates | 69 |
| 2.3 Etude d'une diode laser soumise à une SBS | 72 |
| III.3 Autres activités de recherche | 74 |
| III.4 Résumé | 75 |
| Bibliographies | 76 |

J'ai été recruté à l'Université Paris 13 en 2011. Depuis, je mène mes activités de recherche dans l'équipe Photonique Organique et Nanostructure (PON) du Laboratoire de Physiques des Lasers (LPL). Au sein du LPL, j'ai développé plusieurs activités de recherche, notamment l'optique non linéaire à base d'un cristal photonique non linéaire et la dynamique non linéaire d'une diode laser soumise à un retour optique. Les travaux présentés dans ce chapitre ont été effectués dans le cadre de différentes thèses. Ma principale contribution est donc le co-encadrement de thèses et le développement des deux thématiques en aspects expérimental et théorique dans l'équipe.

III.1 OPTIQUE NON LINÉAIRE DANS UN CRISTAL PHOTONIQUE NON LINÉAIRE

L'ÉTUDE des interactions optiques dans les cristaux photoniques non linéaires (**CPNL**) constitue une de mes principales activités de recherche au LPL. Dans cette section, je vais décrire mes travaux qui ont été menés principalement dans le cadre de deux thèses dans cette thématique.

De nos jours, les lasers se trouvent dans de nombreuses applications et le besoin de développer de nouvelles gammes de sources cohérentes est toujours très fort pour diverses applications. En comparaison aux lasers à semiconducteurs dont les longueurs d'ondes sont souvent limitées par la bande interdite du matériau, les lasers à cristaux non-linéaires offrent un très grand choix de longueurs d'onde (ou fréquences) par une conversion de fréquences grâce aux propriétés optiques non linéaires des cristaux. De ce fait, de tels lasers sont développés avec différents cristaux non linéaires.

Les effets non linéaires dans les cristaux non linéaires sont la génération de second-harmonique (**SHG** : second-harmonic generation), la génération de différence de fréquence (**DFG** : difference-frequency generation), la génération de somme de fréquenc (**SFG** : sum-frequency generation) et la génération paramétrique optique (**OPG** : optical parametric generation). Ces dernières apparaissent grâce à la susceptibilité de second ordre $\chi^{(2)}$ présents dans les cristaux. Afin d'obtenir ces effets, les deux conditions doivent être satisfaites : la conservation d'énergie et l'accord de phase (la conservation de moment). Ces effets sont listés sur le tableau III.1 avec les deux conditions pour chaque processus.

III.1 Pour que la conversion de fréquence soit efficace, l'accord de phase doit être obtenu entre la pompe et les nouvelles longueurs d'onde générées. L'accord de phase ne peut pas être obtenu généralement à cause de la dispersion chromatique dans les cristaux non linéaires. Il existe une méthode qui

TABLE III.1 – Processus non linéaires et les conditions.

| Processus non linéaire | Conservation d'énergie | Condition d'accord de phase |
|------------------------|----------------------------------|---|
| SHG | $\omega + \omega = 2\omega$ | $\mathbf{K}_\omega + \mathbf{K}_\omega = \mathbf{K}_{2\omega}$ |
| SFG | $\omega_1 + \omega_2 = \omega_3$ | $\mathbf{K}_{\omega 1} + \mathbf{K}_{\omega 2} = \mathbf{K}_{\omega 3}$ |
| DFG | $\omega_1 - \omega_2 = \omega_3$ | $\mathbf{K}_{\omega 1} - \mathbf{K}_{\omega 2} = \mathbf{K}_{\omega 3}$ |
| OPG | $\omega_p = \omega_s + \omega_i$ | $\mathbf{K}_{\omega p} = \mathbf{K}_{\omega s} + \mathbf{K}_{\omega i}$ |

s'appelle l'*accord de phase par biréfringence* (**BPM** : birefringence phase matching). Le **BPM** exploite les cristaux biréfringents afin de réaliser un accord de phase suivant les polarisations des ondes optiques en interaction. Cette méthode est très efficace, cependant le choix du cristal et le choix du tenseur $\chi^{[2]}$ limitent les possibilités d'interactions non linéaires [III.1].

Il existe une autre méthode que l'on appelle le *quasi-accord de phase* (**QPM** : quasi-phase matching) qui permet au contraire d'exploiter de façon optimale des cristaux non linéaires sur un grand nombre d'interaction non linéaire. Il s'agit d'inverser le signe de la susceptibilité non linéaire du deuxième ordre $\chi^{(2)}$ toute la longueur de cohérence afin d'introduire un déphasage de π suivant une direction (voir la figure III.1(a)). Ce déphasage de π permet une interférence constructive à chaque longueur de cohérence, ce qui permet d'accroître l'efficacité de conversion. Cette méthode est plus avantageuse que le **BPM** en terme du choix de cristal. De plus, elle permet d'obtenir une grande variété d'interactions pour un même cristal en variant la période d'inversion du $\chi^{[2]}$. **PPLN** (periodically-poled lithium niobate) et **PPLT** (periodically-poled lithium tantalate) sont les cristaux très adaptés pour la conversion de fréquence. Grâce au **QPM**, la conversion de fréquence devient efficace pour la **SHG**, la **SFG**, la **DFG** et l'**OPG**.

Ces cristaux périodiquement polarisés sur une direction possèdent un vecteur de réseau réciproque (**RLV** : Reciprocal Lattice Vector) qui est unique. C'est ce vecteur qui intervient dans le processus de **QPM**, d'une grande efficacité pour la conversion de fréquence. Malgré leur efficacité de conversion de fréquence, cet unique **RLV** limite la souplesse de **QPM** dans ces cristaux.

Les **CPNLs** sont des matériaux dont le signe du $\chi^{(2)}$ est inversé périodiquement dans les deux dimensions de l'échantillon comme illustré sur la figure III.1(b). Les cristaux les plus utilisés sont le niobate de lithium (LiNbO₃) et le tantalate de lithium (LiTaO₃) avec des valeurs du $\chi^{(2)}$ importantes. De ce fait, on les appelle **PPLN-2D** (2 dimension periodically-poled lithium niobate) ou **PPLT-2D** (2 dimension periodically-poled lithium tantalate).

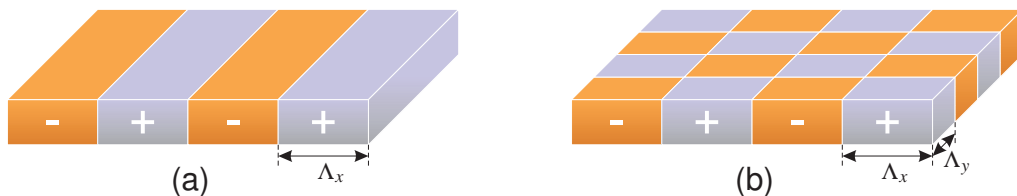


FIGURE III.1 – (a) Cristal non linéaire périodiquement polarisé en 1 dimension. (b) Cristal photonique non linéaire en 2 dimensions avec les pas Δ_x et Δ_y .

Le réseau en 2D permet augmenter le nombre de **RLVs** qui peuvent intervenir dans l'ensemble d'interactions non linéaires. Cette structure de réseau a été proposé par V. Berger en 1998 [III.2] et le retournement de $\chi^{(2)}$ en 2D engendre de nombreux vecteurs de réseau réciproques qui offrent une flexibilité de **QPM** [III.3]. Par conséquent, les processus non linéaires associés à $\chi^{(2)}$ peuvent être obtenus dans les deux directions du plan du cristal ou suivant l'angle d'incidence de la pompe. Par conséquent, de nombreuses études ont été faites en utilisant ce type de cristal pour la **SHG** [III.4, III.5,

[III.6], la SFG [III.7], la DFG [III.8] ou l'OPG [III.9, III.10, III.11].

Les CPNLs ont été utilisés également dans d'autres études telles que la génération Térahertz [III.12], l'amplification d'impulsions ultra-rapides [III.13] et la détection de gaz [III.14]. De plus, le processus OPG dans un CPNL a été utilisé pour la génération d'une paire de photons intriqués pour l'optique quantique [III.15] et même pour la démonstration de protocoles de communications quantiques sur une longue distance en espace libre et en fibres optiques [III.16, III.17]. Donc, en vue de l'application quantique, les CPNLs peuvent être utilisés comme un matériau compétitif pour une source de photon unique.

Les CPNL ont également contribué à la découverte des phénomènes particuliers comme la radiation Cerenkov non linéaire [III.18], le faisceau SHG conique [III.19], l'effet Talbot non linéaire [III.20], les copies des états de moment angulaire orbital [III.21].

Il existe plusieurs structures de réseau. Les réseaux les plus utilisés sont les réseaux hexagonal et carré. La plupart des études ont été faites avec le réseau hexagonal [III.9, III.11, III.19]. Néanmoins, un faible nombre d'études ont été menées sur le réseau carré [III.5, III.6, III.10].

Dans ce contexte, nous avons choisi pour étude les PPLN-2D et PPLT-2D avec le réseau carré. Ces études ont été menées en collaboration depuis le début avec Prof. L.-H. Peng à l'Université National de Taïwan et avec un projet BQR et un projet CNRS PICS. Pendant ces travaux, j'ai participé à co-encadrer M. Quentin RIPAULT et Mlle. Zohra YELLAS.

1.1 SHG dans un guide de PPLN-2D

Dans un premier temps, nous avons travaillé sur la SHG dans un PPLN-2D. Ce processus non linéaire est l'effet optique le plus utilisé pour la conversion de fréquence. Ce processus est obtenu majoritairement dans des CPNLs sous forme de bulk. L'utilisation de ces structures en configuration guide d'onde pourrait être d'un grand intérêt vu l'augmentation des efficacités de conversion possibles et la miniaturisation du composant dans ce cas de figure. Récemment, les guides d'onde de PPLN ont été utilisés pour générer une paire de photons intriqués [III.22, III.23].

Pour la fabrication d'un guide d'onde dans un CPNL, les techniques de fabrication utilisées sont la diffusion de métal et l'échange ionique [III.24]. Cependant, ces techniques altèrent les propriétés optiques non linéaires. De plus, ces deux techniques n'ont pas été utilisées avec des structures 2D à cause de la modification des propriétés optiques non linéaires. Récemment, l'implantation d'ion léger (tel que l'hélium) a été développée et il a été démontré que cette technique est très bien adaptée à la fabrication des guides d'onde dans des structures PPLN et PPLT avec un contrôle extrêmement précis de la variation d'indice et de l'épaisseur imposée au guide [III.25, III.26]. L'avantage de cette technique repose sur le contrôle précis de l'épaisseur de guide par l'énergie d'implantation et sur le changement d'indice de réfraction par la dose d'ions utilisé pour la fabrication du guide. Cette méthode permet également une fabrication de couche mince de cristal non linéaire par la technique de coupe ionique de

cristal (SmartCut) [III.27]. De plus, elle permet de préserver les propriétés optiques non linéaires du matériau contrairement aux autres techniques [III.28].

Dans ce contexte, nous avons étudié pour la première fois le processus **SHG** dans un guide d'onde de **PPLN-2D** fabriqué par la technique d'implantation d'ion He⁺. La plupart des études de **SHG** dans la littérature ont été faites dans un **CPNL** avec un réseau hexagonal. Dans ce travail, nous avons étudié la **SHG** dans un **PPLN-2D** avec un réseau carré. Par la suite, nous avons comparé l'efficacité de conversion du guide d'onde avec celle du cristal massif. Ce travail a été effectué dans le cadre de la thèse de Mr. Q. Ripault que j'ai co-encadré sous la direction du Prof. A. Boudrioua [III.1]. De plus, ce travail a été réalisé en collaboration avec Prof. L.-H. Peng de l'Université Nationale de Taïwan à Taïwan pour la fabrication des échantillons de **PPLN-2D** et avec Prof. E. Nstoenzok du Laboratoire CEMHTI à Orléans pour l'implantation d'ion d'hélium.

Le domaine de $\chi^{(2)}$ de notre échantillons de LiNbO₃ est inversé périodiquement en deux directions avec un pas de 6,92 μm. Sur la figure III.2(a), nous présentons le réseau carré que nous avons utilisé dans cette étude. Les **RLVs** interviennent dans le processus non linaire afin d'obtenir la **SHG** d'une source à 1064 nm par **QPM**.

Afin d'obtenir le processus **SHG**, il faut satisfaire les lois de conservation d'énergie et de moment qui sont écrites par :

$$\omega_{\text{SHG}} = \omega_p + \omega_p \quad (\text{III.1})$$

$$\begin{aligned} \mathbf{K}_{\text{SHG}} - \mathbf{K}_p - \mathbf{K}_p &= \mathbf{K}_{m,n} \\ \rightarrow \frac{n_{\text{SHG}}(\lambda_{\text{SHG}}, T)}{\lambda_{\text{SHG}}} - \frac{n_p(\lambda_p, T)}{\lambda_p} - \frac{n_p(\lambda_p, T)}{\lambda_p} - \frac{\sqrt{m^2 + n^2}}{\Lambda} &= 0 \end{aligned} \quad (\text{III.2})$$

où, ω_{SHG} est la fréquence de **SHG**, ω_p est la fréquence de la pompe, \mathbf{K}_{SHG} est le vecteur d'onde de **SHG**, \mathbf{K}_p est le vecteur d'onde de la pompe et $\mathbf{K}_{m,n}$ est le vecteur de réseau réciproque à l'ordre de **QPM** de m et n . Ces vecteurs interviennent dans un processus **SHG** comme montré sur la figure III.2(a).

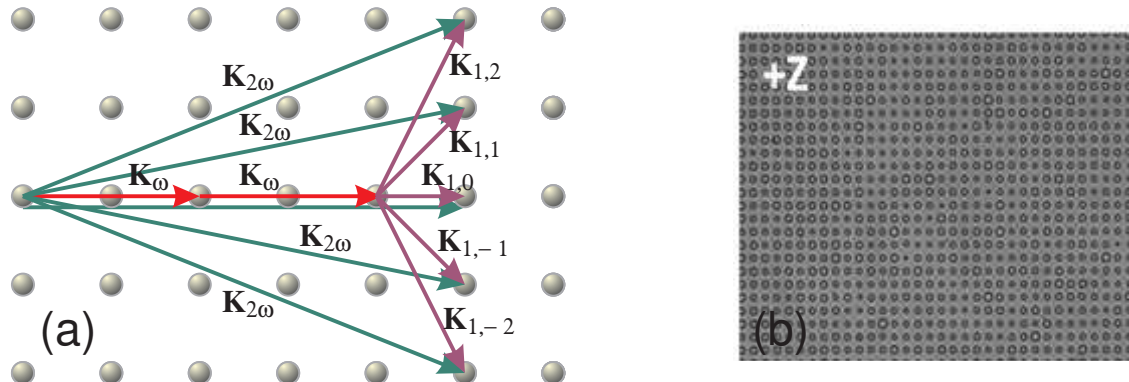


FIGURE III.2 – (a) Réseau carré d'un **CPNL** avec les vecteurs de réseau réciproques pour **SHG**. (b) Image du **PPLN-2D** de réseau carré sur le côté z^+ .

La figure III.2(b) montre notre échantillon de **PPLN-2D** en forme de réseau carré avec un pas de 6,92 μm. Les échantillons ont été fabriqués par l'équipe taïwanaise. L'inversion de domaine se fait par

l’application d’une très haute tension (~ 30 kV/mm) à travers un masque dont la structure porte un réseau carré [III.29, III.1].

Ensuite, une partie des échantillons a subie un bombardement d’ions d’hélium par un accélérateur de Van De Graaff avec une dose de $1,5 \times 10^{16}$ ions/cm² et une énergie de 1,5 MeV. Avec ces paramètres, les ions s’arrêtent à environ 3,6 µm sous la surface des échantillons afin de créer une barrière d’indice, ce qui engendre un guide d’onde planaire. Cette implantation d’ion d’hélium a été réalisée en collaboration avec le Laboratoire CEMHTI à Orléans. Nous avons caractérisé ces échantillons par le processus SHG en pompant par une diode laser continue à 1064 nm avec une puissance de 250 mW. Les échantillons sont chauffés à 53 °C pour exciter le vecteur \mathbf{K}_{10} et à 102 °C pour les vecteurs $\mathbf{K}_{1\pm 1}$.

Sur la figure III.3, l’intensité de SHG est présentée en fonction de l’angle de sortie du cristal. Nous pouvons remarquer deux pics à environ $\pm 5^\circ$ autour du pic central pour le bulk et le guide. Ces pics viennent en effet des vecteurs $\mathbf{K}_{1\pm 1}$ et les angles de $\pm 5^\circ$ sont très proches des angles théoriques de $\pm 4,6^\circ$.

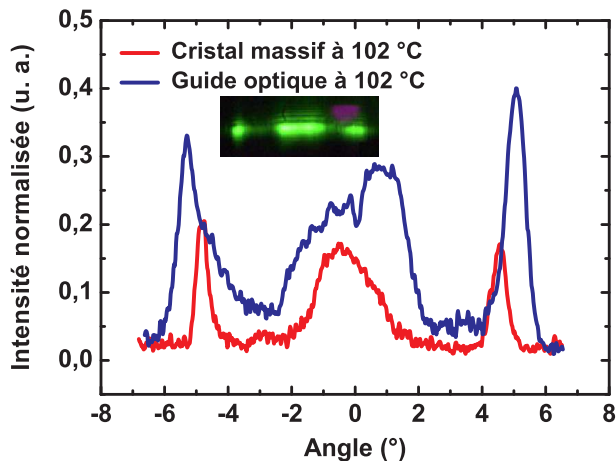
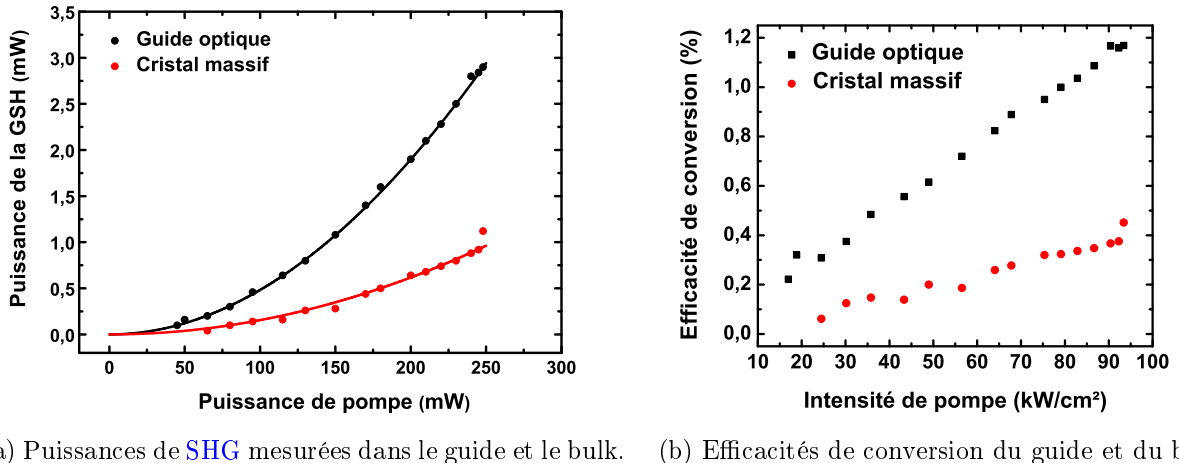


FIGURE III.3 – Intensité normalisée de SHG en fonction de l’angle de sortie. L’image sur la figure est une image obtenue à la sortie du cristal. Source : Ref. [ACL I.36].

Nous avons également mesuré la puissance de SHG comme montré sur la figure III.4(a). À une puissance de pompe de 250 mW, la puissance de SHG dans un guide est mesurée de 2,9 mW tandis que celle dans un bulk est mesurée de 1,1 mW. Les courbes d’ajustement montrent que la puissance dans le guide est trois fois plus élevée que celle dans le bulk. La figure III.4 indique l’efficacité de conversion pour les deux cas. Nous pouvons remarquer que l’efficacité dans le guide est trois fois plus grande que celle dans le bulk. Ces résultats confirment clairement que l’efficacité est beaucoup plus grande dans un guide que dans un bulk grâce au confinement de l’énergie dans le guide.

Les résultats nous ont révélé que grâce aux RLVs nous avons obtenu le processus SHG de 532 nm à différents angles en pompant l’échantillon à 1064 nm. De plus, le guide d’onde par l’implantation d’ion d’hélium a permis d’augmenter trois fois son efficacité de conversion par rapport aux CPNLs massifs grâce au confinement de l’énergie dans le guide [ACL I.36] (voir la page 140, Chapitre IV).



(a) Puissances de SHG mesurées dans le guide et le bulk. (b) Efficacités de conversion du guide et du bulk.

FIGURE III.4 – Comparaison du guide et du bulk. Source : Ref. [ACL I.36].

1.2 OPG dans un PPLT-2D

Par la suite, nous avons travaillé sur la génération paramétrique optique (OPG) dans un PPLT-2D. Le choix de LiTaO₃ s'appuie sur un champs coercitif (17 kV/cm) plus faible que celui de LiNbO₃ (40 kV/cm). Il est donc plus facile de mettre en œuvre un poling dans un laboratoire. Parmi les processus non linéaires associant à $\chi^{(2)}$, le seul processus OPG permet d'accorder les longueurs d'onde générées sans modifier la longueur d'onde de la pompe. L'accordabilité peut se faire alors en variant les paramètres du quasi-accord de phase comme la période du réseau, la température du cristal ou l'angle d'incidence. De manière générale, le processus OPG produit deux longueurs d'onde à partir d'une seule longueur d'onde de pompe, qu'on appelle *signal* et *idler*. Ces avantages ont conduit des études d'OPG dans un CPNL, notamment un PPLT-2D [III.9, III.10, III.11].

De plus, le processus OPG génère deux photons à partir d'un seul photon de pompe. Dans certaines conditions d'accord de phase, deux photons jumeaux peuvent être générés dans un état intriqué [III.30]. Ces deux photons intriqués peuvent être utilisés pour les communications quantiques [III.15, III.16, III.17, III.31]. En effet, une source de photons intriqués est un élément très important pour de nombreuses études de l'information quantique et de la communication quantique. Donc, le PPLN-2D et le PPLT-2D qui possèdent une efficacité de conversion élevée sont des matériaux prometteurs pour de telles applications.

Comme le processus SHG dans un PPLN-2D, le processus OPG a besoin de deux conditions : la conservation de l'énergie et la conservation de moment (QPM). Ces conditions sont données par

$$\omega_p = \omega_s + \omega_i \quad (\text{III.3})$$

$$\begin{aligned} & \mathbf{K}_p - \mathbf{K}_s - \mathbf{K}_i = \mathbf{K}_{m,n} \\ \rightarrow & \frac{n_p(\lambda_p, T)}{\lambda_p} - \frac{n_s(\lambda_s, T)}{\lambda_s} - \frac{n_i(\lambda_i, T)}{\lambda_i} - \frac{\sqrt{m^2 + n^2}}{\Lambda} = 0 \end{aligned} \quad (\text{III.4})$$

où, ω_p est la fréquence de la pompe ω_s est la fréquence de signal, ω_i est la fréquence d'idler, \mathbf{K}_p est le vecteur d'onde de la pompe, \mathbf{K}_s est le vecteur d'onde de signal et \mathbf{K}_i est le vecteur d'onde d'idler.

Afin de satisfaire la condition de QPM, les RLVs peuvent intervenir pour compenser le désaccord de phase comme on peut le voir dans l'Eq.(III.4). La figure III.5(a) illustre le QPM d'un processus OPG dans un réseau 2D. En effet, les RLVs d'un réseau 2D peuvent fournir différentes combinaisons de QPM, ce qui permet une flexibilité de QPM ou une accordabilité des longueurs d'onde signal et idler suivant la direction des vecteurs. Afin de développer une nouvelle source cohérente accordable large bande, il est pertinent d'exploiter le processus OPG avec les RLVs d'un CPNL.

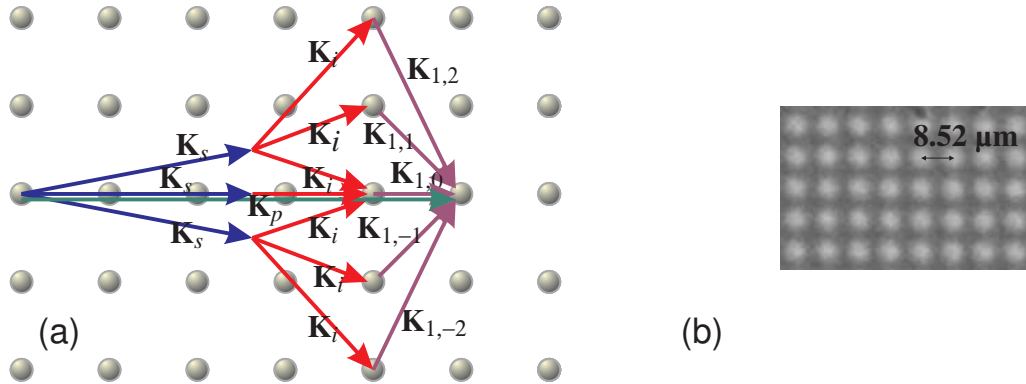


FIGURE III.5 – (a) Quasi-accord de phase dans un réseau carré d'un CPNL avec les RLV pour OPG. (b) Image du PPLT-2D de réseau carré avec un pas de 8,52 μm .

Dans ce contexte, nous nous sommes intéressés à travailler sur l'OPG dans un PPLT-2D. La figure III.5(b) montre une image du PPLT-2D que nous utilisons dans nos travaux. C'est un réseau carré comme le cas de l'étude de SHG, mais sur un PPLT-2D avec un pas de réseau de 8,52 μm . Ces échantillons ont été fabriqués par l'équipe taïwanaise en collaboration.

Afin de caractériser les échantillons de PPLT-2D, un banc expérimental a été monté comme montré sur la figure III.6. Le laser pompe est un laser pulsé à 532 nm sur une durée de 500 ps. Le faisceau laser est injecté dans l'échantillon à l'aide d'une lame demi-onde et d'une lentille. Un four chauffe l'échantillon à 110 °C qui est une température optimale pour obtenir le QPM. Les nouvelles longueurs d'onde générées sont collectées dans une fibre optique après avoir filtré la pompe à 532 nm. Le spectre est enregistré sur un analyseur de spectre optique.

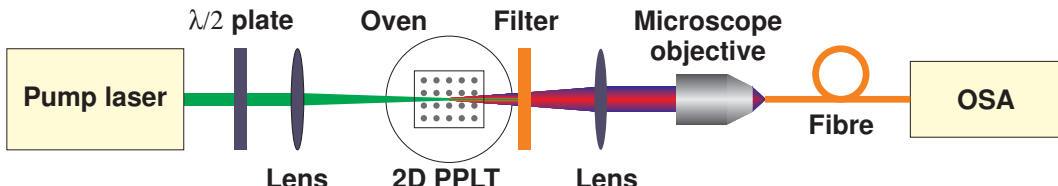


FIGURE III.6 – Banc expérimental de mesure de spectres d'OPG. OSA : Analyseur de spectre optique. Source : Ref. [ACL I.46].

La figure III.7 montre les résultats d'un processus OPG. En pompant le cristal à 532 nm, nous

obtenons deux longueurs d'onde : le signal à 787 nm et l'idler à 1640 nm comme on peut le voir sur la figure III.7(a). Ces deux longueurs d'onde correspondent à la théorie. Sur la figure III.7(b), les longueurs d'onde du signal et de l'idler varient en fonction de la température. Le comportement de ces longueurs d'onde est opposé avec la température. Les courbes simulées à partir des Eq.(III.3) et (III.4) en tenant compte de l'équation de Sellmeir pour le tantalat de lithium [III.32] correspondent aux points mesurés.

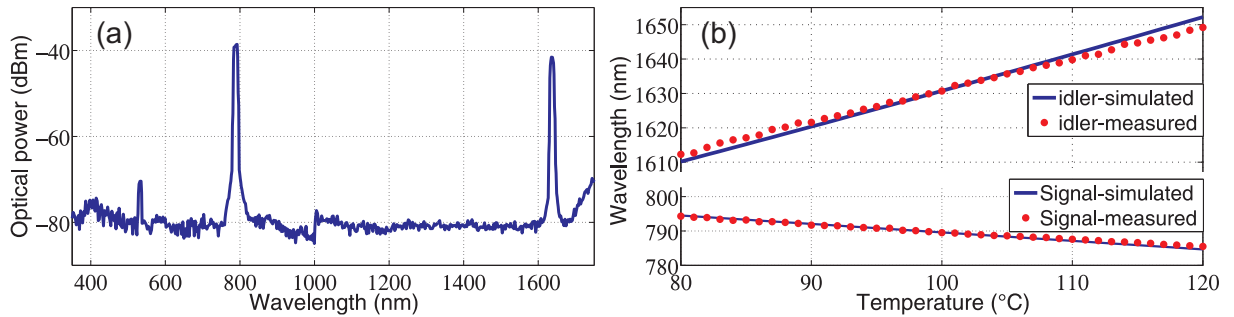


FIGURE III.7 – (a) Spectre d'un processus OPG dans un PPLT-2D. (b) Accordabilité du signal et de l'idler en fonction de la température. Source : Ref. [ACL I.46].

La thématique a démaré au sein de l'équipe dans le cadre de thèse de M. Mohamed LAZOUL [III.33]. Dans son travail, le processus OPG a été démontré dans un PPLT-2D en pompant par un laser à 532 nm. Il a également montré que les vecteurs \mathbf{K}_{10} et $\mathbf{K}_{1\pm 1}$ interviennent dans le processus OPG afin de générer de multiples longueurs d'onde y compris le signal et l'idler [III.10]. Il a aussi travaillé sur la démonstration d'un oscillateur paramétrique optique (OPO) en exploitant le processus dans le PPLT-2D [III.34].

Après sa thèse, nous avons continué à travailler sur cette problématique, notamment dans le cadre des thèses de M. Hocine CHIKH-TOUAMI [III.35] et de Mlle. Zohra YELLAS. Les travaux de thèse de M. Chikh-Touami ont été menés dans le cadre de thèse en cotutelle avec l'Ecole Militaire Polytechnique d'Algérie. Dans ses travaux de thèse, nous avons démontré la contribution des vecteurs \mathbf{K}_{10} et $\mathbf{K}_{1\pm 1}$ en fonction de l'angle incident de la pompe. Quand l'angle d'incidence de la pompe n'est pas zéro ($\theta_p \neq 0$), la condition de QPM se modifie en fonction de l'angle. Par conséquent, les longueurs d'onde du signal et de l'idler varient en fonction de l'angle. De manière générale, chaque RLV intervient à chaque QPM, ce qui donne plusieurs signal-idler associés à différents vecteurs. Cependant, deux vecteurs peuvent intervenir dans la même condition de QPM à un angle donné. Dans ce contexte, nous avons démontré que deux RLVs interviennent à la génération d'une seule longueur d'onde du signal. Cette intervention de deux RLVs permet également d'augmenter le gain paramétrique par rapport au cas de l'intervention d'un seul RLV [ACL I.43]. Le deuxième aspect de ces travaux de thèse est la démonstration de la génération du signal-idler commun. Ceci s'appelle également génération de faisceau jumeaux. Nous avons démontré la génération de deux idlers jumeaux issus du même signal en associant \mathbf{K}_{10} et \mathbf{K}_{11} sur chaque idler [ACL I.44].

1.2.1 Génération multi-longueur d'onde

Ce travail s'appuie sur les travaux de M. Chikh-Touami sur le processus **OPG**. Récemment, des études ont été rapportées sur la démonstration d'un processus **SFG-DFG** simultané dans un **PPLN** par un effet cascade afin de générer deux nouvelles longueurs d'onde [III.36, III.37]. Avec l'effet cascade, trois longueurs d'onde peuvent être générées suivant un processus **SHG** à partir du signal ou de l'idler d'un processus **OPG** dans un **PPLT** [III.38, III.39]. De même, la génération de troisième harmonique peut être réalisée en cascade en combinant la **SHG** et la **SFG** [III.40]. Dans les références [III.41, III.42], un spectre large bande a été obtenu dans un **PPLT** de réseau hexagonal en pompant autour de la longueur d'onde de la dispersion nul du cristal (~ 1820 nm). De plus, les auteurs ont démontré une génération de multi-longueur d'onde en exploitant plusieurs processus non linéaires dans le même cristal [III.43]. Une des applications de multi-longueur d'onde est l'application Lidar [III.44, III.45]. Les **QPM** multi-longueur d'onde et multidirectionnels peuvent également être utilisés comme un milieu de gain paramétrique prometteur pour des sources de photons intriqués multiples pour une application de l'ordinateur quantique [III.46, III.47].

Les travaux précédents de l'équipe ont été menés à une énergie en dessous de $10\text{ }\mu\text{J}$. Dans ce travail, nous avons amélioré le banc expérimental afin d'augmenter l'énergie de la pompe au delà de $10\text{ }\mu\text{J}$. Les spectre de la figure III.8 ont été obtenus pour une énergie de $40\text{ }\mu\text{J}$. Dans le spectre de la figure III.8(a), nous observons huit pics y compris la pompe à 532 nm, le signal à 787 nm et l'idler à 1640 nm. Ces cinq pics supplémentaires sont originaires de différents processus non linéaire. Les longueurs d'onde sont mesurées à 393 nm, 402 nm, 820 nm, 1514 nm et 1574 nm d'après les figure III.8(b), (c) et (d). Nous avons analysé chaque nouvelle longueur d'onde générée.

- La longueur d'onde de 393 nm peut facilement être identifiée du fait qu'elle est la moitié de la longueur d'onde du signal à 787 nm. L'origine de ce pic est donc le processus **SHG**. D'après les Eqs.(III.1) et (III.2), le processus **SHG** est effectué au 3^{ème} ordre de **QPM** avec un pas de $8,4\text{ }\mu\text{m}$ qui est proche du pas de réseau de $8,52\text{ }\mu\text{m}$.
- Le pic de 402 nm est originaire d'un process **SFG** entre la pompe à 532 nm et l'idler à 1640 nm. D'après les Eqs.(III.3) et (III.4), le **QPM** de l'ordre 2 intervient dans le processus avec un pas de $8,1\text{ }\mu\text{m}$.
- Il apparaît que l'idler à 1640 nm lui-même interagit afin de générer une longueur d'onde à 820 nm dans un processus **SHG**. Cependant, le calcul à l'aide des Eqs.(III.1) et (III.2) donne lieu à un pas de $21\text{ }\mu\text{m}$.
- Le signal à 787 nm et l'idler à 1640 nm pourraient encore interagir pour donner une longueur d'onde de 1514 nm dans un processus **DFG**. Cependant, le pas de **QPM** obtenue est alors de $21\text{ }\mu\text{m}$.
- La longueur d'onde de 1574 nm correspond au double de 787 nm. Il se pourrait que ceci est dû à la génération demi-harmonique (**HHG** : Half-harmonique generation) du signal. Là encore, le

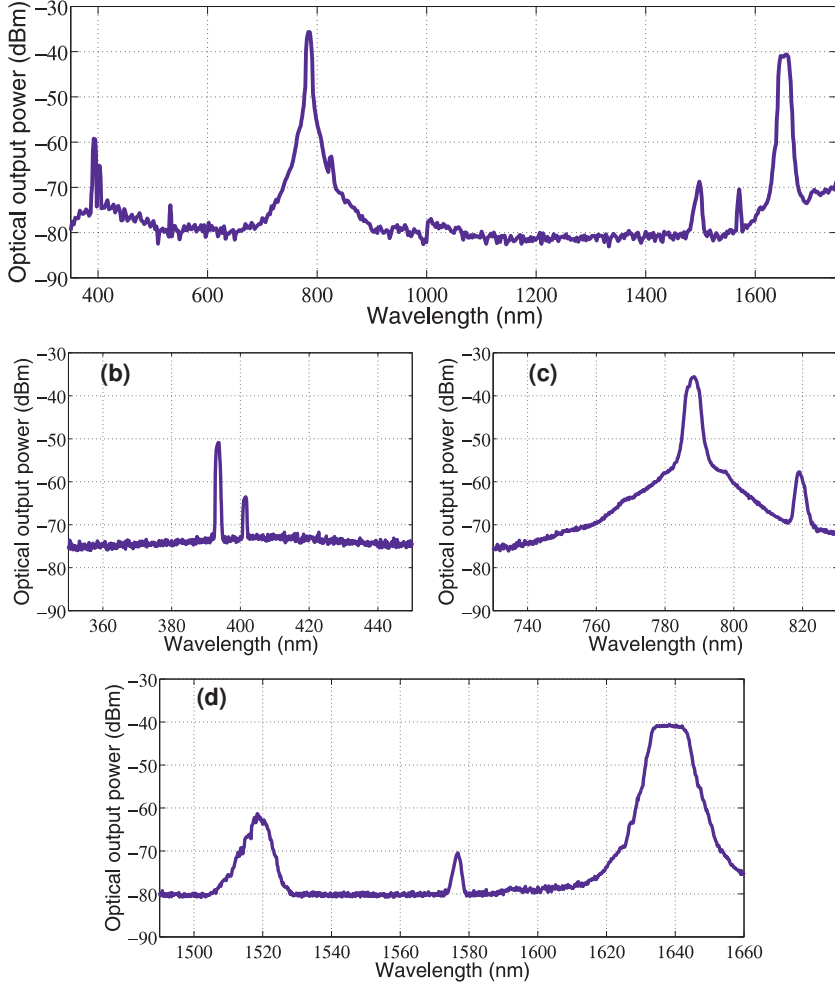


FIGURE III.8 – (a) Spectre d'une multi-longueur d'onde dans un PPLT-2D. Agrandissement de spectre (b) entre 350 nm et 450 nm, (c) entre 730 nm et 830 nm et (d) entre 1490 nm et 1660 nm. Source : Ref. [ACL I.46].

pas de QPM calculé devrait être de 21 μm .

La première analyse nous indique que le processus SHG du signal et le processus SFG de la pompe et de l'idler ont eu lieu avec la vérification des deux conditions. De plus, ces processus sont issus de l'effet cascade à partir du signal et de l'idler. En revanche, la condition de QPM n'est pas respectée pour les pics à 820 nm, à 1514 nm et à 1574 nm. Nous avons analysé ces pics d'une autre manière. En effet, une deuxième analyse nous révèle la possibilité d'un autre processus OPG qui génère des pics à 820 nm et 1514 nm pour un pas de 8,38 μm . Avec cet analyse, nous suggérons l'existence potentielle d'un pic à 803 nm qui proviendrait d'une OPG avec le pic à 1574 nm par la pompe à 532 nm et pour un pas de 8,42 μm (voir le tab. III.2). Ces résultats nous montrent qu'une multi-longueur d'onde est générée en respectant les deux conditions.

Nous avons également effectué une étude en variant l'énergie de la pompe de 7 μJ à 37 μJ . En variant l'énergie par un pas de 1 μJ , une cartographie de spectre optique a été établie comme montré sur la figure III.9. D'après la cartographie, le processus SHG commence à apparaître à une énergie de

TABLE III.2 – Le pas et l’ordre de QPM pour chaque processus non linéaire dans un PPLT-2D.

| λ (nm) | interaction | Pas de QPM Λ (μm) | Ordre de QPM m |
|----------------|-------------|--|------------------|
| 393 | SHG | 8.4 | 3 |
| 402 | SFG | 8.1 | 2 |
| 787, 1640 | OPG 1 | 8.51 | 1 |
| 820, 1514 | OPG 2 | 8.38 | 1 |
| 803, 1574 | OPG 3 | 8.42 | 1 |

10 μJ et le processus SFG à 11 μJ et enfin les autres processus à 15 μJ .

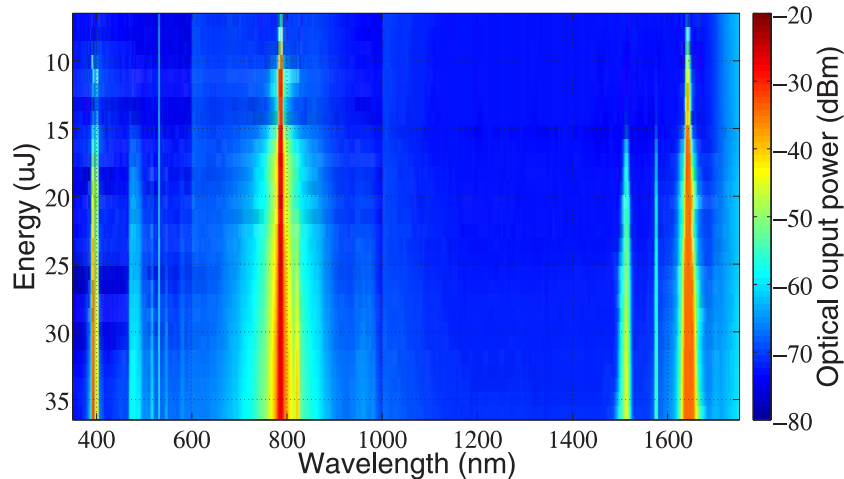


FIGURE III.9 – Cartographie de spectre en fonction de l’énergie de la pompe. Source : Ref. [ACL I.46].

Dans ce travail, nous avons démontré pour la première fois la génération d’une multi-longueur d’onde par différents processus non linéaires dans un PPLT-2D de réseau carré. Les processus SHG et SFG ont été obtenus par l’effet cascade à partir du processus OPG. Les résultats montrent qu’il est possible que deux processus OPG complémentaires se soient produits [ACL I.46] (voir la page 147, Chapitre IV). Ces travaux ont été effectués dans le cadre de thèse de Mlle. Yellas [III.48] que j’ai participé à co-encadré.

1.2.2 Dégénérescence multi-longueur d’onde

Nous avons vu sur la figure III.7(b) l’évolution des longueurs d’onde du signal et de l’idler en fonction de la température. L’évolution des longueurs d’onde obtenues dans la partie précédente a également été étudiée avec la température. Afin d’obtenir le spectre de multi-longueur d’onde en variant la température, le banc expérimental montré sur la figure III.6 a été entièrement automatisé. La figure III.10 présente les spectres de la multi-longueur d’onde de 40 °C à 140 °C. Sur la figure, les différents pics sont observés, notamment le signal pour le pic (5) (ω_s) et l’idler pour le pic (6) (ω_i). La pompe résiduelle est également présente par une ligne droite à 532 nm. On peut remarquer sur la figure que neuf pics sont générés à partir d’une seule pompe (ω_p). Les pics observés sur la figure III.8 sont également tous présents sur la figure III.10. On peut aussi remarquer qu’à côté de la pompe, il

existe deux nouveaux pics (pics (3) et (4)) dont les longueurs d'onde changent avec la température. La cartographie révèle que la multi-longueur d'onde est accordable sur une plage de plus de deux octaves allant de l'UVA au proche infrarouge. Dans ce comportement des pics en fonction de la température, nous pouvons observer deux aspects principaux : l'origine du comportement des pics et le point de croisement à 65 °C.

D'après cette cartographie, nous avons déduit les relations de ces longueurs d'onde qui sont synthétisées sur la table III.3. La conservation d'énergie peut suggérer les processus à l'origine de chaque pic comme indiqué sur la table. Comme nous pouvons remarquer, les nouvelles longueurs d'onde générées à part le signal et l'idler résultent de l'interaction de la pompe, du signal et/ou de l'idler dans un processus en cascade. Ils sont donc correlés entre eux. Le pic (4) apparaît comme un processus **THG** (third-harmonic generation) de l'idler ($3\omega_i$). Comme le **PPLT** n'a pas la symétrie d'inversion, ce pic ne proviendrait pas de la susceptibilité de troisième ordre. Il est plutôt suggéré que le pic est un résultat de **SFG** de $2\omega_i$ et ω_i par un processus cascade. Ce processus **THG** par un processus cascade de **SHG** et **SFG** a également été démontré dans la littérature [III.7, III.40]. Les pics (1), (2), (3), (4), (5) et (9) vérifient les équations de conservation par **QPM** au premier, deuxième ou troisième ordre, pour un pas du cristal de 8,51 μm. En revanche, les pics (6), (7) et (8) ne vérifient pas le **QPM** directement avec ce pas. Il faut cependant remarquer que la relation entre les pics (6) et (7) avec la pompe donne lieu à $\omega_p = 2\omega_i + \omega_s - \omega_i (= \omega_s + \omega_i)$ avec une période de **QPM** d'environ 8,38 μm. Ces longueurs d'onde correspondent à 820 nm pour le pic (6) et à 1514 nm pour le pic (7) à la température de 110 °C comme indiqué sur le tableau III.2. Le pic (8) peut être généré de façon similaire. Une interaction pourrait se faire de la manière suivante : $\omega_p = \omega_s/2 + \omega_s/2 + \omega_i (= \omega_s + \omega_i)$ avec une période de **QPM** d'environ 8,42 μm. Ceci suggère une existence d'un autre pic ($\omega_s/2 + \omega_i$) dont la longueur d'onde correspond à 803 nm à 110 °C. Cette longueur d'onde est également mentionnée sur le tableau III.2. Comme expliqué dans la partie précédente, ce pic serait présent, mais noyé par un large spectre du signal. En tenant compte de cette hypothèse, tous les pics sont générés en accord avec les conditions de **QPM** dans le

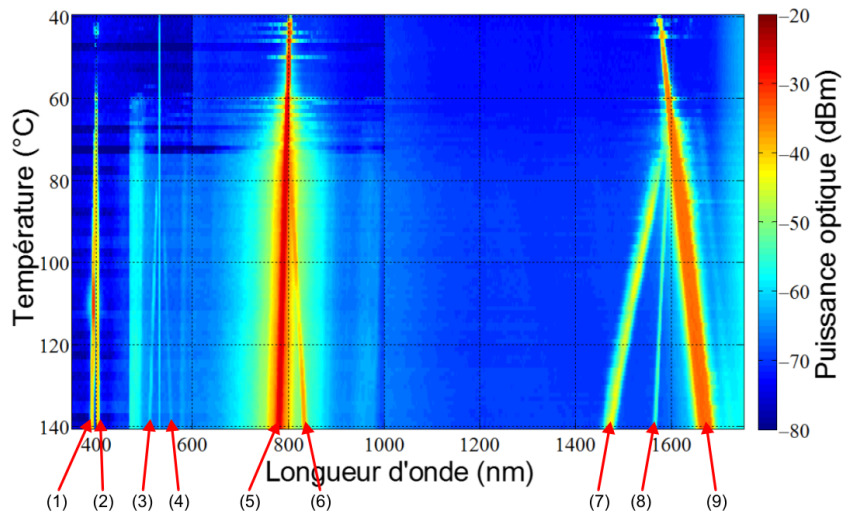


FIGURE III.10 – Spectres mesurés en fonction de la température.

TABLE III.3 – Fréquences des pics générés.

| Numéro de pic | (1) | (2) | (3) | (4) | (5) | (6) | (7) | (8) | (9) |
|-------------------|-------------|-----------------------|------------------------|-------------|------------|-------------|-----------------------|--------------|------------|
| Fréquence | $2\omega_s$ | $\omega_p + \omega_i$ | $2\omega_s - \omega_i$ | $3\omega_i$ | ω_s | $2\omega_i$ | $\omega_s - \omega_i$ | $\omega_s/2$ | ω_i |
| Processus attendu | SHG | SFG | DFG | THG | OPG | SHG | DFG | HHG | OPG |

cristal.

Le processus cascade pour la génération de multi-longueur d'onde est résumé sur la figure III.11. La pompe ω_p déclenche d'abord un processus **OPG** pour générer ω_s et ω_i . Ces trois longueurs d'onde interviennent dans des processus **SHG**, **HHG**, **DFG** et **SFG** dans le premier processus cascade pour générer $2\omega_s$, $\omega_s/2$, $\omega_s - \omega_i$, $2\omega_i$ et $\omega_p + \omega_i$. Dans le second processus cascade, $2\omega_s - \omega_i$ et $3\omega_i$ sont générés par les processus **DFG** et **SFG**. Dans ce travail, tous les processus associés à $\chi^{(2)}$ sont obtenus par deux processus en cascade, à la fois sur une plage de spectre allant de l'UVA au proche infrarouge pour un seul cristal. Ceci est la première démonstration de la génération de multi-longueur d'onde par l'effet cascade avec tous les processus non linéaires associés à $\chi^{(2)}$. D'après ces résultats, il est possible que d'autres processus apparaissent avec une puissance de pompe plus élevée.

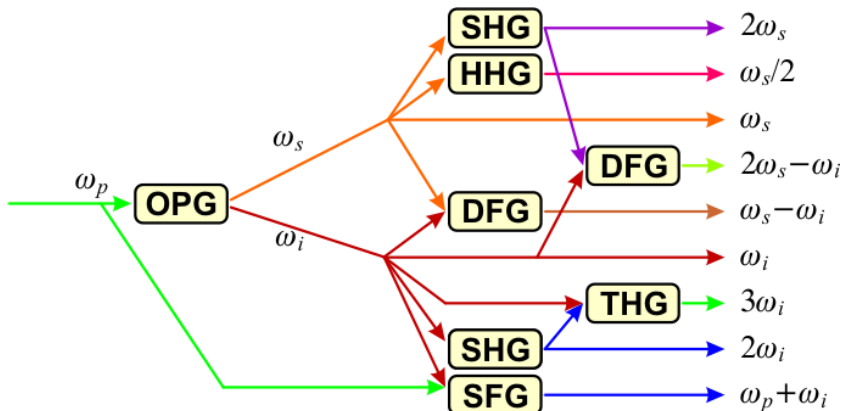


FIGURE III.11 – Schéma du processus cascade de la génération de multi-longueur d'onde.

La cartographie de la figure III.10 révèle un autre phénomène où tous les pics convergent vers quatre longueurs d'ondes à 65 °C. Ainsi, les pics (1) et (2) vers 399 nm ($2\omega_s$), les pics (3) et (4) vers 532 nm (ω_p), les pics (5) et (6) vers 798 nm (ω_s), et les pics (7), (8) et (9) vers 1596 nm (ω_i). Il est évident que le pic à 399 nm correspond à la **SHG** de 798 nm ($\omega_{SHG} = 2\omega_s$), lui-même la **SHG** de l'idler à 1596 nm ($\omega_s = 2\omega_i$) qui est par ailleurs le triple de la pompe à 532 nm ($\omega_p = 3\omega_i$). Ainsi, nous avons obtenu une dégénérescence multi-longueur d'onde. Comme on peut voir sur la figure III.10, la puissance des pics se réduit brutalement en dessous de 65 °C. Par conséquent, il est difficile d'observer les autres pics à part le signal et l'idler. Néanmoins, les pics peuvent être observés parfois en montrant un comportement croisé. La longueur d'onde du pic (2) devient plus faible que celle du pic (1). Les pics (3) et (4) se croisent pour une position opposée en longueur d'onde. Cela se passe également pour les pics (5) et (6). Pour les pics (7), (8) et (9), ils se positionnent à l'ordre inversé : (9), (8) et (7). Ce

point de croisement est un point qui pourrait en effet être gouverné par une relation suivante :

$$\omega_p + \omega_s = \omega_{SHG} + \omega_i \quad (\text{III.5})$$

$$\mathbf{K}_p + \mathbf{K}_s - \mathbf{K}_{SHG} - \mathbf{K}_i = \mathbf{K}_{m,n} \quad (\text{III.6})$$

Ceci ressemble à un mélange à quatre onde, mais sans la contribution de $\chi^{(3)}$ ceci est un processus **SFG** à quatre ondes. Le **QPM** est obtenu à l'ordre 2. A cette température, la conservation d'énergie et la condition d'accord de phase sont respectées. Dans la partie précédente, nous avons interprété le pic (1) comme le processus **SHG** du signal à l'ordre 3. D'après les Eqs.(III.5) et (III.6), il est suggéré que le pic ω_{SHG} viendrait du processus **SFG** à l'ordre 2 plutôt que le processus **SHG** du signal à l'ordre 3. Cette relation n'apparaît évidente qu'à la température de 65 °C. La simulation montre que la longueur d'onde de croisement ne varie qu'avec le changement de la longueur d'onde de la pompe. En revanche, la température de croisement varie avec la période du **PPLT**. Ce point est donc un point où plusieurs processus fusionnent pour le processus **SFG** à quatre ondes.

Ce processus à quatre ondes a aussi été observé dans la littérature [III.39]. Dans ce travail, les auteurs ont généré le signal (870 nm) et l'idler (1370 nm) par une pompe à 532 nm dans un **PPLT** 1D de 7,9 μm dans un processus **OPG**. Par la suite, ils ont obtenu un pic bleu (435 nm) qui résulte d'un processus **SHG** du signal à l'ordre 2 généré par le processus **OPG**. Cependant, ces quatre longueurs d'onde satisfont aussi la conservation d'énergie et la condition d'accord de phase à l'ordre 1 des Eqs.(III.5) et (III.6). Donc, le pic dans le bleu serait aussi à l'origine d'un processus **SFG** à quatre ondes au premier ordre plutôt qu'un processus **SHG** à l'ordre 2. Nous avons donc constaté un nouveau processus **SFG** à quatre ondes à base du processus **OPG**. Un article est en cours de préparation pour soumettre dans un journal.

Grâce aux travaux menés dans cette thématique, j'ai obtenu un projet BQR pour l'année 2017 et un projet PICS CNRS pour une durée de 3 ans. Grâce à ces projets, nous allons développer davantage cette thématique et consolider la coopération scientifique avec Prof. Peng à Taïwan. De plus, nous avons recruté Mlle. Safia MOHAND-OUSAID en thèse en 2017 pour la suite de ces travaux.

III.2 DYNAMIQUE NON LINÉAIRE D'UNE DIODE LASER SOUMISE À UN RETOUR OPTIQUE

LA DYNAMIQUE NON LINÉAIRE D'UNE DIODE LASER soumise à un retour optique est une autre thématique principale dans laquelle je travaille au LPL. Cette thématique était une de mes principales activités de recherche durant mes travaux post-doctoraux au Royaume Uni. Les travaux ont été menés par Mlle. Fadwa BALADI dans un cadre de thèse CIFRE en collaboration avec 3SP Technologies (anciennement 3S Photonics) et par Mlle. Ana Gabriela CORREA-MENA dans un cadre de thèse en collaboration avec l'INAOE (Instituto Nacional de Astrofísica, Óptica y Electrónica) du Mexique. J'ai participé activement à co-encadrer ces thèses.

2.1 Retour optique filtré par FBG

De nos jours, le besoin de télécoms par voie de fibre optique augmente et les liaisons intercontinentales sont déployées plus particulièrement sous la mer. Les liaisons sous-marines sont assurées par des câbles optiques solides et des amplificateurs optiques de type **EDFA** (Erbium-doped fibre amplifier). Les **EDFAs** se constituent principalement d'une diode laser pompe à 980 nm et d'une fibre dopée Erbium de quelque mètre. Grâce à l'émission de l'erbium dans la bande des télécoms optiques, la perte due à la très grande longueur de fibre est compensée par une amplification des signaux optiques. En général, la diode laser pompe est une diode laser soumise à un retour optique par un réseau de Bragg fibré (**FBG** : Fibre Bragg grating). Par conséquent, la pompe est susceptible d'être perturbée par ce retour, induisant une perturbation dans les liaisons.

Dans le chapitre précédent, nous avons vu qu'un retour optique modifie les propriétés de diode laser, notamment son comportement dynamique et l'élargissement spectrale. Durant plus de trois décennies, les comportements dynamiques d'une diode laser soumise à un retour optique ont largement été étudiés [III.49, III.50]. Récemment, ces études ont également étendues à des lasers à cascade quantique à un retour optique [III.51]. La plupart des études ont été effectuées avec un simple miroir, ce qui donne lieu un retour optique conventionnel (**COF** : conventional optical feedback). Cependant, il existe très peu d'études sur des diodes lasers soumises à un retour optique filtré (**FOF** : Filtered optical feedback) [III.52, III.53]. La diode laser pompe d'un **EDFA** est constituée d'une diode laser à forte puissance et d'un **FBG** pour un retour optique comme illustré sur la figure III.12.

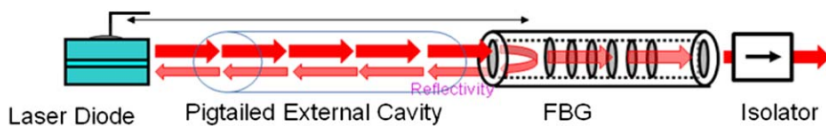


FIGURE III.12 – Module pompe d'un **EDFA** constitué d'une diode laser et d'un **FBG**. Source : [ACL I.40].

Ce module pompe est en effet une diode laser soumise à un **FOF**. Il a été rapporté qu'une telle

configuration peut fournir une émission stabilisée en longueur d'onde [III.54, III.55, III.56, III.57]. Cependant en fonction du taux de retour (la réflectivité de **FBG**), ce module pompe peut aussi montrer différents comportements dynamiques. Parmi les comportements dynamiques, il existe les fluctuations chaotiques et les fluctuations basses fréquences (LFF : Low frequency fluctuations) en régime IV [III.58, III.59]. Le comportement LFF indique les fluctuations chaotiques dont l'intensité chute brutalement et remonte progressivement (voir la figure III.14(a) et (b)). Les fréquences de ces fluctuations se trouvent sur une plage de 10–100 MHz, ce qui est basse fréquence par rapport au chaos développé à une fréquence de quelques GHz. De ce fait, on l'appelle le *LFF dropout*. Ce comportement est une des caractéristiques d'une diode laser soumise à un retour optique. Il peut cependant nuire particulièrement aux liaisons sous-marines. Il est donc très important d'étudier les comportements dynamiques de la diode laser pompe.

Pour cette étude, nous avons choisi de cartographier les comportements en fonction du taux de retour optique et du courant d'injection du laser. Il existe déjà des études sur les cartographies des comportements dynamiques [III.60, III.58, III.61]. Ces cartographies ont été faites sur des diodes lasers soumises à **COF**, mais aucune cartographie sur des diodes lasers à **FOF**. Dans cette étude, une cartographie a été établie pour la première fois sur une diode laser soumise à **FOF** par un **FBG**. Grâce à cette cartographie, nous allons identifier quelques comportements dynamiques.

Afin d'établir une cartographie, nous avons monté un banc de caractérisation d'une diode laser multimode à 980 nm avec un **FBG** comme illustré sur la figure III.13. La réflectivité du **FBG** est de 30 % à 980 nm avec une largeur de raie de 0,6 nm. Dans le module pompe de la figure III.12, nous avons intégré un atténuateur optique variable pour ajuster le taux de retour optique (VOA1), formant ainsi une cavité externe de 4,2 m. Le VOA2 diminue la puissance pour le photodétecteur. Le signal électrique du PD est filtré par un filtre passe-bas de 100 MHz, puis enregistré sur un oscilloscope numérique avec 200 000 points par tracé dans une fenêtre de 40 µs. La puissance de la diode laser est de 350 mW à 500 mA et à 25 °C. Le courant de seuil du laser isolé est de 75 mA. En tenant compte de la perte du VOA 1 sur l'aller-retour et de la réflectivité du **FBG** à 30 %, le taux de retour varie de 0 % à 12,5 %. Le banc est entièrement automatisé par un ordinateur qui commande le contrôleur de courant par une communication GPIB (General purpose interface bus) et le VOA1 par une communication RS232.

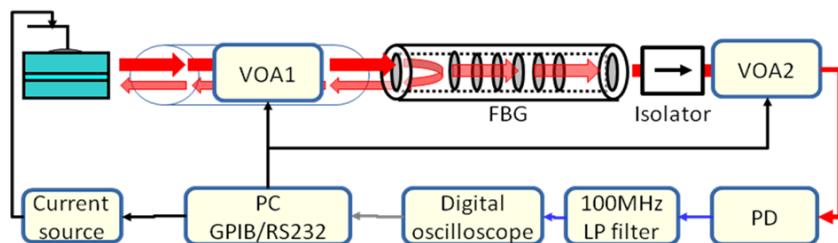


FIGURE III.13 – Banc de caractérisation de comportements dynamiques. VOA : atténuateur optique variable. PD : Photodétecteur. Source : [ACL I.40].

Dans un premier temps, nous avons étudié ses comportements dans le domaine temporel comme

tracé sur la figure III.14. En augmentant le courant, le comportement change. Les figures III.14(a) et (b) montrent un comportement LFF dropout. La figure III.14(c) présente un comportement du régime chaotique complet. La figure III.14(d) affiche un comportement inhabituel, ce que l'on appelle *LFF jump-up*. Ce dernier a été observé pour la première fois dans la réf. [III.60] et peut être observé à un fort retour optique ou à un fort courant de la diode laser. Sur la figure III.14 à droite, nous pouvons remarquer que le pic (mode) des histogrammes se déplace selon ses comportements. Nous avons étudié ces histogrammes avec les longueurs de l'aile gauche (N_{down}) et de l'aile droite (N_{up}) par rapport au pic. Pour le comportement LFF dropout, $N_{down} > N_{up}$, $N_{down} \approx N_{up}$ pour le comportement chaotique complet et $N_{down} < N_{up}$ pour le comportement LFF jump-up.

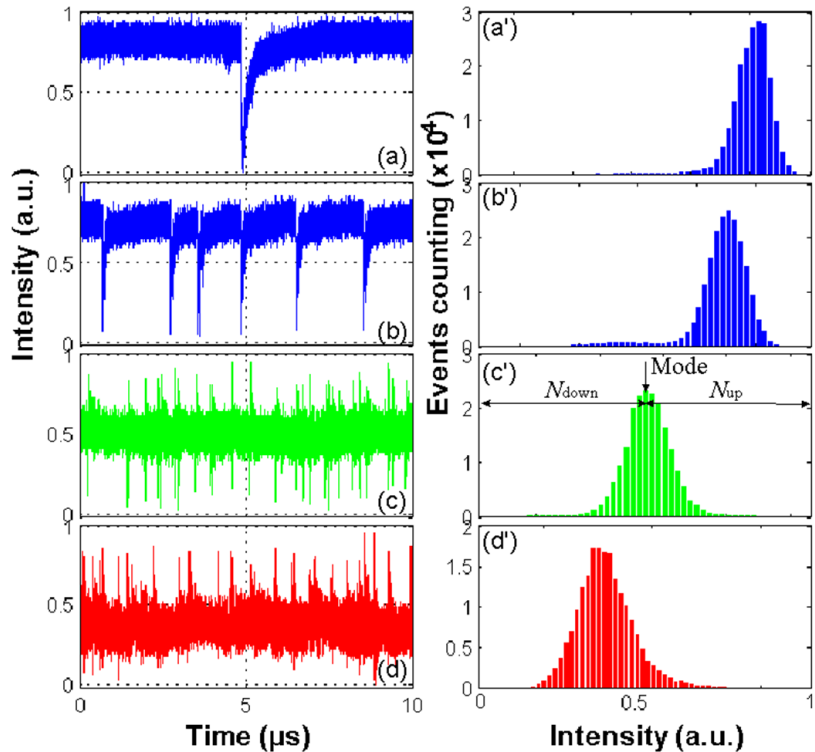


FIGURE III.14 – Tracés temporels (à gauche) et histogrammes (à droite) à 83 mA (a), (a'), à 124 mA (b), (b'), à 189 mA (c), (c') et à 250 mA (d), (d') pour un retour optique de 3.0 %. Source : [ACL I.40].

Nous avons classé ces trois comportements avec des valeurs de $N_{up} - N_{down}$ en code de couleur. Ainsi nous avons établie une cartographie de comportements comme indiqué sur la figure III.15. Sur la cartographie, la couleur verte indique le comportement chaotique complet, la couleur rouge signifie le LFF jump-up et la couleur bleue représente le LFF dropout. La zone grise à faible courant est une indication du seuil laser. Cette cartographie est établie à partir de 11 275 tracés obtenus sur une plage de courant de 50 mA à 500 mA par un pas de 1 mA. Le taux de retour varie quant à lui de 0,5 % à 12,5 % avec un pas de 0,5. Le courant maximum atteint correspond à sept fois le seuil laser. En comparant avec les études précédentes [III.60, III.58], le comportement LFF se trouve dans une très grande plage de courant pour de bas taux de retour. Quand le taux de retour augmente, le zone de LFF dropout augmente comme démontré dans la réf. [III.58], mais se réduit à partir de 3 % et

disparaît au delà de 6 %. Le comportement LFF jump-up domine en fort courant. Notre cartographie est similaire à celle rapportée dans la réf. [III.60], mais elle est plus détaillée. La différence avec les autres cartographies pourrait provenir de deux faits : une diode laser multimode et la présence de **FBG** qui introduit un retour sélectif en fréquence.

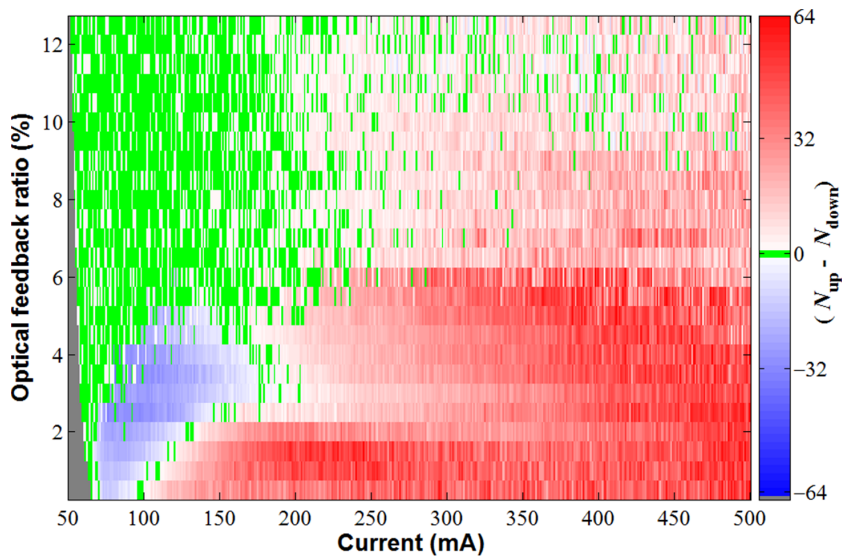


FIGURE III.15 – Cartographie de comportements dynamiques en fonction du taux de retour et du courant. Source : [ACL I.40].

Grâce à l'automatisation totale du banc, nous avons effectué pour la première fois une cartographie des comportements dynamiques en fonction du courant de laser et de la température pour une diode laser multimode à 980 nm avec plus de détails que celles rapportées dans les Refs. [III.60, III.58]. L'expérience a révélé qu'il y a trois types de comportement dans le régime IV : LFF dropout, LFF jump-up et du chaos complet [ACL I.40] (voir la page 153, Chapitre IV). Ce travail a été mené dans le cadre de la thèse de Mlle. Baladi [III.62] et dans le cadre du projet OSEO VERTICAL (Vertically integrated Enhanced pRoducTs for Industrial Chain using Amplifier Lasers) en collaboration avec 3SP Technologies.

2.2 Observation des ondes scélérates

Ces travaux ont commencé par la découverte d'ondes scélérates par hasard pendant les travaux de thèse de F. Baladi. Je vais décrire rapidement ces travaux sur les ondes scélérates.

Les vagues scélérates ont été observées depuis des siècles. En océanologie, elles sont définies comme des vagues supérieures à leurs valeurs moyennes plus de quatre à huit fois la valeur de l'écart type [III.63]. En général, de telles vagues sont considérées comme des événements extrêmes qui sont rares et qui résultent de systèmes non-linéaires. Ces événements ont attiré une attention particulière afin d'étudier des vagues scélérates en océanologie [III.63], le climat extrême [III.64], la crise financière [III.65], etc.

En optique, de telles vagues, dites ondes scélérates ont été observées pour la première fois par Solli

et al. dans un processus de génération de supercontinuum [III.66], suivi d'une étude numérique [III.67]. Depuis ces travaux, les ondes scélérates ont été observées dans la génération de soliton Peregrine [III.68] et dans un laser Ti-Saphire mode-locké par lentille Kerr [III.69]. La génération des ondes scélérates a été démontrée également dans la génération de supercontinuum utilisant un laser d'émission continue [III.70]. Dans ces études, le mécanisme de la génération des ondes scélérates a été étudié dans un système optique non linéaire utilisant l'équation Schrödinger non linéaire [III.71].

Il existe une autre approche qui exploite les comportements déterministes utilisant des diodes lasers [III.72]. Les ondes scélérates ont également été observées dans un système utilisant un VCSEL avec injection externe [III.73, III.74], dans une diode laser soumise à un retour optique conjugué en phase [III.75] et dans une diode laser avec une cavité très courte [III.76].

Dans la section précédente, nous avons vu qu'à certains taux de retour, les diodes lasers soumises à un retour optique peuvent manifester un comportement particulier, notamment fluctuation basse fréquence (LFF) qui est une des caractéristiques typiques avec chute (LFF dropout) ou saut d'intensité (LFF jump-up) dans le régime IV. Contrairement au comportement de LFF dropout, le comportement de LFF jump-up a été très peu étudié [III.60].

Dans ce travail, nous observons pour la première fois des ondes scélérates utilisant une diode laser soumise à FOF comme le système de la figure III.13. Par la suite, nous allons établir une cartographie de l'onde scélérate en fonction du courant de laser et du taux de retour optique. Notre objectif consiste à déterminer la plage des paramètres où le phénomène de l'onde scélérate apparaît. Nous allons également étudier la relation entre l'onde scélérate et la LFF, notamment le jump-up.

Les ondes scélérates ont été obtenues avec le système déjà vu sur la figure III.13 pour de différents courants et taux de retour sur la figure III.16. Dans ce travail, nous utilisons la définition en océanologie pour déterminer le seuil de l'onde scélérate. La ligne rouge sur la figure représente le seuil de l'onde scélérate obtenue suivant cette définition. Sur la figure III.16(a), une onde scélérate est observée sur une fenêtre de 40 μ s et dépasse clairement 8 fois l'écart-type. Il a été vérifié que la trace temporelle montre généralement un comportement dynamique chaotique. Sur la figure 2(b), l'onde scélérate apparaît plus fréquemment. Sur la figure III.16(c), elle apparaît encore plus fréquemment. En occurrence, ce n'est plus un événement rare.

Afin d'étudier la condition d'apparition, le nombre de l'onde scélérate est compté pour chaque trace de 40 μ s en fonction du taux de retour et du courant. Les nombres sont utilisés pour établir une cartographie comme montrée sur la figure III.17. Cette cartographie a été obtenue avec les mêmes paramètres que ceux de la cartographie sur la figure III.15 de la section précédente. Le nombre de l'onde scélérate est codé en échelle de couleur. La figure III.17 montre 2 zones d'apparition de l'onde scélérate. Nous pouvons remarquer que l'onde scélérate disparaît en augmentant encore le courant ou le taux de retour.

Dans la section précédente nous avons identifié les zones des comportements LFF dropout et LFF

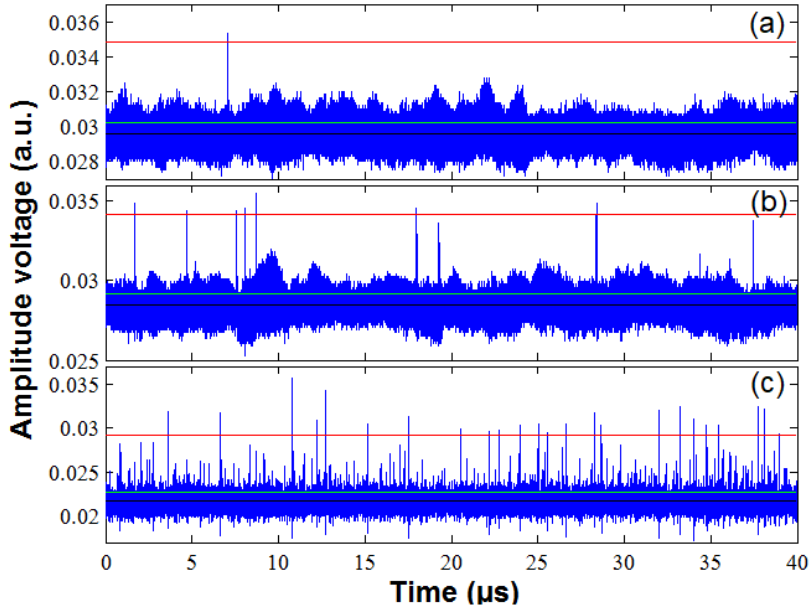


FIGURE III.16 – Ondes scélérates observées pour (a) 5,5 % et 240 mA, (c) 2,0 % et 223 mA, (e) 0,5 % et 167 mA et les histogrammes correspondants. Source : [ACL I.41].

jump-up sur une cartographie [ACL I.40]. A partir de ces travaux, ces zones sont indiquées sur la figure III.17. Nous pouvons remarquer que l'onde scélérate fait en effet partie de LFF jump-ups qui peuvent apparaître rarement avec des impulsions intenses. A haut courant, ces impulsions intenses apparaissent si fréquemment que le seuil de l'onde scélérate dérive vers le haut. Par conséquence, suivant la définition océanologique l'onde scélérate disparaît en augmentant le courant de laser, mais les impulsions existent. Nous pouvons remarquer que l'onde scélérate n'existe plus au delà de 6 % de taux de retour qui est également la limite de existence de LFF dropouts.

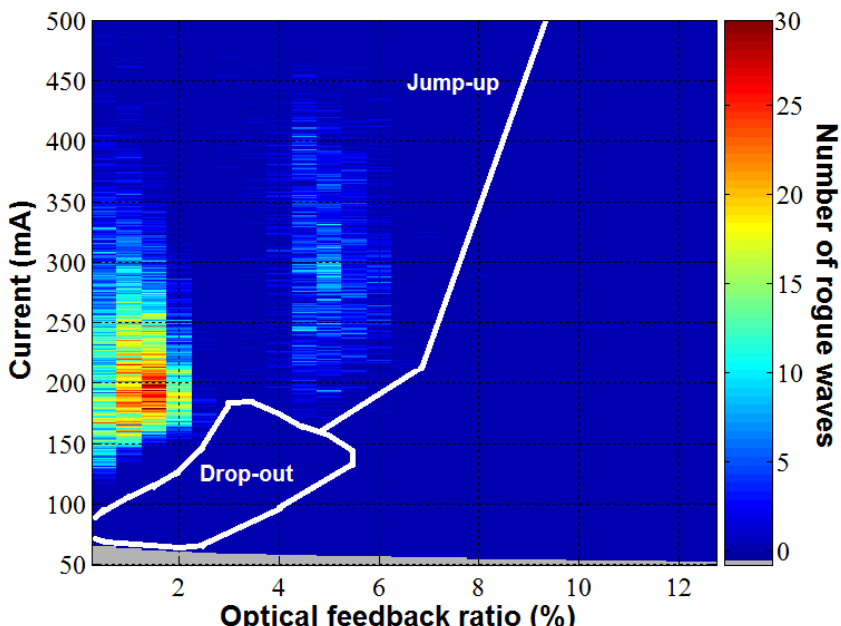


FIGURE III.17 – Cartographie des ondes scélérates en fonction du taux de retour et du courant. Source : [ACL I.41].

Nous avons observé pour la première fois l'onde scélérate en utilisant une diode laser puissante à 980 nm soumise à un retour optique filtré via un **FBG**. Une cartographie de l'onde scélérate a été établie expérimentalement en fonction du courant et du taux de retour. D'après la cartographie, l'onde scélérate existe dans les zones où LFF jump-ups apparaissent [ACL I.41] (voir la page 157, Chapitre IV).

2.3 Etude d'une diode laser soumise à une **SBS**

Depuis 2015 je développe une collaboration avec Dr. I. Zaldivar à l'INAOE (Instituto Nacional de Astrofísica, Optica y Electrónica) au Mexique. En septembre 2017, j'ai accueilli dans le cadre de cette collaboration Mlle. Ana Gabriela CORREA-MENA qui effectue ses travaux de thèse à l'INAOE sous sa direction. Elle est restée 8 mois au LPL pour mener l'étude que je vais décrire dans cette partie.

Jusqu'à présent, nous avons vu les comportements dynamiques chaotiques dans les diodes lasers soumises à un **COF** et à un **FOF** par un **FBG**. Il existe aussi des études avec des diodes lasers soumises à un retour conjugué en phase [III.77, III.78] et des diodes lasers soumises à un retour décalé en fréquence [III.79, III.80]. Nous avons également vu les applications de ces diodes lasers aux communications sécurisées et à la génération des ondes scélérates. Mais ces lasers chaotiques ne se limitent pas uniquement à ces applications. Grâce à leurs comportements très complexes, les lasers chaotiques ont également été utilisés pour des démonstrations de lidar chaotique [III.81], de radar chaotique [III.82], de réflectométrie chaotique dans le domaine temporel (COTDR : chaotic optical time-domain reflectometry) [III.83], de la génération de nombres aléatoires [III.84] et de reservoir computing [III.85, III.86].

Récemment, les lasers chaotiques voient de nouvelles applications en associant à la **SBS** telles que la suppression de **SBS** [III.87], BOCDA (Brillouin optical correlation-domain analysis) [III.88], la génération de réseau Brillouin dynamique [III.89, III.90] et la suppression de la signature de retard temporel utilisant **SBS** [III.91]. Nous avons vu dans le chapitre précédent la **SBS** dans une fibre optique. La rétrodiffusion Stokes d'une fibre monomode standard est décalé de -11 GHz en fréquence par rapport à la pompe à 1550 nm.

Contrairement à un retour optique conventionnel (**COF**), nous envisageons dans ce travail pour la première fois un retour optique par une rétrodiffusion Brillouin stimulée (**SBSOF**) dans une fibre monomode standard de 4 km. Comme le retour optique est décalé de -11 GHz, cette configuration peut être considérée comme une configuration de retour optique décalé en fréquence [III.79, III.80].

Pour cette étude, nous avons monté deux bancs expérimentaux pour une configuration de **COF** et pour une configuration de **SBSOF** comme illustré sur la figure III.18. Les deux bancs sont similaires. L'émission de la diode laser à 1450 nm (3SP Technologies) est injectée dans une fibre monomode de 4 km à travers deux circulateurs optiques (OC1, OC2) et le port-90% d'un coupleur optique. C'est une diode laser puissante utilisé en général pour une pompe d'amplification Raman. Le port-10% du coupleur est utilisé pour observer les comportements dynamiques par un VOA, un photodétecteur (12 GHz) et

un analyseur de spectre RF (26 GHz). Le VOA1 ajuste le niveau de puissance pour le photodétecteur. Pour la configuration de COF sur la figure III.18(a), la sortie de la fibre est réinjectée par le port 1 d'OC1 en passant l'isolateur et le VOA2, formant une boucle fermée. L'isolateur permet d'éviter des réflexions parasites et le VOA2 ajuste le taux de retour optique. Cette configuration correspond à une cavité en anneau, différente de la cavité externe de la figure III.13. La grande longueur de fibre induit un grand retard temporel de 21,3 μ s en prenant en compte également les composants fibrés. Pour la configuration de SBSOF de la figure III.18(b), la SBS reviens vers le port2 de l'OC2 et est injectée à la diode laser par le port3 d'OC2 et par le port1 de l'OC1. Si le port1 n'est pas connecté, c'est une configuration en boucle ouverte. La puissance du laser solitaire est de 270 mW à 1000 mA, mais la puissance est réduite à 140 mW avant d'injecter dans la fibre à cause des pertes intrinsèques des composants optiques.

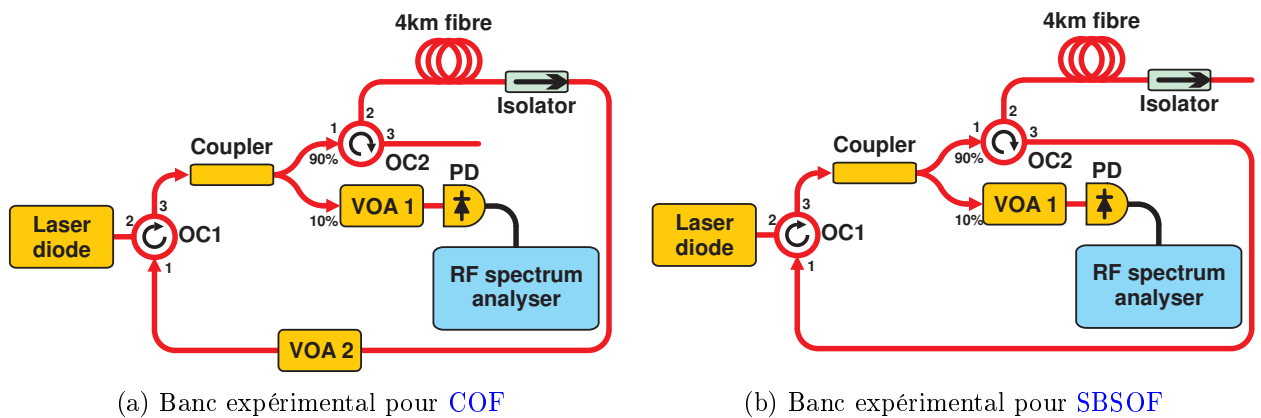


FIGURE III.18 – Bancs expérimentaux pour deux configurations. OC : Circulateur optique. Source : [ACL I.48].

Afin de comparer les deux configurations, nous avons établi pour chaque configuration une cartographie à partir de spectres RF mesurés en fonction de courant comme montré sur la figure III.19. L'allure des deux cartographies sont très différentes. Sur la figure III.19(a), un pic se trouve à 14,41 GHz. Ce dernier pourrait venir de la cavité interne qui a une longueur de 3,1 mm. La cartographie de COF révèle une dynamique très riche jusqu'à 16 GHz. La fréquence de la cavité externe est aussi présente et elle est mesurée à 47 kHz à cause de la fibre de 4 km. En revanche, sur la figure III.19(b), à partir de 295 mA la BFS est observée à 11,46 GHz, ce qui correspond à celle de la théorie pour une pompe de 1450 nm. Ceci est une preuve que la SBS existe et qu'elle influence les comportements dynamiques de la diode laser, ce qui donne lieu un comportement chaotique. La largeur de raie de BGS est mesurée à 30 MHz. La fréquence d'oscillation de relaxation est également visible à partir de 200 mA. Il est suggéré que ceci résulte de la rétrodiffusion Rayleigh qui co-existe avec la SBS. Le pic de la cavité interne est décalé à 15 GHz. Le pic à 3,6 GHz est dû au battement entre la fréquence de la cavité interne et la BFS. La SBS dépend de la largeur spectrale de la diode laser et l'élargissement spectral peut réduire la SBS [III.87]. Les résultats montrent que le système se trouve dans un compromis entre les deux.

L'étude sur les fonctions d'auto-corrélation dévoile que la configuration de SBSOF ne montre pas

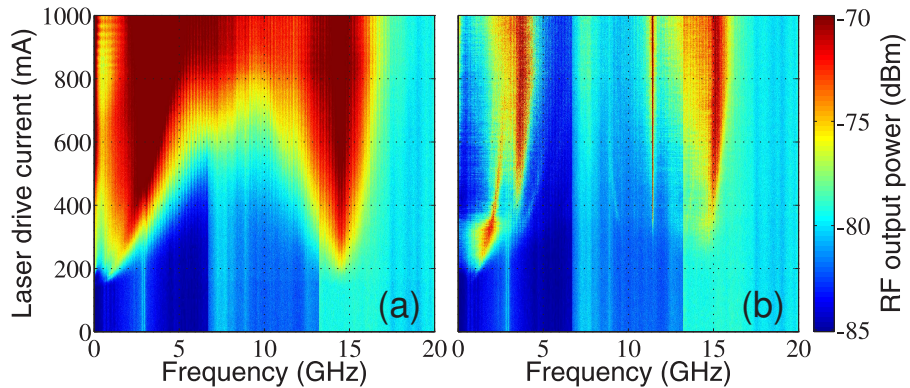


FIGURE III.19 – Cartographie des ondes scélérates en fonction du taux de retour et du courant. Source : [ACL I.48].

la signature de retard temporel contrairement à la configuration de **COF**. Ceci est avantageux pour des applications aux communications sécurisés et à la génération de nombre aléatoire[ACL I.48].

Dans ce travail, nous avons étudié les comportements dynamique d'une nouvelle configuration de diode laser soumise à un retour optique à partir de la **SBS**. Pour cette étude, nous avons utilisé une diode laser puissante à 1450 nm. Les résultats expérimentaux révèlent une allure de comportement pour les configurations de **COF** et de **SBSOF** très différente. Plus particulièrement, les résultats de la configuration de **SBSOF** montrent un comportement qui ressemble à un comportement chaotique avec la **BFS** à 11,41 GHz, ce qui prouve la présence de **SBS**. Ceci est une démonstration importante en vue d'application aux capteurs Brillouin à fibres optiques.

III.3 AUTRES ACTIVITÉS DE RECHERCHE

J'ai également travaillé sur les **OLED** (diode électroluminescente organique) pompée par des impulsions électriques brèves. Il s'agit de la démonstration d'une diode laser organique (**OLD** : organic laser diode). Ces travaux portent un défi scientifique et technologique, car une diode laser organique pompée électriquement n'a jamais été démontrée à cause de la faible mobilité d'électron dans des matériaux organiques, de l'annihilation de singulet-triplet et d'un seuil laser très élevé, etc. Dans une **OLED**, la durée de vie de triplet (non radiatif) est plus longue que celle de singulet qui est radiatif. Pour affranchir l'annihilation, la durée d'excitation des impulsions électriques doit être plus courte que la durée de vie de triplet. Afin d'atteindre le seuil laser, nous avons opté pour une réduction de la taille d'**OLED** à $87 \times 120 \mu\text{m}^2$. La réduction de la taille d'**OLED** permet d'augmenter la densité de courant pour un courant donné et de réduire le temps de réponse. De plus, la structure de l'échantillon d'**OLED** est spécialement conçue pour faire passer des impulsions électriques très courtes dans le circuit comme montré sur la figure III.20. Cette structure innovante est l'objet du dépôt d'un brevet. Dans ce circuit, des impulsions à une amplitude de 100 V sont injectées dans une μ -**OLED** pour l'excitation électrique. Grâce à la structure innovante de l'ensemble de circuit **OLED**, la densité de courant est atteinte à

2 kA/cm^2 par des impulsions de 9 ns. En théorie, il faut une densité de courant de 10 kA/cm^2 pour surmonter le seuil laser. La densité de courant que nous avons obtenue est donc l'avancement d'un pas vers la réalisation d'une **OLD**. La comparaison avec la modélisation d'une **OLED** par un circuit RC nous a permis de déduire la capacitance et les résistances internes de l'**OLED** [ACL I.47] (voir la page 161, Chapitre IV). Ce travail a été mené dans le cadre de thèse de Mr. Alex Chime [III.92].

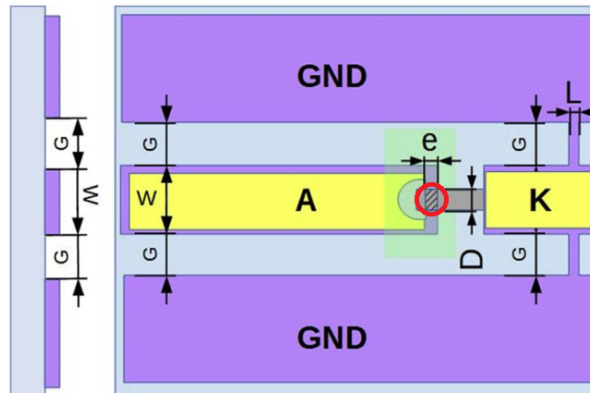


FIGURE III.20 – Structure de **μ-OLED**. L'**OLED** d'une taille de $87 \times 120 \mu\text{m}^2$ se trouve dans le cercle. L'anode et la cathode sont les électrodes en aluminium (en jaune) et la masse est l'ITO (indium tin oxide) (en violet). A : Anode, K : Cathode, GND : masse, Source : [ACL I.47].

Dans le cadre de la collaboration avec le Mexique j'ai travaillé sur la transmission bidirectionnelle utilisant un filtre photonique micro-onde [ACL I.42] et un oscillateur optoélectronique [ACL I.45]. Je souhaite développer davantage cette collaboration pour de futur thèse en cotutelle.

III.4 RÉSUMÉ

Mes activités de recherche au LPL reposent principalement sur la conversion de fréquence par le biais de l'optique non linéaire dans des cristaux photoniques non linéaires et sur l'étude de la dynamique non linéaire d'une diode laser soumise à un retour optique. J'ai également travaillé sur l'**OLED** pompée par des impulsions électriques brèves et sur l'oscillateur optoélectronique. Durant ces travaux, j'ai principalement contribué à l'encadrement de cinq thèses [III.1, III.62, III.92, III.48, III.93] et d'une thèse (Mlle. Safia Mohand-Ousaid) en cours. Mes travaux effectués au sein du Laboratoire de Physiques des Lasers m'ont conduit treize publications [ACL I.34,I.36–I.47] dans des articles à comité de lecture et de nombreuses conférences nationales et internationales. J'ai également développé la collaboration avec l'INAOE et souhaite développer davantage cette collaboration par le biais de l'échange des étudiants et de thèses en cotutelle.

BIBLIOGRAPHIES

- [III.1] Q. Ripault, *Second-Harmonic generation in helium-implanted 2D-PPLN waveguides*, Thèse de doctorat (juillet 2013), <http://www.theses.fr/2013PA132024>.
- [III.2] V. Berger, « Nonlinear Photonic Crystals », *Phys. Rev. Lett.*, **81**(19), pp. 4136–4139 (novembre 1998), <http://link.aps.org/doi/10.1103/PhysRevLett.81.4136>.
- [III.3] A. Arie, N. Habschoosh et A. Bahabad, « Quasi phase matching in two-dimensional nonlinear photonic crystals », *Opt. Quant. Electron.*, **39**(4-6), pp. 361–375 (mars 2007), <http://link.springer.com/article/10.1007/s11082-007-9102-8>.
- [III.4] N. G. R. Broderick, G. W. Ross, H. L. Offerhaus, D. J. Richardson et D. C. Hanna, « Hexagonally Poled Lithium Niobate : A Two-Dimensional Nonlinear Photonic Crystal », *Phys. Rev. Lett.*, **84**(19), pp. 4345–4348 (mai 2000), <http://link.aps.org/doi/10.1103/PhysRevLett.84.4345>.
- [III.5] L.-H. Peng et C.-C. Hsu, « Wavelength tunability of second-harmonic generation from two-dimensional $\chi^{(2)}$ nonlinear photonic crystals with a tetragonal lattice structure », *Appl. Phys. Lett.*, **84**(17), pp. 3250–3252 (avril 2004), <http://aip.scitation.org/doi/abs/10.1063/1.1728303>.
- [III.6] Q. Ripault, M. W. Lee, F. Mériche, T. Touam, B. Courtois, E. Ntsoenzok, L.-H. Peng, A. Fischer et A. Boudrioua, « Investigation of a planar optical waveguide in 2D PPLN using Helium implantation technique », *Opt. Express*, **21**(6), pp. 7202–7208 (mars 2013), <http://www.osapublishing.org/abstract.cfm?uri=oe-21-6-7202>.
- [III.7] Y. Sheng, S. M. Saltiel et K. Koynov, « Cascaded third-harmonic generation in a single short-range-ordered nonlinear photonic crystal », *Opt. Lett.*, **34**(5), pp. 656–658 (mars 2009), <http://www.osapublishing.org/abstract.cfm?uri=ol-34-5-656>.
- [III.8] W. Q. Zhang, F. Yang et X. Li, « Double quasi phase matching for both optical parametric oscillator and difference frequency generation », *Opt. Commun.*, **282**(7), pp. 1406–1411 (avril 2009), <http://www.sciencedirect.com/science/article/pii/S0030401808012479>.
- [III.9] M. Levenius, V. Paskevicius et K. Gallo, « Angular degrees of freedom in twin-beam parametric down-conversion », *Appl. Phys. Lett.*, **101**(12), pp. 121114 (septembre 2012), <http://aip.scitation.org/doi/full/10.1063/1.4754148>.
- [III.10] M. Lazoul, A. Boudrioua, L. M. Simohamed, A. Fischer et L.-H. Peng, « Experimental study of multiwavelength parametric generation in a two-dimensional periodically poled lithium tantalate crystal », *Opt. Lett.*, **38**(19), pp. 3892–3894 (octobre 2013), <http://www.osapublishing.org/abstract.cfm?uri=ol-38-19-3892>.
- [III.11] L. Chen, P. Xu, Y. F. Bai, X. W. Luo, M. L. Zhong, M. Dai, M. H. Lu et S. N. Zhu, « Concurrent optical parametric down-conversion in $\chi^{(2)}$ nonlinear photonic crystals », *Opt. Express*, **22**(11), pp. 13164–13169 (juin 2014), <http://www.osapublishing.org/abstract.cfm?uri=oe-22-11-13164>.
- [III.12] Y. Sasaki, Y. Avetisyan, H. Yokoyama et H. Ito, « Surface-emitted terahertz-wave difference-frequency generation in two-dimensional periodically poled lithium niobate », *Opt. Lett.*, **30**(21), pp. 2927–2929 (novembre 2005), <https://www.osapublishing.org/ol/abstract.cfm?uri=ol-30-21-2927>.
- [III.13] S. Witte et K. S. E. Eikema, « Ultrafast Optical Parametric Chirped-Pulse Amplification », *IEEE J. Sel. Top. Quantum Electron.*, **18**(1), pp. 296–307 (janvier 2012).
- [III.14] T. Töpfer, K. P. Petrov, Y. Mine, D. Jundt, R. F. Curl et F. K. Tittel, « Room-temperature mid-infrared laser sensor for trace gas detection », *Appl. Opt.*, **36**(30), pp. 8042–8049 (octobre 1997), <http://www.osapublishing.org/abstract.cfm?uri=ao-36-30-8042>.
- [III.15] S. Carrasco, A. V. Sergienko, B. E. A. Saleh, M. C. Teich, J. P. Torres et L. Torner, « Spectral engineering of entangled two-photon states », *Phys. Rev. A*, **73**(6), pp. 063802 (juin 2006), <http://link.aps.org/doi/10.1103/PhysRevA.73.063802>.
- [III.16] R. Ursin, F. Tiefenbacher, T. Schmitt-Manderbach, H. Weier, T. Scheidl, M. Lindenthal, B. Blauensteiner, T. Jennewein, J. Perdigues, P. Trojek, B. Ömer, M. Fürst, M. Meyenburg, J. Rarity, Z. Sodnik, C. Barbieri, H. Weinfurter et A. Zeilinger, « Entanglement-based quantum communication over 144 km », *Nat. Phys.*, **3**(7), pp. 481–486 (juillet 2007), <https://www.nature.com/articles/nphys629>.
- [III.17] H. Hübel, M. R. Vanner, T. Lederer, B. Blauensteiner, T. Lorünser, A. Poppe et A. Zeilinger, « High-fidelity transmission of polarization encoded qubits from an entangled source over 100 km of fiber », *Opt. Express*, **15**(12), pp. 7853–7862 (juin 2007), <https://www.osapublishing.org/oe/abstract.cfm?uri=oe-15-12-7853>.

- [III.18] Y. Zhang, Z. D. Gao, Z. Qi, S. N. Zhu et N. B. Ming, « Nonlinear Čerenkov Radiation in Nonlinear Photonic Crystal Waveguides », *Phys. Rev. Lett.*, **100**, pp. 163904 (Apr 2008), <https://link.aps.org/doi/10.1103/PhysRevLett.100.163904>.
- [III.19] P. Xu, S. H. Ji, S. N. Zhu, X. Q. Yu, J. Sun, H. T. Wang, J. L. He, Y. Y. Zhu et N. B. Ming, « Conical Second Harmonic Generation in a Two-Dimensional $\chi^{(2)}$ Photonic Crystal : A Hexagonally Poled LiNbO₃ Crystal », *Phys. Rev. Lett.*, **93**(13), pp. 133904 (septembre 2004), <https://link.aps.org/doi/10.1103/PhysRevLett.93.133904>.
- [III.20] Y. Zhang, J. Wen, S. N. Zhu et M. Xiao, « Nonlinear Talbot Effect », *Physical Review Letters*, **104**(18), pp. 183901 (mai 2010), <https://link.aps.org/doi/10.1103/PhysRevLett.104.183901>.
- [III.21] X. Fang, D. Wei, D. Liu, W. Zhong, R. Ni, Z. Chen, X. Hu, Y. Zhang, S. N. Zhu et M. Xiao, « Multiple copies of orbital angular momentum states through second-harmonic generation in a two-dimensional periodically poled LiTaO₃ crystal », *Appl. Phys. Lett.*, **107**(16), pp. 161102 (octobre 2015), <http://aip.scitation.org/doi/full/10.1063/1.4934488>.
- [III.22] J. Kawashima, M. Fujimura et T. Suhara, « Type-I Quasi-Phase-Matched Waveguide Device for Polarization-Entangled Twin Photon Generation », *IEEE Photonics Technology Letters*, **21**(9), pp. 566–568 (mai 2009).
- [III.23] K. Thyagarajan, J. Lugani, S. Ghosh, K. Sinha, A. Martin, D. B. Ostrowsky, O. Alibart et S. Tanzilli, « Generation of polarization-entangled photons using type-II doubly periodically poled lithium niobate waveguides », *Phys. Rev. A*, **80**(5), pp. 052321 (novembre 2009), <https://link.aps.org/doi/10.1103/PhysRevA.80.052321>.
- [III.24] K. Gallo, C. Codemard, C. B. Gawith, J. Nilsson, P. G. R. Smith, N. G. R. Broderick et D. J. Richardson, « Guided-wave second-harmonic generation in a LiNbO₃ nonlinear photonic crystal », *Opt. Lett.*, **31**(9), pp. 1232–1234 (mai 2006), <https://www.osapublishing.org/ol/abstract.cfm?uri=ol-31-9-1232>.
- [III.25] B. Vincent, A. Boudrioua, R. Kremer et P. Moretti, « Second harmonic generation in helium-implanted periodically poled lithium niobate planar waveguides », *Opt. Commun.*, **247**(4), pp. 461–469 (mars 2005), <http://www.sciencedirect.com/science/article/pii/S0030401804012350>.
- [III.26] F. Chen, « Photonic guiding structures in lithium niobate crystals produced by energetic ion beams », *J. Appl. Phys.*, **106**, pp. 081101 (juin 2009), <https://aip.scitation.org/doi/abs/10.1063/1.3216517?journalCode=jap>.
- [III.27] A. M. Radojevic, M. Levy, R. M. Osgood, D. H. Jundt, A. Kumar et H. Bakhru, « Second-order optical nonlinearity of 10-μm-thick periodically poled LiNbO₃ films », *Opt. Lett.*, **25**(14), pp. 1034–1036 (juillet 2000), <https://www.osapublishing.org/ol/abstract.cfm?uri=ol-25-14-1034>.
- [III.28] J. Rams, J. Olivares, P. J. Chandler et P. D. Townsend, « Second harmonic generation capabilities of ion implanted LiNbO₃ waveguides », *Journal of Applied Physics*, **84**(9), pp. 5180–5183 (1998), <https://doi.org/10.1063/1.368811>.
- [III.29] L.-H. Peng, H.-M. Wu, A. H. Kung et C.-M. Lai, « Fabrication and Characterization of Self-Assembled Ferroelectric Linear and Nonlinear Photonic Crystals : GaN and LiNbO₃ », dans *Ferroelectric Crystals for Photonic Applications*, Springer Series in Materials Science, pp. 21–51, Springer, Berlin, Heidelberg (2009), https://link.springer.com/chapter/10.1007/978-3-540-77965-0_2.
- [III.30] P. G. Kwiat, K. Mattle, H. Weinfurter, A. Zeilinger, A. V. Sergienko et Y. Shih, « New High-Intensity Source of Polarization-Entangled Photon Pairs », *Physical Review Letters*, **75**(24), pp. 4337–4341 (décembre 1995), <https://link.aps.org/doi/10.1103/PhysRevLett.75.4337>.
- [III.31] Y.-X. Gong, P. Xu, J. Shi, L. Chen, X. Q. Yu, P. Xue et S. N. Zhu, « Generation of polarization-entangled photon pairs via concurrent spontaneous parametric downconversions in a single χ⁽²⁾ nonlinear photonic crystal », *Opt. Lett.*, **37**(21), pp. 4374–4376 (novembre 2012), <https://www.osapublishing.org/ol/abstract.cfm?uri=ol-37-21-4374>.
- [III.32] J.-P. Meyn et M. M. Fejer, « Tunable ultraviolet radiation by second-harmonic generation in periodically poled lithium tantalate », *Optics Letters*, **22**(16), pp. 1214–1216 (août 1997), <https://www.osapublishing.org/ol/abstract.cfm?uri=ol-22-16-1214>.
- [III.33] M. Lazoul, *Etude de la génération paramétrique optique dans les cristaux photoniques non linéaires : application aux sources multilongueurs d'onde*, Thèse de doctorat (avril 2013), <http://www.theses.fr/2013PA132009>.

- [III.34] M. Lazoul, A. Boudrioua, L.-M. Simohamed et L.-H. Peng, « Multi-resonant optical parametric oscillator based on 2D-PPLT nonlinear photonic crystal », *Opt. Lett.*, **40**(8), pp. 1861–1864 (avril 2015), <https://www.osapublishing.org/ol/abstract.cfm?uri=ol-40-8-1861>.
- [III.35] H. Chikh-Touami, *Etude théorique et expérimentale des mécanismes de conversion des fréquences dans les cristaux photoniques non linéaires*, Thèse de doctorat (juillet 2017), <http://www.theses.fr/2017USPCD010>.
- [III.36] C.-Q. Xu et B. Chen, « Cascaded wavelength conversions based on sum-frequency generation and difference-frequency generation », *Opt. Lett.*, **29**(3), pp. 292–294 (février 2004), <http://www.osapublishing.org/abstract.cfm?uri=ol-29-3-292>.
- [III.37] X. Lin, H. Zhang, A. Yao, Y. Kong, G. Wang et Z. Xu, « Multi-wavelength generation in periodically poled lithium niobate pumped by a Q-Switched Nd :YVO₄ laser », dans *ICO20 : Lasers and Laser Technologies*, tome 6028, p. 60280T. International Society for Optics and Photonics (janvier 2006), <https://www.spiedigitallibrary.org/conference-proceedings-of-spie/6028/60280T/Multi-wavelength-generation-in-periodically-poled-lithium-niobate-pumped-by/10.1117/12.667153.short>.
- [III.38] P. Xu, J. F. Wang, C. Li, Z. D. Xie, X. J. Lv, H. Y. Leng, J. S. Zhao et S. N. Zhu, « Simultaneous optical parametric oscillation and intracavity second-harmonic generation based on a hexagonally poled lithium tantalate », *Opt. Express*, **17**(6), pp. 4289–4294 (mars 2009), <http://www.osapublishing.org/abstract.cfm?uri=oe-17-6-4289>.
- [III.39] C.-M. Lai, I.-N. Hu, Y.-Y. Lai, Z.-X. Huang, L.-H. Peng, A. Boudrioua et A.-H. Kung, « Upconversion blue laser by intracavity frequency self-doubling of periodically poled lithium tantalate parametric oscillator », *Opt. Lett.*, **35**(2), pp. 160–162 (janvier 2010), <http://www.osapublishing.org/abstract.cfm?uri=ol-35-2-160>.
- [III.40] N. Fujioka, S. Ashihara, H. Ono, T. Shimura et K. Kuroda, « Cascaded third-harmonic generation of ultrashort optical pulses in two-dimensional quasi-phase-matching gratings », *JOSA B*, **24**(9), pp. 2394–2405 (septembre 2007), <https://www.osapublishing.org/josab/abstract.cfm?uri=josab-24-9-2394>.
- [III.41] M. Levenius, V. Pasiskevicius, F. Laurell et K. Gallo, « Ultra-broadband optical parametric generation in periodically poled stoichiometric LiTaO₃ », *Opt. Express*, **19**(5), pp. 4121–4128 (février 2011), <http://www.osapublishing.org/abstract.cfm?uri=oe-19-5-4121>.
- [III.42] M. Conforti, F. Baronio, M. Levenius et K. Gallo, « Broadband parametric processes in $\chi^{(2)}$ nonlinear photonic crystals », *Opt. Lett.*, **39**(12), pp. 3457–3460 (juin 2014), <http://www.osapublishing.org/abstract.cfm?uri=ol-39-12-3457>.
- [III.43] M. Levenius, V. Pasiskevicius et K. Gallo, « Cascaded up-conversion of twin-beam OPG in nonlinear photonic crystals », dans *2013 Conference on Lasers Electro-Optics Europe International Quantum Electronics Conference CLEO EUROPE/IQEC*, pp. 1–1 (mai 2013), <https://ieeexplore.ieee.org/document/6800870/>.
- [III.44] S. A. Kingsley, S. Sriram et P. E. Powers, « High-sensitivity 3 to 5 micron PPLN LA-DAR wavelength converter system », dans *Proc. SPIE 5791, Laser Radar Technology and Applications X*, tome 5791, pp. 262–273. International Society for Optics and Photonics (mai 2005), <https://www.spiedigitallibrary.org/conference-proceedings-of-spie/5791/0000/High-sensitivity-3-to-5-micron-PPLN-LADAR-wavelength-converter/10.1117/12.606396.short?SS0=1>.
- [III.45] M. Wirth, A. Fix, P. Mahnke, H. Schwarzer, F. Schrandt et G. Ehret, « The airborne multi-wavelength water vapor differential absorption lidar WALES : system design and performance », *Applied Physics B*, **96**(1), pp. 201 (juillet 2009), <https://link.springer.com/article/10.1007/s00340-009-3365-7>.
- [III.46] C.-Y. Lu, X.-Q. Zhou, O. Gühne, W.-B. Gao, J. Zhang, Z.-S. Yuan, A. Goebel, T. Yang et J.-W. Pan, « Experimental entanglement of six photons in graph states », *Nat. Phys.*, **3**(2), pp. 91–95 (février 2007), <https://www.nature.com/articles/nphys507>.
- [III.47] M. L. Fanto, R. K. Erdmann, P. M. Alsing, C. J. Peters et E. J. Galvez, « Multi-entangled photon spontaneous parametric down-conversion source », dans *Quantum Information and Computation IX*, tome 8057, p. 805705. International Society for Optics and Photonics (juin 2011), <https://www.spiedigitallibrary.org/conference-proceedings-of-spie/8057/805705/Multi-entangled-photon-spontaneous-parametric-down-conversion-source/10.1117/12.883261.short>.

- [III.48] Z. Yellas, *Génération paramétrique optique ; longueurs d'ondes dans les cristaux photoniques non linéaires de type PPLT-2D*, Thèse de doctorat (septembre 2018).
- [III.49] L. Mashal, R. M. Nguimdo, G. V. d. Sande, M. C. Soriano, J. Danckaert et G. Verschaffelt, « Low-Frequency Fluctuations in Semiconductor Ring Lasers With Optical Feedback », *IEEE J. Quantum Electron.*, **49**(9), pp. 790–797 (septembre 2013).
- [III.50] M. Sciamanna et K. A. Shore, « Physics and applications of laser diode chaos », *Nat. Photonics*, **9**(3), pp. 151–162 (mars 2015), <https://www.nature.com/articles/nphoton.2014.326>.
- [III.51] L. Jumpertz, K. Schires, M. Carras, M. Sciamanna et F. Grillot, « Chaotic light at mid-infrared wavelength », *Light : Science & Applications*, **5**(6), pp. e16088 (juin 2016), <https://www.nature.com/articles/lsa201688>.
- [III.52] M. Yousefi et D. Lenstra, « Dynamical behavior of a semiconductor laser with filtered external optical feedback », *IEEE Journal of Quantum Electronics*, **35**(6), pp. 970–976 (juin 1999).
- [III.53] A. P. A. Fischer, M. Yousefi, D. Lenstra, M. W. Carter et G. Vemuri, « Filtered Optical Feedback Induced Frequency Dynamics in Semiconductor Lasers », *Physical Review Letters*, **92**(2), pp. 023901 (janvier 2004), <http://link.aps.org/doi/10.1103/PhysRevLett.92.023901>.
- [III.54] M. Achtenhagen, S. Mohrdiek, T. Pliska, N. Matuschek, C. Harder et A. Hardy, « L-I characteristics of fiber Bragg grating stabilized 980-nm pump lasers », *IEEE Photon. Technol. Lett.*, **13**(5), pp. 415–417 (mai 2001), <http://ieeexplore.ieee.org/lpdocs/epic03/wrapper.htm?arnumber=920735>.
- [III.55] A. Ferrari, G. Ghislotti, S. Balsamo, V. Spano et F. Trezzi, « Subkilohertz Fluctuations and Mode Hopping in High-Power Grating-Stabilized 980-nm Pumps », *J. Lightwave Technol.*, **20**(3), pp. 515 (mars 2002), <http://www.osapublishing.org/abstract.cfm?uri=jlt-20-3-515>.
- [III.56] M. K. Davis et A. Echavarria, « Polarization-Induced Feedback Effects in Fiber Bragg Grating-Stabilized Diode Lasers », *J. Lightwave Technol.*, **22**(12), pp. 2816 (décembre 2004), <http://www.osapublishing.org/abstract.cfm?uri=jlt-22-12-2816>.
- [III.57] A. Naumenko, P. Besnard, N. Loiko, G. Ughetto et J. C. Bertreux, « Characteristics of a semiconductor laser coupled with a fiber Bragg grating with arbitrary amount of feedback », *IEEE J. Quantum Electron.*, **39**(10), pp. 1216–1228 (octobre 2003).
- [III.58] T. Heil, I. Fischer et W. Elsäßer, « Coexistence of low-frequency fluctuations and stable emission on a single high-gain mode in semiconductor lasers with external optical feedback », *Phys. Rev. A*, **58**(4), pp. R2672–R2675 (octobre 1998), [https://link.aps.org/doi/10.1103/PhysRevA.58.R2672](http://link.aps.org/doi/10.1103/PhysRevA.58.R2672).
- [III.59] G. Huyet, S. Balle, M. Giudici, C. Green, G. Giacomelli et J. R. Tredicce, « Low frequency fluctuations and multimode operation of a semiconductor laser with optical feedback », *Optics Communications*, **149**(4), pp. 341–347 (avril 1998), <http://www.sciencedirect.com/science/article/pii/S0030401897007517>.
- [III.60] M.-W. Pan, B.-P. Shi et G. R. Gray, « Semiconductor laser dynamics subject to strong optical feedback », *Opt. Lett.*, **22**(3), pp. 166 (février 1997), <http://www.osapublishing.org/abstract.cfm?URI=ol-22-3-166>.
- [III.61] S. Donati et R. H. Horng, « The Diagram of Feedback Regimes Revisited », *IEEE J. Sel. Topics Quantum Electron.*, **19**(4), pp. 1500309–1500309 (juillet 2013).
- [III.62] F. Baladi, *Comportement dynamique de diodes laser de puissance multimodes à 980 nm soumises à un retour optique sélectif en fréquence provenant d'un réseau de Bragg photoinscrit.*, Thèse de doctorat (décembre 2015), <http://www.theses.fr/s163098>.
- [III.63] C. Kharif, E. Pelinovsky et A. Slunyaev, *Rogue Waves in the Ocean*, Advances in Geophysical and Environmental Mechanics and Mathematics, Springer Berlin Heidelberg, Berlin, Heidelberg, <http://link.springer.com/10.1007/978-3-540-88419-4> (2009).
- [III.64] R. W. Katz, « Statistics of extremes in climate change », *Climatic Change*, **100**(1), pp. 71–76 (mai 2010), <http://link.springer.com/article/10.1007/s10584-010-9834-5>.
- [III.65] H. E. Roman, R. A. Siliprandi, C. Dose et M. Porto, « Long-time correlations in company profit fluctuations : Presence of extreme events », *Phys. Rev. E*, **80**(3), pp. 036114 (septembre 2009), <http://link.aps.org/doi/10.1103/PhysRevE.80.036114>.
- [III.66] D. R. Solli, C. Ropers, P. Koonath et B. Jalali, « Optical rogue waves », *Nature*, **450**(7172), pp. 1054–1057 (décembre 2007), <http://www.nature.com/nature/journal/v450/n7172/abs/nature06402.html>.

- [III.67] J. M. Dudley, G. Genty et B. J. Eggleton, « Harnessing and control of optical rogue waves in supercontinuum generation », *Opt. Express*, **16**(6), pp. 3644–3651 (mars 2008), <https://www.osapublishing.org/oe/abstract.cfm?uri=oe-16-6-3644>.
- [III.68] B. Kibler, J. Fatome, C. Finot, G. Millot, F. Dias, G. Genty, N. Akhmediev et J. M. Dudley, « The Peregrine soliton in nonlinear fibre optics », *Nat. Phys.*, **6**(10), pp. 790–795 (octobre 2010), <https://www.nature.com/articles/nphys1740>.
- [III.69] M. G. Kovalsky, A. A. Hnilo et J. R. Tredicce, « Extreme events in the Ti:sapphire laser », *Opt. Lett.*, **36**(22), pp. 4449–4451 (novembre 2011), <http://ol.osa.org/abstract.cfm?URI=ol-36-22-4449>.
- [III.70] A. Mussot, A. Kudlinski, M. Kolobov, E. Louvergneaux, M. Douay et M. Taki, « Observation of extreme temporal events in CW-pumped supercontinuum », *Opt. Express*, **17**(19), pp. 17010–17015 (septembre 2009), <https://www.osapublishing.org/oe/abstract.cfm?uri=oe-17-19-17010>.
- [III.71] N. Akhmediev, B. Kibler, F. Baronio, M. Belic, W.-P. Zhong, Y. Zhang, Wonkeun Chang, J. M. Soto-Crespo, P. Vouzas, P. Grelu, C. Lecaplain, K. Hammani, S. Rica, A. Picozzi, M. Tlidi, K. Panajotov, A. Mussot, A. Bendahmane, Pascal Sriftgiser, G. Genty, J. Dudley, A. Kudlinski, A. Demircan, U. Morgner, Shalva Amiraranashvili, C. Bree, G. Steinmeyer, C. Masoller, N. G. R. Broderick, A. F. J. Runge, Miro Erkintalo, S. Residori, U. Bortolozzo, F. T. Arecchi, S. Wabnitz, C. G. Tiofack, S. Coulibaly et M. Taki, « Roadmap on optical rogue waves and extreme events », *J. Opt.*, **18**(6), pp. 063001 (2016), <http://stacks.iop.org/2040-8986/18/i=6/a=063001>.
- [III.72] J. Ahuja, D. B. Nalawade, J. Zamora-Munt, R. Vilaseca et C. Masoller, « Rogue waves in injected semiconductor lasers with current modulation : role of the modulation phase », *Opt. Express*, **22**(23), pp. 28377–28382 (novembre 2014), <https://www.osapublishing.org/oe/abstract.cfm?uri=oe-22-23-28377>.
- [III.73] C. Bonatto, M. Feyereisen, S. Barland, M. Giudici, C. Masoller, J. R. R. Leite et J. R. Tredicce, « Deterministic Optical Rogue Waves », *Phys. Rev. Lett.*, **107**(5), pp. 053901 (juillet 2011), <https://link.aps.org/doi/10.1103/PhysRevLett.107.053901>.
- [III.74] K. Schires, A. Hurtado, I. D. Henning et M. J. Adams, « Rare disruptive events in polarisation-resolved dynamics of optically injected 1550 nm VCSELs », *Electron. Lett.*, **48**(14), pp. 872–874 (juillet 2012), <http://digital-library.theiet.org/content/journals/10.1049/el.2012.1838>.
- [III.75] A. K. Dal Bosco, D. Wolfersberger et M. Sciamanna, « Extreme events in time-delayed nonlinear optics », *Optics Letters*, **38**(5), pp. 703–705 (mars 2013), <https://www.osapublishing.org/ol/abstract.cfm?uri=ol-38-5-703>.
- [III.76] J. A. Reinoso, J. Zamora-Munt et C. Masoller, « Extreme intensity pulses in a semiconductor laser with a short external cavity », *Phys. Rev. E*, **87**(6), pp. 062913 (juin 2013), <https://link.aps.org/doi/10.1103/PhysRevE.87.062913>.
- [III.77] D. Rontani, E. Mercier, D. Wolfersberger et M. Sciamanna, « Enhanced complexity of optical chaos in a laser diode with phase-conjugate feedback », *Opt. Lett.*, **41**(20), pp. 4637–4640 (octobre 2016), <https://www.osapublishing.org/ol/abstract.cfm?uri=ol-41-20-4637>.
- [III.78] E. Mercier, D. Wolfersberger et M. Sciamanna, « High-frequency chaotic dynamics enabled by optical phase-conjugation », *Sci. Rep.*, **6**, pp. 18988 (janvier 2016), <https://www.nature.com/articles/srep18988>.
- [III.79] K. A. Shore et D. M. Kane, « Comb generation bandwidth for frequency-shifted feedback semiconductor lasers », *IEEE J. Quantum Electron.*, **35**(7), pp. 1053–1056 (juillet 1999).
- [III.80] Y. Noblet, J. P. Toomey et D. M. Kane, « Dynamics of a semiconductor laser with frequency shifted feedback », dans *Proc. SPIE 8980, Physics and Simulation of Optoelectronic Devices XXII*, tome 8980, p. 89800C. International Society for Optics and Photonics (mars 2014), <https://www.spiedigitallibrary.org/conference-proceedings-of-spie/8980/89800C/Dynamics-of-a-semiconductor-laser-with-frequency-shifted-feedback/10.1117/12.2038871.short>.
- [III.81] F.-Y. Lin et J.-M. Liu, « Chaotic lidar », *IEEE J. Sel. Topics Quantum Electron.*, **10**(5), pp. 991–997 (septembre 2004).
- [III.82] L. Wang, Y. Guo, P. Li, T. Zhao, Y. Wang et A. Wang, « White-Chaos Radar With Enhanced Range Resolution and Anti-Jamming Capability », *IEEE Photon. Technol. Lett.*, **29**(20), pp. 1723–1726 (octobre 2017).

- [III.83] L. Xia, D. Huang, J. Xu et D. Liu, « Simultaneous and precise fault locating in WDM-PON by the generation of optical wideband chaos », *Opt. Lett.*, **38**(19), pp. 3762–3764 (octobre 2013), <https://www.osapublishing.org/ol/abstract.cfm?uri=ol-38-19-3762>.
- [III.84] A. Uchida, K. Amano, M. Inoue, K. Hirano, S. Naito, H. Someya, I. Oowada, T. Kurashige, M. Shiki, S. Yoshimori, K. Yoshimura et P. Davis, « Fast physical random bit generation with chaotic semiconductor lasers », *Nat. Photonics*, **2**(12), pp. 728–732 (décembre 2008), <https://www.nature.com/articles/nphoton.2008.227>.
- [III.85] L. Larger, M. C. Soriano, D. Brunner, L. Appeltant, J. M. Gutierrez, L. Pesquera, C. R. Mirasso et I. Fischer, « Photonic information processing beyond Turing : an optoelectronic implementation of reservoir computing », *Opt. Express*, **20**(3), pp. 3241–3249 (janvier 2012), <https://www.osapublishing.org/oe/abstract.cfm?uri=oe-20-3-3241>.
- [III.86] Y. Kuriki, J. Nakayama, K. Takano et A. Uchida, « Impact of input mask signals on delay-based photonic reservoir computing with semiconductor lasers », *Opt. Express*, **26**(5), pp. 5777–5788 (mars 2018), <https://www.osapublishing.org/oe/abstract.cfm?uri=oe-26-5-5777>.
- [III.87] X. Fu, S.-C. Chan, Q. Liu et K. K.-Y. Wong, « Broadband optical chaos for stimulated Brillouin scattering suppression in power over fiber », *Appl. Opt.*, **50**(25), pp. E92–E96 (septembre 2011), <https://www.osapublishing.org/ao/abstract.cfm?uri=ao-50-25-E92>.
- [III.88] J. Zhang, M. Zhang, M. Zhang, Y. Liu, C. Feng, Y. Wang et Y. Wang, « Chaotic Brillouin optical correlation-domain analysis », *Opt. Lett.*, **43**(8), pp. 1722–1725 (avril 2018), <https://www.osapublishing.org/ol/abstract.cfm?uri=ol-43-8-1722>.
- [III.89] M. Santagiustina et L. Ursini, « Dynamic Brillouin gratings permanently sustained by chaotic lasers », *Opt. Lett.*, **37**(5), pp. 893–895 (mars 2012), <https://www.osapublishing.org/ol/abstract.cfm?uri=ol-37-5-893>.
- [III.90] J. Zhang, Z. Li, Y. Wu, M. Zhang, Y. Liu et M. Li, « Optimized chaotic Brillouin dynamic grating with filtered optical feedback », *Sci. Rep.*, **8**(1), pp. 827 (janvier 2018), <https://www.nature.com/articles/s41598-018-19180-w>.
- [III.91] J. Zhang, C. Feng, M. Zhang, Y. Liu et Y. Zhang, « Suppression of Time Delay Signature Based on Brillouin Backscattering of Chaotic Laser », *IEEE Photon. J.*, **9**(2), pp. 1–8 (avril 2017).
- [III.92] A. C. Chime, *Etude théorique et expérimentale de micro-OLEDs rapides sur électrodes coplanaires en régime d'impulsions à haute densité de courant*, Thèse de doctorat (décembre 2017).
- [III.93] A. G. Correa-Mena, *Use of a Microwave Photonic Architecture for Simultaneous Transmission of Analog and Digital Signals*, Thèse de doctorat (septembre 2018).

CONCLUSION ET PERSPECTIVES

IV.1 CONCLUSION GÉNÉRALE

DURANT ma carrière, j'ai acquis des compétences et des connaissances scientifiques dans les domaines de la dynamique non linéaire dans des diodes lasers soumises à un retour optique et de l'optique non linéaire dans des fibres optiques en effectuant ma thèse au Laboratoire d'Optique P.-M. Duffieux et mes recherches postdoctorales à la Bangor University et à l'Institut FEMTO-ST. Depuis 2011, je mène mes travaux de recherche au Laboratoire de Physique des Lasers (LPL) dans les domaines de la dynamique non linéaire dans des diodes lasers soumises à un retour optique et de l'optique non linéaire dans des cristaux photoniques non linéaires.

Au LPL, j'ai encadré les thèses de Q. Ripault, de F. Baladi, de Z. Yellas, de A. G. Correa-Mena, et de A. Chime. Actuellement j'encadre aussi la thèse de S. Mohand-Ousaid. Durant cette période, j'ai travaillé en collaboration industrielle avec l'entreprise 3SP Technologies et en collaborations internationales avec la National Taiwan University et avec l'INAOE au Mexique.

Toute ma carrière, j'ai publié 47 articles dans les journaux avec la comité de lecture et je suis en train de préparer deux articles avec les derniers résultats. J'ai aussi été invité dans trois conférences. Durant ma carrière, j'ai travaillé dans le cadre de différents projets parmi lesquels j'ai obtenu un projet BQR et un projet PICS (Projet International de Coopération Scientifique).

IV.2 PERSPECTIVES

APRÈS tant d'années de recherche, je souhaite m'investir plus dans le domaine de l'optique non linéaire. Récemment, nous avons obtenu des échantillons circulaires de **PPLT**-2D comme montré sur la figure [IV.1](#). En général, les échantillons sont rectangulaires et le faisceau de la pompe injecté dans ces échantillons est dévié à la sortie des cristaux lorsque l'angle d'incidence de la pompe n'est pas nul. Ceci est contraignant pour la détection des nouvelles longueurs d'onde générées. Afin d'éviter ce problème, je souhaite travailler avec des échantillons circulaires pour l'étude de la génération paramétrique optique (**OPG**) avec l'angle. La forme circulaire permettra de garder la position de faisceau quelque soit l'angle d'incidence de la pompe et d'étudier l'**OPG** avec l'angle plus facilement. Ceci permettra également d'accorder dynamiquement les longueurs d'onde générées avec différents vecteurs de réseau réciproques. Pour cette étude, je souhaite développer une collaboration avec Monsieur Benoît BOULANGER à l'Institut Néel de l'Université Grenoble-Alpes qui travaille avec ce type d'échantillons depuis des années. Ceci est aussi le sujet de thèse de Mlle. Mohand-Ousaid que j'encadre actuellement. Je souhaite également consolider la collaboration avec la National Taiwan University.

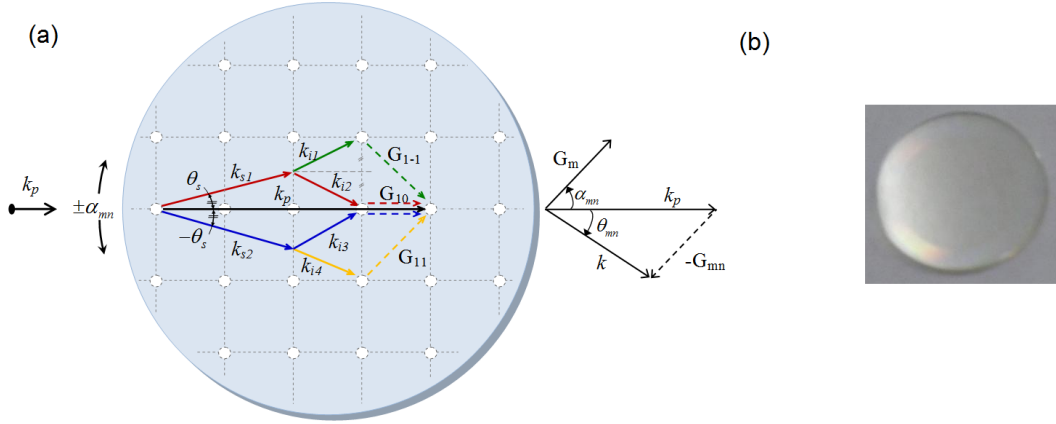


FIGURE IV.1 – (a) Quasi-accord de phase dans un échantillon circulaire. (b) Image de l'échantillon poli et préparé par T. Billeton.

A long terme, je souhaite également développer un système compact d'une source cohérente utilisant un cristal photonique non linéaire. Pour ce développement d'un système compact, il est important de pomper le cristal par une diode laser comme montré sur la figure IV.2. Le cristal du système sera en configuration guide d'onde pour une meilleur efficacité de conversion de fréquence. Une fois développé, je souhaite valoriser le savoir-faire par un transfert de technologies vers l'industrie.

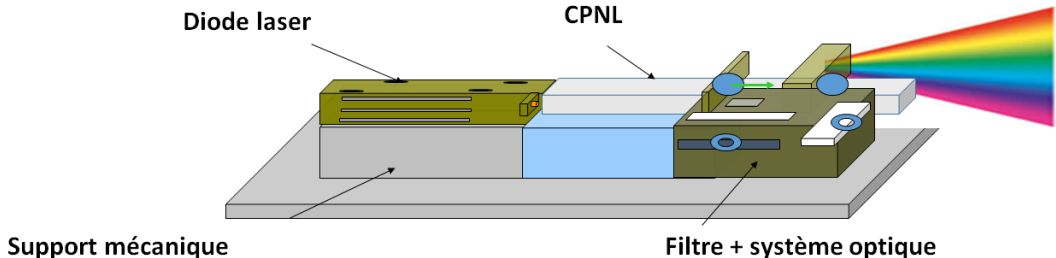


FIGURE IV.2 – Système compact d'une source cohérente avec un cristal photonique non linéaire en guide d'onde.

Dans le domaine de la dynamique non linéaire, j'ai développé une collaboration avec l'INAOE au Mexique. Je souhaite donc continuer cette collaboration par des accueils de doctorants ou des thèses en cotutelle.

PUBLICATIONS SIGNIFICATIVES

CE CHAPITRE a pour but une compilation de quelques publications significatives après ma thèse. Ces publications sont les fruits de mes travaux de recherche effectués avec des collègues et des doctorants au sein du School of Computer Science and Electronic Engineering à Bangor, de l’Institut FEMTO-ST à Besançon et du Laboratoire de Physique des Lasers à Villeurbanne. Je les remercie tous chaleureusement d’avoir contribué à ces travaux.

Sommaire

| | | |
|------|---|-----|
| V.1 | Opt. Lett., 28, pp. 2168 (2003) | 86 |
| V.2 | Electron. Lett., 40, pp. 614 (2004) | 89 |
| V.3 | Opt. Lett., 29, pp. 2497 (2004) | 91 |
| V.4 | Opt. Lett., 29, pp. 1215 (2004) | 94 |
| V.5 | Phot. Tech. Lett., 16, pp. 2392 (2004) | 97 |
| V.6 | J. Opt. Soc. Am. B, 23, pp. 846 (2006) | 100 |
| V.7 | Phot. Tech. Lett., 18, pp. 169 (2006) | 106 |
| V.8 | IEE Proceeding on Optoelectronics, 152, pp. 97 (2005) | 109 |
| V.9 | J. Lightwave Technol., 28, pp. 2173 (2010) | 115 |
| V.10 | Opt. Express, 18, pp. 20136 (2010) | 121 |
| V.11 | Phot. Tech. Lett., 24, pp. 667 (2012) | 128 |
| V.12 | Phot. Tech. Lett., 24, pp. 79 (2012) | 131 |
| V.13 | Phot. Tech. Lett., 25, pp. 94 (2013) | 134 |
| V.14 | Opt. Lett., 37, pp. 130 (2012) | 137 |
| V.15 | Opt. Express, 21, pp. 7202 (2013) | 140 |
| V.16 | Opt. Express, 25, pp. 30253 (2017) | 147 |
| V.17 | Opt. Lett., 41, pp. 2950 (2016) | 153 |
| V.18 | Opt. Lett., 41, pp. 4476 (2016) | 157 |
| V.19 | Org. Electron., 56, pp. 284 (2018) | 161 |

Comparison of closed-loop and open-loop feedback schemes of message decoding using chaotic laser diodes

Min Won Lee, Jon Paul, Sivaraman Sivaprakasam, and K. Alan Shore

School of Informatics, University of Wales, Bangor, Dean Street, Bangor LL57 1UT, Wales, UK

Received May 18, 2003

An experimental study of a chaotic optical communication scheme using an external cavity laser diode to encode a message is reported. The message is decoded in closed- and open-loop receiver schemes. Both schemes show effective decoding of a 1-GHz message. The synchronization and effectiveness of encoding are compared in both schemes. © 2003 Optical Society of America

OCIS codes: 140.1540, 060.4510, 140.2020.

Chaos cryptography has been a hot topic in the past decade in the context of secure communications. Chaotic signals can mask information inside their broadband noise, and the synchronization of two chaotic systems makes it possible to extract information from the noise. Since the work of Pecora and Carroll,¹ who introduced the idea of synchronization between two chaotic oscillators, a variety of research has been undertaken with the aim of achieving chaos cryptography.² Several schemes have been proposed to achieve this.^{3–7} Diode lasers have a particular advantage in that they offer high-speed operation in the chaotic regime. Demonstrations of this capability have been reported,^{8–10} and novel forms of synchronization of chaos anticipation have also been investigated.^{11,12} Recently, a chaotic optical modulation scheme was demonstrated for secure message transmission in an open-loop configuration.¹³ In the open-loop configuration the receiver is a solitary laser, whereas in the closed-loop configuration the receiver is a chaotic external cavity laser. The optical modulation scheme can easily encode a message through direct message injection into the chaotic transmitter. This previous experimental work showed that the receiver laser is capable of robust message extraction in an open-loop configuration. Theory¹⁴ suggests that the system should also work in a closed-loop configuration. However, to the best of our knowledge, there has been no experimental report comparing open- and closed-loop schemes for chaotic message transmission. In this Letter we report an experimental comparison of the performance of a high-frequency communication system in which the message is decrypted in both closed- and open-loop schemes. In the open-loop scheme the transmitter laser drives the receiver laser. As such it may be expected that such a configuration will offer superior performance to that of the closed-loop scheme.

The experimental setup is shown schematically in Fig. 1. Three single-mode Fabry–Perot laser diodes emitting at 830 nm are used as the message laser, the transmitter laser, and the receiver laser. The message laser's drive current is modulated by a 1-GHz sine waveform, which is considered the message to be transmitted. Beam splitter BS1 is used to couple the message and the transmitter laser. BS2

and BS4 are used to couple the transmitter laser to the receiver laser. The outputs of the transmitter laser and receiver laser are coupled to photodetectors PD1 and PD2 via BS3 and BS5, respectively. The coupling strength between the message and transmitter lasers is controlled by coupling attenuator CA1. Likewise, the coupling strength between the transmitter and receiver lasers is controlled by CA2. The transmitter laser is subjected to optical feedback from external cavity mirror M1, placed at a distance of 70 cm. In the closed-loop scheme M2 is adjusted such that the receiver has the same external cavity length as the transmitter, and in the open-loop scheme M2 is removed. The optical feedback levels of the transmitter and receiver in the closed-loop scheme are varied by neutral-density filters NDF1 and NDF2 so that the lasers can be rendered chaotic. OI1–OI3 are optical isolators that provide –41 dB of isolation and ensure that the lasers are free from parasitic feedback.

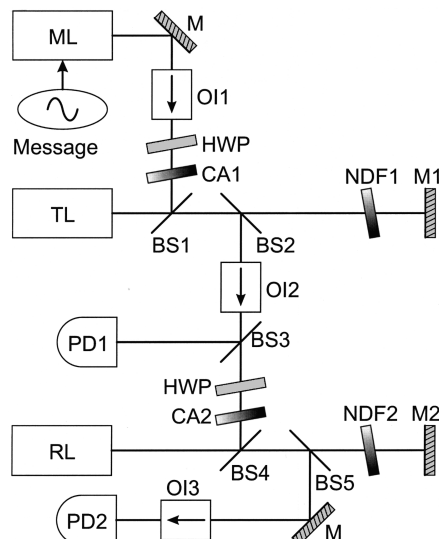


Fig. 1. Schematic of the experimental setup: ML, message laser; TL, transmitter laser; RL, receiver laser; BS1–BS5, beam splitters; M1–M3, mirrors; OI1–OI3, optical isolators; CA1, CA2, coupling attenuators; NDF1, NDF2, neutral-density filters; HWPs, half-wave plates; PD1, PD2, photodetector.

Each isolator introduces a change of polarization by 45° . Two half-wave plates are used to correct the polarization change introduced by OI1 and OI2. Large-bandwidth (6-GHz) photodetectors (PD1, PD2) are used in the experiments to ensure high-frequency operation of the chaotic system.

In this experiment the most critical parameter to match is the center wavelength of all three lasers. The temperature and current of the message laser (26.26°C and 36.17 mA) and transmitter laser (22.10°C and 34.74 mA) are adjusted such that they operate at the same wavelength. For the receiver laser, the temperature and current are adjusted to 25.78°C and 28.10 mA in the case of the closed-loop scheme and 25.78°C and 28.80 mA in the case of the open-loop scheme. 20% of the modulated output power from the message laser is injected into the transmitter via CA1, constituting a 10-dB chaos-to-signal ratio for good message encoding. The transmitter has an external cavity round-trip time of 4.67 ns and a cavity mirror that provides 1% optical feedback that drives the transmitter laser into the low-frequency fluctuation regime. The system generates chaotic signals with a bandwidth up to 5 GHz, which allows encoding of high-frequency messages. In the closed-loop configuration, 0.7% of the transmitter output power and 0.3% of the receiver feedback intensity are injected into the receiver. Thus, the total receiver input power is 1%, which is the same as the transmitter feedback intensity. In the open-loop configuration, 3% of the transmitter output power is injected into the receiver.

Measurements of the quality of chaotic synchronization without a message were made for both closed- and open-loop configurations. Intensity synchronization of the transmitter and receiver lasers is obtained, and Fig. 2 shows their synchronization diagrams. The quality of the synchronization is measured with a correlation factor that is obtained by calculation of the correlation between the broadened width of the synchronization plot and a fitted line. The correlation would be unity for perfect synchronization and zero for two independent systems. The system shows good synchronization, with a correlation factor of 0.942 in the closed-loop case and 0.949 in the open-loop case. The open-loop scheme shows higher synchronization quality than the closed-loop scheme. When the transmitter and receiver are decoupled in the closed-loop scheme, the chaotic outputs of the transmitter and the receiver have a correlation factor of less than 0.06. Hence, as expected, they are completely independent chaos generators when they are decoupled.

To measure the synchronization quality as a function of current, we scanned the receiver laser current from 23 to 33 mA while fixing the laser operating temperature. The current and the temperature of the message and transmitter lasers were held constant. Figure 3 shows the correlation factors as a function of the receiver laser current for the closed- and open-loop configurations. The synchronization quality of the open-loop configuration remains higher than that of the closed-loop configuration. The coupling rate and feedback level of the transmitter were found not to

have a significant effect on this result. Moreover, the near-constant value of the synchronization quality near the drive current of 28 mA indicates that the synchronization in the open-loop scheme is more stable than in the closed-loop scheme. For currents of $23.5\text{--}25\text{ mA}$, the correlation factor is high, but this does not imply good synchronization, because the slope of the synchronization plot is due to the low output intensity of the laser below threshold.

Synchronization was implemented by transmission of a 1-GHz message to the receiver. Figure 4 shows the synchronization between the transmitter and receiver in both the closed- and open-loop schemes. The correlation factors, again obtained by fitting the synchronization plot to a straight line, are 0.937 for the closed-loop scheme and 0.953 for the open-loop scheme. Even with the message, the synchronization performance of the open-loop scheme is better than that of the closed-loop scheme.

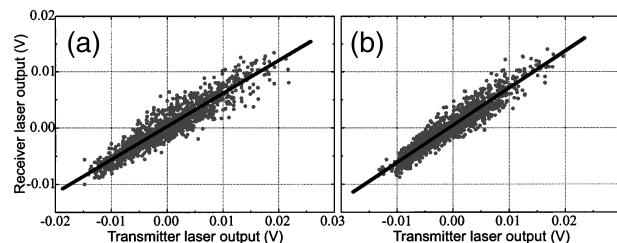


Fig. 2. Synchronization plots of the transmitter and receiver outputs without a message. (a) Closed-loop case. (b) Open-loop case.

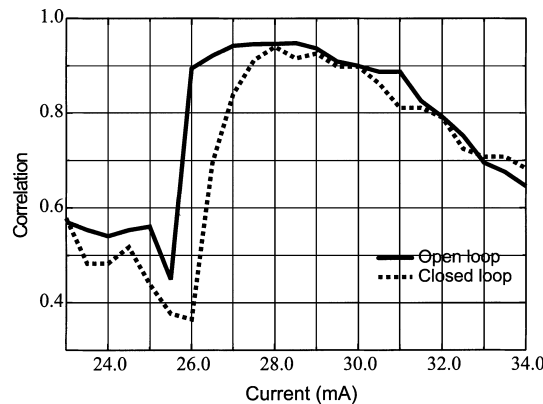


Fig. 3. Correlation factor as a function of the slave laser current.

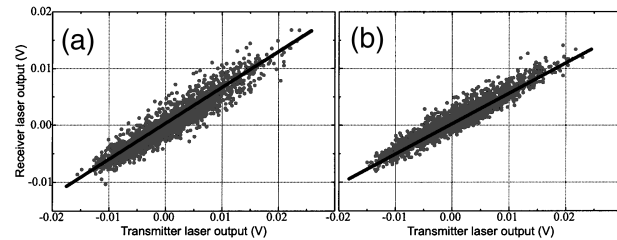


Fig. 4. Synchronization plots of the transmitter and receiver outputs with a message. (a) Closed-loop case. (b) Open-loop case.

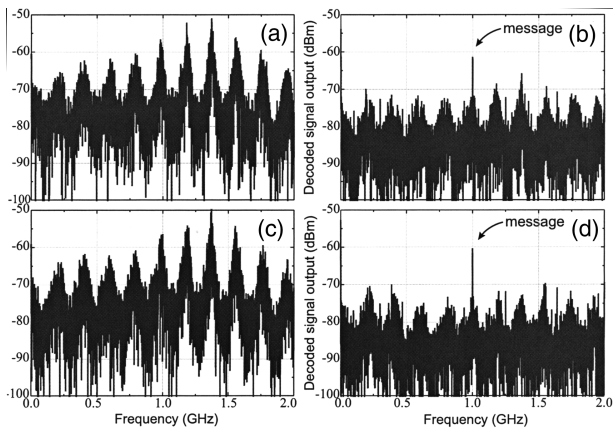


Fig. 5. Fast Fourier transform of an encoded and a decoded message, showing (a) the transmitted signal in the closed-loop scheme, (b) the recovered message in the closed-loop scheme, (c) the transmitted signal in the open-loop scheme, and (d) the recovered message in the open-loop scheme.

Finally, message decoding was performed in both schemes. The technique used for message subtraction was that proposed by Goedgebuer *et al.*⁶ The message laser supplies the message to the chaotic transmitter laser, where the message is encoded into the chaotic output of the laser and then transmitted to the receiver. A part of the transmitted signal is coupled to PD1. The receiver laser output is coupled to PD2. The message is recovered by simple subtraction of the electronic output from PD2 from that of PD1. The results of message encoding and decoding are shown in Fig. 5. Figure 5(a) shows the power spectra of the transmitted chaotic signal in which the message is masked for the closed-loop case. The 5-GHz bandwidth chaotic output is able to mask the message. Figure 5(b) shows the power spectra of the recovered message, where a strong peak indicates the detection of the message at 1 GHz. The decoded message shows ~ 13 dB of signal-to-noise ratio. It is apparent from Fig. 5(c) that in the open-loop case the message is masked as effectively as in the closed-loop case. Figure 5(d) shows the

decoded message in the open-loop scheme, where the signal-to-noise ratio of the message is ~ 16 dB. This value is higher than that of the closed-loop scheme. Thus, even the message decoding quality in the open-loop scheme is better than in the closed loop.

In conclusion, we have compared the qualities of synchronization and message decoding using closed- and open-loop schemes. From the results, it can be seen that the open-loop scheme shows better performance both quantitatively and qualitatively than the closed-loop scheme. This conclusion is not affected by changes in the optical feedback level and coupling rate. Future work will be directed toward improving the message decoding quality of the closed-loop scheme.

This work is financed by the European Union Optical Chaos Communication using Laser Transmitters (OC-CULT) project (IST-2000-29683). K. A. Shore's e-mail address is alan@informatics.bangor.ac.uk.

References

1. L. M. Pecora and T. L. Carroll, Phys. Rev. Lett. **64**, 821 (1990).
2. K. M. Cuomo and A. V. Oppenheim, Phys. Rev. Lett. **71**, 65 (1993).
3. G. D. VanWiggeren and R. Roy, Phys. Rev. Lett. **81**, 3547 (1998).
4. H. Fujino and J. Ohtsubo, Opt. Lett. **25**, 625 (2000).
5. T. Heil, J. Mulet, I. Fischer, C. R. Mirasso, M. Peil, P. Colet, and W. Elsässer, IEEE J. Quantum Electron. **38**, 1162 (2002).
6. J.-P. Goedgebuer, L. Larger, and H. Porte, Phys. Rev. Lett. **80**, 2249 (1998).
7. M. W. Lee, L. Larger, and J.-P. Goedgebuer, IEEE J. Quantum Electron. **39**, 931 (2003).
8. I. Fischer, Y. Liu, and P. Davis, Phys. Rev. Lett. **62**, 1 (2000).
9. J. Paul, S. Sivaprakasam, P. Spencer, P. Rees, and K. A. Shore, Electron. Lett. **38**, 28 (2002).
10. S. Tang and J. M. Liu, Opt. Lett. **26**, 1843 (2001).
11. C. Masoller, Phys. Rev. Lett. **86**, 2782 (2001).
12. S. Sivaprakasam, E. M. Shahverdiev, and K. A. Shore, Phys. Rev. Lett. **87**, 154101 (2001).
13. J. Paul, S. Sivaprakasam, P. Spencer, and K. A. Shore, J. Opt. Soc. Am. B **20**, 497 (2003).
14. R. Vicente, T. Prez, and C. R. Mirasso, IEEE J. Quantum Electron. **38**, 1197 (2002).

Chaotic message broadcasting using DFB laser diodes

M.W. Lee and K.A. Shore

An experimental demonstration has been performed of gigahertz message broadcasting at telecommunication wavelengths using a chaotic external-cavity DFB laser transmitter and two standalone DFB laser receivers. Message recovery was achieved with greater than 14 dB signal-to-noise ratio.

Introduction: Private optical communication based on chaos encryption has attracted much attention in recent years. Several optical systems have been proposed for using chaos in laser intensity, wavelength and optical delay [1–4]. Attention is turning to applying these approaches in practical private optical communication where high bit-rate message decoding [5], chaotic telecommunication lasers [6], open-loop and closed-loop message decoding [7] and chaos multiplexing [8] may be utilised. To implement a chaotic communications network, it is highly attractive to have the capability of broadcasting a message from one transmitter to several receivers. A key element of chaos message transmission is the requirement for achieving chaos synchronisation between transmitter and receiver so as to allow message extraction at the receiver. The challenge to the successful demonstration of chaos broadcasting is to ensure that such synchronisation can be robustly achieved between the transmitter and several receivers. In the case of optical chaotic communication the particular requirement is to provide appropriate optical coupling between the transmitter and the receivers to enable synchronisation and hence message transmission. In this Letter we report an experimental demonstration of a proof of principle of chaos broadcasting by transmitting and extracting a 1 GHz message using a chaotic external cavity laser diode transmitter and two chaotic laser diode receivers.

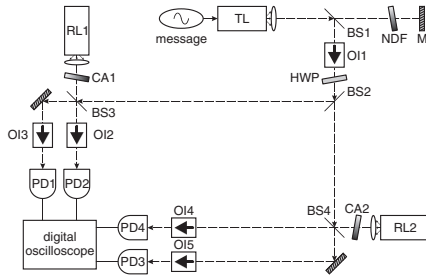


Fig. 1 Schematic experimental setup

TL: transmitter laser; RL: receiver laser; BS: beamsplitter; M: mirror; OI: optical isolator; CA: coupling attenuator; NDF: neutral density filter; HWP: half-wave plate; PD: photodetector

Experiment: The experimental setup is shown schematically in Fig. 1. The transmitter consists of an external-cavity laser diode, and both receiver lasers are standalone lasers, that is the receivers operate in the open-loop configuration. Because of their relevance to conventional optical-fibre communication systems, three singlemode DFB laser diodes emitting at 1550 nm are used, as the transmitter laser (TL), receiver laser 1 (RL1) and receiver laser 2 (RL2), respectively. These lasers are stabilised by temperature controllers with 28.7°C for TL, 20.5°C for RL1 and 24.7°C for RL2. The broadcast distance of TL–RL1 is 80 cm and that of TL–RL2 is 97.5 cm. The transmitter laser is subject to optical feedback from the mirror M in an external-cavity length of 30 cm, corresponding to a 2 ns external-cavity round trip time. The optical feedback level of the transmitter is varied by using the neutral density filter NDF so that the laser can be rendered chaotic. Direct modulation of TL using a 1 GHz sine-waveform signal provides the message to be transmitted. The TL output is sent to both the receivers using the beamsplitters BS1 and BS2. BS3 is used to couple TL and RL1 and BS4 is used to couple TL and RL2. The optical isolators OI1–5 ensure one-way beam propagation by eliminating parasitic reflection with –40 dB isolation. The half-wave plate HWP is used to correct the polarisation change introduced by OI1. The coupling attenuators CA1 and CA2 are used to vary the coupling ratios of TL–RL1 and TL–RL2. The photodetector PD1 is used to detect the RL1 input and PD2 is used to detect the RL1 output. PD3 is

used to detect the RL2 input and PD4 is used to detect the RL2 output. All photodetectors have a sufficiently large bandwidth (12 GHz) to enable high-frequency communication. The outputs of the photodetectors are recorded by a digital oscilloscope with 4 GHz bandwidth and 20 GS/s sampling rate.

Principle of operation: The centre wavelengths of all three lasers need to be matched to synchronise the lasers. For our setup, the currents of TL, RL1 and RL2 are adjusted to 34.48, 44.9 and 33.43 mA, respectively, to match the centre wavelengths of the lasers at 1549.12 nm. The synchronisation occurs within 12.5 GHz laser frequency detuning range. Varying the optical feedback level of TL, several dynamical regimes, including chaotic regimes, are obtained in the transmitter. Among them, the LFF (low-frequency fluctuation) regime—obtained with 1.6% of optical feedback intensity—is used here for message encoding. The bandwidth of the chaotic outputs is more than 4 GHz, which is adequate to encode the 1 GHz message. The technique used for message encoding is that of chaotic modulation where TL is directly modulated. A –20.7 dB RMS modulation depth over chaotic signals is used to ensure efficient message encoding. The 1 GHz message encoded inside the chaotic signal is transmitted to both the receiver lasers. A part of the broadcast signal is sent to RL1 and another part is sent to RL2. In this scheme, 3.2% of the TL output power is injected into each receiver laser.

Results: For message decoding, chaos synchronisation between the transmitter laser and the receiver lasers is required. Here the lasers are synchronised by injection locking in an LFF regime. Fig. 2 shows the synchronisation plots obtained from the time series recorded with a 5 GS/s sampling rate. The synchronisation plot of the outputs from PD1 (RL1 input) and from PD2 (RL1 output) is shown in Fig. 2a and that of the outputs from PD3 (RL2 input) and from PD4 (RL2 output) is shown in Fig. 2b. Such plots are indicative of good synchronisation between the chaotic lasers. The quality of the synchronisation is measured by calculating the cross-correlation between two time series of receiver laser input and output. But note that the inputs of the receiver lasers are the outputs of the transmitter laser. The correlation would be unity for perfectly synchronised systems and zero for independent systems. The correlations obtained experimentally here are 0.859 for Fig. 2a and 0.849 for Fig. 2b. High-quality synchronisation is thus obtained between the transmitter and both receivers.

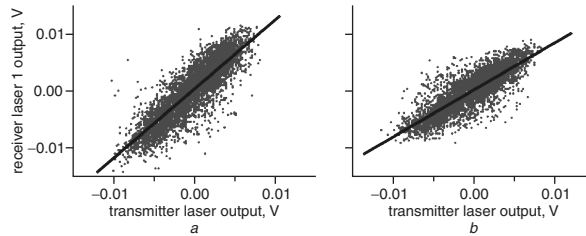


Fig. 2 Synchronisation diagrams of transmitter and receiver outputs

- a Transmitter laser output and receiver laser 1 output
b Transmitter laser output and receiver laser 2 output

Using this synchronisation, broadcast message decoding has been implemented at the two receivers at the same time. The technique used for message decoding is similar to that proposed previously. In RL1, the digitised time series from PD2 is normalised to that from PD1. The time series from PD1 is the transmitted chaotic signal, which includes the message, and the time series from PD2 is the locally generated chaotic signal, which does not contain the message. Hence, by subtracting the normalised time series of PD2 from the time series of PD1, the message can be recovered. Likewise, RL2 recovers the message through a subtraction of the outputs from PD3 and PD4. Fig. 3 shows the power spectra as a result of message encoding and decoding. They are calculated from the time series of the encoded and decoded messages in each receiver. The power spectra of the signal broadcasted to RL1, in which the message is encoded, is shown in Fig. 3a. Since the dominant LFF peak appears at 1 GHz, the 1 GHz message cannot be noticed in the Figure, demonstrating that the message encoding is effective. Fig. 3b displays the power spectra of

the message recovered from RL1, where the message is clearly visible at 1 GHz. The extracted message has a 14.7 dB signal-to-noise ratio, which indicates efficient message recovery. Fig. 3c shows the power spectra of the signal broadcast to RL2. As in Fig. 3a, the Figure displays an effective message encoding. Fig. 3d shows the power spectra of the recovered message from RL2. The decoded message has 14.5 dB signal-to-noise ratio, which again indicates efficient message recovery.

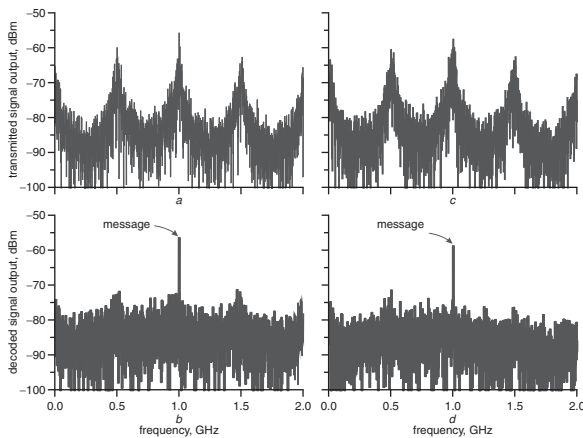


Fig. 3 Power spectra of encoded and decoded message

- a Transmitted signal from PD1
- b Recovered message in receiver laser 1
- c Transmitted signal from PD3
- d Recovered message in receiver laser 2

Conclusions: We have experimentally demonstrated broadcasting of a high-frequency message to two receiver lasers using a chaotic optical carrier generated in a DFB laser subject to optical feedback. Measurements show that high-quality chaos synchronisation can be achieved between all three lasers and the broadcast message is decoded with an efficient signal-to-noise ratio in both receivers.

Acknowledgment: The work is supported by the European Union OCCULT (Optical Chaos Communication Using Laser Transmitters) project (IST-2000-29683).

© IEE 2004

17 March 2004

Electronics Letters online no: 20040429

doi: 10.1049/el:20040429

M.W. Lee and K.A. Shore (*School of Informatics, University of Wales, Bangor, Dean Street, Bangor LL57 1UT, United Kingdom*)

E-mail: alan@informatics.bangor.ac.uk

References

- 1 VanWiggeren, G.D., and Roy, R.: 'Optical communication with chaotic waveforms', *Phys. Rev. Lett.*, 1998, **81**, (16), pp. 3547–3550
- 2 Paul, J., Sivaprakasam, S., Spencer, P., Rees, P., and Shore, K.A.: 'GHz bandwidth message transmission using chaotic diode lasers', *Electron. Lett.*, 2002, **38**, (1), pp. 28–29
- 3 Goedgebuer, J.-P., Larger, L., and Porte, H.: 'Optical cryptosystem based on synchronization of hyperchaos generated by a delayed feedback tunable laser diode', *Phys. Rev. Lett.*, 1998, **80**, (10), pp. 2249–2252
- 4 Lee, M.W., Larger, L., and Goedgebuer, J.-P.: 'Transmission system using chaotic delays between lightwaves', *IEEE J. Quantum Electron.*, 2003, **39**, (7), pp. 931–935
- 5 Tang, S., and Liu, J.M.: 'Message encoding-decoding at 2.5 Gbit/s through synchronization of chaotic pulsing semiconductor lasers', *Opt. Lett.*, 2001, **26**, (23), pp. 1843–1845
- 6 Annovazzi-Lodi, V., Merlo, S., Norgia, M., and Scirè, A.: 'Characterization of a chaotic telecommunication laser for different fiber cavity lengths', *IEEE J. Quantum Electron.*, 2002, **38**, (9), pp. 1171–1177
- 7 Lee, M.W., Paul, J., Sivaprakasam, S., and Shore, K.A.: 'Comparison of closed-loop and open-loop feedback schemes of message decoding using chaotic laser diodes', *Opt. Lett.*, 2003, **28**, (22), pp. 2168–2170
- 8 Paul, J., Sivaprakasam, S., and Shore, K.A.: 'Dual-channel chaotic optical communications using external-cavity semiconductor lasers', *J. Opt. Soc. Am. B*, 2004, **21**, (3), pp. 514–521

Effect of chaos pass filtering on message decoding quality using chaotic external-cavity laser diodes

Jon Paul, Min Won Lee, and K. Alan Shore

School of Informatics, University of Wales, Bangor, Bangor LL55 1UT, Wales, UK

Received August 12, 2004

An experimental demonstration of the effect of chaos pass filtering on high-frequency message transmission in the complete synchronization regime is reported. The opportunity for chaotic message decoding at frequencies up to 6 GHz is shown. © 2004 Optical Society of America

OCIS codes: 140.0140, 140.1540, 060.4510.

The ability to control chaos has been a stimulus in the recent past for the development of secure communication systems. Since the introduction of the idea of synchronization of chaotic oscillators,¹ much research has been undertaken toward achieving secure chaotic communications.^{2–13} Of particular interest are semiconductor lasers because they are readily available, can be driven to chaos with external-cavity feedback, and are widely employed in optical communication systems. In a chaotic optical communications scheme, a message is masked in the broadband-noise-like output of a chaotic transmitter laser, and message recovery is achieved by synchronization of the transmitter and a chaotic receiver laser. In such systems it has been demonstrated that the receiver laser synchronizes with the chaos produced in the transmitter but that the masked message amplitude is much reduced in the receiver compared with that in the transmitter.⁴ This effect has been termed chaos pass filtering.⁴ Thus, when the difference is taken between the input of the receiver (the transmitter output) and the output of the receiver, the transmitted message may be extracted. Sinusoidal message encoding and decoding at 1 GHz was recently demonstrated,⁸ and a scheme that employs chaotic pulsing lasers yielded message encoding and decoding at 2.5 Gbits/s.⁷ The quality of the recovered message depends on the quality of the synchronization between transmitter and receiver lasers and on the difference in amplitudes of the message at the receiver input and output. The effects of chaos pass filtering on high-frequency message signals in the strong injection-locking synchronization regime was previously investigated.¹⁴ In this Letter we present results of the effects of chaos pass filtering on message recovery for signals up to 6 GHz in the complete synchronization regime and demonstrate that message recovery is possible up to the relaxation oscillation frequency of the receiver laser.

The experimental arrangement used in the research reported here is shown schematically in Fig. 1. Distributed-feedback lasers (Luminent C-15-DFB-E-ANT, $I_{th} = 13.1$ mA at 25 °C, where I_{th} is the threshold current of the free-running laser) emitting at ~1550 nm are used as transmitter and receiver. The side-mode suppression ratio in these lasers is -40 dB. The lasers are driven by ultralow-noise current sources (ILX-Lightwave, LDX-3620) and are temperature con-

trolled by thermoelectric controllers (ILX-Lightwave, LDT-5412) to a precision of 0.01 K. The laser output is collimated by antireflection-coated laser diode objective lenses (Newport, FLA11).

The transmitter laser is subject to optical feedback from external mirror M1; the feedback strength is controlled with a continuously variable neutral-density filter (NDF). The external-cavity length is 42 cm. Optical isolators OI1 and OI2 ensure that the lasers are free from backreflection except from the external-cavity mirror; the typical isolation is -41 dB/isolator. The fast photodetectors have 12-GHz bandwidth. The transmitter is coupled to the receiver through beam splitters BS1 and BS3; the coupling strength is controlled by a coupling attenuator (CA). A half-wave plate (HWP) corrects a shift in the transmitter emission polarization introduced by the optical isolator. Beam splitter BS2 couples the transmitter output to photodetector PD1. Mirrors M2 and M3 couple the receiver output to photodetector PD2. The output of the photodetectors is recorded with a 20-Gsample/s oscilloscope.

The transmitter's bias current (27.41 mA), operating temperature (25.85 °C), and external-cavity feedback

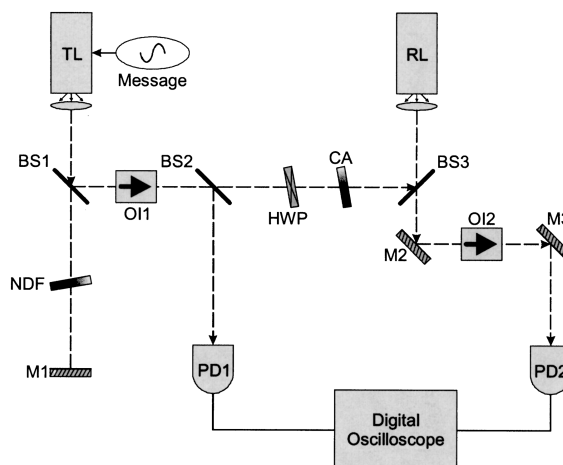


Fig. 1. Schematic diagram of the experiment: TL transmitter laser; RL, receiver laser; other abbreviations defined in text.

ratio (3.1%) are set such that the transmitter is rendered chaotic. The receiver laser's bias current (27.32 mA), operating temperature (26.7 °C), and coupling attenuator (2.5% of the transmitter output power coupled to receiver) are adjusted such that the transmitter and the receiver are synchronized. These values of bias current are the minimum values at which good synchronization between transmitter and receiver is achievable.

The bias current of the transmitter laser is modulated with a relatively strong 2.2-GHz message, thus enabling the message frequency to be clearly seen in the power spectrum of the transmitter. The message frequency is varied up to 6 GHz, and recordings are made of the transmitter and receiver outputs.

Figures 2(a), 2(b), and 2(c) show the power spectrum of the transmitter for message frequencies of 2.2, 5.3, and 6 GHz, respectively. The amplitude of the message remains relatively constant compared with the power spectrum of the chaos. Figures 2(d), 2(e), and 2(f) show the power spectrum of the receiver for message frequencies of 2.2, 5.3, and 6 GHz. Unlike in the transmitter, the message amplitude in the receiver's power spectrum is not constant but is of greater amplitude at 5.3 than at 6 GHz and is almost unseen at 2.2 GHz. The quality of message recovery in such systems is shown to depend not only on the synchronization quality but also on the difference in amplitude of the message in the transmitter and receiver outputs.

Figure 3 shows the amplitude of the message in the power spectrum of the transmitter (dotted curve) and the receiver (dashed curve) for message frequencies of 2.2–6 GHz. The message component in the transmitter's power spectrum remains relatively constant over the frequency range. The message amplitude in the receiver's power spectrum peaks at ~5.3 GHz and then starts to decline. The difference in the message components in the transmitter and the receiver is directly related to quality of message recovery. The solid curve, showing the difference in power of the message in the transmitter and the receiver, is minimum at 5.3 GHz. Thus the quality of message recovery is expected to be minimum at 5.3 GHz, and on either side of this value the message recovery quality is expected to increase.

For Figs. 2 and 3 the relaxation oscillation frequency of the receiver laser was 5.38 GHz, close to the region where there is minimum chaos pass filtering (i.e., minimum amplitude difference between the message at the transmitter and the message at the receiver).

Next we investigate a situation in which the relaxation oscillation frequency is greater. The transmitter (31.23-mA) and receiver (31.04-mA) bias currents are increased such that the transmitter and the receiver are synchronized, and the receiver's relaxation oscillation frequency is now 6.58 GHz. Once again the message frequency is varied from 2.2 to 6 GHz and the transmitter and receiver outputs are recorded.

Figure 4 shows the amplitude of the message in the power spectrum of the transmitter (dotted curve) and the receiver (dashed curve) for message frequencies from 2.2 to 6 GHz. Once again, the message component in the transmitter's power spectrum remains rela-

tively constant over the frequency range. However, the message amplitude in the receiver's power spectrum is not seen to peak but continues increasing up

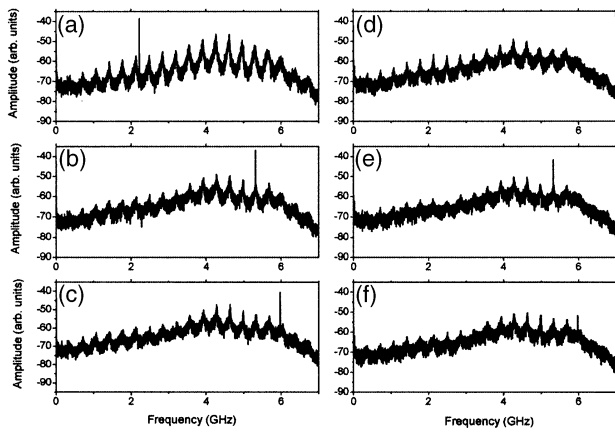


Fig. 2. (a), (b), (c) Power spectra of the transmitter for message frequencies of 2.2, 5.3, and 6 GHz; (d), (e), (f) power spectra of the receiver for message frequencies of 2.2, 5.3, and 6 GHz, respectively.

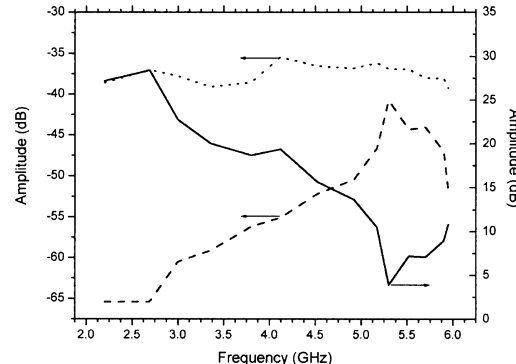


Fig. 3. Amplitude of the message in the power spectrum of the transmitter (dotted curve) and the receiver (dashed curve) and the difference between message components in the transmitter and the receiver (solid curve) for message frequencies of 2.2–6 GHz for a receiver relaxation oscillation frequency of 5.38 GHz.

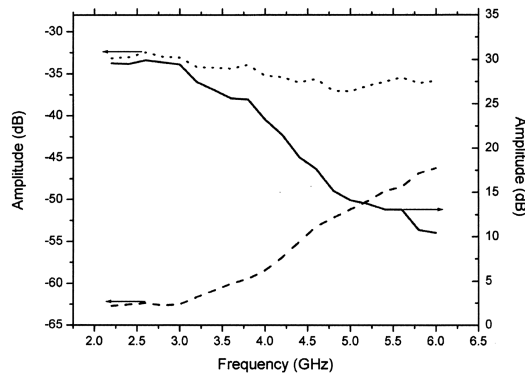


Fig. 4. Amplitude of the message in the power spectrum of the transmitter (dotted curve) and the receiver (dashed curve) and the difference between message components in the transmitter and the receiver (solid curve) for message frequencies of 2.2–6 GHz for a receiver relaxation oscillation frequency of 6.58 GHz.

to 6 GHz, the maximum frequency that could be derived from the signal generator employed. The solid curve in Fig. 4 shows that the difference between the strength of the message in the transmitter and that in the receiver decreases up to 6 GHz and appears to tend to a minimum at a relaxation oscillation frequency of 6.58 GHz.

In conclusion, we have demonstrated that the chaos pass filtering exhibited by synchronized laser diodes is frequency dependent: The closer the message frequency is to the relaxation oscillation frequency, the worse is the filtering of the message in the receiver laser. This property is expected to be highly important for the practical implementation of chaotic synchronized lasers in secure communication systems. Also, for the first time to our knowledge we have shown an opportunity for achieving message recovery at frequencies up to 6 GHz.

This research is supported by Engineering and Physical Sciences Research Council (UK) grant GR/S22936/01 and by the European Union Optical Chaos Communication Using Laser Transmitters project (IST-2000-29683). J. Paul's e-mail address is jpaul@informatics.bangor.ac.uk.

References

1. L. M. Pecora and T. L. Carroll, Phys. Rev. Lett. **64**, 821 (1990).
2. G. D. VanWiggeren and R. Roy, Science **279**, 1198 (1998).
3. S. Sivaprakasam and K. A. Shore, Opt. Lett. **24**, 1200 (1999).
4. I. Fischer, Y. Liu, and P. Davis, Phys. Rev. A **62**, 11801 (2000).
5. S. Sivaprakasam and K. A. Shore, IEEE J. Quantum Electron. **36**, 35 (2000).
6. A. Uchida, S. Yoshimori, M. Shinozuka, T. Ogawa, and F. Kannari, Opt. Lett. **26**, 866 (2001).
7. S. Tang and J. M. Liu, Opt. Lett. **26**, 1843 (2001).
8. J. Paul, S. Sivaprakasam, P. S. Spencer, P. Rees, and K. A. Shore, Electron. Lett. **38**, 28 (2002).
9. C. R. Mirasso, J. Mulet, and C. Masoller, IEEE Photon. Technol. Lett. **14**, 456 (2002).
10. T. Heil, J. Mulet, I. Fischer, C. R. Mirasso, M. Peil, P. Colet, and W. Elsässer, IEEE J. Quantum Electron. **38**, 1162 (2002).
11. J. Ohtsubo, IEEE J. Quantum Electron. **38**, 1141 (2002).
12. M. W. Lee, J. Paul, S. Sivaprakasam, and K. A. Shore, Opt. Lett. **28**, 2168 (2003).
13. J. Paul, S. Sivaprakasam, P. S. Spencer, and K. A. Shore, J. Opt. Soc. Am. B **20**, 479 (2003).
14. A. Uchida, Y. Liu, and P. Davis, IEEE J. Quantum Electron. **39**, 963 (2003).

Synchronization of chaos in unidirectionally coupled vertical-cavity surface-emitting semiconductor lasers

Yanhua Hong, Min Won Lee, Paul S. Spencer, and K. Alan Shore

School of Informatics, University of Wales, Bangor, Bangor LL57 1UT, Wales, UK

Received December 22, 2003

Synchronization of chaos is achieved experimentally in unidirectionally coupled external-cavity vertical-cavity surface-emitting semiconductor lasers operating in an open-loop regime. Synchronization is observed when the polarization of the transmitter is perpendicular to the polarization (x polarization) of the free-running receiver. The ratio of transmitter output to y -polarized receiver output power shows normal (positive-slope) synchronization. However, inverse (negative-slope) synchronization is found to arise between the transmitter output and the x -polarized receiver output power. © 2004 Optical Society of America

OCIS codes: 140.1540, 250.7260, 260.5430, 060.4510.

The use of chaos in secure communication has attracted considerable attention in recent years. The idea is to encode a message into the noiselike chaotic transmitter and then decode the message by using a receiver that is chaos-synchronized to the transmitter. Synchronization of chaotic systems has been demonstrated in Nd:YAG,¹ CO₂,² and fiber lasers³ and in distributed Bragg reflection laser diodes.⁴ Much effort has been devoted to the study of chaos synchronization and message encoding and decoding in edge-emitting semiconductor lasers.^{5–8} Vertical-cavity surface-emitting lasers (VCSELs) have many desirable characteristics, such as low threshold current, single-longitudinal operation, circular output-beam profiles, and wafer-scale integrability. It can be anticipated that, owing to the relatively low output powers of VCSELs, chaos synchronization may require operation of the lasers well above threshold. A salient feature of VCSELs is their tendency to exhibit changes in emission polarization that are due to changes, e.g., in bias current and operating temperature. Polarization effects may therefore be expected to be of some importance in VCSEL synchronization. Interest in implementing chaotic communications by using VCSELs is demonstrated by previous theoretical and experimental work performed on chaotic synchronization in VCSELs.^{9,10} Recently Fujiwara *et al.*¹⁰ reported experimental observation of chaotic synchronization in mutually coupled stand-alone VCSELs.

In this Letter we experimentally demonstrate chaos synchronization in unidirectionally coupled VCSELs. The transmitter was rendered chaotic by optical feedback, whereas the receiver was a stand-alone VCSEL. One polarization component of the transmitter was coupled into the receiver. Synchronization was observed when the polarization of the transmitter was perpendicular to the polarization (x polarization) of the free-running receiver.

The experimental arrangement is shown schematically in Fig. 1. Two commercial VCSELs (Avalon Photonics, V-850-GMP) were used, one in the transmitter and one in the receiver. Both VCSELs were driven by a low-noise current source (Profile LDC 202), and their temperatures were controlled to within 0.01 °C.

VCSEL1 was used as the transmitter. VCSEL2 was used as a receiver. The free-running threshold current (I_{th}) of VCSEL1 and VCSEL2 was 3.2 and 2.5 mA, respectively. Near threshold, VCSEL1 lased in one polarization direction (x polarization). When the current was increased to 7.25 mA, the polarization abruptly switched to orthogonal polarization (y polarization), whereas with decreasing current the polarization switched back to the x direction at 6.66 mA. This result indicates that there is a bistability regime in VCSEL1. VCSEL2 lased along one polarization direction (x polarization) near threshold and remained lasing in this direction up to a bias current of 8.7 mA. When the bias current was higher than 8.7 mA, the y -polarization component started to lase and the x -polarization component saturated. VCSEL1 was collimated by an antireflection-coated laser diode objective (Newport F-LA11). A nonpolarizing beam splitter (BS1) directed ~50% of VCSEL1's output power to a mirror (M1), which formed an external cavity. The cavity length was approximately 39 cm. The optical feedback ratio was adjusted by a variable attenuator (NDF1) such that the transmitter was rendered chaotic. A half-wave plate (HWP1) was used to adjust the polarization of the transmitter beam to ensure that only the x -polarized component

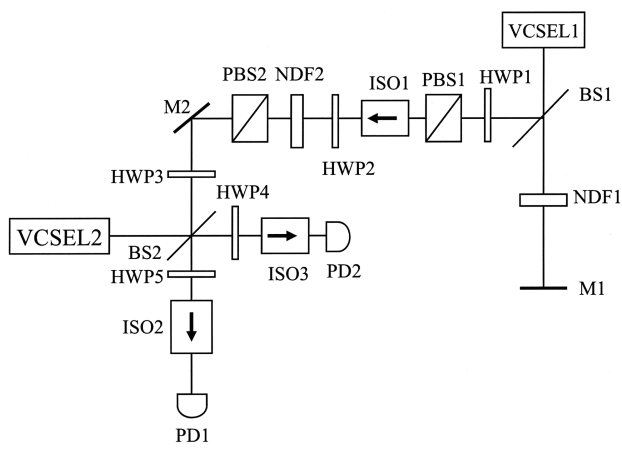


Fig. 1. Experimental setup.

was coupled into the receiver. HWP2 was used to rotate polarization of the injected beam to make the entire beam transmit through a polarizing beam splitter (PBS2). PBS2 and an isolator (ISO1) together ensured that the output from the receiver was not injected back into the transmitter; the typical isolation was -40 dB. NDF2 and HWP3 were used to change the injected power and polarization, respectively. HWP4 and HWP5 were used to direct the orthogonal polarization to a detector (PD2). ISO2 and ISO3 were used to prevent feedback of light into the VCSELs. PD1 and PD2 are two identical photodetectors (Newport Model AD-70xr) with a 6-GHz bandwidth. M2 directed the transmitter output power to BS2, which then coupled transmitter output power into both the receiver and PD1. The output power of the receiver was measured by PD2. The outputs from the photodetectors were stored in a digital oscilloscope (Tektronix TDS 7404, 4 GHz) and then acquired by a PC.

In the experiment, VCSEL1 was biased at 7.58 mA ($2.4I_{th}$). At this bias current, almost all the output power was in the y -polarized lasing mode. The lasing wavelength was 853.2 nm. We define the optical feedback ratio as the ratio of the feedback power to the free-running output power. The feedback power was measured just before the light returned to the laser diode objective (in front of the laser). When the feedback ratio was 20%, VCSEL1 exhibited large irregular fluctuations in the output power. VCSELs have feedback regimes similar to that of an edge-emitting laser,¹¹ and chaotic behavior is seen in the output power over a wide range of operating currents for longer external cavities.¹² So the large irregular fluctuation is associated with chaotic dynamics. The x -polarized component was excited and showed antiphase dynamics with the y -polarized component. Because VCSEL1 was biased at relatively higher currents,¹³ within the experimentally available feedback level VCSEL1 exhibited fully developed chaos; the low-frequency fluctuation regime was not observed. VCSEL2 was biased at 8.27 mA ($3.3I_{th}$). Most of the output power was contained in the x -polarized mode. The lasing wavelength was 853.2 nm. The x -polarized component of the transmitter was selected and rotated to y polarization and injected into receiver VCSEL2. The spectrum, output power, and dynamics of the transmitter remained unchanged when the transmitter was coupled into the receiver. The setup is thus clearly unidirectionally coupled. The ratio of the injection power to the output power of the receiver is termed the injection ratio. The injection power is measured just before the light is injected into the laser diode objective (in front of the receiver).

Figure 2 shows the time evolution of chaos synchronization when the injection ratio was $\sim 3.3\%$. Figure 2(a) shows a time trace of the injected beam and a time trace of VCSEL2 in y polarization. The time trace of the injected beam has been shifted up for clarity. These time traces show evidence of synchronization between the injected beam and the y -polarization component of VCSEL2. Figure 2(b) shows a time trace of the injected beam and a time

trace of VCSEL2 in x polarization taken at a slightly different time from those in Fig. 2(a). For clarity, the time trace of the injected beam was also shifted up. The fluctuations in the time trace of the injected beam and the VCSEL2 time trace in x polarization can be seen to be in antiphase, consistent with previous observations of antiphase dynamics of orthogonal polarizations in unstable VCSELs.^{14,15}

One can readily demonstrate synchronization by plotting the instantaneous injected power against the receiver output power at the same time. As described in many papers,^{8,10} one measures the quality of the synchronization by calculating the cross correlation between the time series of the transmitter and the receiver. Because the detector noise level was ~ 25 dB lower than the chaos signal, the detector noise level was neglected in the measurement. Figure 3(a) shows the injected power versus the y -polarization component of the receiver. It demonstrates that good synchronization was obtained between the injected beam and the y -polarization component of the receiver. The correlation coefficient was 0.844. Figure 3(b) shows the injected power as a function of the x -polarization component of the receiver. The injected power and the x -polarization component of the receiver also show reasonable synchronization; however, the gradient of the synchronization is negative. Such synchronization has been termed “inverse synchronization.”¹⁶ The absolute correlation coefficient is 0.768, which is lower than that of chaotic synchronization between the injected beam and the y -polarization component of the receiver. The reason for the better correlation between the y -polarization output power of the receiver and the injected beam is that the y -polarization mode of the receiver was locked to the transmitter’s frequency.^{17,18} x - and y -polarization components of the receiver laser show

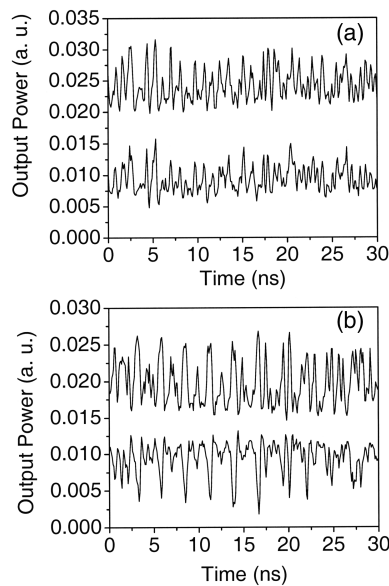


Fig. 2. Time series plots of (a) the injected beam (top trace) and the receiver output (bottom trace) in y polarization and (b) the injected beam (top trace) and the receiver output (bottom trace) in x polarization.

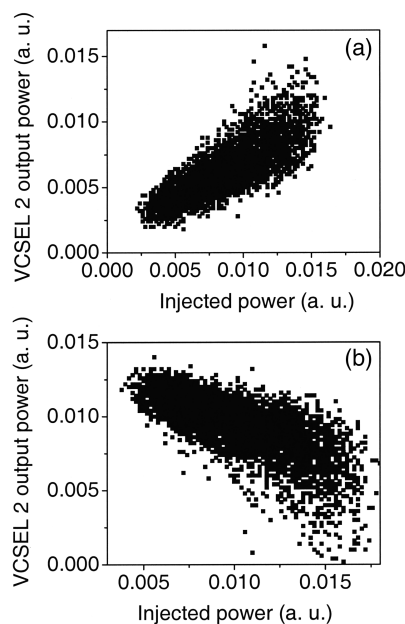


Fig. 3. Synchronization plots: (a) injected beam versus the y -polarization component of the receiver, (b) injected beam versus the x -polarization component of the receiver.

antiphase correlation with optical feedback (without optical injection from the transmitter) at 8.27-mA bias current, and antiphase dynamics of orthogonal polarizations in unstable VCSELs were previously reported.^{14,15} It is clear that the x -polarization component of the receiver and the injected beam shows inverse (negative-slope) chaos synchronization because the x -polarization component is in antiphase to the y -polarization component.

We achieved the chaos synchronization described above by adjusting the optical injection power, bias current, and VCSEL temperature. It was not necessary to adjust the position of the injected beam carefully; hence the approach is quite robust. It would, of course, be interesting to undertake detailed studies of the effects of the spatial modes on the chaos synchronization.

In conclusion, we have experimentally demonstrated, for the first time to our knowledge, synchronization of chaos in unidirectionally coupled VCSELs. In the experiment, one polarization component of the transmitter was coupled to the receiver. The polarization of the injected beam was perpendicular to that of the free-running receiver (x polarization). The injected beam and the y -polarized component of the receiver show good synchronization. The injected beam and the x -polarized component of the

receiver exhibit inverse synchronization because of the antiphase dynamics between the two orthogonal polarizations in the unstable operation regime of a VCSEL. The results presented here show the possibility of chaos communication in VCSELs, and future effort will examine the feasibility of encoding and decoding messages by use of this configuration.

This study was supported by the UK Engineering and Physical Sciences Research Council under grant GR/S22936/01 and by the European Union Optical Chaos Communication Using Laser Transmitters (OCCULT) project (grant IST-2000-29683). K. A. Shore's e-mail address is alan@informatics.bangor.ac.uk.

References

- R. Roy and K. S. Thornburg, Jr., Phys. Rev. Lett. **72**, 2009 (1994).
- T. Sugawara, M. Tachikawa, T. Tsukamoto, and T. Shimizu, Phys. Rev. Lett. **72**, 3502 (1994).
- G. D. VanWiggeren and R. Roy, Science **279**, 1198 (1998).
- J.-P. Goedgebuer, L. Larger, and H. Porte, Phys. Rev. Lett. **80**, 2249 (1998).
- S. Sivaprakasam and K. A. Shore, Opt. Lett. **24**, 1200 (1999).
- T. Heil, J. Mulet, I. Fischer, C. R. Mirasso, M. Peil, P. Colet, and W. Elsässer, IEEE J. Quantum Electron. **38**, 1162 (2002).
- J. Ohtsubo, IEEE J. Quantum Electron. **38**, 1141 (2002).
- P. Rees, P. S. Spencer, I. Pierce, S. Sivaprakasam, and K. A. Shore, Phys. Rev. A **68**, 033818 (2003).
- P. S. Spencer, C. R. Mirasso, P. Colet, and K. A. Shore, IEEE J. Quantum Electron. **34**, 1673 (1998).
- N. Fujiwara, Y. Takiguchi, and J. Ohtsubo, Opt. Lett. **28**, 1677 (2003).
- Y. C. Chung and Y. H. Lee, IEEE Photon. Technol. Lett. **3**, 597 (1991).
- P. S. Spencer, C. R. Mirasso, and K. A. Shore, IEEE Photon. Technol. Lett. **10**, 191 (1998).
- M. Sondermann, H. Bohnet, and T. Ackemann, Phys. Rev. A **67**, 021802(R) (2003).
- C. Masoller and N. B. Abraham, Phys. Rev. A **59**, 3021 (1999).
- S. Bandyopadhyay, Y. Hong, P. S. Spencer, and K. A. Shore, Opt. Commun. **202**, 145 (2002).
- S. Sivaprakasam, I. Pierce, P. Rees, P. S. Spencer, K. A. Shore, and A. Valle, Phys. Rev. A **64**, 013805 (2001).
- Z. G. Pan, S. Jiang, M. Dagenais, R. A. Morgan, K. Kojima, M. T. Asom, R. E. Leibenguth, G. D. Guth, and M. W. Focht, Appl. Phys. Lett. **63**, 2999 (1993).
- Y. Hong, K. A. Shore, A. Larsson, M. Ghisoni, and J. Halonen, IEE Proc. Optoelectron. **148**, 31 (2001).

Experimental Demonstration of VCSEL-Based Chaotic Optical Communications

Min Won Lee, Yanhua Hong, and K. Alan Shore

Abstract—Message encoding and decoding using chaotic vertical-cavity surface-emitting lasers (VCSELs) has been experimentally demonstrated. A 200-MHz message has been successfully encoded in an external-cavity VCSEL transmitter and decoded in a stand-alone VCSEL receiver. Message recovery has been achieved with 9-dB signal-to-noise ratio.

Index Terms—Chaos, cryptography, encoding, semiconductor lasers, synchronization.

VERTICAL-CAVITY surface-emitting lasers (VCSELs) subject to optical feedback exhibit some nonlinear behavior, such as transverse mode dynamics and polarization mode hopping dynamics [1]–[3], which do not arise in edge-emitting laser diodes. On the other hand, VCSELs subject to delayed optical feedback show similar sensitivity to optical injections and similar chaotic optical intensity fluctuations as found in edge-emitters [4], [5]. Recently, edge-emitting lasers diodes have been used in a number of demonstrations of optical communications based on chaotic data encryption [6]–[10]. The occurrence of chaotic dynamics in VCSELs offers potential for their use in such an application. Theoretical studies of chaos synchronization and chaos data encryption in VCSELs have been forthcoming [11]–[13], but little experimental work has been reported. A fundamental requirement for such an application is the capability to effect chaos synchronization between the transmitter and receiver of such a system. A specific feature of VCSELs which militates against an experimental demonstration of chaos synchronization is the polarization switching which may occur when VCSELs are subject to optical feedback or optical injection [14]. Recently, an experimental demonstration of the chaos synchronization of mutually coupled VCSELs was reported [15], but such a configuration does not provide the capability for chaotic optical communications. However, chaos synchronization has now been achieved experimentally using unidirectionally coupled VCSELs [16] in a configuration which allows chaotic optical data encryption to be performed. In this letter, we describe an experimental demonstration of message encoding and decoding using unidirectionally coupled chaotic VCSELs. The chaotic transmitter utilizes the polarization dynamics of a VCSEL subject to optical feedback. The receiver is a stand-alone VCSEL. A 200-MHz message is decoded when the receiver is synchronized to the chaotic transmitter.

Manuscript received February 27, 2004; revised May 27, 2004. This work was supported by the European Union OCCULT (Optical Chaos Communication Using Laser Transmitters) Project (IST-2000-29 683) and by the UK EPSRC under Grant GR/S22936/01.

The authors are with the School of Informatics, University of Wales, Bangor LL57 1UT, Wales, U.K. (e-mail: alan@informatics.bangor.ac.uk).

Digital Object Identifier 10.1109/LPT.2004.834446

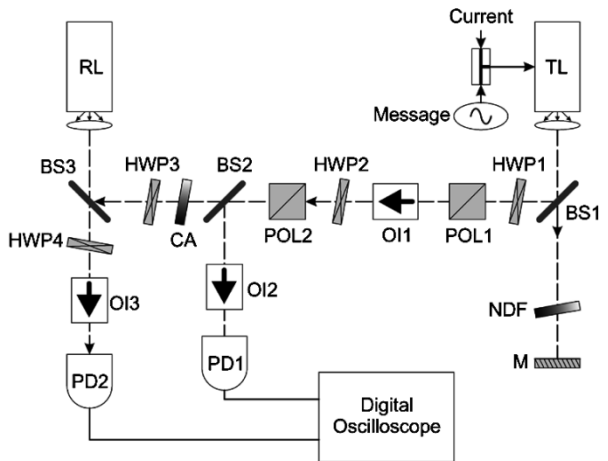


Fig. 1. Schematic diagram of the experimental setup. BS: Beam splitter. M: Mirror. OI: Optical isolator. CA: Coupling attenuator. NDF: Neutral density filter. PD: Photodetector.

The experimental setup shown in Fig. 1 uses VCSELs emitting at 850 nm as the transmitter laser (TL) and the receiver laser (RL). The TL and RL are pumped by low-noise current sources and have their temperatures stabilized at 23.1 °C and 26.2 °C, respectively, using temperature controllers with ± 0.01 °C accuracy. Because of the low power characteristics of VCSELs, the TL and RL are pumped well above threshold with drive currents of 6.73 mA ($2.1 J_{th}$, where J_{th} is the threshold current of the free-running laser) and 7.57 mA ($3.03 J_{th}$), respectively. An aspheric lens is used to collimate the VCSEL emission. The collimated beam of the TL is coupled to the receiver through beam splitters BS1 and BS3. The TL is subject to optical feedback by a mirror which forms an external cavity of length 60 cm corresponding to 4 ns roundtrip time. Using the neutral density filter, the optical feedback intensity is adjusted to around 2% of the TL output power which allows the TL to be rendered chaotic. At the bias current indicated above, the free-running TL lases in one polarization. In the chaotic regime generated by optical feedback, the TL exhibits dynamics in two orthogonal linearly polarized states, that is transverse electric (TE) and transverse magnetic (TM) dynamics. The TE emission is selected using the half-wave plate (HWP1) and the polarization beam-splitter (PBS1). The selected TE dynamics is coupled to the receiver through the isolator OI1 (−40-dB isolation), HWP2, and PBS2 which ensure unidirectional coupling. A 200-MHz sine-waveform signal which directly modulates the TL through a bias-tee is used as the message to be transmitted. The receiver consists of a stand-alone VCSEL, thus forming an open-loop configuration. A part of the transmitted signal is coupled to the RL and

the remainder is sent to the photodetector PD1 by BS2. The coupling attenuator CA is used to adjust the injection ratio to 3.3% of output power of the receiver. HWP3 is used to change the polarization of dynamics coupled to the receiver and HWP4 is used to adjust the polarization of the receiver output. ISO2 and ISO3 provide -40-dB isolation to prevent back-reflection from the photodetectors. The photodetectors PD1 and PD2 are used to detect the input and output of the receiver have 6-GHz bandwidth which potentially enables high-speed communications. The detected signals are recorded through the 20 GS/s sampling rate digital oscilloscope which provides some mathematical functions such as fast Fourier transform and subtraction.

In order to decode the message, the transmitter and receiver must be chaos synchronized. Because the VCSELs show antiphase dynamics between the TE and TM outputs [14], polarization-resolved dynamics is used here for chaos synchronization. It is noted that the use of direct modulation for message encoding can produce a perturbation which may deteriorate the chaos synchronization achieved between the transmitter and receiver in the absence of a message. At the bias current and optical feedback level given above, chaos synchronization has been successfully achieved in the presence of the message. In particular, synchronization has been achieved when HWP3 was used to rotate the transmitter's TE output which is then coupled to the RL whose free-running polarization is orthogonal to the light injected from the TL [16]. VCSELs are known to be very sensitive to optical injection whose polarization is orthogonal to that of the free-running laser. In addition, it is known that VCSELs can undergo polarization switching due to orthogonal optical injection. For parallel-polarized optical injection scheme, significantly greater optical injection power would be required to achieve polarization switching [17]. From this it is apparent that synchronization may be achieved at lower optical injection power by the use of orthogonal optical injection. This approach is, thus, used in the present experiments. When synchronized to the TL, the RL supports both TE and TM dynamics. Either of these polarizations can be selected by HWP4 and ISO3.

Fig. 2 demonstrates the achievement of chaos synchronization between the TE dynamics of the transmitter and TM dynamics of the receiver in the presence of the message. Because the output of the RL lags only by the time of flight between the TL and RL, the synchronization achieved in this experiment is generalized synchronization through injection-locking characteristics [18]. But the lag time is compensated by adjusting the PD1 distance for message decoding. Antiphase synchronization can be observed between the TE dynamics of the transmitter and receiver [16], but because of the lower quality of synchronization it is not used here for message recovery. It is pointed out that for clarity, different scales are used in Fig. 2(a) for the dynamics displayed. The upper trace corresponds to the TE dynamics of the transmitter in which the message is encoded and the lower trace corresponds to the TM dynamics of the receiver. The time traces of the both dynamics are shown in Fig. 2(a) to be well-synchronized. Fig. 2(b) shows a synchronization plot of TE dynamics of the transmitter versus TM dynamics of the receiver. In the figure, it can be seen that good chaos synchronization between the orthogonal dynamics is achieved. From the synchronized dynamics, the cross correlation is obtained as

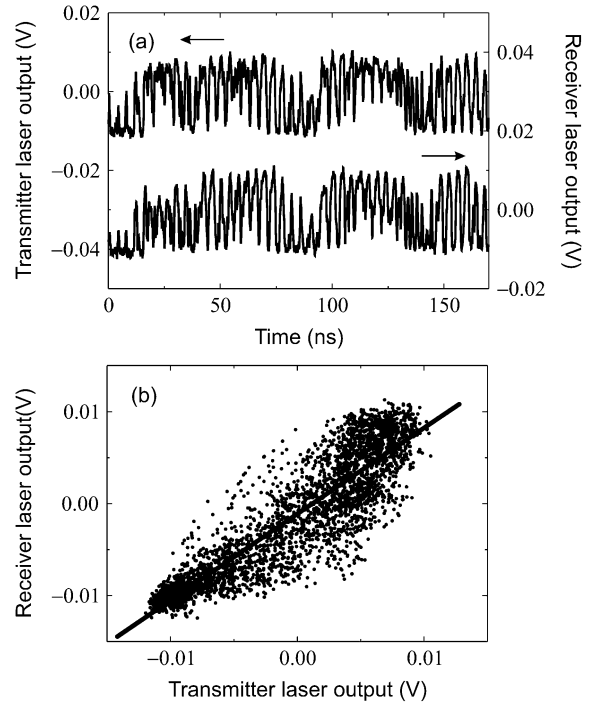


Fig. 2. (a) Time evolution of the dynamics. Upper trace: TE dynamics of the transmitter. Lower trace: TM dynamics of the receiver. (b) Synchronization plot of TE dynamics of the transmitter and TM dynamics of the receiver.

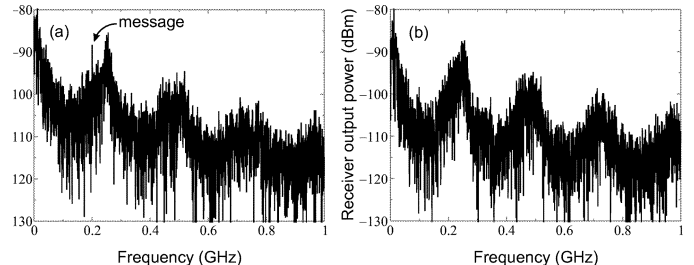


Fig. 3. (a) Power spectra of TE dynamics of the transmitter. The message is indicated at 200 MHz. (b) Power spectra of TM dynamics of the receiver.

0.84 which confirms quantitatively the quality of synchronization. This quality of synchronization is more than adequate to enable message extraction at the receiver.

The power spectra of the dynamics recorded directly by the digital oscilloscope are shown in Fig. 3. The peak-to-peak frequency is measured as around 250 MHz which corresponds to the 4-ns external-cavity roundtrip time. Fig. 3(a) exhibits the power spectra of the TE dynamics of the transmitter. From the spectral distribution in the figure, it is seen that operation occurs in a regime of chaotic dynamics with relatively limited bandwidth (\sim 300 MHz). This regime we term weakly developed chaos. Operation in this regime assists with the achievement of high quality synchronization in the presence of the message. The 200-MHz message which is indicated in Fig. 3 is shown, but the power of the message is 2.5 dB below the chaotic peak at 250 MHz. Hence, the message is encoded in the spectrum. The power spectra of the TM dynamics of the receiver are displayed in Fig. 3(b) where the presence of the message is not revealed in the spectrum. As seen in the figures, the power spectra of the TM dynamics reproduced in the receiver is similar to that of

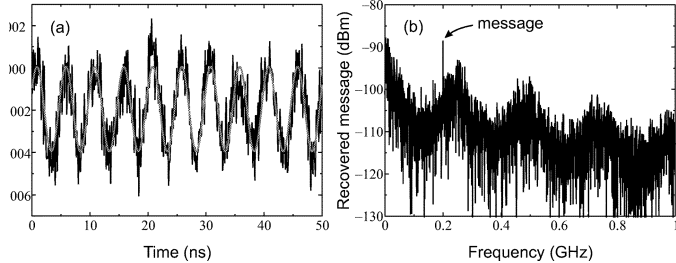


Fig. 4. Decoded message in the receiver. (a) Black trace: Decoded 200-MHz message. Gray trace: Fitted 200-MHz sine-wave signal. (b) Power spectra of decoded message. The presence of the message is clearly revealed at 200 MHz.

the TE dynamics of the transmitter. Therefore, the receiver can reproduce the chaotic carrier where the message component is much suppressed. This procedure is very important for chaotic message decoding.

The conventional decoding technique is used to extract the message in the experiment [6]–[10]. In order to decode the message, the digital oscilloscope is used to subtract the TM dynamics of the receiver from the TE dynamics of the transmitter. Fig. 4 displays the recovered message recorded directly from the oscilloscope. The recovered 200-MHz message (black trace) contains some noise in Fig. 4(a), but the sine-waveform message can be clearly seen in the figure. From the fitted sine-wave signal (gray trace), the signal-to-noise ratio is calculated as 9 dB which indicates effective message recovery. The power spectra of the recovered message in Fig. 4(b) clearly shows the message at 200 MHz, which is 5 dB higher than the chaotic peak at 250 MHz. It is apparent from Fig. 4 that the message has been extracted from the chaotic carrier. Preliminary measurements have been made of message transmission at frequencies up to a gigahertz albeit with a deterioration in the quality of the received message.

In conclusion, we have experimentally demonstrated message encoding and decoding using synchronized chaotic VCSELs. With the 200-MHz message included, synchronization has been maintained with 0.836 cross correlation. The results show efficient message encoding in the transmitter and effective message decoding in the receiver with 8.98-dB signal-to-noise ratio. It can be expected that VCSEL may also be used for high-bandwidth chaotic communications.

REFERENCES

- [1] M. S. Torre, C. Masoller, and P. Mandel, "Transverse-mode dynamics in vertical-cavity surface-emitting lasers with optical feedback," *Phys. Rev. A*, vol. 66, pp. 053 817-1–053 817-9, Nov. 2002.
- [2] M. Giudici, S. Balle, T. Ackemann, S. Barland, and J. R. Tredicce, "Polarization dynamics in vertical-cavity surface-emitting lasers with optical feedback: Experiment and model," *J. Opt. Soc. Amer. B*, vol. 16, no. 11, pp. 2114–2123, Nov. 1999.
- [3] M. Sciamanna, K. Panajotov, H. Thienpont, I. Veretennicoff, P. Mégret, and M. Blondel, "Optical feedback induces polarization mode hopping in vertical-cavity surface-emitting lasers," *Opt. Lett.*, vol. 28, no. 17, pp. 1543–1545, Sept. 2003.
- [4] S. Jiang, Z. Pan, M. Dagenais, R. A. Morgan, and K. Kojima, "Influence of external optical feedback on threshold and spectral characteristics of vertical-cavity surface-emitting lasers," *IEEE Photon. Technol. Lett.*, vol. 6, pp. 34–36, Jan. 1994.
- [5] C. Masoller and N. B. Abraham, "Low-frequency fluctuations in vertical-cavity surface-emitting semiconductor lasers with optical feedback," *Phys. Rev. A*, vol. 59, no. 4, pp. 3021–3031, Apr. 1999.
- [6] C. R. Mirasso, J. Mulet, and C. Masoller, "Chaos shift-keying encryption in chaotic external-cavity semiconductor lasers using a single-receiver scheme," *IEEE Photon. Technol. Lett.*, vol. 14, pp. 456–458, Apr. 2002.
- [7] J. Ohtsubo, "Chaos synchronization and chaotic signal masking in semiconductor lasers with optical feedback," *IEEE J. Quantum Electron.*, vol. 38, pp. 1141–1154, Sept. 2002.
- [8] T. Heil, J. Mulet, I. Fischer, C. R. Mirasso, M. Peil, P. Colet, and W. Elsäßer, "ON/OFF phase shift keying for chaos-encrypted communication using external-cavity semiconductor lasers," *IEEE J. Quantum Electron.*, vol. 38, pp. 1162–1170, Sept. 2002.
- [9] J. Paul, S. Sivaprakasam, P. S. Spencer, and K. A. Shore, "Optically modulated chaotic communication scheme with external-cavity length as a key to security," *J. Opt. Soc. Amer. B*, vol. 20, no. 3, pp. 497–503, Mar. 2003.
- [10] M. W. Lee, J. Paul, S. Sivaprakasam, and K. A. Shore, "Comparison of closed-loop and open-loop feedback schemes of message decoding using chaotic laser diodes," *Opt. Lett.*, vol. 28, no. 22, pp. 2168–2170, Nov. 2003.
- [11] P. S. Spencer, C. R. Mirasso, P. Colet, and K. A. Shore, "Modeling of optical synchronization of chaotic external-cavity VCSELs," *IEEE J. Quantum Electron.*, vol. 34, pp. 1673–1679, Sept. 1998.
- [12] S. F. Yu, P. Shum, and N. Q. Ngo, "Performance of optical chaotic communication systems using multimode vertical cavity surface emitting lasers," *Opt. Commun.*, vol. 200, pp. 143–152, Dec. 2001.
- [13] A. Scire, J. Mulet, C. R. Mirasso, J. Danckaert, and M. San Miguel, "Polarization message encoding through vectorial chaos synchronization in vertical-cavity surface-emitting lasers," *Phys. Rev. Lett.*, vol. 90, no. 11, pp. 113 901-1–113 901-4, Mar. 2003.
- [14] S. Bandyopadhyay, Y. Hong, P. S. Spencer, and K. A. Shore, "Experimental observation of anti-phase polarization dynamics in VCSELs," *Opt. Commun.*, vol. 202, pp. 145–154, Feb. 2002.
- [15] N. Fujiwara, Y. Takiguchi, and J. Ohtsubo, "Observation of the synchronization of chaos in mutually injected vertical-cavity surface-emitting semiconductor lasers," *Opt. Lett.*, vol. 28, no. 18, pp. 1677–1679, Sept. 2003.
- [16] Y. Hong, M. W. Lee, P. S. Spencer, and K. A. Shore, "Synchronization of chaos in unidirectionally coupled vertical-cavity surface-emitting semiconductor lasers," *Opt. Lett.*, vol. 29, no. 11, pp. 1215–1217, June 2004.
- [17] Y. Hong, K. A. Shore, A. Larsson, M. Ghisoni, and J. Halonen, "Polarization switching in a vertical cavity surface emitting semiconductor laser by frequency detuning," in *Proc. Inst. Elect. Eng. Optoelectron.*, vol. 148, Feb. 2001, pp. 31–34.
- [18] Y. Liu, P. Davis, Y. Takiguchi, T. Aida, S. Saito, and J.-M. Liu, "Injection locking and synchronization of periodic and chaotic signals in semiconductor lasers," *IEEE J. Quantum Electron.*, vol. 39, pp. 269–278, Feb. 2003.

Observation of cascade complete-chaos synchronization with zero time lag in laser diodes

Min Won Lee, Jon Paul, Cristina Masoller, and K. Alan Shore

School of Informatics, University of Wales, Bangor, Dean Street, Bangor LL57 1UT, Wales, United Kingdom, and Departament de Fisica i Enginyeria Nuclear, Universitat Politècnica de Catalunya, Colom 11, E-08222 Terrassa, Barcelona, Spain

Received June 22, 2005; revised November 11, 2005; accepted November 28, 2005; posted December 8, 2005 (Doc. ID 62926)

This paper reports the first experimental observation and theoretical description of zero time lag, complete-chaos synchronization using three laser diodes coupled in a unidirectional cascade configuration. The master laser is rendered chaotic by optical feedback from an external mirror. The output intensity of the master laser is injected into an intermediate laser, and the output intensity of this intermediate laser is in turn injected into a slave laser. The distances between the lasers are carefully adjusted such that the times of flight between the lasers are equal to the delay time in the external-cavity of the master laser. When the three lasers are subject to the same optical injection strength it is observed that their output intensities synchronize with zero time lag. The chaos synchronization has been confirmed by time traces and synchronization diagrams of the three laser outputs, and the null lag time has been measured from cross-correlation diagrams. Numerical simulations based on single-mode rate equations are in good qualitative agreement with the experimental observations. © 2006 Optical Society of America

OCIS codes: 140.1540, 060.4510, 140.5960.

1. INTRODUCTION

Chaos synchronization has received much attention since the pioneering work of Pecora and Carroll,¹ with particular emphasis being given to the implementation of chaotic data encryption. A large number of encryption schemes using optical systems have been reported, with efficient message encoding and decoding having been achieved.^{2–10} There have been extensive studies of synchronization of coupled chaotic oscillators; see, e.g., Refs. 11 and 12. The present work acts to develop concepts from both of these fields.

Because of their nonlinear response and ease of operation, the synchronization of semiconductor lasers subject to optical feedback has been given particular attention¹³, with novel forms of chaos synchronization in unidirectionally coupled semiconductor lasers having been investigated. These include anticipating synchronization^{14,15}, dual synchronization^{16,17}, synchronization in a phase-locking scheme,¹⁸ and two-mode synchronization.¹⁹ Chaos synchronization has also been achieved in mutually coupled semiconductor lasers.^{20–22} It was recently experimentally demonstrated that vertical-cavity surface-emitting lasers can also be synchronized in both mutual²³ and unidirectional coupling configurations.²⁴

Semiconductor lasers subject to optical feedback can exhibit two different regimes of chaos synchronization, referred to as complete synchronization and generalized synchronization. These regimes can be distinguished by the lag time between the outputs of the synchronized lasers.^{25–27} In complete synchronization the lag time $\Delta\tau$ between the lasers is equal to the difference between the time of flight τ_c from the master laser to the slave laser and the round-trip time τ in the external cavity of the master laser ($\Delta\tau = \tau_c - \tau$).²⁸ The achievement of complete

synchronization requires two similar lasers operating under similar conditions. The other regime of synchronization is termed generalized synchronization. Such synchronization is more robust to parameter mismatches between the lasers and can be achieved by injection locking using strong optical injection²⁹ or via optical frequency detuning.^{30,31} In this regime the slave laser follows the dynamics of the master laser with a lag time equal to the time of flight ($\Delta\tau = \tau_c$).

In this paper we demonstrate complete synchronization with zero time lag using three unidirectionally cascade-coupled distributed feedback (DFB) lasers for the first time. The lasers are termed master, intermediate, and slave lasers. The master laser is subject to optical feedback from an external-cavity mirror, whereas the intermediate and slave lasers are stand-alone lasers (open-loop configuration).^{32,33}

Complete synchronization has been widely studied in master–slave configurations, but no previous report has been made of complete synchronization using a cascade-coupled laser configuration. Generalized synchronization would be expected when a stand-alone intermediate laser and a stand-alone slave laser are coupled in a three-laser configuration. However, within the operating parameters that are required to effect generalized synchronization, there is a narrow window of operating parameters that can induce the intermediate and slave lasers to achieve complete synchronization, as has been demonstrated in the present work. The operating requirements to access this window are that the master feedback strength matches the injection strength of the master to the intermediate laser, and matches the injection strength of the intermediate laser to the slave.

We have also demonstrated, for the first time to our

knowledge, zero-time-lag synchronization between the three lasers. When the intermediate laser is synchronized with the master laser, the dynamics of the intermediate laser is the same as that of an external-cavity laser with delay time τ , and therefore, in general the slave laser synchronizes with a lag time of $\tau_{c2} - \tau$ (τ_{c2} is the time of flight between the intermediate and slave lasers). In the present system, we consider a specific setup in which the flight time from the master to the intermediate laser, τ_{c1} , and the flight time from the intermediate laser to the slave, τ_{c2} , match the round-trip time τ of the master external cavity. For this case the time lag is zero. It is pointed out that in generalized synchronization, zero time lag between the lasers cannot be achieved. Therefore the presence of zero time lag gives further confirmation that complete synchronization has been achieved.

As such, this is the first report of complete synchronization of three lasers and also the first demonstration of three lasers synchronized with zero time lag in a cascade-coupled configuration. The synchronization of three cascade-coupled lasers was demonstrated previously³⁴ and was used to extract messages in wavelength-multiplexed chaotic communications.³⁵ However, in those demonstrations the observed lag time between any two lasers was equal to the corresponding time of flight, and therefore the observed behavior was generalized, not complete synchronization.

This paper is organized as follows. Section 2 describes the experimental setup. Section 3 presents the experimental results on cascaded synchronization without time lag between three laser diodes. Section 4 presents the theoretical model used for the numerical simulations, which are presented in Section 5. Finally, Section 6 provides a summary of the results and the conclusion from the work.

2. EXPERIMENTAL SETUP

Figure 1 depicts schematically the experimental setup in which three DFB lasers are used as the master laser (ML), the intermediate laser (IL), and the slave laser (SL). The emission of each laser is collimated by an aspheric lens. The mirror M1 forms for the ML an external

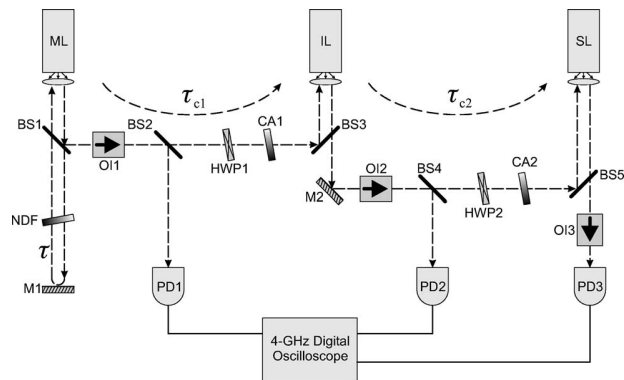


Fig. 1. Schematic diagram of the experimental setup. ML, master laser; IL, intermediate laser; SL, slave laser; τ , external-cavity round-trip time of the ML; τ_{c1} , time of flight of ML-IL; τ_{c2} , time of flight of IL-SL; BS, beam splitter; NDF, neutral density filter; M, mirror; OI, optical isolator; CA, coupling attenuator; HWP, half-wave plate; PD, photodetector.

cavity with 42 cm length that gives a round-trip time of $\tau = 2.8$ ns. The neutral density filter NDF is used to vary the optical feedback ratio so that the ML is rendered chaotic. The ML is coupled to the IL through the beam splitters BS1 and BS3, and the IL is coupled to the SL through M2 and BS5. By these means, the lasers are coupled in a cascade configuration. The unidirectional coupling between the lasers is ensured by the optical isolators OI1 and OI2, which each provide -33 dB isolation. The half-wave plates HWP1 and HWP2 are used to adjust the polarization of coupling light with respect to the polarization of coupling laser emission. The coupling attenuators CA1 and CA2 are used to adjust the coupling ratios between the ML and IL and between the IL and SL, respectively. The isolator OI3 prevents back reflection from the photodetector PD3. The output of each laser is detected by 12 GHz bandwidth photodetectors PD1, PD2, and PD3 through BS2, BS4, and BS5, respectively. The photodetectors are all positioned at the same distance (73 cm) from the corresponding laser to ensure a zero lag time. The outputs of the photodetectors are recorded with a 4 GHz bandwidth digital oscilloscope with 10 GS/s sampling rate.

To observe complete chaos synchronization between the three lasers, two conditions need to be satisfied. First, the optical frequencies of the lasers have to be identical. The lasers used for the experiment are driven by low noise current sources, and the bias currents are set as $J_M = 30.73$ mA, $J_I = 31.6$ mA, and $J_S = 34.7$ mA (corresponding to $2.34J_{th}$, $2.40J_{th}$, and $2.68J_{th}$ respectively, where J_{th} is the threshold current of the free-running laser). The temperatures of the ML (28.55°C), IL (24.8°C), and SL (24.23°C) are controlled with an accuracy of $\pm 0.01^\circ\text{C}$. For these operating parameters, the lasers support single-mode emission at a wavelength of 1549.02 nm with 40 dB side-mode suppression.

Secondly, the coupling ratios between the ML and the IL and between the IL and the SL have to be the same as the optical-feedback ratio of the ML. In the present experiment the optical-feedback ratio is adjusted to 2.4% of the ML output power, and suitably the optical injection ratios are adjusted to 2.4%.

In order to observe zero-time-lag synchronization regime, a third condition must be met; the time of flight τ_{c1} from the ML to the IL and the time of flight τ_{c2} from the IL to the SL must be the same as the external cavity round-trip time τ . In the experimental setup the distances between the ML and the IL and between the IL and the SL are set as 84 cm, which is twice the external cavity length. This gives $\tau_{c1} = \tau_{c2} = \tau = 2.8$ ns.

3. EXPERIMENTAL RESULTS

Figure 2 displays the waveforms of the chaotic outputs of the three lasers in the complete synchronization regime. The waveforms have been recorded with 1000 data points with a 10 ns time interval. For clarity, the time traces of the IL and the SL are displaced; the upper trace is the output of the ML, the middle trace is the output of the IL, and the lower trace is the output of the SL. The waveforms are seen to be synchronized, and the time shift between them is zero.

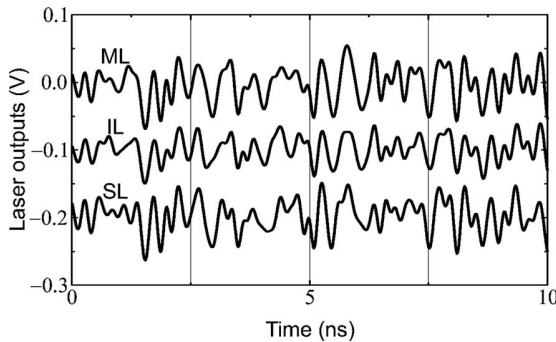


Fig. 2. Experimental time series of the synchronized chaotic laser outputs.

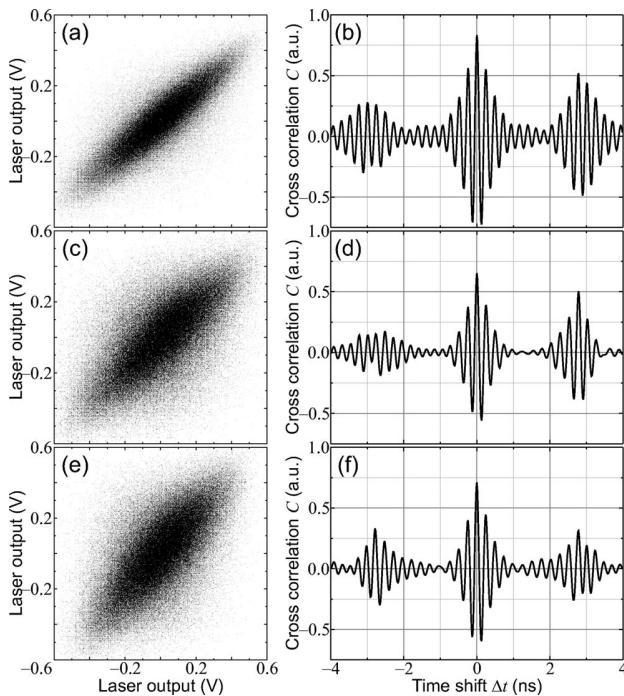


Fig. 3. Experimental results. Synchronization diagram (a) of the ML versus the IL, (c) of the ML versus the SL, and (e) of the IL versus the SL; cross-correlation diagram (b) of the ML and the IL, (d) of the ML and the SL, and (f) of the IL and the SL.

The quality of chaos synchronization and the lag time between the waveforms of any two lasers can be quantified by the synchronization diagram and the maximum of the cross-correlation coefficient $C(\Delta t)$. Figure 3 displays results when zero-time-lag synchronization is achieved. The synchronization diagrams were obtained from the time traces recorded with 200 000 data points spanning a 4 μ s time interval. $C(\Delta t)$ was obtained by calculating the correlation coefficient between the outputs of two lasers when the output of one laser is continuously shifted an amount Δt with respect to the output of the other laser (time traces with 25 000 data points spanning a 400 ns time interval were used).³¹ The function $C(\Delta t)$ reveals the internal periodicity of the waveforms; the periodicity at the relaxation oscillation period corresponds to the time interval between two consecutive peaks of $C(\Delta t)$, and the periodicity at the external-cavity delay time corresponds to the time interval between two consecutive envelope peaks of $C(\Delta t)$.

The time lag $\Delta\tau$ between two lasers is measured by the time shift Δt at which the cross-correlation coefficient is maximum. If the lasers are in complete synchronization, the maximum coefficient occurs at $\Delta t = \tau_c - \tau = 0$. On the other hand, if the lasers are in generalized synchronization, the maximum coefficient occurs at $\Delta t = \tau_c = 2.8$ ns.

The synchronization diagram of the ML versus the IL is displayed in Fig. 3(a), from which it can be seen that good quality synchronization is achieved. In Fig. 3(b) $C(\Delta t)$ is shown to peak at $\Delta t = 0$ [this peak is dominant compared to the subpeaks at $\Delta t = \pm 2.8$ ns; the maximum cross-correlation coefficient is $C(0) = 0.83$]. This proves that the ML and the IL are synchronized with zero time lag, i.e., with no lag time between them.

The synchronization diagram of the ML versus the SL is displayed in Fig. 3(c). The degree of synchronization is reduced compared with Fig. 3(a), but it can clearly be seen that the lasers are synchronized. The cross-correlation diagram [Fig. 3(d)] has a dominant peak at $\Delta t = 0$ [the maximum coefficient is $C(0) = 0.65$], which proves that the ML and the SL are also synchronized without a lag time.

The synchronization diagram of the IL versus the SL is displayed in Fig. 3(e). From this figure it can be seen that good quality synchronization is also achieved. The cross-correlation coefficient displayed in Fig. 3(f) also peaks at $\Delta t = 0$ [the maximum coefficient is $C(0) = 0.71$], which indicates again good synchronization without lag time.

4. MODEL

In this section we present the theoretical model used to describe the above experimental findings. Each laser is modeled using single-mode rate equations. The equations for the ML include a delayed term for optical feedback, the equations for the IL include a term representing optical injection from the ML, and the equations for the SL include a term representing optical injection from the IL. The equations are

$$\begin{aligned} \dot{E}_M &= k(1+j\alpha)(N_M - 1)E_M + \gamma_T E_M(t - \tau) \exp(-i\omega_0\tau) \\ &\quad + \sqrt{D}\xi_M(t), \end{aligned} \quad (1)$$

$$\dot{N}_M = \gamma_n(J - N_M - N_M|E_M|^2), \quad (2)$$

$$\begin{aligned} \dot{E}_I &= k(1+j\alpha)(N_I - 1)E_I + \gamma_I E_M(t - \tau_{c1}) \exp(-i\omega_0\tau_{c1}) \\ &\quad + \sqrt{D}\xi_I(t), \end{aligned} \quad (3)$$

$$\dot{N}_I = \gamma_n(J - N_I - N_I|E_I|^2), \quad (4)$$

$$\begin{aligned} \dot{E}_S &= k(1+j\alpha)(N_S - 1)E_S, \\ &\quad + \gamma_R E_I(t - \tau_{c2}) \exp(-i\omega_0\tau_{c2}) + \sqrt{D}\xi_S(t) \end{aligned} \quad (5)$$

$$\dot{N}_S = \gamma_n(J - N_S - N_S|E_S|^2). \quad (6)$$

Here E_M , E_I , and E_S (N_M , N_I , and N_S) are the slowly varying complex amplitudes (carrier densities) of the master, intermediate, and slave lasers, respectively. The lasers

are assumed to have identical free-running optical frequency (ω_0) and parameters; k is the cavity loss, α is the linewidth enhancement factor, D is the spontaneous emission noise intensity, ξ is a Gaussian white noise, γ_n is the inverse carrier lifetime and J is the normalized injection current ($J_{th}=1$). γ_M is the feedback strength, and γ_I and γ_S are the injection strengths.

It can be observed from Eqs. (1)–(6) that when $\gamma_M=\gamma_I=\gamma_S$ and $D=0$ the lasers can be synchronized with the slowly varying complex amplitudes related as

$$E_I(t-\tau)\exp(-i\omega_0\tau)=E_M(t-\tau_{c1})\exp(-i\omega_0\tau_{c1}), \quad (7)$$

$$E_S(t-\tau)\exp(-i\omega_0\tau)=E_I(t-\tau_{c2})\exp(-i\omega_0\tau_{c2}) \quad (8)$$

and the output intensities related by

$$I_S(t)=I_I(t-\tau_{c2}+\tau)=I_M(t+2\tau-\tau_{c1}-\tau_{c2}). \quad (9)$$

In particular, when $\tau_{c1}=\tau_{c2}=\tau$ the intensities are synchronized without a lag time.

In generalized synchronization the output intensities of the lasers are related by the usual lag times, which are the flight times between them:

$$I_M(t)=a_1I_I(t+\tau_{c1}), \quad I_I(t)=a_2I_S(t+\tau_{c2}), \quad (10)$$

Since the lasers are identical, $a_1=a_2=a$; an approximated analytical expression for the coefficient a was given in Eq. (10) of Ref. 36.

In Section 5 we show that, in spite of the important simplifications of the model (which neglects the detailed feedback geometry of the DFB grating and the nonlinear gain saturation due to spatial and spectral hole burning), the simulations from this model are in good qualitative agreement with the experimental observations.

5. NUMERICAL RESULTS

The equations are simulated with the parameters $k=600$ ns $^{-1}$, $\gamma_n=1$ ns $^{-1}$, $\alpha=3$, $\tau_{c1}=\tau_{c2}=\tau=3$ ns, $\omega_0\tau=0$ rad, $J=2.4$, and $D=10^{-5}$ ns $^{-1}$. With 5 ps time integration step, time traces are obtained as output intensities of the lasers ($I_{M,I,S}=|E_{M,I,S}|^2$). A digital low-pass filter is applied to the intensity time series to simulate the 4 GHz bandwidth recording. The correlation functions are calculated using time series spanning 1 μ s.

Figure 4 displays results when the master laser exhibits its weakly developed chaos ($\gamma_M=50$ ns $^{-1}$), and the injection parameters satisfy the complete synchronization condition ($\gamma_M=\gamma_I=\gamma_S$). The synchronization diagrams and cross-correlation plots show features remarkably similar to the experimental observations. In the three cross-correlation plots the peak at $\Delta t=0$ is dominant with respect to the peaks at $\Delta t=\pm 3$ ns. The maximum cross-correlation coefficient is, for the ML–IL $C(0)=0.94$; for the ML–SL $C(0)=0.8$, and for the IL–SL $C(0)=0.78$.

Figure 5 displays the chaotic waveforms of the ML (upper trace), the IL (middle trace), and the SL (lower trace). Zero time lag synchronized chaotic oscillations are clearly observed.

The numerical simulations indicate that the complete synchronization solution of the three lasers is stable both in the parameter region, where the master laser exhibits

weakly developed chaos, and in the parameter region, where it exhibits so-called low-frequency fluctuations (which case is not presented here).

For comparison, the optical injection strengths of the IL and the SL are much larger than the feedback strength of the ML ($\gamma_I=\gamma_S=8\gamma_M=400$ ns $^{-1}$; other parameters as in Fig. 4). In Fig. 6 generalized synchronization is achieved with time lags. In obtaining Figs. 6(a), 6(c), and 6(e), the time lags between the lasers have been taken into account. In Figs. 6(b), 6(d), and 6(f), the dominant peak in the cross-correlation diagrams occurs at $\Delta t=3$ ns [$C(3)=0.96$] for the ML–IL; $\Delta t=6$ ns [$C(6)=0.86$] for the ML–SL; $\Delta t=3$ ns [$C(3)=0.95$] for the IL–SL.

Figure 7 displays the numerically simulated intensity time traces in generalized synchronization regime. As in

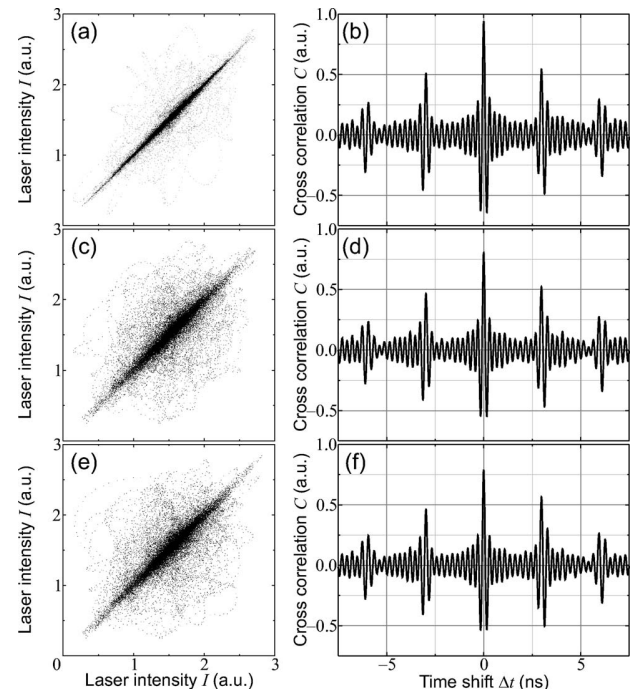


Fig. 4. Numerical results for parameters such that $\gamma_M=\gamma_I=\gamma_S=50$ ns $^{-1}$. (a) Synchronization diagram of the master laser versus the intermediate laser, (b) the corresponding cross-correlation diagram as a function of time shift Δt , (c) the synchronization diagram of the master laser versus the slave laser, (d) the corresponding cross-correlation diagram, (e) the synchronization diagram of the intermediate laser versus the slave laser, and (f) the corresponding cross-correlation diagram.

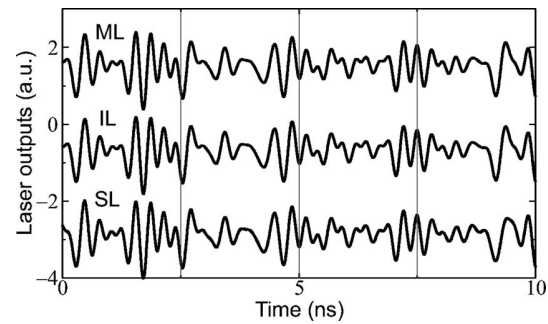


Fig. 5. Numerically simulated output intensities in complete synchronization (parameters as in Fig. 4).

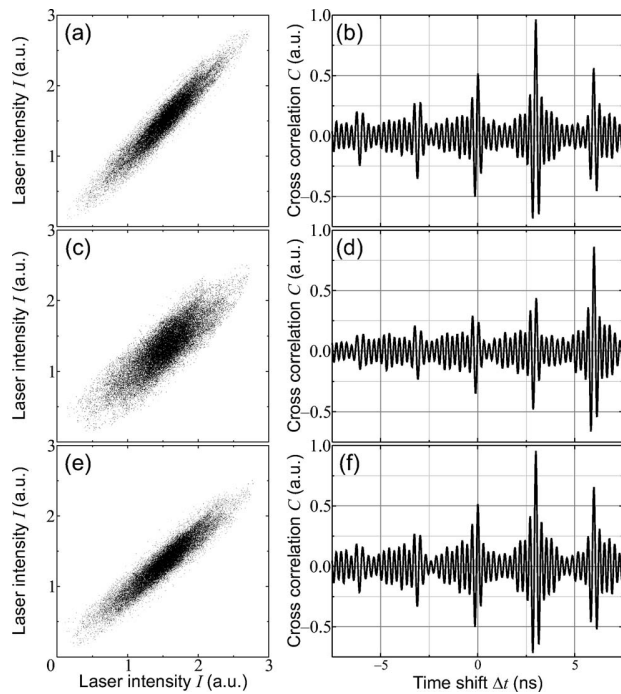


Fig. 6. Results of numerical simulations with parameters corresponding to generalized synchronization ($\gamma_T=50 \text{ ns}^{-1}$, $\gamma_I=\gamma_R=400 \text{ ns}^{-1}$). Synchronization diagram (a) of the ML versus the IL, (c) of the ML versus the SL, and (e) of the IL versus the SL; cross-correlation diagram (b) of the ML and the IL, (d) of the ML and the SL, and (f) of the IL and the SL.

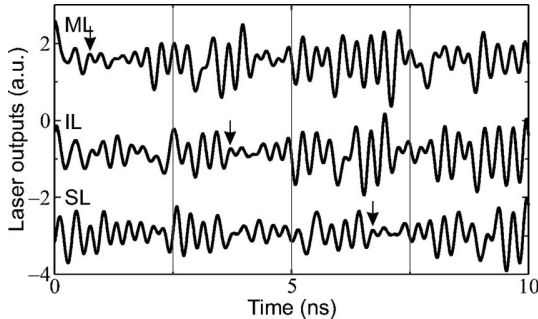


Fig. 7. Numerically simulated output intensities in the generalized synchronization regime (parameters as in Fig. 6). The arrows indicate the lag times between the synchronized intensities.

Fig. 2, the time traces of the IL and the SL are displaced for clarity (the arrows indicate the synchronization lag points). It is observed that the chaotic oscillations are synchronized with lag times corresponding to the flight times $\tau_{c1}=\tau_{c2}=3 \text{ ns}$.

6. CONCLUSIONS

We have studied experimentally and theoretically zero-time-lag synchronization of three DFB lasers in a unidirectional cascade configuration. We have considered a setup consisting of a master laser that is subject to optical feedback, an intermediate laser that is subject only to optical injection from the master, and a slave laser that is subject only to optical injection from the intermediate laser. From this we have demonstrated, for the first time to

our knowledge, complete chaos synchronization of the three lasers without a time lag. For such synchronization, three conditions have to be satisfied. (1) The lasers need to operate at the same wavelength. (2) The optical feedback rate of the master laser should be equal to the optical injection rates of the intermediate and slave lasers. (3) The flight times of master–intermediate laser and the intermediate–slave laser need to match the delay time of the master external cavity.

The cross-correlation diagrams have shown that the three lasers are in complete synchronization with the maximum cross-correlation coefficient for zero time lag. Based on a simple model for three coupled single-mode lasers, the experimental findings have been qualitatively well reproduced theoretically. The proposed scheme can also be employed to synchronize with zero time lag any number of slave systems to a master system that has a time delay, as long as the time of flight between each system is equal to the master delay time.

ACKNOWLEDGMENTS

The work is supported by the European Union OCCULT (Optical Chaos Communication Using Laser Transmitters) project (IST-2000-29683) and EPSRC (Engineering and Physical Sciences Research Council) project (GR/S78650/01). C. Masoller acknowledges support from the “Ramon y Cajal” Program (Spain).

M. W. Lee is the corresponding author and can be reached via e-mail at minlee@informatics.bangor.ac.uk.

REFERENCES

1. L. M. Pecora and T. L. Carroll, “Synchronization in chaotic systems,” *Phys. Rev. Lett.* **64**, 821–824 (1990).
2. I. Fischer, Y. Liu, and P. Davis, “Synchronization of chaotic semiconductor laser dynamics on sub-ns timescales and its potential for chaos communication,” *Phys. Rev. A* **62**, 801–4 (2000).
3. A. Uchida, S. Yoshimori, M. Shinozuka, T. Ogawa, and F. Kannari, “Chaotic on–off keying for secure communications,” *Opt. Lett.* **26**, 866–868 (2001).
4. S. Tang and J.-M. Liu, “Message encoding–decoding at 2.5 Gbits/s through synchronization of chaotic pulsing semiconductor lasers,” *Opt. Lett.* **26**, 1843–1845 (2001).
5. J.-B. Cuenot, L. Larger, J.-P. Goedgebuer, and W. T. Rhodes, “Chaos shift keying with an optoelectronic encryption system using chaos in wavelength,” *IEEE J. Quantum Electron.* **37**, 849–855 (2001).
6. C. R. Mirasso, J. Mulet, and C. Masoller, “Chaos shift-keying encryption in chaotic external-cavity semiconductor lasers using a single-receiver scheme,” *IEEE Photonics Technol. Lett.* **14**, 456–458 (2002).
7. T. Heil, J. Mulet, I. Fischer, C. R. Mirasso, M. Peil, P. Colet, and W. Elsäßer, “ON/OFF phase shift keying for chaos-encrypted communication using external-cavity semiconductor lasers,” *IEEE J. Quantum Electron.* **38**, 1162–1170 (2002).
8. J. Paul, S. Sivaprakasam, P. S. Spencer, and K. A. Shore, “Optically modulated chaotic communication scheme with external-cavity length as a key to security,” *J. Opt. Soc. Am. B* **20**, 497–503 (2003).
9. M. W. Lee, L. Larger, and J.-P. Goedgebuer, “Transmission system using chaotic delays between lightwaves,” *IEEE J. Quantum Electron.* **39**, 931–935 (2003).
10. J. Paul, M. W. Lee, and K. A. Shore, “3.5-GHz signal transmission in an all-optical chaotic communication

- scheme using 1550-nm diode lasers," *IEEE Photonics Technol. Lett.* **17**, 920–922 (2005).
11. M. G. Rosenblum, A. S. Pikovsky, and J. Kurths, "From phase to lag synchronization in coupled chaotic oscillators," *Phys. Rev. Lett.* **78**, 4193–4196 (1997).
 12. D. J. DeShazer, R. Breban, E. Ott, and R. Roy, "Detecting phase synchronization in a chaotic laser array," *Phys. Rev. Lett.* **87**, 044–101 (2001).
 13. S. Sivaprakasam and K. A. Shore, "Demonstration of optical synchronization of chaotic external-cavity laser diodes," *Opt. Lett.* **24**, 466–468 (1999).
 14. C. Masoller, "Anticipation in the synchronization of chaotic semiconductor lasers with optical feedback," *Phys. Rev. Lett.* **86**, 2782–2785 (2001).
 15. S. Tang and J.-M. Liu, "Experimental verification of anticipated and retarded synchronization in chaotic semiconductor lasers," *Phys. Rev. Lett.* **90**, 101–1–4 (2003).
 16. Y. Liu and P. Davis, "Dual synchronization of chaos," *Phys. Rev. E* **61**, R2176–R2179 (2000).
 17. A. Uchida, S. Kinugawa, T. Matsuura, and S. Yoshimori, "Dual synchronization of chaos in one-way coupled microchip lasers," *Phys. Rev. E* **67**, 220–1–8 (2003).
 18. A. Murakami, "Phase locking and chaos synchronization in injection-locked semiconductor lasers," *IEEE J. Quantum Electron.* **39**, 438–447 (2003).
 19. M. W. Lee and K. A. Shore, "Two-mode chaos synchronization using a multi-mode external-cavity laser diode and two single-mode laser diodes," *J. Lightwave Technol.* **23**, 1068–1073 (2005).
 20. J. Mulet, C. Masoller, and C. R. Mirasso, "Modeling bidirectionally coupled single-mode semiconductor lasers," *Phys. Rev. A* **65**, 815–1–12 (2002).
 21. J. M. Buldú, R. Vicente, T. Pérez, C. R. Mirasso, M. C. Torrent, and J. García-Ojalvo, "Periodic entrainment of power dropouts in mutually coupled semiconductor lasers," *Appl. Phys. Lett.* **81**, 5105–5107 (2002).
 22. T. Heil, I. Fischer, W. Elsäßer, J. Mulet, and C. R. Mirasso, "Chaos synchronization and spontaneous symmetry-breaking in symmetrically delay-coupled semiconductor lasers," *Phys. Rev. Lett.* **86**, 795–798 (2001).
 23. N. Fujiwara, Y. Takiguchi, and J. Ohtsubo, "Observation of the synchronization of chaos in mutually injected vertical-cavity surface-emitting semiconductor lasers," *Opt. Lett.* **28**, 1677–1679 (2003).
 24. Y. Hong, M. W. Lee, P. S. Spencer, and K. A. Shore, "Synchronization of chaos in unidirectionally coupled vertical-cavity surface-emitting semiconductor lasers," *Opt. Lett.* **29**, 1215–1217 (2004).
 25. I. V. Koryukin and P. Mandel, "Two regimes of synchronization in unidirectionally coupled semiconductor lasers," *Phys. Rev. E* **65**, 201–1–5 (2002).
 26. A. Locquet, C. Masoller, and C. R. Mirasso, "Synchronization regimes of optical-feedback-induced chaos in unidirectionally coupled semiconductor lasers," *Phys. Rev. E* **65**, 205–1–12 (2002).
 27. A. Uchida, N. Shibusaki, S. Nogawa, and S. Yoshimori, "Transient characteristics of chaos synchronization in a semiconductor laser subject to optical feedback," *Phys. Rev. E* **69**, 201–1–9 (2004).
 28. Y. Liu, Y. Takiguchi, P. Davis, T. Aida, S. Saito, and J.-M. Liu, "Experimental observation of complete chaos synchronization in semiconductor lasers," *Appl. Phys. Lett.* **80**, 4306–4308 (2002).
 29. Y. Liu, P. Davis, Y. Takiguchi, T. Aida, S. Saito, and J.-M. Liu, "Injection locking and synchronization of periodic and chaotic signals in semiconductor lasers," *IEEE J. Quantum Electron.* **39**, 269–278 (2003).
 30. A. Murakami and J. Ohtsubo, "Synchronization of feedback-induced chaos in semiconductor lasers by optical injection," *Phys. Rev. A* **65**, 826–1–7 (2002).
 31. M. W. Lee, J. Paul, I. Pierce, and K. A. Shore, "Frequency-detuned synchronization switching in chaotic DFB laser diodes," *IEEE J. Quantum Electron.* **41**, 302–307 (2005).
 32. R. Vicente, T. Pérez, and C. R. Mirasso, "Open-versus closed-loop performance of synchronized chaotic external-cavity semiconductor lasers," *IEEE J. Quantum Electron.* **38**, 1197–1204 (2002).
 33. M. W. Lee, J. Paul, S. Sivaprakasam, and K. A. Shore, "Comparison of closed-loop and open-loop feedback schemes of message decoding using chaotic laser diodes," *Opt. Lett.* **28**, 2168–2170 (2003).
 34. S. Sivaprakasam and K. A. Shore, "Cascaded synchronization of external-cavity laser diodes," *Opt. Lett.* **26**, 253–255 (2001).
 35. J. Paul, S. Sivaprakasam, and K. A. Shore, "Dual-channel chaotic optical communications using external-cavity semiconductor lasers," *J. Opt. Soc. Am. B* **21**, 514–521 (2004).
 36. J. Revuelta, C. R. Mirasso, P. Colet, and L. Pesquera, "Criteria for synchronization of coupled chaotic external-cavity semiconductor lasers," *IEEE Photonics Technol. Lett.* **14**, 140–142 (2002).

Demonstration of a Chaotic Optical Message Relay Using DFB Laser Diodes

Min Won Lee and K. Alan Shore

Abstract—The demonstration of chaotic message relay using three chaotic distributed feedback diode lasers is reported. A 1-GHz message has been encoded in a chaotic carrier and relayed to a terminal receiver laser via a mediator laser. The message has been successfully extracted at both the mediator and receiver lasers. The message relay capability thereby demonstrated provides a key functionality for chaotic optical communication networks.

Index Terms—Chaos, distributed feedback (DFB) lasers, semiconductor lasers, synchronization.

THE STRONG demand for private or secure communications has motivated the development of chaotic data encryption techniques. The fundamental concept underpinning this approach is that of transmitting information using a noise-like chaotic carrier. With a view to direct application of such techniques in optical communication systems, a particular effort has been given to the utilization of chaotic semiconductor lasers or laser diodes to provide a chaotic optical carrier signal. Schemes for message extraction using laser diodes have been demonstrated in a number of optical chaos encryption systems [1]–[6]. In these circumstances, investigations have progressed to apply chaotic communication techniques in fiber transmission [7] and digital message transmission [8]. More recently, vertical-cavity surface-emitting lasers (VCSELs) have also been demonstrated to be suitable for application in chaotic communications [9], [10].

In the preceding investigations, a rather simple transmitter–receiver or master–slave configuration has generally been utilized for message transmission. However, to meet the requirements of network communications systems means are required for communicating between a single transmitter and multiple receivers and also to enable transmission of several messages over a single transmission channel. Such capabilities would enable chaotic optical communications systems to provide effective networking services. Already, chaotic message broadcasting [11] has been demonstrated as a potential means for distributing messages to a number of receivers. Chaos message multiplexing has also been reported wherein several messages have been transmitted using a number of channels [12], [13]. These achievements confirm the suitability of chaos communications techniques for realizing networking functionality.

Manuscript received June 8, 2005; revised August 3, 2005. This work was supported by the European Union Optical Chaos Communication Using Laser Transmitters Project IST-2000-29683.

The authors are with the School of Informatics, University of Wales, Bangor LL57 1UT, U.K. (e-mail: minlee@informatics.bangor.ac.uk).

Digital Object Identifier 10.1109/LPT.2005.860039

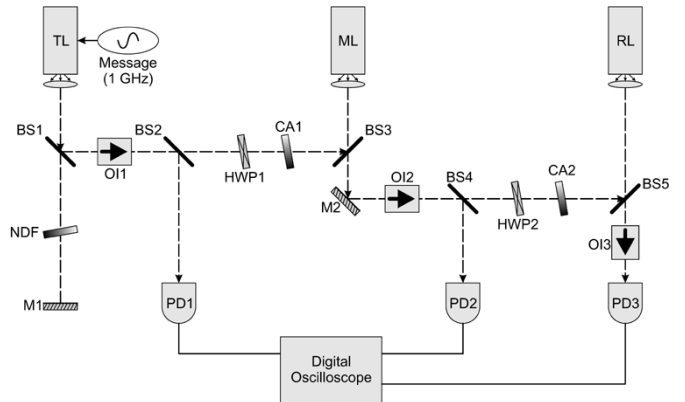


Fig. 1. Schematic diagram of experimental setup: TL is transmitter laser, ML is mediator laser, RL is receiver laser, BS is beam splitter, NDF is neutral density filter, M is mirror, OI is optical isolator, CA is coupling attenuator, HWP is half-wave plate, and PD is photodetector.

In this letter, we report a successful achievement of another feature of communication networks through the demonstration of a chaotic optical relay. In conventional communications systems, network operations are often performed with the assistance of relay stations which provide the opportunity to enhance the distance over which information can be transmitted. A similar functionality would be extremely attractive in chaotic optical communications. In order to implement such a system, the requirement is to couple three or more chaotic transmitters and receivers in cascade configuration and then successfully extract a message at the terminal receiver. A basic requirement for successful message transmission in such a configuration is the achievement of robust chaos synchronization between the cascaded transmitters and receivers. Cascade synchronization has been recently reported using three diode lasers [14]. Based on such cascade synchronization, we demonstrate in this letter the successful relay of a 1-GHz chaotic message using three cascade-coupled distributed feedback (DFB) laser diodes, termed here the transmitter, mediator, and receiver lasers. In the arrangement used here, the transmitter laser is rendered chaotic due to the application of optical feedback in an external cavity. A 1-GHz message is encoded using the chaotic carrier. The mediator laser performs as a chaotic relay. Message recovery in both the mediator and receiver lasers is also demonstrated.

The experimental setup shown in Fig. 1 uses three DFB lasers as the transmitter laser (TL), the mediator laser (ML), and the receiver laser (RL). While the TL is subject to optical feedback, the ML and RL consist of solitary lasers thereby operating in the open-loop configuration. The lasers are driven by low-noise high-accuracy current sources at about three times

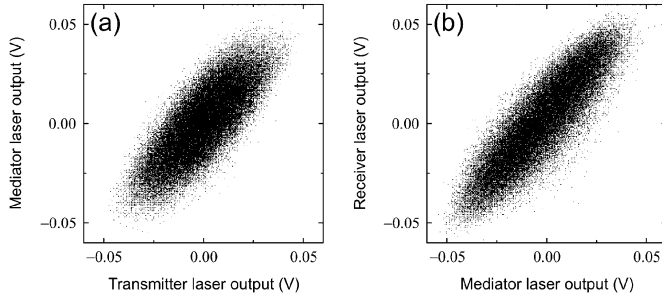


Fig. 2. Synchronization of lasers. (a) Synchronization diagram of TL versus ML. (b) Synchronization diagram of ML versus RL.

their free-running threshold currents and specifically for the TL, ML, and RL, respectively, at 39.79 mA ($3.03J_{\text{th}}$, where J_{th} is the threshold current of free-running laser), 39.6 mA ($3.01J_{\text{th}}$), and 39.26 mA ($3.03J_{\text{th}}$). Using temperature controllers with ± 0.01 °C accuracy, the three lasers are stabilized at temperatures of 28.55 °C, 24.71 °C, and 24.73 °C, respectively. For these operating parameters, the lasers support single-mode emission at a wavelength of 1549.29 nm with 40-dB side-mode suppression. A 1-GHz sine-waveform signal is used to directly modulate the TL through a bias-tee to provide the message to be transmitted. The emission of each of the lasers is collimated by an aspheric lens. The mirror M1 defines for the TL an external cavity whose length of 45 cm corresponds to an external cavity round-trip time of $\tau = 3$ ns. Using the neutral density filter (NDF), the optical feedback intensity is adjusted to 6% of the TL output power, which allows the emission of the TL to be rendered chaotic. The output of the TL is coupled to the ML through the beam splitters BS1 and BS3, and the ML is coupled to the RL through M2 and BS5. Hence, the lasers are coupled in cascade configuration. The optical isolators OI1-3 are used to ensure unidirectional coupling. The half-wave plates HWP1-2 are used to adjust emission polarizations to ensure effective coupling. The coupling attenuators CA1-2 are used to adjust the injection ratios to the ML and RL which are 2.3% and 3.8%, respectively, with respect to the output power of the ML and RL. The coupling distance between the TL and ML is fixed at 117 cm and the coupling distance between the ML and RL is fixed at 105 cm. The 12-GHz bandwidth photodetectors PD1-3 are used to detect the output of the lasers through BS2, BS4, and BS5. A 4-GHz digital oscilloscope is used to record the outputs of the lasers with a 10-GS/s sampling rate.

Generally, the first requirement for message recovery is to achieve chaos synchronization between lasers. In the present system, cascade chaos synchronization must be achieved for message recovery in both the mediator and receiver lasers. Fig. 2 shows the cascade synchronization achieved between the three lasers in the presence of the message. For clarity, the time lag between the lasers has been taken into account in the figure. Fig. 2(a) displays a synchronization diagram of TL output in the abscisse and ML output in the coordinate. It is clear that the laser outputs are well synchronized. The cross-correlation coefficient [15] for this synchronization is obtained as 0.71, which shows a good quality of synchronization. Chaos synchronization achieved between ML and RL is shown in Fig. 2(b). The cross-correlation coefficient for this synchronization is obtained as 0.75, which confirms a good quality synchronization.

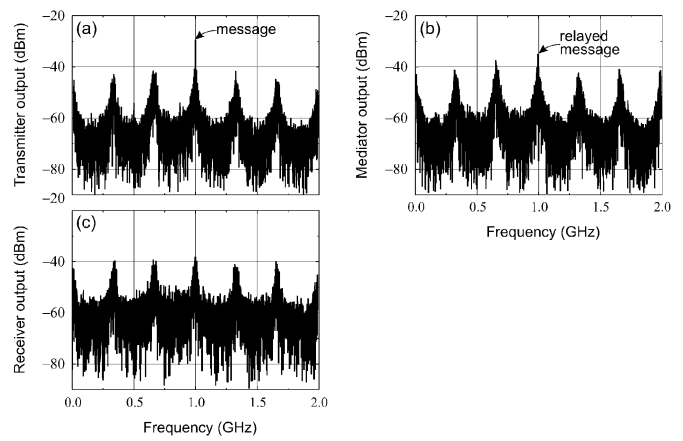


Fig. 3. (a) Power spectra of transmitter laser output. Message is indicated at 1 GHz. (b) Power spectra of mediator laser output. Relayed message is indicated at 1 GHz. (c) Power spectra of receiver laser output.

A key aspect of the functionality expected in chaotic relays is the capability of extracting the message at intermediate stages. Such a capability, in association with message broadcasting, will allow the implementation of complex chaotic communication networks. In the present case, the requirement is to confirm the presence of the message in the mediator laser. In order to establish that the ML relays the chaotic message, we have measured the power spectra of the lasers which are displayed in Fig. 3. The power spectra of the TL are shown in Fig. 3(a), where a 1-GHz message is mixed with the chaotic output of the TL. The chaotic spectrum clearly shows the 335-MHz external-cavity frequency which corresponds to the 3-ns external cavity round-trip time. The laser output is used as a chaotic carrier to encode the 1-GHz message. For the present proof-of-principle demonstration, a relatively strong message has been utilized; nevertheless, it is effectively encoded. Fig. 3(b) exhibits the power spectra of the ML synchronized to the TL. The figure shows that the ML can relay the chaotic message transmitted from the TL although, as expected, the message strength is reduced. It is seen, therefore, that the ML can decode the message and relay it to transmit to the RL. The power spectra of the RL synchronized to the ML are depicted in Fig. 3(c). In the figure, the chaotic carrier is reproduced in the RL, but the message is not reproduced. This indicates that the RL is able to recover the relayed 1-GHz message from the chaotic carrier.

Using the synchronization obtained above, message recovery can be implemented in both the ML and the RL by signal subtraction [11]. Fig. 4 shows the message recovery at both the ML and RL. As seen in Fig. 3(b), the ML duplicates the chaotic carrier and the message. However, since the message amplitude in the ML is lower than that in the TL, the message is recovered at the ML as the difference of the amplitudes by a subtraction between the input and output of ML (note that the ML input is the TL output). The spectrum of the message decoded in the ML is shown in Fig. 4(a). The chaotic carrier is suppressed and the 1-GHz message is clearly revealed in the spectra. Because of the good suppression of the chaotic carrier, the external-cavity frequency does not appear and the spectra in the figure are very flat. It is thus confirmed that the ML has performed efficient message recovery. The recovered message has been numerically filtered by a fast Fourier transform (FFT) filter. The bandwidth of the

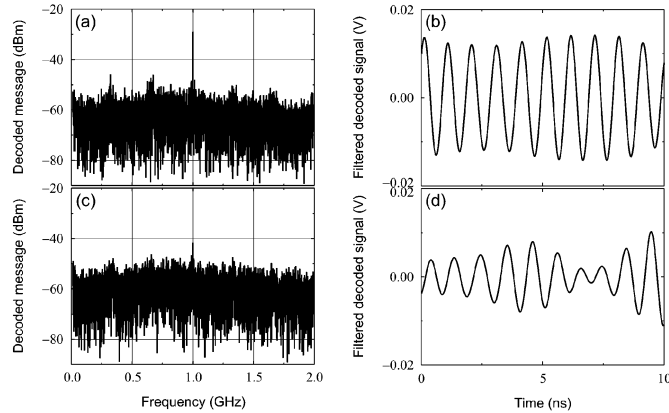


Fig. 4. (a) Power spectra of message decoded in mediator side. Presence of message is clearly revealed at 1 GHz. (b) Filtered decoded message. (c) Power spectra of message decoded from relayed chaotic message in receiver side. Presence of message is clearly revealed at 1 GHz. (d) Filtered decoded message.

filter is from 0.8 and 1.2 GHz, which is ± 200 MHz in the center of the 1-GHz message. In Fig. 4(b), the filtered message clearly shows the 1-GHz sine-waveform signal.

The RL input contains the chaotic carrier and message, and the RL output includes only the chaotic carrier. Therefore, a subtraction of the input and output of RL allows recovery of the relayed message. Fig. 4(c) displays the power spectra of the message decoded at the RL. As in the case of the ML, a good suppression of the chaotic carrier results in the flat spectra seen in the figure. Despite such good suppression of the chaotic carrier, the message recovery is, as expected, poorer than in the ML. The decoded message is filtered in the same way as for the ML. As expected from Fig. 4(c), the filtered message is a little degraded in Fig. 4(d). But, it is apparent that it contains the 1-GHz sine-waveform signal. This confirms an efficient message recovery of the relayed chaotic message at the RL.

In order to examine the efficiency of chaotic message relay and message degradation, the signal-to-noise ratio (SNR) and linewidth of the message center frequency have been measured for the messages recovered at the ML and RL. The SNR for the message recovered at the ML has been measured as 23 dB, while the SNR for the message recovered at the RL has been obtained as 12 dB, which is 11 dB lower. This indicates that the setup used here allows only a two-stage process. In order to enable multistage chaotic message relay, attention will need to be given to performance optimization through an improved SNR of the relayed message as well as enhancing the quality of chaos synchronization. Measurements of the 3-dB linewidth of the decoded message reveal no significant broadening from the TL via the ML to the RL. As such, the message degradation in Fig. 4(d) is considered to be caused by the SNR change rather than linewidth broadening.

Using a cascade configuration comprising transmitter, mediator, and receiver lasers, we have experimentally demonstrated chaotic message relay and recovery of a 1-GHz message. As a prerequisite for this demonstration, we have achieved cascade chaos synchronization in the presence of the 1-GHz message.

The cross-correlation coefficients between the emissions of the lasers confirm the high quality of the chaos synchronizations required for message decoding. Care has been taken to establish, via the power spectra of the mediator laser, that the chaotic message has successfully been relayed in the mediator laser. Furthermore, it has been established that decoding of the message can be accomplished at the mediator laser. It has been shown that message extraction at the receiver laser can be affected, albeit with an expected degradation of recovered signal. An optical amplifier could possibly be used to enhance the transmission distance. However, message recovery cannot be performed at the optical amplifier. The chaotic message relay capability reported here, together with the previously demonstrated chaotic broadcasting [11] and chaos multiplexing capabilities [12], [13] offers the opportunity to construct effective chaotic optical communication networks.

REFERENCES

- [1] I. Fischer, Y. Liu, and P. Davis, "Synchronization of chaotic semiconductor laser dynamics on sub-ns timescales and its potential for chaos communication," *Phys. Rev. A, Gen. Phys.*, vol. 62, pp. 011 801–1–4, 2000.
- [2] J.-B. Cuenot, L. Larger, J.-P. Goedgebuer, and W. T. Rhodes, "Chaos shift keying with an optoelectronic encryption system using chaos in wavelength," *IEEE J. Quantum Electron.*, vol. 37, no. 7, pp. 849–855, Jul. 2001.
- [3] C. R. Mirasso, J. Mulet, and C. Masoller, "Chaos shift-keying encryption in chaotic external-cavity semiconductor lasers using a single-receiver scheme," *IEEE Photon. Technol. Lett.*, vol. 14, no. 4, pp. 456–458, Apr. 2002.
- [4] A. Uchida, S. Yoshimori, M. Shinozuka, T. Ogawa, and F. Kannari, "Chaotic on-off keying for secure communications," *Opt. Lett.*, vol. 26, no. 12, pp. 866–868, Jun. 2001.
- [5] T. Heil, J. Mulet, I. Fischer, C. R. Mirasso, M. Peil, P. Colet, and W. Elsäßer, "ON/OFF phase shift keying for chaos-encrypted communication using external-cavity semiconductor lasers," *IEEE J. Quantum Electron.*, vol. 38, no. 9, pp. 1162–1170, Sep. 2002.
- [6] M. W. Lee, L. Larger, and J.-P. Goedgebuer, "Transmission system using chaotic delays between lightwaves," *IEEE J. Quantum Electron.*, vol. 39, no. 7, pp. 931–935, Jul. 2003.
- [7] V. Anoovazzi-Lodi, S. Merlo, M. Norgia, and A. Scirè, "Characterization of a chaotic telecommunication laser for different fiber cavity lengths," *IEEE J. Quantum Electron.*, vol. 38, no. 9, pp. 1171–1177, Sep. 2002.
- [8] S. Tang and J.-M. Liu, "Message encoding-decoding at 2.5 Gbits/s through synchronization of chaotic pulsing semiconductor lasers," *Opt. Lett.*, vol. 26, no. 23, pp. 1843–1845, Dec. 2001.
- [9] S. F. Yu, P. Shum, and N. Q. Ngo, "Performance of optical chaotic communication systems using multimode vertical cavity surface emitting lasers," *Opt. Commun.*, vol. 200, pp. 143–152, Dec. 2001.
- [10] M. W. Lee, Y. Hong, and K. A. Shore, "Experimental demonstration of VCSEL-based chaotic optical communications," *IEEE Photon. Technol. Lett.*, vol. 16, no. 10, pp. 2392–2394, Oct. 2004.
- [11] M. W. Lee and K. A. Shore, "Chaotic message broadcasting using DFB laser diodes," *Electron. Lett.*, vol. 40, no. 10, pp. 614–615, May 2004.
- [12] J. K. White and J. V. Moloney, "Multichannel communication using an infinite dimensional spatiotemporal chaotic system," *Phys. Rev. A Gen. Phys.*, vol. 59, no. 3, pp. 2422–2426, Mar. 1999.
- [13] J. Paul, S. Sivaprakasam, and K. A. Shore, "Dual-channel chaotic optical communications using external-cavity semiconductor lasers," *J. Opt. Soc. Amer. B, Opt. Phys.*, vol. 21, no. 3, pp. 514–521, Mar. 2004.
- [14] S. Sivaprakasam and K. A. Shore, "Cascaded synchronization of external-cavity laser diodes," *Opt. Lett.*, vol. 26, no. 5, pp. 253–255, Mar. 2001.
- [15] M. W. Lee, J. Paul, I. Pierce, and K. A. Shore, "Frequency-detuned synchronization switching in chaotic DFB laser diodes," *IEEE J. Quantum Electron.*, vol. 41, no. 3, pp. 302–307, Mar. 2005.

Dynamical characterisation of laser diode subject to double optical feedback for chaotic optical communications

M.W. Lee, P. Rees, K.A. Shore, S. Ortin, L. Pesquera and A. Valle

Abstract: A chaotic semiconductor laser subject to double optical feedback is characterised in terms of the statistical analysis, power spectrum analysis and forecast error analysis of the chaotic dynamics. Varying the relative lengths of the two external cavities, the dynamics are observed and compared to that of a single cavity. We show that in the case of integer multiple external-cavity lengths the round-trip time delays can be deduced from the forecast error analysis. In the case of fractional multiple cavity lengths, only the mean value of the cavity resonance frequencies can be deduced from the power spectra and hence the cavity time delays cannot be found. Cavity time delays that differ more than 0.4 ns can be obtained from the forecast error analysis. In the case of similar cavity lengths, the cavity time delays cannot be extracted. The results show that double optical feedback may offer particular advantages for enhancing security in chaos encryption.

1 Introduction

Owing to its high security potential, chaos cryptography is of great interest for data encryption for private communications. Chaos can provide a noise-like, flat broadband carrier and dynamical complexity associated with a high-dimensional attractor. An encryption technique based on such chaos was developed for private communication systems by Cuomo *et al.* [1]. In such a scheme, chaos is used as a carrier to transmit and encode messages in the transmitter. In the receiver, chaos synchronisation [2] is required to decode the message. When the receiver is synchronised to the transmitter, the chaotic carrier can be subtracted and the message can be recovered. Several optical systems based on the chaos encryption have been proposed and have shown good performance in message encryption and decryption using different optical dynamic variables such as laser intensity [3, 4], wavelength [5] and optical delay [6]. In such systems, the message security depends, for example, on the number of decoding keys and the complexity of the chaotic dynamics. Diverse architectures have been proposed for effecting such secure optical communications [7–12]. Since the dynamics generated by a delay system can easily have a very high attractor dimension,

many optical systems are based on delayed optical or optoelectronic feedback. Thus, among several parameters, the effects of the time delay have been investigated in the context of chaos generation and chaos encryption. It is known that the time delay is a crucial parameter for decoding the message, because a small mismatch in time delay gives rise to a large error in message decoding [13].

In optical delay systems, external-cavity laser diodes are often used for chaos encryption. This is because when laser diodes are subject to optical feedback owing to an external mirror, they can easily generate GHz-bandwidth chaos, which permits the encoding of high frequency messages. Moreover, the external-cavity round-trip time in such lasers introduces a time delay that can be changed very easily by varying the cavity length. Hence, research focussing on external-cavity length has been undertaken on, for example, the short cavity dynamical regime [14] and chaotic laser with external fibre cavity [15].

Although the time delay is a crucial parameter in chaos encryption, recent work has shown that the time delay can be estimated by a time series analysis technique and, owing to this estimation, the security of chaos encryption can be compromised [16–18]. In this case the time delay is not a secure key. For this reason, it is of interest to examine means for generalising the effects of time delay in order to restore the security of the system. Semiconductor laser diodes subject to double optical feedback have been previously studied for stabilisation of chaotic dynamics [19–21]. In this paper, we characterise a semiconductor laser subject to double optical feedback in the context of chaotic communications. Compared to single optical feedback, it is expected that the use of two time delays through double optical feedback can have the potential advantage of providing a secure decoding key. An optoelectronic chaos generator using two time delays has been recently reported to increase the dimension of the chaotic attractor [22]. In that work, it was shown that the dynamics arising with a double time delay are very different to those due to single time delay. Moreover, on the basis of the Lyapunov

© IEE, 2005

IEE Proceedings online no. 20045025

doi: 10.1049/ip-opt:20045025

Paper first received 30th June 2004 and in final revised form 31st January 2005

M.W. Lee, P. Rees, and K.A. Shore are with the School of Informatics, University of Wales, Bangor, Dean Street, Bangor LL57 1UT, Wales, United Kingdom

S. Ortin, L. Pesquera, and A. Valle are with the Instituto de Física de Cantabria, CSIC-Universidad de Cantabria, Avda. Los Castros s/n, 39005 Santander, Spain

S. Ortin is also with the Departamento de Física Moderna, Universidad de Cantabria, Spain

E-mail: minlee@informatics.bangor.ac.uk

exponents and dimensions of the dynamics, the complexity of the dynamics for double delay is greater than that for single delay. Systems using two or more delays have also been implemented in code division multiple access (CDMA) communications [23] and in neural networks [24]. In this paper, we focus on how the dynamics owing to double delay can affect time delay estimation. The results are presented in terms of the statistical analysis of the time series of optical intensity, power spectrum of the dynamics and forecast errors.

2 Experimental arrangement

The experimental setup is shown schematically in Fig. 1. The system has two external-cavities; Cavity 1 and Cavity 2. The cavities are formed using mirrors M1 and M2 and, in general, have different cavity lengths L_1 and L_2 , respectively. A Fabry-Pérot type diode laser emitting at 1550 nm is used as the optical source. The laser operates at a temperature of 24.1 °C temperature and 23.54 mA drive current which is around 1.5 times the stand-alone laser threshold current. The emission of the laser is collimated by an aspheric lens. The beam splitter BS1 is used to couple the laser to photodetector PD. BS2 is used to separate the laser output in two arms for double optical feedback through M1 and M2. The neutral density filters NDF1 and NDF2 are used to vary the optical feedback intensity for each cavity. The optical isolator OI eliminates back-reflection with a -40 dB isolation. The 12 GHz photodetector PD enables detection of the chaotic laser output at high frequency. A 20 GS/s oscilloscope is used to record the photodetector outputs.

Experiments have been performed for three cases by varying the cavity lengths L_1 and L_2 : case 1) $L_1 = 30$ cm and $L_2 = 60$ cm; case 2) $L_1 = 30$ cm and $L_2 = 33$ cm; case 3) $L_1 = 30$ cm and $L_2 = 40$ cm. NDF1 and NDF2 are adjusted to give a 3.2% optical feedback intensity of the laser output for each cavity and the laser is thereby rendered chaotic. The output of the photodetector is recorded via an oscilloscope.

3 Characterisation of chaotic dynamics

3.1 Single delay case

Figure 2 shows chaotic dynamics generated from single delay configuration ($L_1 = 30$ cm). Figure 2a is a time series recorded using the oscilloscope operating in the conventional mode. In the Figure, the time delay is not

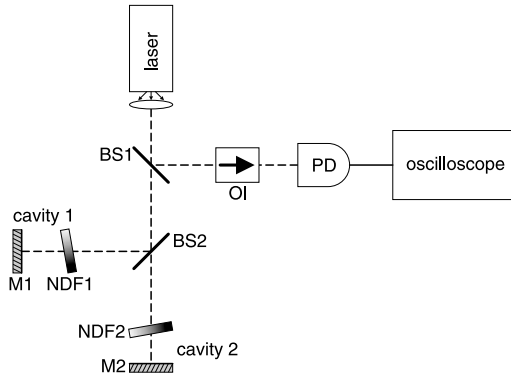


Fig. 1 Schematic experimental setup

BS: beam splitter, M: mirror, OI: optical isolator, NDF: neutral density filter, PD: photodetector

revealed in the chaotic time traces recorded in conventional mode. Figure 2b is a time series recorded by operating the oscilloscope in statistical mode. Unlike the conventional oscilloscope mode which gives information in two dimensions (time against amplitude), this mode gives waveform information in three dimensions: time, amplitude, and probability density of the waveform (based on statistical analysis of a large number of waveforms). In Fig. 2b, the probability density of the waveform evolution is shown in grey scale intensity. The dark grey tone represents high probability density and light grey tone represents low probability density. From this Figure, the time delay in the experiment is easily obtained as $\tau_1 = 2$ ns by measuring the period of the time series. Therefore, the single time delay is not a secure decoding key for chaos encryption. Figure 2c displays the power spectra of the dynamics over a GHz range. In the Figure,

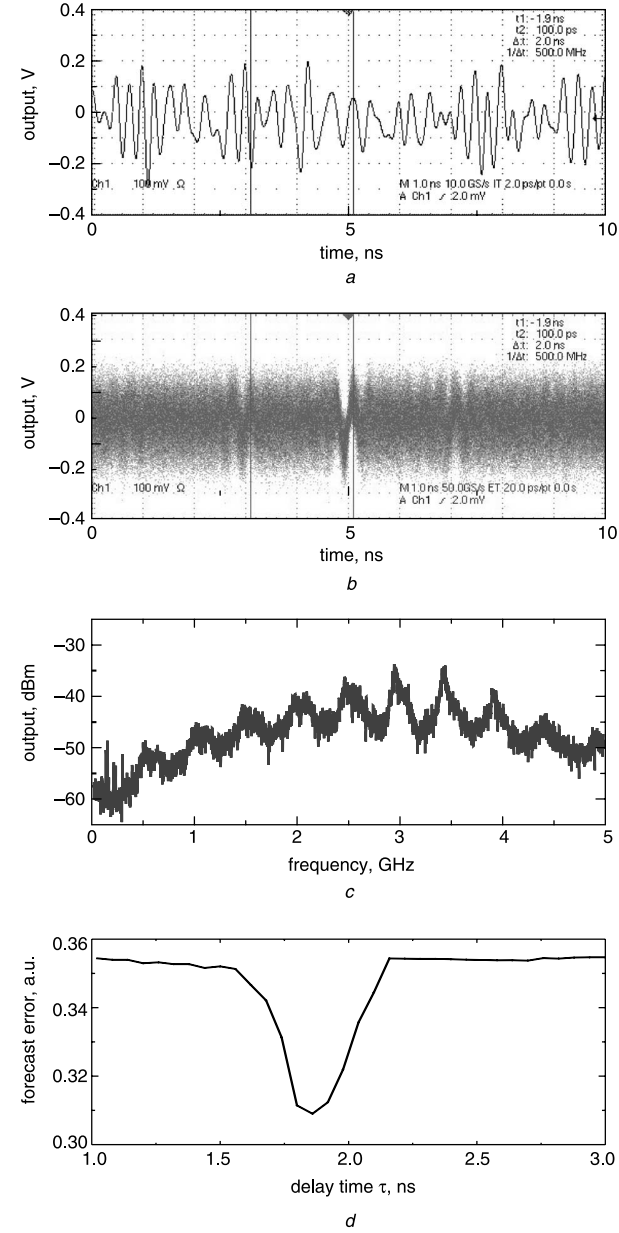


Fig. 2 Chaotic dynamics characterisation in single delay case $L_1 = 30$ cm

- a Time trace recorded by conventional mode
- b Time series in statistical mode
- c Power spectrum of the chaotic dynamics
- d Forecast errors against delay time τ

the time delay is also easily deduced as $\tau_1 = 2$ ns by measuring the external-cavity resonance frequency ($f_1 = 500$ MHz). Figures 2b and c indicate that the time series in statistical mode and power spectra can easily enable estimation of the time delay of the system. Figure 2d displays forecast errors as a function of delay time τ , which allow extraction of the time delay. The forecast errors are calculated from the experimental time series of optical intensity $I(t)$ by using a global linear model with input data delayed by both the embedding time $t_e = 75$ ps and the delay time τ : $I(t - t_e), I(t - 2t_e), I(t - 3t_e); I(t - \tau), I(t - \tau - t_e), I(t - \tau - 2t_e)$. The delay time τ where the forecast error becomes minimum corresponds to the time delay of the system. This method is based on an embedding-like approach similar to that used in [16], but a simpler global model is used instead of a local linear one. From the Figure, the minimum is obtained at $\tau = 1.88$ ns which corresponds closely to the time delay of the physical system. Note that the cavity length estimated from the statistical analysis of the time series of optical intensity and from the power spectrum is the optical cavity length which is slightly greater than the physical length owing to the presence of various optical components in the cavity [25].

3.2 Double delay case

Since double delay provides high complexity in the system, we deal hereafter with chaotic dynamics generated in a double external-cavity configuration. First, chaotic dynamics characterisation is performed in the statistical mode. In case 1, the lengths of the cavities are $L_1 = 30$ cm and $L_2 = 60$ cm, respectively. The frequency and time delay are measured as $f_1 = 500$ MHz and $\tau_1 = 2$ ns for Cavity 1, and $f_2 = 250$ MHz and $\tau_2 = 4$ ns for Cavity 2, respectively. Using the double cavity in this case, the time series in statistical mode in Fig. 3a appears to be the same as that in Fig. 2b. From the Figure, the frequency and time delay are measured as $f_d = 500$ MHz

and $\tau_d = 2$ ns, respectively. Thus, even though the system has a double cavity, it appears that the system has single cavity with a 2 ns time delay.

In case 2, the lengths of Cavity 1 and Cavity 2 are slightly different: $L_1 = 30$, $L_2 = 33$ cm. The cavity lengths produce round-trip times of $\tau_1 = 2$ ns and $\tau_2 = 2.2$ ns, and give resonance frequencies of $f_1 = 500$ MHz and $f_2 = 454.5$ MHz, respectively. The time series in statistical mode for the double cavity are shown in Fig. 3b. The dynamics is different to that in Fig. 2b and no periodicity is revealed in the Figure. Thus, the external-cavity round-trip time cannot be estimated from the time series in statistical mode.

In case 3, the length of Cavity 1 is $L_1 = 30$ cm, and Cavity 2 is $L_2 = 40$ cm. For Cavity 2, the frequency and time delay are measured as $f_2 = 375$ MHz and $\tau_2 = 2.67$ ns, respectively. Figure 3c shows the time series in statistical mode for this case. The time series in Fig. 3c does not show the periods of Cavity 1 and Cavity 2. Because of a superposition of two different periodicities which are fractional multiples, the period of the laser output in case 2 and case 3 is obscured and cannot be directly measured by recording time series in the statistical mode.

Figure 4 exhibits the power spectra of the chaotic dynamics for each case. The power spectra of the dynamics in case 1 are shown in Fig. 4a. Although the system has two external cavities, the power spectra for the double cavity appears quite similar to that for Cavity 1. The resonance frequency is measured as $f_d = 500$ MHz which is the same as Cavity 1. The system can be recognised as using a single cavity with $\tau_d = 2$ ns time delay as the Figure does not show strongly the frequency owing to Cavity 2. Thus, the results indicate Cavity 1 is the dominant cavity in the system and the presence of the double cavity is not revealed. Figure 4b displays the power spectra of the chaotic dynamics for case 2. Compared to Fig. 2c, the power spectra in this case appear similar to a conventional single cavity one. However,

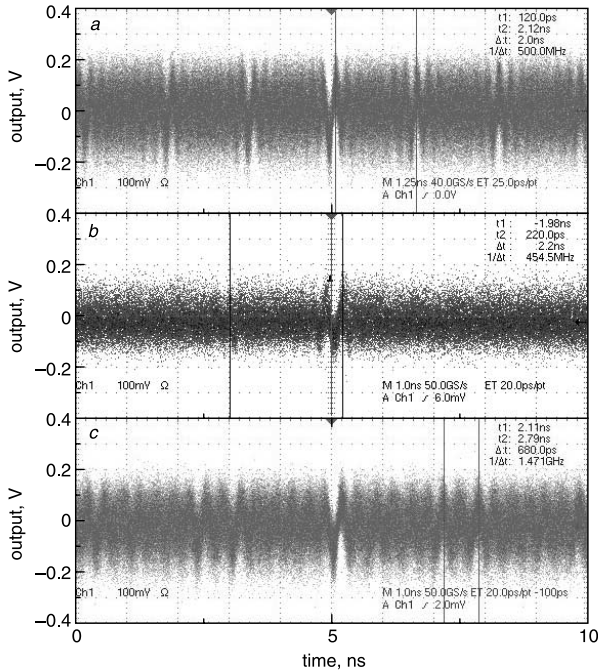


Fig. 3 Time series in statistical mode

- a Case 1; $L_1 = 30$ cm, $L_2 = 60$ cm
- b Case 2; $L_1 = 30$ cm, $L_2 = 33$ cm
- c Case 3; $L_1 = 30$ cm, $L_2 = 40$ cm

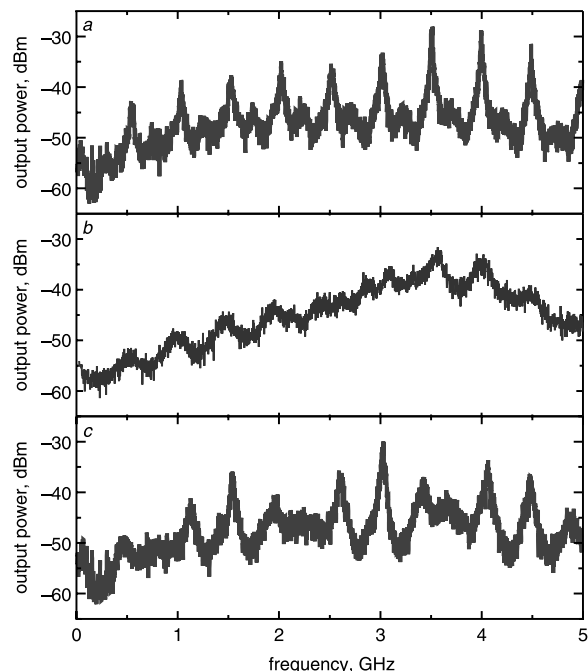


Fig. 4 Power spectra of chaotic dynamics

- a Case 1; $L_1 = 30$ cm, $L_2 = 60$ cm
- b Case 2; $L_1 = 30$ cm, $L_2 = 33$ cm
- c Case 3; $L_1 = 30$ cm, $L_2 = 40$ cm

the resonance frequency is obtained as $f_d = 477.3$ MHz which does not correspond to that of either Cavity 1 or Cavity 2. From the frequency obtained in Fig. 4b, the time delay is obtained as $\tau_d = 2.1$ ns which is slightly different from the time delays of the single cavities. This indicates that the time delay for a double cavity is more difficult to estimate than a single cavity. Moreover, the power spectra in Fig. 4b appear to be that of a single cavity with a small error in the time delay. The power spectra shown in Fig. 4c for case 3 are very different to the single cavity case. The periodicity of the system is obscured and the system exhibits a number of resonance frequencies. One resonance frequency is measured as $f_d = 437.5$ MHz. From this frequency, the time delay is obtained as $\tau_d = 2.29$ ns which is completely different to the time delays of the individual cavities. We note that the frequency f_d can be obtained quite accurately by simple arithmetic averaging of the two single cavity frequencies f_1 and f_2 :

$$f_d = \frac{f_1 + f_2}{2} = \frac{500 + 375}{2} = 437.5 \text{ MHz.} \quad (1)$$

Likewise in case 2, the frequency $f_d = 477.3$ MHz obtained in Fig. 4b can be found by simple averaging. Thus, if the system has a double cavity with fractional multiple cavity lengths, the frequencies from each cavity cannot be directly measured and only the mean value of resonance frequencies of the two cavities can be obtained. Even if the presence of a double cavity becomes known in this case, it is difficult to estimate the time delays of each cavity.

The time delays are not revealed by the above characterisations of the double cavity. But the time delays

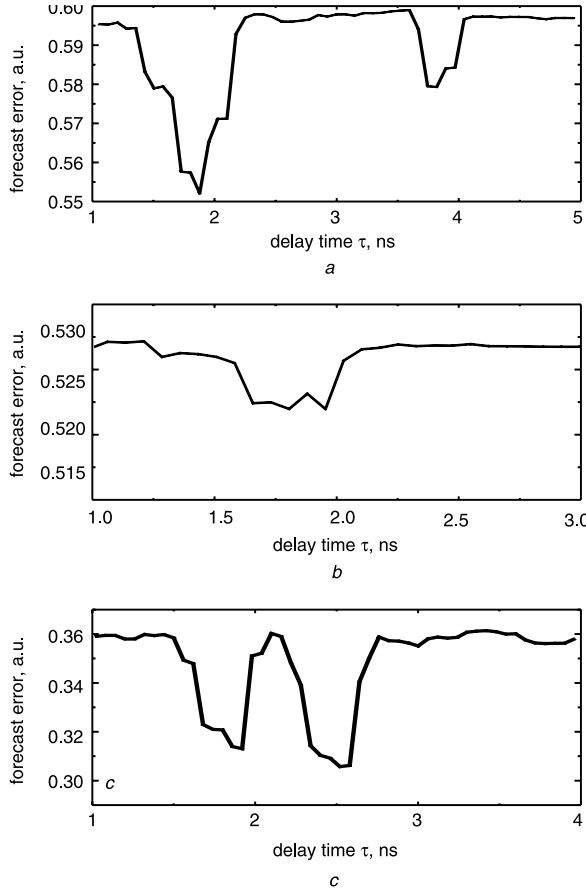


Fig. 5 Forecast errors against delay time τ

- a Case 1; $L_1 = 30$ cm, $L_2 = 60$ cm
- b Case 2; $L_1 = 30$ cm, $L_2 = 33$ cm
- c Case 3; $L_1 = 30$ cm, $L_2 = 40$ cm

can be revealed by calculating forecast errors as shown in Fig. 5. The forecast errors in Fig. 5 are calculated using the procedure described above. The forecast errors against delay time for case 1 are shown in Fig. 5a where the forecast errors exhibit two minima. The first minimum forecast error occurs at a delay time of $\tau = 1.88$ ns and the second minimum appears at $\tau = 3.83$ ns. These delay times correspond to the time delays τ_1 and τ_2 , respectively for this case. The forecast errors for case 2 are shown in Fig. 5b over a range between 1 and 3 ns of delay time. Compared to Fig. 2d, the minimum forecast error is broadened by a few 100 ps of delay time which introduces significant uncertainty into the estimation. It is shown that the presence of double time delay can be deduced, but because of the spread of minimum forecast errors, the values of each time delay cannot be extracted from the Figure. The centre of the spread of minimum forecast error is measured as 1.6 ns, which does not correspond to the time delays of the physical system. Figure 5c displays the forecast errors for case 3. Compared to Fig. 5b, the first and second minimum forecast errors are prominent in this case. From the first and second forecast errors the delay times τ are measured respectively as 1.92 ns and 2.52 ns which correspond to the time delays of each cavity. This indicate that when the difference of the cavity lengths become larger, the time delay can be extracted by calculating the forecast errors. In the case of integer multiple external-cavity lengths a method based on a filling factor analysis have been used to obtain the delay times [25]. In this method one has to estimate the time derivative of the signal from experimental time series, which is sensitive to noise, and a special care has to be taken for that purpose.

4 Numerical characterisation

A numerical simulation has been made to confirm the values of the frequency averaging performed in case 3. The dynamics of the double optical feedback is modelled using the following equations for the normalised complex electric field $E(t)$ and normalised carrier number above threshold $N(t)$ [26, 27]:

$$\begin{aligned} \frac{d}{dt}E(t) &= [(1 + i\alpha)N(t) + i\omega]E(t) \\ &\quad + \kappa_1E(t - \tau_1) + \kappa_2E(t - \tau_2) \end{aligned} \quad (2)$$

$$T \frac{d}{dt}N(t) = P - N(t) - (1 + 2N(t))|E(t)|^2 \quad (3)$$

where $\alpha = 3.5$ is the linewidth enhancement factor, $\kappa_1 = \kappa_2 = 0.001$ are the optical feedback coefficients which are adjusted the same for each cavity, $\omega = 3.08 \times 10^{12}$ is the normalised optical frequency of the laser, $T = 700$ is the ratio of the photon and carrier lifetimes, and $P = 1.5I_{th}$ is the pumping level above threshold of the laser. From the cavity lengths $L_1 = 30$ cm and $L_2 = 40$ cm, the time delays can be obtained as $\tau_1 = 2$ ns and $\tau_2 = 2.67$ ns, respectively.

The simulation is performed with 100 ps integration step using the parameters shown above. The numerical results are shown in Fig. 6. In Fig. 6a, the spectrum of dynamics from Cavity 1 is obtained. The resonance frequency is found to be $f_1 = 500$ MHz which indicates a $\tau_1 = 2$ ns time delay. Likewise, the power spectrum of the dynamics from Cavity 2 is shown in Fig. 6b. The resonance frequency is found to be $f_2 = 375$ MHz which indicates $\tau_2 = 2.67$ ns time delay. It is seen therefore that the frequencies and time delays can be found from the numerical simulations and the numerical

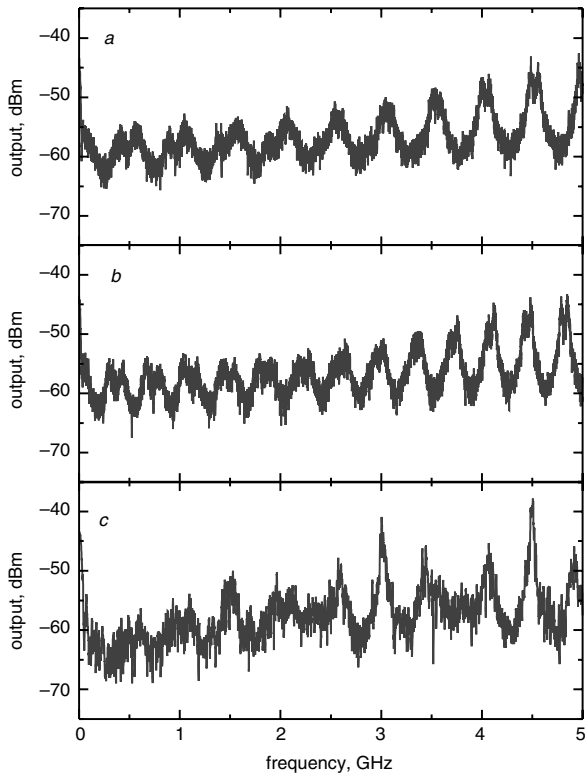


Fig. 6 Numerical results corresponding to *Fig. 4c*

- a Single cavity 1; $L_1 = 30\text{ cm}$
- b Single cavity 2; $L_2 = 40\text{ cm}$
- c Double cavity

results show a good agreement with the experimental results. As is expected from the experimental results for case 3, the power spectra of the double optical feedback dynamics exhibit an unusual behaviour which is shown in **Fig. 6c**. The cavity round-trip frequency is found to be $f_d = 435\text{ MHz}$ which is very close to the one obtained through (1): $f_m = (500 + 375)/2 = 437.5\text{ MHz}$.

The simulations undertaken here have had as their focus the confirmation of the frequency averaging undertaken in (1). It is noted that opportunities exist to perform more detailed simulations indicating statistical analysis of the laser waveform and the forecast error. Such extensive work is beyond the scope of the present paper.

5 Conclusions

In conclusion, we have characterised chaotic laser diodes subject to double optical feedback in terms of the chaotic time series in statistical mode, cavity round-trip frequency and forecast errors. In the case that two cavity lengths are integer multiples, the dynamics generated from double optical feedback are similar to that for a single cavity case. Despite using two external cavities, one finds only one time delay from the time series of the optical intensity in statistical mode and its power spectra whilst the forecast errors reveal the presence of two cavities. In the case that two cavity lengths are fractional multiples, the dynamics of the double feedback case is very different to that for single feedback. For the double feedback case the time delays are obscured in the statistical analysis of the time series. The resonance frequencies due to each cavity cannot be deduced from the power spectrum analysis but only the mean value of the frequencies can be obtained. This experimental result has been compared

to numerical simulations using the model described by (2) and (3). Good agreement is obtained between the experimental and numerical results. It is thus demonstrated experimentally and numerically that the generated dynamics can be more robust against the time delay estimation. The forecast errors reveal the presence of two time delays for case 3, but not for case 2 because of the spread of the minimum forecast error. This demonstrates that similar time delays as in case 2 are more robust against detection of the time delays. The dynamic regime used for individual cavities is the low-dimensional chaotic regime where the periodicity owing to the external-cavity significantly appears. It can be expected that in a high-dimensional chaotic regime of individual cavities the estimation of double time delay becomes more difficult. From the results, we expect that the use of a system based on double cavity configuration may provide advantages to improve the message security when its chaotic dynamics are used in a chaos encryption system. In particular, similar time delays can provide more secure decoding keys than in the other cases.

6 Acknowledgments

This work is supported by the European Union OCCULT (Optical Chaos Communication Using Laser Transmitters) project (IST-2000-29683). S. Ortín, L. Pesquera and A. Valle also acknowledge financial support from the Ministerio de Educación y Ciencia (Spain), Project TIC2002-04255-C04-02K.

7 References

- 1 Cuomo, K.M., and Oppenheim, A.V.: ‘Circuit implementation of synchronized chaos with applications to communications’, *Phys. Rev. Lett.*, 1993, **71**, pp. 65–68
- 2 Pecora, L.M., and Carroll, T.L.: ‘Synchronization in chaotic systems’, *Phys. Rev. Lett.*, 1990, **64**, pp. 821–824
- 3 Van Wijgeren, G.D., and Roy, R.: ‘Optical communication with chaotic waveforms’, *Phys. Rev. Lett.*, 1998, **81**, pp. 3547–3550
- 4 Sivaprakasam, S., and Shore, K.A.: ‘Message encoding and decoding using chaotic external-cavity diode lasers’, *IEEE J. Quantum Electron.*, 2000, **36**, pp. 35–39
- 5 Goedgebuer, J.-P., Larger, L., and Porte, H.: ‘Optical cryptosystem based on synchronization of hyperchaos generated by a delayed feedback tunable laserdiode’, *Phys. Rev. Lett.*, 1998, **80**, pp. 2249–2252
- 6 Lee, M.W., Larger, L., and Goedgebuer, J.-P.: ‘Transmission system using chaotic delays between lightwaves’, *IEEE J. Quantum Electron.*, 2003, **39**, pp. 931–935
- 7 Uchida, A., Yoshimori, S., Shinozuka, M., Ogawa, T., and Kannari, F.: ‘Chaotic on-off keying for secure communications’, *Opt. Lett.*, 2001, **26**, pp. 866–868
- 8 Tang, S., and Liu, J.-M.: ‘Message encoding-decoding at 2.5 Gbits/s through synchronization of chaotic pulsing semiconductor lasers’, *Opt. Lett.*, 2001, **26**, pp. 1843–1845
- 9 Mirasso, C.R., Mulet, J., and Masoller, C.: ‘Chaos shift-keying encryption in chaotic external-cavity semiconductor lasers using a single-receiver scheme’, *IEEE Photonics Technol. Lett.*, 2002, **14**, pp. 456–458
- 10 Paul, J., Sivaprakasam, S., Spencer, P.S., and Shore, K.A.: ‘Optically modulated chaotic communication scheme with external-cavity length as a key to security’, *J. Opt. Soc. Am. B*, 2003, **20**, pp. 497–503
- 11 Lee, M.W., Paul, J., Sivaprakasam, S., and Shore, K.A.: ‘Comparison of closed-loop and open-loop feedback schemes of message decoding using chaotic laser diodes’, *Opt. Lett.*, 2003, **28**, pp. 2168–2170
- 12 Heil, T., Mulet, J., Fischer, I., Mirasso, C.R., Peil, M., Colet, P., and Elsäßer, W.: ‘ON/OFF phase shift keying for chaos-encrypted communication using external-cavity semiconductor lasers’, *IEEE J. Quantum Electron.*, 2002, **38**, pp. 1162–1170
- 13 Cuenot, J.-B., Larger, L., Goedgebuer, J.-P., and Rhodes, W.T.: ‘Chaos shift keying with an optoelectronic encryption system using chaos in wavelength’, *IEEE J. Quantum Electron.*, 2001, **37**, pp. 849–855
- 14 Heil, T., Fischer, I., Elsäßer, W., and Gavrielides, A.: ‘Dynamics of semiconductor lasers subject to delayed optical feedback: the short cavity regime’, *Phys. Rev. Lett.*, 2001, **87**, pp. 243901-1–243901-4
- 15 Anoovazhi-Lodi, V., Merlo, S., Norgia, M., and Scirè, A.: ‘Characterization of a chaotic telecommunication laser for different fiber cavity lengths’, *IEEE J. Quantum Electron.*, 2002, **38**, pp. 1171–1177
- 16 Hegger, R., Büunner, M.J., and Kantz, H.: ‘Identifying and modeling delay feedback systems’, *Phys. Rev. Lett.*, 1998, **81**, pp. 558–561

- 17 Yank, T., Yang, L.-B., and Yang, C.-M.: 'Breaking chaotic secure communication using a spectrogram', *Phys. Lett. A*, 1998, **247**, pp. 105–111
- 18 Udal'tsov, V.S., Goedgebuer, J.-P., Larger, L., Cuenot, J.-B., Levy, P., and Rhodes, W.T.: 'Cracking chaos-based encryption systems ruled by nonlinear time delay differential equations', *Phys. Lett. A*, 2003, **308**, pp. 54–60
- 19 Liu, Y., and Ohtsubo, J.: 'Dynamics and chaos stabilization of semiconductor lasers with optical feedback from an interferometer', *IEEE J. Quantum Electron.*, 1997, **33**, pp. 1163–1169
- 20 Rogister, F., Sukow, D.W., Gavrielides, A., Mégré, P., Deparis, O., and Blondel, M.: 'Experimental demonstration of suppression of low-frequency fluctuations and stabilization of an external-cavity laser diode', *Opt. Lett.*, 2000, **25**, pp. 808–810
- 21 Erneux, T., Rogister, F., Gavrielides, A., and Kovaxis, V.: 'Bifurcation to mixed external cavity mode solutions for semiconductor lasers subject to optical feedback', *Optics Commun.*, 2000, **183**, pp. 467–477
- 22 Lee, M.W., Larger, L., Udal'tsov, V.S., Genin, E., and Goedgebuer, J.-P.: 'Demonstration of a chaos generator using two time delays', *Opt. Lett.*, 2003, **29**, pp. 325–327
- 23 Penaud, S., Guittard, J., Bouysse, P., and Quéré, R.: 'DSP implementation of self-synchronised chaotic encoder decoder', *Electron. Lett.*, 2000, **36**, pp. 366–377
- 24 Wei, J., and Ruan, S.: 'Stability and bifurcation in a neural network model with two delays', *Physica D*, 1999, **130**, pp. 255–272
- 25 Bünnér, M.J., Kittel, A., Parisi, J., Fischer, I., and Elsäßer, W.: 'Estimation of delay times from a delayed optical feedback laser experiment', *Europhys. Lett.*, 1998, **42**, pp. 353–358
- 26 Hohl, A., Gavrielides, A., Erneux, T., and Kovaxis, V.: 'Localized synchronization in two coupled nonidentical semiconductor lasers', *Phys. Rev. Lett.*, 1997, **78**, pp. 4745–4748
- 27 Rees, P., Spencer, P.S., Pierce, I., Sivaprakasam, S., and Shore, K.A.: 'Anticipated chaos in a nonsymmetric coupled external-cavity-laser system', *Phys. Rev. A*, 2003, **68**, pp. 033818-1–033818-7

Demonstration of an All-Fiber Broadband Optical Parametric Amplifier at $1\text{ }\mu\text{m}$

Min Won Lee, Thibaut Sylvestre, Michaël Delqué, Alexandre Kudlinski, Arnaud Mussot, J.-F. Gleyze, Alain Jolly, and Hervé Maillotte

Abstract—In this paper, an optical parametric amplifier and wavelength converter in an all-fiber optical configuration is experimentally demonstrated for photonic applications in the $1\text{ }\mu\text{m}$ band. This is achieved by using a microstructured fiber which provides anomalous dispersion at $1\text{ }\mu\text{m}$ and an LiNbO_3 electro-optic intensity modulator specially designed at this operating wavelength for generating pump pulses. A gain of greater than 30 dB together with highly efficient wavelength conversion is obtained at 1053 nm. The gain bandwidth and gain-power efficiency are also investigated. Experimental results agree well with the theory of parametric amplification including Raman scattering.

Index Terms—Fiber optical parametric amplifiers, optical fiber amplifiers.

I. INTRODUCTION

FIBER optical parametric amplifiers (FOPAs) have evinced tremendous interest over the years in view of their potential application to all-optical signal processing technologies [1]–[3]. In addition to providing large gain and wide bandwidth, they offer access to arbitrary wavelength ranges, simultaneous wavelength conversion and low noise figures. Much effort has been spent on FOPAs for telecommunication applications in the $1.5\text{ }\mu\text{m}$ wavelength band and some outstanding progress have been made such as 70 dB net gain and bandwidth of a few hundred nanometers in standard and highly-nonlinear dispersion shifted optical fibers [1]. The use of microstructured optical fibers (MOF) in parametric devices such as amplifiers, generators and oscillators has been the subject of much recent work [4]–[7]. MOFs indeed offer the promise of extending the range of attainable wavelengths and efficiency of parametric devices. FOPA in the $1\text{ }\mu\text{m}$ band is also of great interest because of the need of all-optical broadband signal processing techniques for Ytterbium-doped fiber laser and amplifier systems. Recently, an FOPA has been reported in the $1\text{-}\mu\text{m}$ band by

using an MOF that provides anomalous dispersion in the band [8]. This FOPA was demonstrated in free space as a proof of principle and cannot be implemented in practical fiber-based systems. In this work, optical parametric amplification in the $1\text{-}\mu\text{m}$ band is experimentally achieved, for the first time to our knowledge, in a fully integrated all-fiber and polarization-maintaining (PM) optical system, paving the way for practical applications to all-optical pulse processing in the $1\text{-}\mu\text{m}$ window. The FOPA demonstrated in this work is implemented with a pump pulsed by an electro-optic intensity modulator specially designed to operate at $1\text{ }\mu\text{m}$ with a minimum insertion loss, enhanced extinction ratio and a high optical damage threshold. Efficient parametric gain and wavelength conversion are demonstrated by pumping at 1065 nm near the zero-dispersion wavelength of the MOF and by using a signal at a centre-wavelength of 1053 nm. The choice of the signal wavelength, which is located in the anti-Stokes band of the FOPA, matches the specific needs of the search of Inertial Confinement Fusion (ICF) in large laser systems [9], [10]. Our experimental results show a net parametric gain of greater than 30 dB at 1053 nm with a good quality of optical amplification and higher idler wavelength conversion efficiency due to the additional contribution of the Raman gain. This all-fiber pulsed-pump parametric device provides efficient amplification and conversion for applications such as optical parametric chirped-pulse amplification (OPCPA) [11], [12], pulse optical replication or regeneration, ultrafast optical sampling and next generation optical oscilloscopes [13], [14]. These applications may take a large benefit from FOPA to provide a fairly uniform spectral gain over broad bandwidth.

II. EXPERIMENTAL SETUP

Setting an all-fiber PM OPA in the $1\text{-}\mu\text{m}$ band is a big challenge because of the need for low insertion loss fiber optic components, electro-optical modulators and a suitable optical fiber as a nonlinear medium. At such a wavelength, anomalous dispersion can be provided only by the use of a MOF whose photonic crystal cladding ensures a high single-mode field confinement together with the dispersion characteristics [15], [16]. MOF has been widely used for fiber optical parametric oscillators. In our experimental setup shown schematically in Fig. 1, the pump is provided by a 6 mW tunable DFB laser source at 1060 nm with a tuning range from 1040 nm to 1080 nm. The linearly-polarised CW emission of the laser is converted to pulse emission by an LiNbO_3 electro-optic Mach-Zhender intensity modulator manufactured by Photline Technologies (NIR-MX series). The modulator is specially designed for operation at 1060 nm with low insertion loss ($<5\text{ dB}$), high extinction ratio and high optical

Manuscript received March 09, 2010; revised June 10, 2010; accepted June 10, 2010. Date of publication June 21, 2010; date of current version July 26, 2010.

M. W. Lee, T. Sylvestre, M. Delqué and H. Maillotte are with the Département d'optique P. M. Duffieux, Institut FEMTO-ST, Université de Franche-Comté, CNRS UMR 6174, F-25030 Besançon cedex, France (email: thibaut.sylvestre@univ-fcomte.fr).

A. Kudlinski and A. Mussot are with the Laboratoire de Physique des Lasers Atomes et Molécules, IRCICA, Université de Lille 1, CNRS UMR 8523, 59655 Villeneuve d'Ascq Cedex, France.

J.-F. Gleyze and A. Jolly are with the Commissariat à l'Energie Atomique (CEA), Centre d'Etudes Scientifiques et Techniques Aquitaine, Chemin des sablières, 33144 Le Barp, BP2, France.

Color versions of one or more of the figures in this paper are available online at <http://ieeexplore.ieee.org>.

Digital Object Identifier 10.1109/JLT.2010.2053195

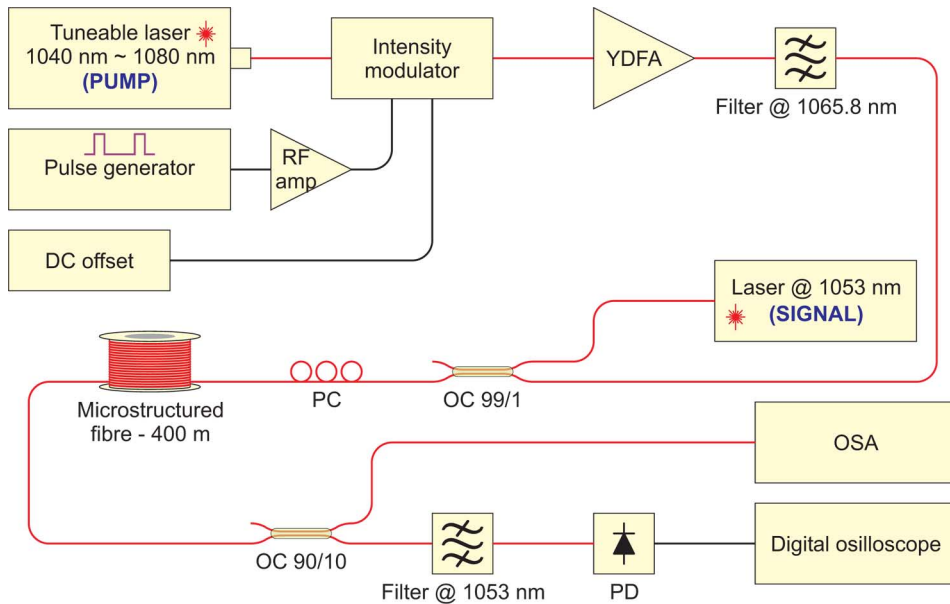


Fig. 1. Schematic diagram of the experimental setup. RF Amp: RF amplifier, YDFA: Ytterbium-doped fiber amplifier, OC: optical coupler, PC: polarization controller, PD: photodetector, OSA: optical spectrum analyzer. The polarisation is maintained in the whole setup.

damage threshold. A pulse generator is used to generate rectangular pulses and an RF amplifier amplifies pulses so as to drive the modulator over V_π of modulation. In this experiment, a short pulse (<10 ns) is used to avoid any Brillouin backscattering that limits the OPA gain [1]. The pulselength and duty cycle of pulse train are then set to 3.4 ns and 1/16, respectively. A DC offset is added into the modulator to suppress residual CW emission in the pulse emission. A high-power polarization-maintaining (PM) Ytterbium-doped fiber amplifier (YDFA) amplifies the pump pulse. A bandpass filter with a 2.5 nm of 3 dB-linewidth is adjusted to 1065.8 nm of center-wavelength to ensure suppression of amplified spontaneous emission (ASE) of the YDFA. Another distributed feedback (DFB) PM fiber laser emitting CW at 1053 nm is used as a signal source to be amplified by the fiber OPA. A 99/1 PM fiber optical coupler at 1060 nm is used to couple both the pump and the signal at the MOF's input. Only 1% of the signal power is injected into the fiber amplifier whilst 99% of the pump is injected into the amplifier to keep the pump power at a maximum level. As parametric amplification is polarization dependent, the states of polarization (SOP) of the pump and signal are maintained in the whole system as well as in the MOF by use of PM elements. We additionally use a polarization controller (PC) before the MOF to align both the pump and signal polarizations parallel to one of the birefringent axes of the MOF. The signal power is set to be 40 dB lower than the maximum average pump power. The input signal power is then measured as -15 dBm. The fiber output is split into two outputs by another 90/10 PM fiber optical coupler. The 10% port is sent to an optical spectrum analyzer (OSA) and the 90% port is injected into another bandpass filter centered at the signal wavelength of 1053 nm. The amplified signal is then detected by a photodetector (PD) and recorded by a real-time digital oscilloscope.

The MOF used in this work was specifically designed and manufactured to provide both anomalous dispersion required for phase-matching and a high nonlinearity coefficient for efficient

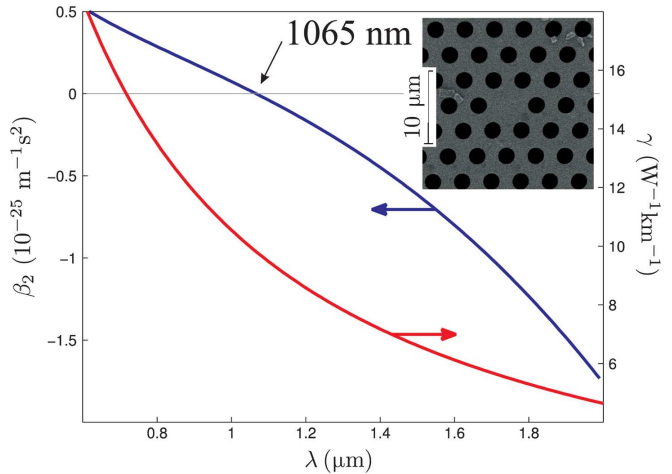


Fig. 2. Dispersion curve for the fundamental mode exhibiting a zero-dispersion wavelength at 1065 nm and nonlinear coefficient as a function of the wavelength. The inner plot shows a SEM image of the microstructured fiber cross-section.

parametric gain. A zoom of the fiber cross section of the MOF is shown in the inset of Fig. 2. The group velocity dispersion coefficient of the fundamental mode has been calculated using a finite element method and is shown in Fig. 2. As seen in the figure, the MOF has a zero-dispersion wavelength (ZDW) close to 1065 nm and a small dispersion slope ($\beta_3 = 0.56 \text{ ps}^3 \text{ km}^{-1}$) at this wavelength. The pitch and hole diameter are $4.14 \mu\text{m}$ and $2.61 \mu\text{m}$, respectively. The effective area is measured as $A_{\text{eff}} = 16.2 \mu\text{m}^2$ at 1065 nm. Its nonlinearity coefficient is also evaluated as $\gamma = 9.4 \text{ W}^{-1} \text{ km}^{-1}$. The optical loss of MOF is measured as 13.5 dB/km at 1060 nm. The 400 m-long MOF used in the setup produces 8.1 dB of optical loss including loss from the fiber splicing at each end with single-mode fiber pigtailed. The peak pump power P at the input of MOF is changed by varying the YDFA gain. It is obtained by dividing the average power by

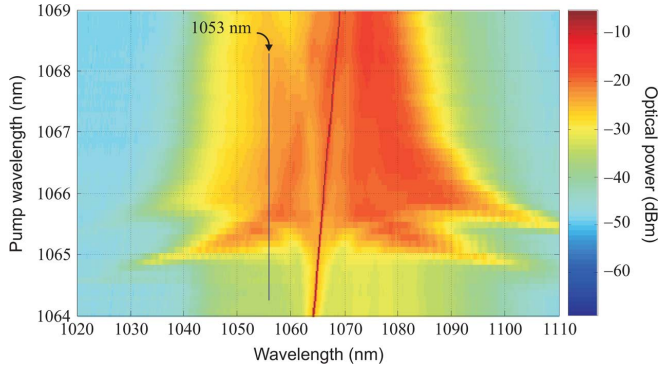


Fig. 3. Color plot of output spectra of the microstructured optical fiber as a function of the pump wavelength and without input signal. The pump power is set to $P = 2.4$ W. The vertical line indicates the signal wavelength used for parametric amplification.

the duty cycle and taking into account the optical loss (-1.25 dB) due to the fiber splicing at the input of FOPA. A peak pump power of as much as 4 W is coupled into the MOF.

III. RESULTS

First, we have performed OPA experiments in the absence of an input signal by tuning the center-wavelength of the pump so as to find the best pump wavelength that provides the maximum parametric gain for the signal at 1053 nm. Fig. 3 depicts the experimental output spectra as a color plot when scanning the pump wavelength from 1064 nm to 1069 nm. Here the power of the YDFA is set to yield approximatively 3.6 W of output pump power. The ASE spectra reveal a number of new frequency components created by four-wave mixing (FWM) process at both the sides of the pump wavelength in a range of 1030–1100 nm [16]. We can see in particular a large power asymmetry in the output spectra from 1060 nm pump wavelength. This asymmetry is mainly due to the additional contribution of Raman scattering that leads to higher-power (lower-power) Stokes (anti-Stokes) components [17]–[19]. This combined contribution of both the parametric and Raman gains is significant because the maximum Raman gain is located at 1100 nm. Nevertheless, we are able to identify the maximum ASE power at 1053 nm for a pump wavelength λ_p located at 1065.8 nm. This pump wavelength is kept in the following work.

The peak pump power is now set to $P = 2.4$ W to undertake parametric amplification process in presence of an input signal. Fig. 4 shows input and output spectra of FOPA when pump is switched on and off, respectively. For a fair comparison, the spectra are recorded with the 90/10 optical coupler at the input of OSA. In Fig. 4(a) the pump at $\lambda_p = 1065.8$ nm and signal at $\lambda_s = 1053$ nm are present at the input of FOPA. The signal power at pump-on is measured as -25.4 dBm. The signal power is 40 dB lower than that of the pump. On the other hand, Fig. 4(b) shows -9 dBm of the signal power at the output of FOPA when the pump is on. Comparing these two powers, it is seen that the signal is amplified by 16.4 dB in FOPA. This gain is obtained with the average power of the amplified signal. As the signal is converted from CW to rectangular pulses, the duty cycle of pump pulses needs to be taken into account. The duty cycle is 1/16 and it gives 11.1 dB of extra gain. Hence,

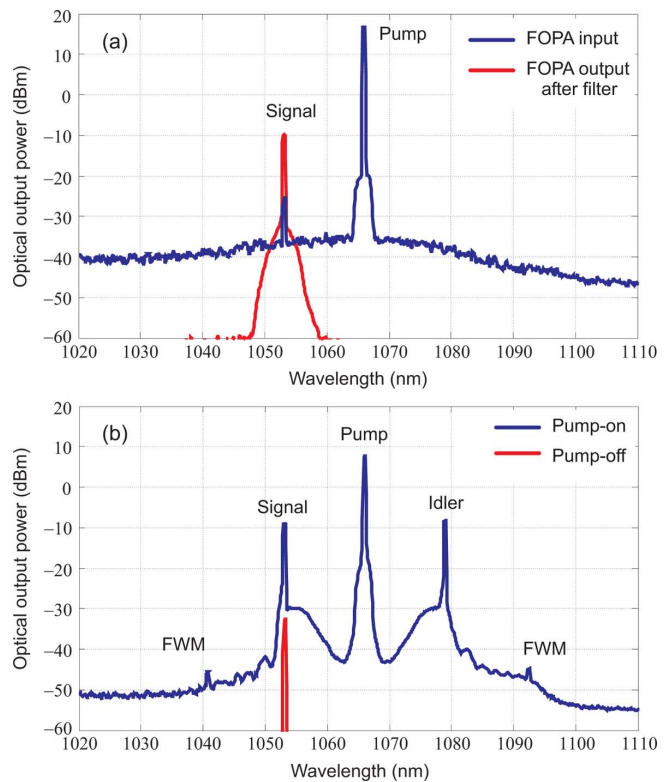


Fig. 4. Spectra of input and output of the microstructured fiber-based OPA for the 1053 nm signal at $P = 2.4$ W. In (a) the blue curve is a spectrum of the FOPA input and the red curve is a spectrum of the FOPA output filtered at 1053 nm. In (b) the blue curve is a spectrum of the FOPA output at pump-on whilst the red curve at pump-off.

this results in 27.5 dB of net gain. The output signal filtered at 1053 nm is also depicted in Fig. 4(a) that shows a good quality of amplification. A gross gain can also be obtained simply by comparing the output signal powers at pump-on and -off from optical spectra in Fig. 4(b). The signal power at pump-off is as low as -33.5 dBm at the output. Therefore, the gross gain of FOPA is obtained as much as 35.6 dB. This difference of 8.1 dB originates from the optical loss in the MOF. In Fig. 4(b), the idler appears at 1079 nm with the similar power to the signal. Cascaded four-wave mixing (FWM) signals also exist at 1040.7 nm and 1092.4 nm, respectively [20]. Second-order cascaded FWM signals can also be observed with the peak power over 3.4 W. Therefore, the FOPA exhibits high wavelength conversion efficiency. Despite of the filter at 1065.8 nm, residual ASE noise from the YDFA still remains at the FOPA input in Fig. 4(a). Due to this input ASE noise, parametric amplified spontaneous emission (ASE) bands are very significant in Fig. 4(b). As the input ASE noise is quite flat, the parametric gain bandwidth of FOPA would be estimated from the parametric ASE noise. This will be discussed later.

Time traces of the amplified signal at the output of FOPA are also measured. The output of FOPA is filtered at 1053 nm to suppress the residual pump and parametric ASE noise and measured by the PD and oscilloscope. Fig. 5 shows time traces of the amplified signal and pulsed pump at $P = 3.6$ W. For the sake of clarity, the time trace of the pump is displaced; the upper trace (blue trace) is the signal trace amplified by the pulsed pump

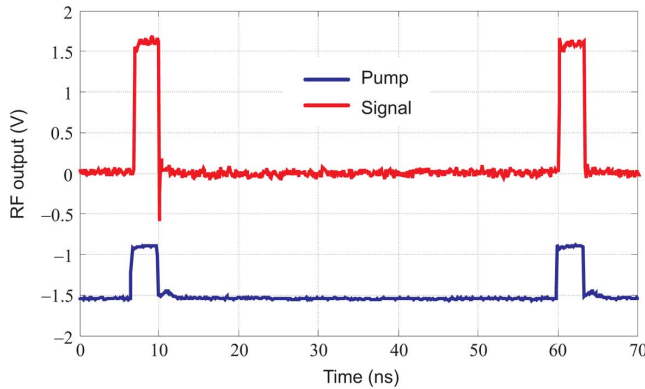


Fig. 5. Time traces recorded by the oscilloscope. The upper trace is a time trace of the signal amplified at $P = 3.6$ W at the output of FOPA. The lower trace is a time trace of the pulsed pump at the input of FOPA. The pump power is attenuated for PD.

at the output of FOPA and the lower trace is the pulsed pump trace at the input of FOPA. The pulsewidth and duty cycle of the amplified signal are measured as 3.4 ns and 1/16, respectively. These values correspond to those of the pump pulses and the signal is transformed to pulses by the pulsed pump. As such, it is clearly shown from the figure that a good quality of parametric amplification is achieved.

The parametric gain efficiency is also investigated with respect to the peak pump power P . Fig. 6(a) displays parametric gains for peak powers P from 0.4 W to 3.8 W. These gains are net parametric gains. The circle dots are parametric gains calculated with optical powers of the signal between input and output spectra of FOPA measured from OSA. On the other hand, the square dots are parametric gains obtained by comparing with RF outputs of the signal from the oscilloscope, i.e., time traces at the output of FOPA. Because of the low sensitivity of the PD, the RF gains below $P = 1.4$ W could not be measured. The negative gains below $P = 1$ W are in fact losses due to 8.1 dB of the fiber loss. The gains after $P = 1.2$ W overcome the fiber loss. As the power increases thereafter, the gains for the 1053 nm signal increases exponentially. However, the gain seems to saturate for the power over 2.8 W. This is because of the pump depletion and particularly parametric ASE noise. In fact, the parametric ASE noise increases significantly above $P = 2.8$ W. It is seen from the figure that the maximum net parametric gain is obtained as 35 dB for the optical gain at $P = 2.8$ W and 32.7 dB for the RF gain at $P = 3.8$ W. By taking into account 8.1 dB of the fiber loss, the maximum gross optical gain can be estimated as 43.1 dB.

Wavelength conversion efficiency of the FOPA is further studied with the idler at 1079 nm. Fig. 6(b) shows optical output powers of the signal and idler measured from optical spectra. The idler power is lower than that of signal below $P = 1.2$ W. However, the idler power overtakes the signal one at $P = 1.2$ W and the idler power is greater than the signal one thereafter. It is speculated that Raman gain involves in the idler power. Although the pump power is estimated below the Raman threshold, a small amount of Raman gain is expected to be present in the idler which is located at 3.2 THz of frequency

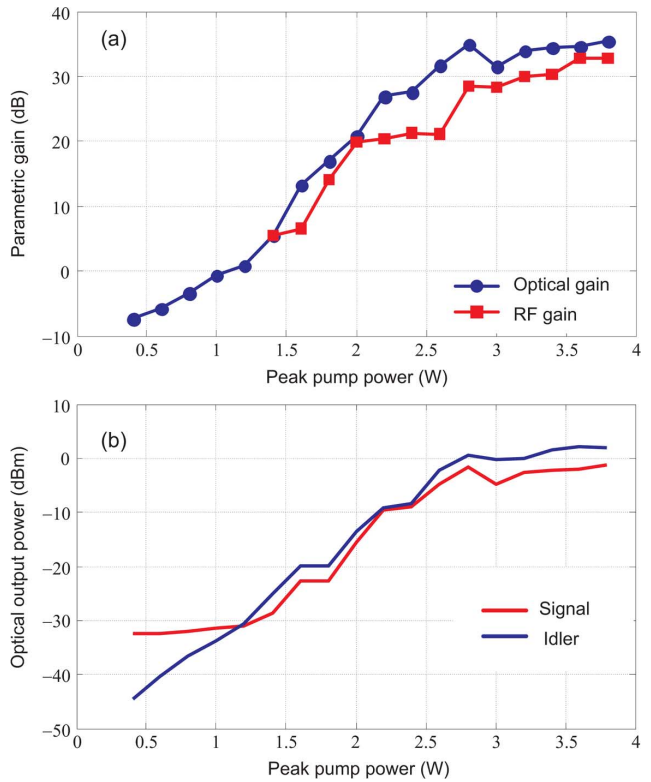


Fig. 6. (a) Net parametric gains with respect to the pump power. Circle dot (blue): parametric gains calculated with powers of the signal from optical spectra. Square dot (red): parametric gains calculated with RF signal outputs from the PD. (b) Optical output power of the signal (blue curve) and the idler (red curve).

offset from the pump. This leads to Raman-assisted parametric frequency conversion, as previously demonstrated [18].

IV. CURVE FITS

In order to compare the experimental measurements with the theory, the gain bandwidth and gain over power are fitted. The theoretical parametric gain is given by [1]

$$G_P(\Omega) = 1 + \left(\frac{\gamma P}{g(\Omega)} \sinh(g(\Omega)L_{\text{eff}}) \right)^2 \quad (1)$$

where $g^2 = (\gamma P)^2 - ((\kappa)/(2))^2$ is the parametric gain factor by unit length, and $\kappa = \beta_2 \Omega^2 + \beta_4 \Omega^4 + 2\gamma P$, the phase mismatch. $\Omega = 2\pi c(\lambda_s - \lambda_p)/(\lambda_s \lambda_p)$. $\beta_2 = -2\pi c \beta_3 (\lambda_p - \lambda_{ZDW})/\lambda_{ZDW}^2$ is the group velocity dispersion coefficient at the pump wavelength. β_4 is the fourth-order dispersion as $\beta_4 = -1.06 \cdot 10^{-55} \text{s}^4 \text{m}^{-1}$ obtained from numerical simulations. The fiber length is 400 m, but the effective length is obtained as $L_{\text{eff}} \simeq 229$ m by taking into account the fiber loss [21].

Fig. 6(b) clearly shows output power asymmetry between the signal and idler because of the involvement of Raman gain. The Raman gain is given by [21]

$$G_R(\Omega) = \exp \left(\frac{g_R(\Omega) P L_{\text{eff}}}{A_{\text{eff}}} \right) \quad (2)$$

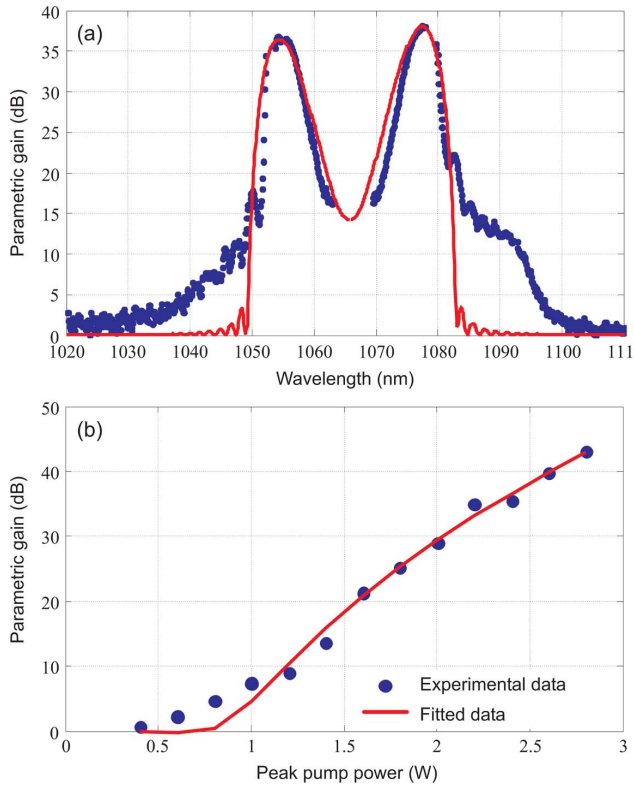


Fig. 7. (a) Gross parametric gain bandwidth. Circle dots (blue): Experimental gain bandwidth extracted from Fig. 4(b). Solid line (red): fitted curve using (3). (b) Gross parametric gain with respect to the peak pump power. Dotted line (blue): parametric gains retrieved from Fig. 6(a). Solid line (red): fitted curve.

where g_R is the Raman gain coefficient for fused silica fiber. As the signal is located on the anti-Stokes side of the pump, we must consider the whole Raman gain including both the anti-Stokes and Stokes gain band [19]. Therefore, the total gain can be approximated by

$$G(\Omega) = G_P(\Omega) + G_R(\Omega). \quad (3)$$

As the laser used for signal generation is not tunable, the experimental gain bandwidth at $P = 2.4$ W can be extracted readily from Fig. 4(b) for the case of gain bandwidth fitting. The extracted gain bandwidth is shown in Fig. 7(a). The signal, pump, idler and FWM sidebands are all suppressed and the gain values are adjusted so that the gain at 1053 nm matches to 35.6 dB of gross gain obtained in Fig. 4(b). Fig. 7(a) also shows in red the fitting curve obtained from (3). In this curve fit, λ_{ZDW} , γ and $g_{R\max}$ are set to be the fitting parameters and obtained as 1065 nm, $9.1 \text{ W}^{-1}\text{km}^{-1}$ and $2 \cdot 10^{-14} \text{ m/W}$ respectively. These values are close to those estimated by a finite element method. By taking into account the whole Raman gain curve including both the anti-Stokes and Stokes bands, the fitted curve in Fig. 7(a) shows a power asymmetry of the gain bandwidth and matches closely to the experimental curve. The idler power is greater than the signal power by around 2 dB. The power asymmetry is similar to the result reported in [19]. From the figure, the gain bandwidth of FOPA is estimated as a range of 1049–1083 nm for the given pump power. This is in good agreement with our previous measurement done in free space [8].

A gain-power curve is obtained from Fig. 6(a) for the case of gain-power fitting. As the gain seems to be saturated beyond $P = 2.8$ W, those values are not considered in the curve fit. The gains in Fig. 7(b) are set to gross gains. The same parameters as in the case of gain bandwidth fitting are used in the fitting. A fitting of gain-power curve gives $\lambda_{ZDW} = 1065.2 \text{ nm}$, $\gamma = 9.1 \text{ W}^{-1}\text{km}^{-1}$ and $g_R = 2 \cdot 10^{-14} \text{ m/W}$. The ZDW is slightly different to that obtained in the case of gain bandwidth fitting whilst γ remains the same in both the cases.

V. CONCLUSION

In conclusion, we have demonstrated a microstructured fiber-based optical parametric amplifier in a wavelength range near the $1 \mu\text{m}$ band in a fully all-fiber polarization-maintaining optical configuration. This has been achieved using a pump wave pulsed by an LiNbO₃ electro-optic intensity modulator specially designed for operating at 1060 nm. A CW input signal at 1053 nm is converted to a pulsed signal and amplified by the pulsed pump at 1065.8 nm. Maximum net gains of 35 dB and 32.7 dB have been measured both optically and electrically, respectively. From the amplified signal time traces, it is shown that a good quality of parametric amplification has been achieved in terms of optical contrast and temporal stability. By investigating the idler conversion efficiency, it is observed that the idler power is greater than the signal power because of Raman-assisted parametric wavelength conversion. The gain bandwidth of FOPA has also been estimated by means of parametric ASE spectra in a range of 1049–1083 nm. A fitting with the experimental results has given the values of γ and ZDW which are in a good agreement with those estimated from numerical simulations.

The FOPA demonstrated here may be used for optical sampling, optical parametric chirped-pulse amplification (OPCPA) and short pulse processing in the $1-\mu\text{m}$ Ytterbium band. It is important to stress here that parametric amplification has been undertaken in the continuous-wave pumping regime by use of a phase modulator specially designed at 1060 nm but only 3.5 dB net gain has been obtained. This can easily be improved by reducing the whole optical loss of the fiber optic components and the microstructured fiber, and using the Stokes band instead of the anti-Stokes one of the FOPA. For completeness, we expect in a future work to measure the whole gain bandwidth and the noise figure of the FOPA with a tunable signal source.

ACKNOWLEDGMENT

The authors acknowledge the European INTERREG-IVA programme and the Fond Européen de Développement Régional (FEDER). They thank Photline Technologies for manufacturing the electro-optic modulator.

REFERENCES

- [1] M. E. Marhic, *Fiber Optical Parametric Amplifiers, Oscillators and Related Devices*. Cambridge, U.K.: Cambridge University Press, 2007.
- [2] J. Hansryd, P. A. Andrekson, M. Westlund, J. Lie, and P.-O. Hedekvist, “Fiber-based optical parametric amplifiers and their applications,” *IEEE J. Sel. Top. Quantum Electron.*, vol. 8, no. 3, pp. 506–520, May 2002.
- [3] C. J. McKinstry, S. Radic, and A. H. Gnauck, “All-optical signal processing by fiber-based parametric devices,” *Opt. Photon. News*, vol. 18, no. 3, pp. 34–40, 2007.

- [4] J. Fan, A. Dogariu, and L. J. Wang, "Parametric amplification in a microstructure fiber," *Appl. Phys. B*, vol. 81, pp. 801–805, 2005.
- [5] J. E. Sharping, M. Fiorentino, P. Kumar, and R. S. Windeler, "Optical-parametric oscillator based on four-wave mixing in microstructure fiber," *Opt. Lett.*, vol. 27, no. 19, pp. 1675–1677, 2002.
- [6] A. Chen, G. Wong, S. Murdoch, R. Leonhardt, J. Harvey, J. Knight, W. Wadsworth, and P. Russell, "Widely tunable optical parametric generation in a photonic crystal fiber," *Opt. Lett.*, vol. 30, pp. 762–764, 2005.
- [7] J. E. Sharping, "Microstructure fiber based optical parametric oscillators," *J. Lightw. Technol.*, vol. 26, no. 14, pp. 2184–2191, 2008.
- [8] T. Sylvestre, A. Kudlinski, A. Mussot, J.-F. Gleyze, A. Jolly, and H. Maillotte, "Parametric amplification and wavelength conversion in the 1040–1090 nm band by use of a photonic crystal fiber," *Appl. Phys. Lett.*, vol. 94, no. 11, pp. 111104-1–111104-3, 2009.
- [9] D. Besnard, "The megajoule laser program - ignition at hand," *Eur. Phys. J. D*, vol. 44, no. 2, pp. 207–213, 2007.
- [10] C. A. Haynam *et al.*, "National ignition facility laser performance status," *Appl. Opt.*, vol. 46, no. 16, pp. 3276–3303, 2007.
- [11] M. Hanna, F. Druon, and P. Georges, "Fiber optical parametric chirped-pulse amplification in the femtosecond regime," *Opt. Exp.*, vol. 14, no. 7, pp. 2783–2790, 2006.
- [12] C. Caucheteur, D. Bigourd, E. Hugonnot, P. Sriftgiser, A. Kudlinski, M. Gonzalez-Herraez, and A. Mussot, "Experimental demonstration of optical parametric chirped pulse amplification in optical fiber," *Opt. Lett.*, vol. 35, no. 11, pp. 1786–1788, 2010.
- [13] A. Jolly, J.-F. Gleyze, P. Di Bin, and V. Kermène, "Demonstration of a true single-shot 100 GHz-bandwidth optical oscilloscope at 1053–1064 nm," *Opt. Exp.*, vol. 17, no. 14, pp. 12109–12120, 2009.
- [14] P. A. Andrekson, "Ultrahigh bandwidth optical sampling oscilloscope," in *Optical Fiber Communications*, Los Angeles, CA, 2004, no. Paper TuO1.
- [15] P. S. J. Russell, "Photonic crystal fibers," *J. Lightwave Technol.*, vol. 24, no. 12, pp. 4729–4749, 2006.
- [16] W. J. Wadsworth, N. Joly, J. C. Knight, T. A. Birks, F. Biancalana, P. St., and J. Russell, "Supercontinuum and four-wave mixing with Q-switched pulses in endlessly single-mode photonic crystal fibres," *Opt. Exp.*, vol. 12, no. 2, pp. 209–309, 2004.
- [17] D. A. Chestnut, C. J. S. de Matos, and J. R. Taylor, "Raman-assisted fiber optical parametric amplifier and wavelength converter in highly nonlinear fiber," *J. Opt. Soc. Amer. B*, vol. 19, no. 8, pp. 1901–1904, 2002.
- [18] T. Sylvestre, H. Maillotte, E. Lantz, and P. Tchofo Dinda, "Raman-assisted parametric frequency conversion in a normally dispersive single-mode fiber," *Opt. Lett.*, vol. 24, pp. 1561–1563, 1999.
- [19] A. S. Y. Hsieh, G. K. L. Wong, S. G. Murdoch, S. Coen, F. Vanholsbeeck, R. Leonhardt, and J. D. Harvey, "Combined effect of raman and parametric gain on single-pump parametric amplifiers," *Opt. Exp.*, vol. 15, pp. 8104–8114, 2007.
- [20] T. T. Ng, J. L. Blows, J. T. Mok, R. W. McKerracher, and B. J. Eggleton, "Cascaded four-wave mixing in fiber optical parametric amplifiers: Application to residual dispersion monitoring," *J. Lightw. Technol.*, vol. 23, no. 2, pp. 818–826, Feb. 2005.
- [21] G. P. Agrawal, *Nonlinear Fiber Optics*. New York: Academic, 2007.

Min Won Lee received the M.Sc. degree from Ajou university, Suwon, South Korea in 1998 and the Ph.D. degree from the Université de Franche-Comté, Besançon, France in 2002. His doctoral research was concerned with chaotic dynamics behavior, chaos synchronization, optical telecommunications and chaos encryption.

After his Ph.D., he worked in Optoelectronic group at Bangor University, United Kingdom from 2002 to 2008. He was involved in development of chaos communications systems using external-cavity laser diodes. He joined FEMTO-ST institute, Besançon, France in 2009. His current research interests include fibre optical parametric amplifiers, Raman fibre lasers, Brillouin sensing applications using photonic crystal fibres.

Thibaut Sylvestre was born in Besançon, France, in 1973. He received the M.Sc. and Ph.D. degrees in "Sciences Pour l'Ingénieur" from the Université de Franche-Comté, Besançon, France, in 1995 and 1999, respectively.

He then started a two-year postdoctoral stay abroad in the field of nonlinear fiber optics with the Optics and Acoustics Department, Université libre de Bruxelles (ULB), Brussels, Belgium. In 2001, he was appointed a full-time researcher in charge with the Centre National de la Recherche Scientifique (CNRS), FEMTO-ST institute, Besançon, France. He is involved with theo-

retical and experimental studies of fundamental nonlinear optical phenomena with the aim of investigating potential applications to telecommunications and other domains.

Dr. Sylvestre is a member of the Optical Society of America and of the IEEE society.

Michaël Delqué was born in Belfort, France, in 1980. He received the M.Sc. and the Ph.D. degrees in "Sciences Pour l'Ingénieur" from the Université de Franche-Comté, Besançon, France, in 2002 and 2006, respectively.

He started in 2007 a two-year postdoctoral stay in the field of instabilities in nonlinear optics with the OPERA-Photonics Service, Université libre de Bruxelles (ULB), Brussels, Belgium. Since 2009, he is involved in a postdoctoral project in FEMTO-ST Institute, Besançon, France. This international program aims at deep understanding of Brillouin effect in photonic crystal fibers.

Alexandre Kudlinski was born in Béthune, France, on November 25, 1979. He received the Ph.D. degree in photonics from the University of Science and Technology, Lille, France, in 2005.

From 2005 to 2006, he was with the Centre for Photonics and Photonic Materials of the University of Bath, Bath, U.K., where he worked on photonic crystal fibers (PCFs). Since 2006, he has been working at the Laboratoire de Physique des Lasers, Atomes et Molécules (PhLAM), University of Lille I, Villeneuve d'Ascq, France, where his research interests are on the design, fabrication, and characterization of PCFs for new optical applications, including supercontinuum sources.

Arnaud Mussot was born in Vesoul, France, on August 4, 1976. He received the Ph.D. degree in optical engineering in 2004 from the Université de Franche-Comté, Besançon, France.

From 2004 to 2005 he was with the Commissariat à l'Energie Atomique in Bordeaux, France, and worked on high energy Ytterbium lasers. Since 2005, he has been working at the Laboratoire de Physique des Lasers, Atomes et Molécules (PhLAM), University of Lille I, Villeneuve d'Ascq, France, where is mainly engaged in supercontinuum generation and in the study of instability processes in fiber ring cavities. His research interests were parametric amplification and supercontinuum generation in optical fibers.

Alain Jolly was born in Nantes, France, in 1959. He received the Electronical Engineer Degree from the Conservatoire National des Arts et Métiers in 1987, in Paris, then completed with the Ph.D. degree in physics, and more recently the HDR Degree from the University of Paris XVIII, France.

He is working with the Commissariat à l'Energie Atomique (CEA) in France. His research topics have covered the field of electronics developments for high energy physics prototyping dedicated to CERN experiments, then the field of opto-electronics dedicated to nuclear physics, laser physics developments and fibered laser systems under the auspices of laser programs dedicated to the search of Inertial Confinement Fusion. He initiated a couple of research projects in the areas of diode-pumped solid-state materials and of ultrafast all-optical sampling using fiber systems. Since 2010, his more recent research work include simulation within the frame of Infrared and ElectroMagnetics fields design dedicated to spatial applications.

Hervé Maillotte was born in Besançon, France, in 1962. He received the Ph.D. degree in engineering science from the Université de Franche-Comté, Besançon, France, in 1990.

After about two years with a laser company and a spacecraft firm, he joined the Laboratoire d'Optique P.M. Duffieux, in 1991, as a CNRS Researcher, where he initiated a research project on parametric amplification in optical fibres. He is also involved with the development of third-order nonlinear organic materials and Z-scan measurements, spatial soliton in Kerr and photorefractive media, four-wave mixing and stimulated scattering in conventional and microstructured fibers, supercontinuum generation, opto-acoustics in microstructured fibers. Since 2005, he is the head of the Département d'Optique P.M. Duffieux, FEMTO-ST Institute.

Photonic crystal fiber mapping using Brillouin echoes distributed sensing

B. Stiller,¹ S. M. Foaleng,² J.-C. Beugnot,² M. W. Lee,¹ M. Delqué,¹
G. Bouwmans,³ A. Kudlinski,³ L. Thévenaz,² H. Maillotte,¹ and
T. Sylvestre¹

¹Institut FEMTO-ST, Université de Franche-Comté, F-25030 Besançon, France

²Group for Fibre Optics, École Polytechnique Fédérale de Lausanne, CH-1015 Switzerland

³Université Lille 1, IRCICA, Laboratoire PhLAM, 59655 Villeneuve d'Ascq, France

[*birgit.stiller@femto-st.fr](mailto:birgit.stiller@femto-st.fr)

Abstract: In this paper we investigate the effect of microstructure irregularities and applied strain on backward Brillouin scattering by comparing two photonic crystal fibers drawn with different parameters in order to minimize diameter and microstructure fluctuations. We fully characterize their Brillouin properties including the gain spectrum and the critical power. Using Brillouin echoes distributed sensing with a high spatial resolution of 30 cm we are able to map the Brillouin frequency shift along the fiber and get an accurate estimation of the microstructure longitudinal fluctuations. Our results reveal a clear-cut difference of longitudinal homogeneity between the two fibers.

© 2010 Optical Society of America

OCIS codes: (060.2270) Fiber characterization; (060.2280) Fiber design and fabrication; (060.2370) Fiber optics sensors; (060.4005) Microstructured fibers; (060.5295) Photonic crystal fibers; (290.5830) Scattering, Brillouin.

References and links

1. E. P. Ippen, and R. H. Stolen, "Stimulated Brillouin scattering in optical fibers," *Appl. Phys. Lett.* **21**(11), 539–541 (1972).
2. M. Niklès, L. Thévenaz, and P. A. Robert, "Simple distributed fiber sensor based on Brillouin gain spectrum analysis," *Opt. Lett.* **21**(10), 758–760 (1996).
3. L. Thévenaz, "Brillouin distributed time-domain sensing in optical fibers: state of the art and perspectives," *Front. Optoelectron. China* **3**(1), 13–21 (2010).
4. L. Zou, X. Bao, and L. Chen, "Distributed Brillouin temperature sensing in photonic crystal fiber," *Smart Mater. Struct.* **14**(3), S8 (2005).
5. P. Dainese, P. S. J. Russell, N. Joly, J. C. Knight, G. S. Wiederhecker, H. L. Fragnito, V. Laude, and A. Khelif, "Stimulated Brillouin scattering from multi-GHz-guided acoustic phonons in nanostructured photonic crystal fibres," *Nat. Phys.* **2**(6), 388–392 (2006).
6. A. Minardo, R. Bernini, W. Urbanczyk, J. Wojcik, N. Gorbatov, M. Tur, and L. Zeni, "Stimulated Brillouin scattering in highly birefringent microstructure fiber: experimental analysis," *Opt. Lett.* **33**, 2329–2331 (2008).
7. J.-C. Beugnot, T. Sylvestre, D. Alasia, H. Maillotte, V. Laude, A. Monteville, L. Provino, N. Traynor, S. Foaleng Mafang, and L. Thévenaz, "Complete experimental characterization of stimulated Brillouin scattering in photonic crystal fiber," *Opt. Express* **15**(23), 15517–15522 (2007), <http://www.opticsinfobase.org/abstract.cfm?uri=oe-15-23-15517>.
8. M. Karlsson, "Four-wave mixing in fibers with randomly varying zero-dispersion wavelength," *J. Opt. Soc. Am. B* **15**(8), 2269–2275 (1998).
9. M. Niklès, L. Thévenaz, and P. A. Robert, "Brillouin gain spectrum characterization in single-mode optical fiber," *J. Lightwave Technol.* **15**(10), 1842–1851 (1997).
10. R. G. Smith, "Optical power handling capacity of low loss optical fibers as determined by stimulated Raman and Brillouin scattering," *Appl. Opt.* **11**(11), 2489 (1972).

11. G. P. Agrawal, *Nonlinear fiber optics*, 3rd ed. (Academic Press, 2001).
 12. M. O. V. Deventer and A. J. Boot, "Polarisation properties of stimulated Brillouin scattering in single mode fibers," *J. Lightwave Technol.* **12**(4), 585–590 (1994).
 13. R. Boyd, K. Rzazewski and P. Narum, "Noise initiation of stimulated Brillouin scattering," *Phys. Rev. A* **42**(9), 5514–5521 (1990).
 14. S. L. Floch and P. Cambon, "Theoretical evaluation of the Brillouin threshold and the steady-state Brillouin equations in standard single-mode optical fibers," *J. Opt. Soc. Am. A* **20**(6), 1132–1137 (2003).
 15. S. Foaleng Mafang, J.-C. Beugnot and L. Thévenaz, "Optimized configuration for high resolution distributed sensing using Brillouin echoes," *Proc. SPIE*, UK, Edinburgh 75032C, 7503 (2009).
 16. F. Poletti, K. Furusawa, Z. Yusoff, N. G. R. Broderick, and D. J. Richardson, "Nonlinear tapered holey fibers with high stimulated Brillouin scattering threshold and controlled dispersion," *J. Opt. Soc. Am. B* **24**(9), 2185–2194 (2007).
 17. Crystal Fibres, <http://www.nktphotronics.com/>.
 18. T. G. Euser, J. S. Y. Chen, M. Scharrer, P. S. J. Russell, N. J. Farrer, and P. J. Sadler, "Quantitative broadband chemical sensing in air-suspended solid-core fibers," *J. Appl. Phys.* **103**, 103108 (2008).
-

1. Introduction

Brillouin Scattering in optical fibers results from the interaction between light and acoustic waves through the effects of electrostriction [1]. The Brillouin gain and Brillouin frequency shift (BFS) depend on the overlap of these waves in the fiber core and on the material. Temperature and strain influence the velocity of the acoustic wave and thus the BFS. Since the acoustic modes are sensitive to temperature and strain, Brillouin backscattering has widely been studied for distributed sensing in single mode fibers (SMF) [2, 3] as well as in photonic crystal fibers (PCF) [4]. Due to their high nonlinear efficiency, PCFs have received particular attention for temperature and strain sensing. It has recently been reported that PCF with small core exhibit in most cases a multi-peak Brillouin spectrum due to the periodic air-hole microstructure [5–7]. This aspect could be advantageously used for simultaneous strain and temperature distributed measurements. However, when multi peaks overlap, the spectrum broadens and the data analysis becomes more difficult. Another aspect that limits distributed measurements is the inhomogeneity of opto-geometrical parameters along the fiber which has an influence on the BFS. This is even more crucial in PCFs since their fabrication requires an accurate control of more parameters than for SMF during the drawing process. In this work we fully characterize two PCFs with the nearly same air-hole microstructure but drawn with different parameters in order to minimize diameter fluctuations. The experiments presented in this work are twofold: we first perform an integrated measurement of the Brillouin gain spectrum (BGS) and the critical power (also called Brillouin threshold) and then a Brillouin-echoes distributed sensing (BEDS) measurement. Our results show that these two fibers exhibit a single peak in the gain spectrum like an SMF and that their critical powers of stimulated scattering are in good agreement with theory. The impact of structural irregularities and strain on the BFS is also clearly evidenced. We observe in particular long- and short-scale fluctuations in the BFS. Although short-scale longitudinal fluctuations were studied in Ref. [8], it is the first time that the short-scale fluctuations are investigated in optical fibers using the BEDS technique. We further show that it is possible to extract the effective refractive index all along the fiber from the distributed BFS measurements, which allows a quantitative estimation of fiber irregularities. With these measurements we are able to draw conclusions about the fiber inhomogeneity induced by the drawing process.

2. Experimental results

The two PCFs under test have a hexagonal hole structure and their cross-sections are shown in the insets of Fig. 1. They originate from the same stack, but from different intermediate canes. The cane used to manufacture fiber #1 was 3.8 mm in outer diameter and drawn at a relatively

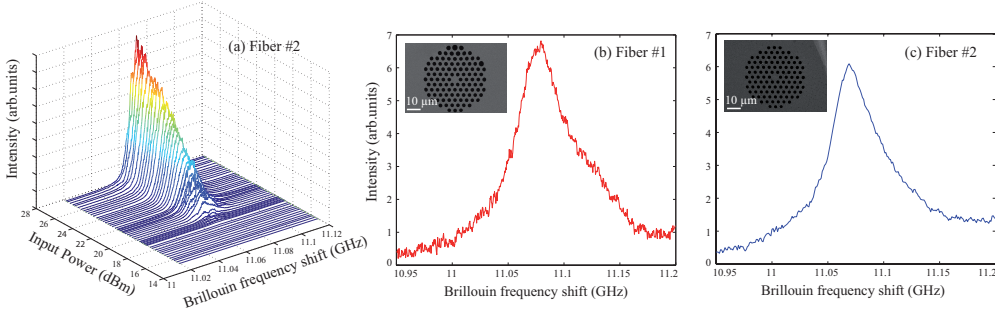


Fig. 1. (a) Brillouin gain spectrum for fiber #2 with increasing input power. Brillouin spectrum for an input pump power of 11 dBm, which is under the critical power, for (b) fiber #1 and (c) fiber #2. The PCF cross-sections are shown in the insets.

high temperature (low tension). For fiber #2 the cane was drawn with the same parameters, except for the temperature that was much lower than for fiber #1, leading to a much higher tension during the drawing process. At this stage, the outer diameter fluctuations of both canes were comparable, but the air holes were slightly smaller in cane #1 than in cane #2. The canes were then inserted into jacketing tubes, and drawn down into fibers. Both fibers were drawn with comparable parameters, although a slightly higher pressure was used for fiber #1 to inflate air holes. The outer diameter fluctuations measured during the drawing process were about 2% for fiber #1 and less than 1% for fiber #2. Both of the fibers are designed to get a zero-dispersion-wavelength around 1060 nm and have an attenuation of 5 dB/km (#1) and 8.6 dB/km (#2) at 1.5 μm . Their effective mode area (EMA) is about 15 μm^2 (#1) and 16 μm^2 (#2) at 1.5 μm found by calculation based on scanning electron microscopy (SEM) images. The core, hole diameter, pitch, and length are about 5.5 μm , 2.7 μm , 4.1 μm , 100 m for fiber #1 and 5.5 μm , 2.3 μm , 3.9 μm , 400 m for fiber #2.

2.1. Brillouin gain spectrum

Before the distributed analysis of the BFS along the fibers we have first performed a direct measurement of the gain spectrum and the critical power using the same experimental setup as in Ref. [7]. Since in the latter case the scattered light is affected by strain, differences of temperature and air-hole microstructure fluctuations along the fiber, it is called integrated measurement. As an example, the Brillouin spectrum dynamics in function of the pump power obtained from fiber #2 is shown in Fig. 1(a). The full width at half maximum (FWHM) for fiber #1 and #2 narrows from 55 MHz and 60 MHz respectively in the spontaneous regime to 10 MHz in the stimulated one. For comparison the FWHM in a single-mode fibers (SMF) in the spontaneous regime is about 27 MHz [9]. This Brillouin linewidth broadening is due to fiber inhomogeneities and to the photonic crystal cladding that allows the simultaneous generation of several longitudinal acoustic modes, as previously demonstrated [7]. To get better insight, Fig. 1(b) and 1(c) show the Brillouin spectra at 11 dBm which is below the critical power of stimulated scattering. One can see that there exists a single peak as in an SMF and an asymmetry in the spectra can be noticed, particularly for fiber #1. This asymmetry suggests the presence of two or more acoustic modes with close Brillouin frequency shift and thus overlapping gain spectra. Let us now briefly recall the relation that links the BFS to the effective refractive index of the fiber that reads [9]:

$$v_B = \frac{2n_{\text{eff}}V_L}{\lambda_P} \quad (1)$$

For a refractive index of $n_{\text{eff}} \approx n = 1.44$ and an acoustic velocity of $V_L = 5960 \text{ m/s}$ (longitu-

dinal) the frequency of the Stokes wave is shifted by $v_B = 11.07$ GHz at $\lambda_P = 1.55$ μm pump wavelength, in very good agreement with the measured Brillouin spectra shown in Fig. 1.

2.2. Critical power of stimulated Brillouin scattering

The critical power is also measured for the two fibers. The estimated value for the critical power is given by [10]:

$$P_{\text{cr}} = \frac{C \cdot K \cdot A_{\text{eff}}}{g_B \cdot L_{\text{eff}}} \quad (2)$$

where A_{eff} is the EMA, L_{eff} the effective length, $C=21$ and g_B the Brillouin gain. The Brillouin gain can be determined by measuring the FWHM in the spontaneous Brillouin regime¹. For fiber #1 the Brillouin gain is $g_B = 1.25 \cdot 10^{-11} \text{ mW}^{-1}$ and for fiber #2 we obtain $g_B = 1.15 \cdot 10^{-11} \text{ mW}^{-1}$. The value of K depends on the fiber type. In a polarization maintaining fiber $K=1$ whereas in an SMF $K=3/2$ as the polarization changes randomly [12]. This definition assumes that the critical power is reached when the reflected Stokes power equals the transmitted power. However, for practical reasons the critical power can be defined at the point where the reflected power is 1% of the injected one [13]. This requires to modify Eq. (2). The numerical factor 21 is approximately the natural logarithm of the gain [10]. Floch et al. [14] adjusted this factor depending on the fiber length. Adapting the equation to the 1%-definition changes the numerical factor C depending on fiber length and attenuation to 15.5 for fiber #1 and 16 for fiber #2 which is obtained by numerical approximations. With the measured and calculated values the theoretical critical power can be estimated at 25.1 dBm for fiber #1 and 20.2 dBm for fiber #2. The critical power for stimulated scattering is measured with the same setup as for the Brillouin spectrum without the heterodyne detection [7]. The results for the backscattered and transmitted power depending on the input power for both fibers are shown in Fig. 2. The experimental value of the critical power is obtained as 26.7 dBm for fiber #1 and 20.2 dBm for fiber #2 taking into account splicing losses of about 1.5 dB. Comparing the theoretical values with the experimental ones we found them in good agreement for both fibers. Assuming the fairly high birefringence in those fibers, the factor 3/2 is probably too large, Fiber #1 being shorter. This may be a tentative explanation of the discrepancy with Fiber #1.

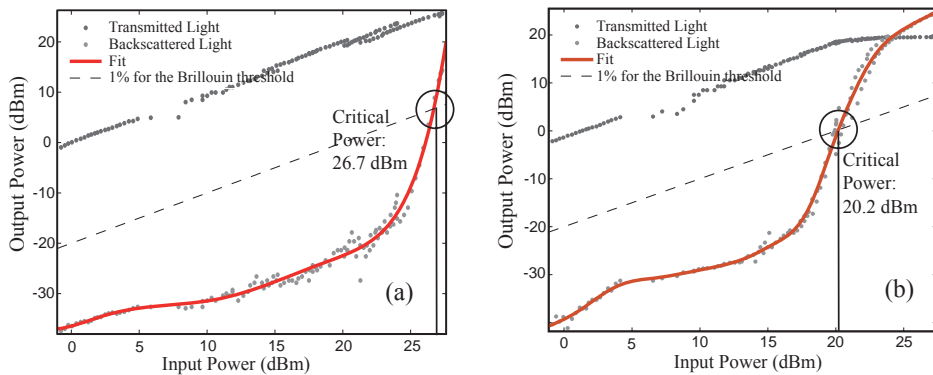


Fig. 2. Backscattered and transmitted power versus input power of (a) fiber #1 and (b) fiber #2

¹using $g_B = \frac{2\pi n^2 p_{12}^2}{c \lambda_p^2 \rho_0 v_A \Delta v_B}$ [11]

2.3. Distributed Sensing using Brillouin Echoes

The BEDS technique basically differs from a conventional Brillouin optical time domain analysis (BOTDA) [2]. Indeed, the distributed measurement of precise Brillouin gain spectrum (BGS) can be made with enhanced spatial resolution by applying short π -phase shifts in the CW pump wave instead of using rectangular intensity pulses. This configuration offers the advantage to measure a gain spectrum unaltered by the pump spectrum and to experimentally estimate the acoustic lifetime. The experimental setup is schematically shown in Fig. 3(a) and a complete description of the method can be found in Refs. [3, 15]. The output of an external cavity laser at 1551 nm is split into two arms by a polarization-maintaining coupler. One arm serves for the cw probe and the other one for the pump. An intensity modulator, driven by a microwave generator, creates two sidebands tuned to the BFS of the two PCF measured above.

The probe wave is then amplified by an EDFA and injected into the PCF. The other arm is connected to the opposite end of the PCF through an optical circulator. The pump wave is modulated at a 10 kHz repetition rate via a phase modulator driven by a pulse generator. A π -phase shift is applied on the pump for a 3-ns short time, so that the reflected Stokes light interferes destructively with the probe signal, equivalent to a Brillouin loss process. A tunable fiber Bragg grating (FBG) connected to a second optical circulator filters out the Stokes-wave and residual pump light. The output cw probe is then monitored with an oscilloscope while it is scanned around the BFS so that all BFS shifts due to inhomogeneities and strain can be detected. The spatial resolution is about 30 cm which is determined by the pulse duration. Since the acoustic wave has a finite lifetime of several ns the backscattered response of the BEDS system is partially decaying during the phase pulse duration. This creates a second echo when the pump is restored to its original state after the pulse [15]. To avoid this undesirable effect we turn off the pump immediately after the phase pulse so that no more light can be reflected after the pulse end and no trailing light is present [3]. This is achieved by adding in the experimental setup a second intensity modulator before the phase modulator to produce a pump intensity pulse of 30 ns with a π phase pulse (3 ns) at its end. Fig. 3(b) illustrates the result of the BEDS measurement for fiber #1 while the probe modulation frequency is swept around the BFS. The data were averaged and fitted by using a convolution with a rectangle to reduce measurement noise. Figure 3 gets further insight into the longitudinal fluctuations of the BFS. As it can be seen, the distributed BFS exhibit both long- and short scale longitudinal fluctuations that are due to diameter fluctuations. Particularly for fiber #1 we can identify a long-scale sinusoidal variations of about 8 MHz with a half-period of approximatively 50 m that corresponds to the middle of the fiber. This BFS variation is due to the strain induced by the fiber coiling as a half of the fiber length is coiled on the other half. This was easily confirmed

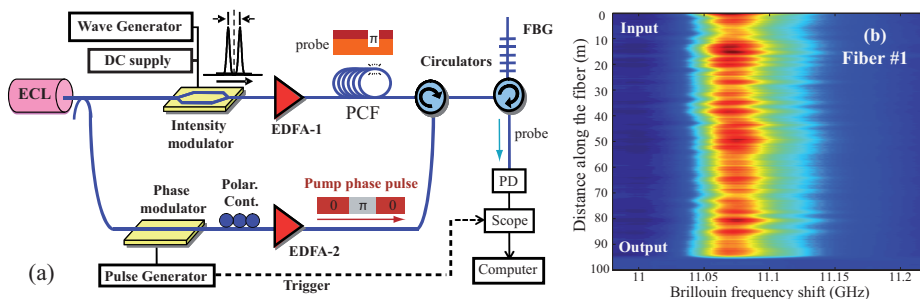


Fig. 3. (a) Experimental setup of the BEDS system. ECL: external cavity laser; EDFA: erbium-doped fiber amplifier; PD: photodiode. (b) Color plot of Brillouin frequency shift along fiber #1. The spatial resolution is 30 cm and the frequency resolution is 2 MHz.

by inverting the PCF in the setup. On the other hand, the short-scale longitudinal fluctuation (about 5 ± 1 MHz every 2 m) seen in Fig. 4(a) indicates a random geometric variation of the air-hole microstructure. Note that this cannot be attributed to the influence of birefringence in the PCF since the variation on the refractive index can be estimated to $7 \cdot 10^{-4}$ using Eq. (1) which is well above the birefringence of the PCF (estimated phase birefringence by simulation: $\approx 1.5 \cdot 10^{-5}$, measured group birefringence: $\approx 5 \cdot 10^{-6}$). Figure 4(b) shows a 5 MHz shift in BFS for fiber #2 between 80 m and 180 m which corresponds to one layer of the fiber coil. In this way we are able to detect the strain applied to one layer. The short scale fluctuation is smaller (3 ± 1 MHz, every 2-3 m of the fiber) and can be attributed to geometrical fluctuations of the air-hole microstructure.

It is clear from Fig. 4 that the longitudinal fluctuations in BFS are less significant for fiber #2 than fiber #1 as the drawing process was better controlled. This is verified by studying the fast Fourier transform of the BFS trace shown in the insets of Fig. 4. We notice that for fiber #1 the frequencies pedestal around the main peak is wider than for fiber #2. In order to obtain an estimation of the diameter or microstructure fluctuations along the fibers, we have derived the distributed effective refractive index n_{eff} from the distributed BFS as they are proportionately linked by Eq. (1) (V_L and λ_P are known). In the following, we assume that the main contributions to these fluctuations are due to homothetic variations of the microstructure, i.e. to fluctuations of the outer diameter only. We neglect here possible longitudinal inhomogeneities of individual air holes or pitch, as well as possible twists induced during the drawing process because of several reasons. The variation of the effective refractive index can derive from different origins: applied strain, temperature variation, longitudinal variations of the microstructure, individual air holes inhomogeneities or variation of the pitch. We assume that the temperature do not influence the experiment because of the short experiment duration. The impact of strain is observed in long scale fluctuations which indicate the effect of the fiber coiling. Moreover the variation of the pitch has an important impact on the effective refractive index, which can be found in Ref. [16]. However several SEM-images at different sections of the fibers show that there is no measurable variation of the pitch and singular air holes. From our numerical simulation using Comsol it is found that the variation of the microstructure scale is the main cause of the variation of the effective refractive index. So we decided to vary the scale of the microstructure since this seemed to be the most general variation. To relate geometrical variations to n_{eff} the dependency of n_{eff} on the microstructure scale has been computed by using the PCF cross-section of the two fibers via Comsol software (Fig. 5). A simulation based on the original image (corresponding to 100% in Fig. 5) yields a certain amount of n_{eff} (1.434 for #2 and 1.432 for #1). By varying the scale of the original SEM-image different values of n_{eff} are obtained and depicted in Fig. 5 for the two fibers.

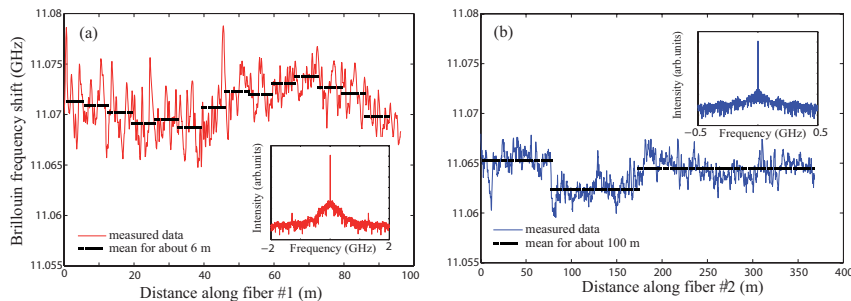


Fig. 4. Mapping of the Brillouin frequency shift along (a) fiber #1 and (b) fiber #2 showing the effect of inhomogeneities and strain. The insets show the Fourier transforms.

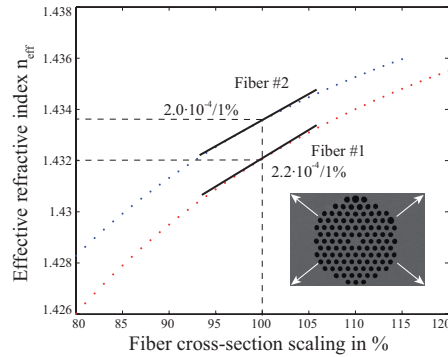


Fig. 5. Variation of the effective refractive index while tuning the scale of the SEM-image

We have computed the local derivation of the obtained relation between n_{eff} and the geometrical scale around 100% as indicated by the tilt solid lines in Fig. 5. The effective refractive index changes by $2.2 \cdot 10^{-4}$ (#1) and $2.0 \cdot 10^{-4}$ (#2) for 1%. This is compared to the fluctuations of the effective refractive index in the fibers under test by using Eq. (1). The variation of the short scale fluctuations (5 ± 1 MHz for fiber #1 and 3 ± 1 MHz for fiber #2) corresponds to $2.9 \pm 0.6\%$ and $1.9 \pm 0.6\%$ of scale or diameter fluctuations, respectively. The large scale variation is 4.7% (8 MHz for #1) and 3.2% (5 MHz for #2). This means that the maximum core diameter fluctuation is 5.5 ± 0.3 μm (fiber #1) and 5.5 ± 0.2 μm (fiber #2). Since polarization and strain can influence the variation of the effective refractive index the contribution of the structure size is expected to be below these values. This estimation confirms the higher quality of the drawing process obtained for fiber #2. Note that the fluctuations measured in the present work are in good agreement with the specifications from state-of-the-art PCF manufacturers [17, 18].

3. Conclusion

In this work we have proposed and demonstrated an useful technique mapping geometrical structure fluctuations along a photonic crystal fiber using Brillouin echoes distributed sensing. With this technique, we have been able to identify and quantify both long- and short-scale longitudinal fluctuations in the Brillouin frequency shift resulting from residual strain due to fiber coiling and air-hole microstructure or diameter fluctuations, respectively. The homogeneity of two photonic crystal fibers drawn from the same preform but with a different drawing process has been investigated and the fluctuations were logically found less important in the case of a fiber fabricated with a better process control. Our results finally demonstrate the great potential of the Brillouin echoes distributed sensing technique for small scale optical fiber characterization. Moreover, these results show the need for characterization of structural irregularities in fibers before they can be used for distributed sensing.

Acknowledgements

We thank the COST299 Action for financial support and V. Laude for helpful discussions. This work was funded by the European Interreg IV A program and the Fond Européen de Développement Régional (FEDER).

SBS Mitigation in a Microstructured Optical Fiber by Periodically Varying the Core Diameter

Birgit Stiller, Alexandre Kudlinski, Min Won Lee, Géraud Bouwmans, Michaël Delqué,
Jean-Charles Beugnot, Hervé Maillotte, and Thibaut Sylvestre

Abstract—In this letter, we experimentally demonstrate a 4-dB increase of the stimulated Brillouin scattering threshold in a microstructured optical fiber. This result is obtained by periodically varying the size of the air-hole structure by only 7% amplitude, while keeping a low attenuation coefficient. The efficiency of this passive technique is verified by use of the Brillouin echoes-distributed sensing technique where the Brillouin frequency-shift oscillation is clearly observed.

Index Terms—Brillouin threshold, distributed Brillouin measurement, microstructured optical fiber, stimulated Brillouin scattering.

I. INTRODUCTION

IN RECENT years, there have been active efforts to suppress stimulated Brillouin scattering (SBS) in optical fibers as it is detrimental to nonlinear optical processing fiber technologies and high-power narrow-linewidth fiber lasers. In addition to conventional active techniques, several passive methods have been demonstrated by applying strain or temperature distributions along the fiber [1], [2], or by fiber design [3], [4]. SBS mitigation has also been proposed using microstructured optical fibers (MOF) due to their ability to reduce the acousto-optic overlap or widen the Brillouin gain spectrum [5]. More recently, Poletti *et al.* suggested to increase the SBS threshold through longitudinal variations of the structural parameters of the MOF [6]. In this letter, we experimentally demonstrate 4 dB improvement of SBS threshold in a MOF with a periodically-varied core diameter. By varying only 7% of the air-hole microstructure over a period of 30 m, the Brillouin frequency shift (BFS) changes significantly and the Brillouin gain spectrum (BGS) broadens. This results in 4 dB increase of SBS threshold, compared to a uniform fiber with an invariant core. In the following we will describe and characterize the properties of this core-diameter

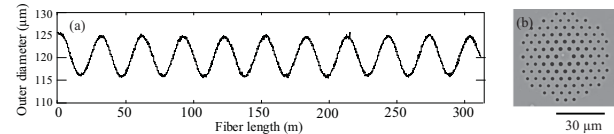


Fig. 1. (a) Outer diameter along the fiber length. (b) SEM image at the maximum outer diameter (125 μm).

varied MOF by measuring the SBS threshold and the BGS linewidth. The SBS threshold is compared to the theoretical value calculated from the standard theory for a homogeneous fiber with an invariant core and to the experimental value of a MOF with a similar air-hole structure but without varying periodically the structure size. We further perform a distributed measurement of the oscillating BFS using Brillouin echoes distributed sensing (BEDS) technique. We finally estimate the corresponding effective refractive index variations from scanning electron microscopy (SEM) images and found a very good agreement with outer diameter variations.

II. OSCILLATING MICROSTRUCTURED OPTICAL FIBER

The MOF with the periodically varying microstructure, shown in Fig. 1, has been drawn directly on a fiber tower. Figure 1(a) shows the evolution of its outer diameter (OD) as a function of length, measured during the drawing stage. It closely follows a sine evolution over 320 m with a period of 30 m and a modulation amplitude rate of 7% (OD variations from 116 to 125 μm). Figure 1(b) shows a scanning electron microscope (SEM) image of the input cross-section for the largest OD. The core diameter in Fig. 1(b) is 6.4 μm and the hole diameter of the two first rows around the core is 1.8 μm , but becomes smaller for the outer rows due to deformations during the cane drawing process. The lattice pitch Λ is nearly constant across the whole structure and equal to 4.1 μm . Drawing parameters were adjusted so that OD variations only modify the pitch Λ and keep the d/Λ ratio approximately constant all along the fiber length. The linear attenuation of the 320m-long PCF sample is measured as 7.7 dB/km at 1.55 μm . Using the commercial finite element method solver COMSOL, we have calculated from the SEM image zero-dispersion wavelength (ZDW) variations from 1.07 μm to 1.095 μm . The corresponding group-velocity dispersion (GVD) parameter D at the operating wavelength of 1.55 μm slightly shifts from 48.5 to 53.0 ps/nm/km.

III. BRILLOUIN THRESHOLD POWER

The Brillouin threshold has been graphically solved from Fig. 2 that shows the transmitted and backscattered powers as a

Manuscript received July 21, 2011; revised October 4, 2011; accepted January 20, 2012. Date of publication January 31, 2012; date of current version March 28, 2012. This work was supported in part by the European Interreg IV A Program (FEDER).

B. Stiller, M. W. Lee, M. Delqué, J.-C. Beugnot, H. Maillotte, and T. Sylvestre are with the Département d'Optique, Institut FEMTO-ST, CNRS-Université de Franche-Comté, CNRS-UMR 6174, Besançon 25030, France (e-mail: birgit.stiller@femto-st.fr; minlee@femto-st.fr; michael.delque@femto-st.fr; herve.maillotte@univ-fcomte.fr; thibaut.sylvestre@univ-fcomte.fr).

A. Kudlinski and G. Bouwmans are with the Laboratoire PhLAM, CNRSUMR 8523, IRCICA, Université Lille 1, Sciences et Technologies, Villeneuve d'Ascq 59655, France (e-mail: alexandre.kudlinski@univ-lille1.fr; geraud.bouwmans@phlam.univ-lille1.fr).

Color versions of one or more of the figures in this letter are available online at <http://ieeexplore.ieee.org>.

Digital Object Identifier 10.1109/LPT.2012.2186286

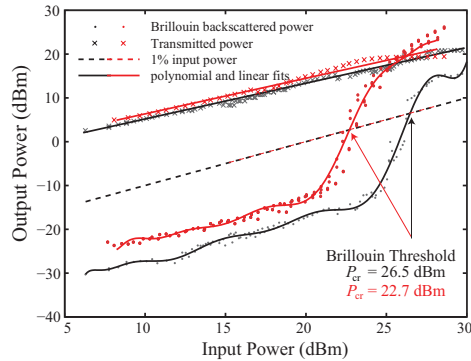


Fig. 2. Experimental measurements of the Brillouin backscattered and transmitted powers through the periodically varying MOF (black curves) and the homogenous MOF with the same microstructure but without varying structure size (red curves). The Brillouin thresholds of the two MOFs are indicated by arrows for 1% fraction of the input power.

function of the input power. In our experimental setup, we used as a pump laser a 1550 nm distributed feedback (DFB) fiber laser with a 45 kHz linewidth amplified by an erbium-doped fiber amplifier (EDFA). An optical circulator was inserted at the input end of the fiber to monitor simultaneously the reflected and transmitted power. We define here the Brillouin threshold as the input power whereby the reflected power is 1% of the injected one. A polynomial fit of our experimental measurements yields the Brillouin threshold power. For the periodically varying MOF the Brillouin threshold is measured as 26.5 dBm, as shown in Fig. 2. Theoretically the Brillouin threshold for homogeneous fibers can be written as [6]:

$$P_{\text{cr}} = \frac{C \cdot K \cdot A_{\text{eff}}}{g_B \cdot L_{\text{eff}}}, \quad (1)$$

where A_{eff} is the effective mode area, L_{eff} the effective length and g_B the Brillouin gain. C can be expressed as $C = \psi(1 + \frac{3/2 \cdot \ln(\psi)}{\psi - 3/2})$ where ψ depends amongst others on the fiber parameters, the BFS, the BGS and the 1% pump power fraction [7]. $K = 3/2$ is a factor that accounts for random polarization evolution in the MOF. g_B can be calculated by measuring the full width at half maximum (FWHM) of the BGS in the spontaneous Brillouin regime [7].

Figures 3(a) and 3(b) show the BGS (FWHM) with variable input power and the BGS at 12 dBm, respectively. Measurements have been performed using a standard heterodyne detection technique where the back-scattered Brillouin signal beats with the input one [8]. As can be seen, we measure in the low-power regime (5 dBm) an average 54 MHz SBS linewidth (FWHM) that narrows to 10 MHz near the threshold power (25 dBm). This indicates a strong spectral broadening of the BGS compared to the standard value for single-mode fiber (SMF) below threshold (FWHM $\Delta\nu_B = 29$ MHz). This effect has already been reported in other MOFs as resulting from the impact of air-hole microstructure on the acoustic waves distribution [8]. It leads to a significant reduction of the Brillouin gain. Assuming an FWHM $\Delta\nu_B = 54$ MHz, we have estimated $g_B = 1.30 \cdot 10^{-11} \text{ mW}^{-1}$. With $L_{\text{eff}} = 244.2$ m, $C = 14.3$, $A_{\text{eff}} = 22.63 \mu\text{m}^2$, the theoretical Brillouin threshold for a uniform silica fiber is calculated to 21.8 dBm. Thus the experimental threshold increases by more than 4 dB

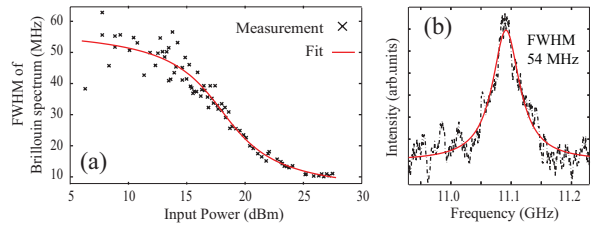


Fig. 3. (a) Brillouin gain spectrum (FWHM) with increasing input power. (b) Brillouin gain spectrum at 12-dBm input power.

compared to this estimation. Note that this increase can be seen as a higher limit since we assumed in our calculation a uniform MOF without any periodic variation or structural irregularities that increase the Brillouin threshold [8]. Unfortunately, the model can not be used to derive a correct value in the case of periodic variation or structural irregularities. An improved theory adapted to MOFs is clearly needed.

However, to go further into detail, we have investigated a homogeneous MOF with similar air-hole microstructure. This MOF was drawn without inducing a periodic size variation. It has a length of 350 m, 4.35 μm lattice pitch, 6.2 μm core diameter and a mode area of 22.3 μm^2 at 1.55 μm . Compared to the periodically varying MOF the structural parameters are slightly different but lead to a very close effective mode area which is crucial for a fair comparison of the Brillouin threshold. The fiber attenuation is about 14 dB/km which results in an effective fiber length of 207.6 m. The Brillouin threshold has been measured using the same technique as for the oscillating MOF. One can see in Fig. 2 that the critical power for the Brillouin threshold (red curve) is reached at 22.7 dBm which is almost 4 dB below the value for the periodically varying MOF, in good agreement with our theoretical estimation. Taking into account the important fact that the effective length of the uniform fiber is lower than for the periodically varying MOF, the Brillouin threshold can be expected to be even lower than 22.7 dBm and the impact of the BFS variation higher than 4 dB. Note that the FWHM of the BGS has also been measured to about 55 MHz. Thus, the periodic variations have less influence on the BGS broadening than the air-hole structure itself.

IV. DISTRIBUTED MEASUREMENT

The increase of Brillouin threshold may result from the varying BFS due to core diameter and effective refractive index variations. In order to verify this fact we have performed a distributed measurement of the BFS by use of the BEDS technique that provides a higher spatial resolution than conventional Brillouin optical time domain analysis (BOTDA) [9] without spectral broadening. The experimental setup is sketched in Fig. 4 and a detailed description can be found in Ref. [9]. In short, an amplified DFB fiber laser is split into two signals by a 50:50 tap coupler that are injected at opposite end of the fiber. One signal serves as a probe shifted by the BFS while the other one is used as a pump pulse. More precisely, a 3ns-long π -phase pulse is applied at the end of the pump pulse which causes a drop in the Brillouin gain

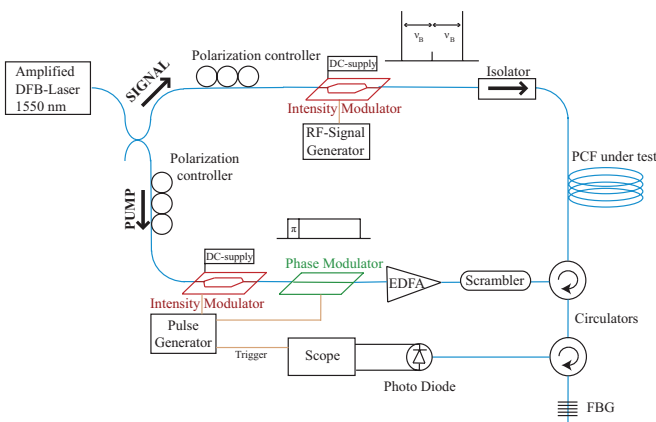


Fig. 4. Experimental setup of the Brillouin echoes distributed sensor used to measure the Brillouin frequency shift sine variations along the fiber length. DFB: distributed-feedback laser. EDFA: erbium-doped fiber amplifier. FBG: fiber Bragg grating.

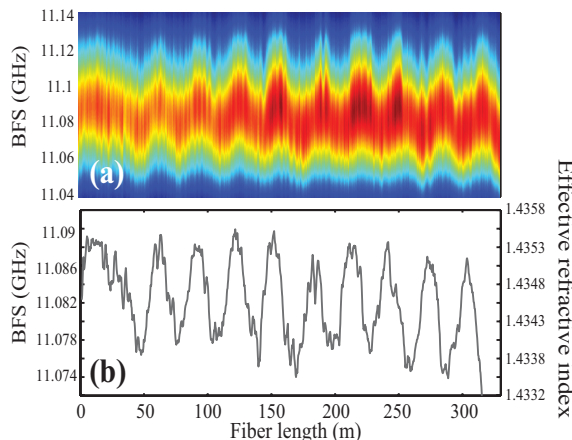


Fig. 5. Mapping of the Brillouin frequency shift along the fiber. The spatial resolution is 30 cm and the frequency resolution is 1 MHz. (a) Color plot of the recorded BEDS trace of the periodically varying MOF. (b) Retrieved Brillouin frequency shift variations along the fiber distance. Mean maximal BFS: 11.088 GHz; mean minimal BFS: 11.076 GHz.

detected on the counter-propagating probe. The frequency shift of the probe is obtained by an intensity modulator driven at V_π where two side bands shifted by the BFS are generated while suppressing the carrier wave. The output continuous-wave probe is filtered by a fiber Bragg grating (FBG) and monitored with a photodiode and an oscilloscope. The Brillouin gain is scanned by the intensity modulator around the BFS so that all variations can be detected along the fiber. The spatial resolution is set by the phase pulse duration and corresponds to 30 cm and the frequency resolution is 1 MHz. The input powers of the probe and pump wave are 481 μ W and 27 mW, respectively.

Figures 5 (a) and (b) show a color plot of the raw BEDS trace and the retrieved BFS along the propagation distance, respectively. The periodic sinusoidal variations of the BFS can clearly be observed in these two figures. The comparison with the outer diameter variations previously shown in Fig. 1(a) is very good except in the beginning of the fiber where the first period is not observed. In addition, one can also see

short-scale fluctuations of meter scale that can be attributed to structural irregularities along the fiber. In addition to the periodic variations and the BGS broadening, these short scale variations also impact on the Brillouin threshold. As the BFS is linked to the effective refractive index n_{eff} by $v_B = \frac{2n_{\text{eff}}V_L}{\lambda_p}$, we can calculate the corresponding effective refractive index variations using a FEM method by scaling the fiber cross-section shown in Fig. 1(b) [10]. For the maximal and minimal sizes (corresponding to 125 and 116 μ m in outer diameter) of the air-hole microstructure they reveal a difference of 0.0013 in the effective refractive index. This value is consistent with the one retrieved from the distributed BFS measurement that varies from 1.4337 to 1.4353. This confirms that the BEDS technique can provide accurate measurement of the diameter or structural variations from the BFS ones.

V. CONCLUSION

We have fabricated a microstructured optical fiber with a periodically-varying core diameter in order to mitigate the detrimental effect of stimulated Brillouin scattering. Only 7% of outer variation enables an increase of the Brillouin threshold power by 4 dB compared to a homogeneous microstructured optical fiber, which is a promising result for further investigations with higher amplitude variations. The periodic oscillations of the Brillouin frequency shift has been checked by an accurate distributed measurement based on Brillouin echoes distributed sensing. Such an oscillating-core microstructured fiber may have an interesting potential for applications where Brillouin backscattering is an obstacle.

REFERENCES

- [1] J. Hansryd, F. Dross, M. Westlund, P. A. Andrekson, and S. N. Knudsen, "Increase of the SBS threshold in a short highly nonlinear fiber by applying a temperature distribution," *J. Lightw. Technol.*, vol. 19, no. 11, pp. 1691–1697, Nov. 2001.
- [2] J. M. C. Boggio, J. D. Marconi, and H. L. Fragnito, "Experimental and numerical investigation of the SBS-threshold increase in an optical fiber by applying strain distributions," *J. Lightw. Technol.*, vol. 23, no. 11, pp. 3808–3814, Nov. 2005.
- [3] K. Shiraki, M. Ohashi, and M. Tateda, "Suppression of stimulated Brillouin scattering in a fibre by changing the core radius," *Electron. Lett.*, vol. 31, no. 8, pp. 668–669, Apr. 1995.
- [4] V. Laude, *et al.*, "Phononic band-gap guidance of acoustic modes in photonic crystal fibers," *Phys. Rev. B*, vol. 71, no. 4, pp. 045107-1–045107-6, Jan. 2005.
- [5] J. Spring and B. Ward, "Brillouin gain suppression in photonic crystal fibers with random acoustically microstructured cores," *Opt. Lett.*, vol. 35, no. 1, pp. 31–33, 2010.
- [6] F. Poletti, K. Furusawa, Z. Yusoff, N. G. Broderick, and D. J. Richardson, "Nonlinear tapered holey fibers with high stimulated Brillouin scattering threshold and controlled dispersion," *J. Opt. Soc. Amer. B*, vol. 24, no. 9, pp. 2185–2194, 2007.
- [7] A. Kobyakov, M. Sauer, and D. Chowdhury, "Stimulated Brillouin scattering in optical fibers," *Adv. Opt. Photon.*, vol. 2, no. 1, pp. 1–59, 2010.
- [8] J.-C. Beugnot, *et al.*, "Complete experimental characterization of stimulated Brillouin scattering in photonic crystal fiber," *Opt. Express*, vol. 15, no. 15, pp. 15517–15522, 2007.
- [9] S. M. Foaleng, M. Tur, J.-C. Beugnot, and L. Thévenaz, "High spatial and spectral resolution long-range sensing using Brillouin echoes," *J. Lightw. Technol.*, vol. 28, no. 20, pp. 2993–3003, Oct. 15, 2010.
- [10] B. Stiller, *et al.*, "Photonic crystal fiber mapping using Brillouin echoes distributed sensing," *Opt. Express*, vol. 18, no. 19, pp. 20136–20142, 2010.

Differential Phase-Shift-Keying Technique-Based Brillouin Echo-Distributed Sensing

Min Won Lee, Birgit Stiller, Jérôme Hauden, Hervé Maillotte, Carole Roch, Luc Thévenaz, and Thibaut Sylvestre

Abstract—In this letter, we experimentally demonstrate Brillouin echoes-based distributed optical fiber sensing with centimeter spatial resolution. It is based on a differential phase-shift-keying technique using a single Mach–Zehnder modulator to generate a pump pulse and a π -phase-shifted pulse with an easy and accurate adjustment of delay. The results are compared to those obtained in standard Brillouin echo-distributed sensing system with two optical modulators and clearly show a resolution of 5 cm in a spliced segment between two fibers by applying a π -phase-shifted pulse of 500 ps.

Index Terms—Brillouin echo-distributed sensing, Brillouin optical time-domain analysis.

I. INTRODUCTION

OVER the last two decades, Brillouin scattering has widely been studied for distributed sensing applications using optical fibers [1]–[3]. Two main sensing analyses have been developed for this purpose: Brillouin optical correlation-domain analysis (BOCDA) and Brillouin Optical Time-Domain Analysis (BOTDA). BOCDA offers a very good spatial resolution [4] down to 1 mm [5]. Nevertheless, it is difficult to perform over a long distance using this technique. On the other hand, BOTDA has attracted particular attention for distributed sensing of temperature and/or strain in petrol and civil engineering industries. This analysis offers fast measurement and long-haul distributed sensing by measuring Brillouin frequency shift (BFS) produced by temperature and/or strain in optical fibers [6], [7]. Recently, enhanced BOTDA systems have been reported such as vector [8] and simplex-coded BOTDA systems [9]. Basically, the technique uses a pump-probe counter-propagative configuration with a pulse longer than 10 ns for pump. However, its spatial resolution is limited to 1 m due to the acoustic decay time of 10 ns. In order to overcome this limit,

other techniques have been developed such as dark-pulse Brillouin scattering [10], differential pulse-width pair BOTDA [11] and Brillouin echo-distributed sensing (BEDS) [12], [13]. They all have neither physical nor technical limit down to 1-cm resolution sensing. However, in the dark-pulse sensing technique, residual peaks appear in the measurement spectra whereas the other two techniques suppress such peaks. Recently, it has been demonstrated that the BEDS approach offers a double contrast with respect to the other techniques [13]. This technique uses an optical short π -phase pulse in addition to a long intensity pulse and centimeter resolution sensing can be achieved by the short phase pulse with a very good quality. Despite of the advantage over high spatial resolution, the conventional BEDS systems exploit two modulators: a phase modulator for generating short π -phase pulses and an intensity modulator for generating long intensity pulses. Besides, measurements can be undertaken using a differential gain approach taking the difference between two successive measurements with and without the π -phase pulse. Therefore, a good accuracy sensing requires a sophisticated adjustment of the delay between the two pulses.

In this work, we propose a new concept to perform BEDS in which an optical π -phase pulse is directly generated using a single intensity modulator by differential phase-shift keying (DPSK) technique. The system we propose in this letter is to implement BEDS with an optical scheme as simple as other high spatial resolution techniques, but with a double contrast. A long positive and a short negative electrical pulses are applied to the modulator to generate an optical π -phase shift and centimeter resolution sensing is achieved in our DPSK-based BEDS system (DPSK-BEDS). Moreover, the pulse delay can easily be adjusted as the pulses are generated in intensity. For this purpose, we investigate a fiber section where two different fibers are spliced with a 5 cm-protection sleeve. The results will be compared with those obtained in a conventional BEDS system. Elongation measurements over a 5-cm fiber section will also be carried out using DPSK-BEDS.

II. π -PHASE PULSE GENERATION BASED ON DPSK TECHNIQUE

DPSK technique is widely used in telecommunication industry to transmit bit-sequence messages in form of π -phase shift using an intensity modulator, i.e. Mach–Zehnder interferometer modulator (MZI). In the principle of DPSK, optical phase can be shifted by modulating an MZI with an amplitude of double half-wave voltage ($2V_\pi$). When the MZI is driven at its minimum bias point by a positive voltage $0 < V < V_\pi$ and successively a negative voltage $0 > V > -V_\pi$, the relative phase-shift between the optical fields at the two voltages is π ,

Manuscript received June 24, 2011; revised September 01, 2011; accepted October 06, 2011. Date of publication October 14, 2011; date of current version December 21, 2011. This work was supported by the European INTERREG IVA Program, by the Conseil Régional de Franche-comté, and by the European COST action 299-FIDES.

M. W. Lee, B. Stiller, H. Maillotte, C. Roch, and T. Sylvestre are with the Département d’Optique P. M. Duffieux, Institut FEMTO-ST, Université de Franche-Comté, CNRS UMR 6174, F-25030 Besançon Cedex, France (e-mail: thibaut.sylvestre@univ-fcomte.fr).

J. Hauden is with PHOTLINE Technologies, F-25001 Besançon, France.

L. Thévenaz is with the Institute of Electrical Engineering, Ecole Polytechnique Fédérale de Lausanne, CH-1015, Lausanne, Switzerland.

Color versions of one or more of the figures in this letter are available online at <http://ieeexplore.ieee.org>.

Digital Object Identifier 10.1109/LPT.2011.2172255

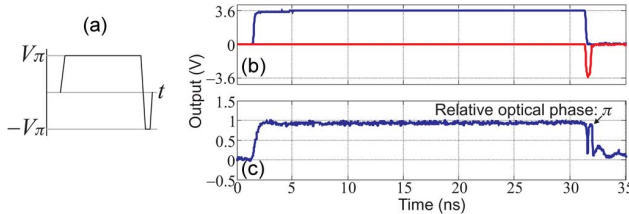


Fig. 1. (a) Schematic drawing of a positive/negative electrical pulse. (b) Positive (blue trace) and negative (red trace) electrical pulses are generated separately and applied to the MZI. The durations of the long and short intensity pulses are 30 ns and 500 ps, respectively. (c) The intensity pulses at the MZI output. The phase is shifted by π for 500 ps at the pulse end.

or vice-versa [14]. Therefore, when a negative pulse of V_π (or a pulse of $-V_\pi$) is applied to the modulator just after a positive pulse of V_π at the minimum bias point as illustrated in Fig. 1(a), the output optical intensity remains unchanged whilst the phase of the optical field at the negative pulse part is shifted by π with respect to the positive pulse part. In order to generate such an electrical pulse, the positive and negative electrical pulses are generated separately in this work as shown in Fig. 1(b). Their peak-to-peak amplitude is 7.6 V and applied to the MZI used in the work (Photline MXPE series, $V_\pi = 6.2$ V, 20-GHz bandwidth). The pulse durations are set to 30 ns and 500 ps, respectively. In telecommunication, such pulses are applied to a dual-drive MZI [15]. In our work, these long and short pulses are applied to the direct current (DC) and radio-frequency (RF) inputs of the MZI, respectively. An impedance matching of 50Ω is made at the DC port and it provides a sufficient bandwidth for the 30-ns pulse. As the pulses are generated in intensity at the output of the MZI, the delay between the pulses is readily adjusted. Fig. 1(c) exhibits two intensity pulses at the modulator output, which are generated by the electrical pulses seen in Fig. 1(b). A 30-ns intensity pulse is followed by a 500-ps intensity pulse with π -shifted phase. The rise/fall times of the long and short pulses are 700 ps and 200 ps, respectively. A short drop between the two pulses is seen due to the fast transition from the positive pulse to the negative pulse. The 500-ps duration of the short pulse defines a spatial resolution of 5 cm in our DPSK-based BEDS system.

III. EXPERIMENTAL SETUP

This dual-phase state intensity pulse is used as the pump wave in the experimental setup shown in Fig. 2 schematically. The setup is based on BOTDA system with an additional electrical pulse which is negative and applied to the MZI of the pump. The continuous wave (CW) emission of a distributed feedback (DFB) laser at 1550 nm is split into the pump and probe arms by a 50:50 tap coupler. In the pump side, an RF bias-T is used to combine the positive pulse and DC bias and the DC bias of the MZI is adjusted to be at the minimum bias point. The optical pulses in Fig. 1(c) are amplified by an Erbium-doped fiber amplifier (EDFA) with a peak power of 1.3 W. They are then polarization-scrambled by a polarization scrambler to average out polarization-sensitive Brillouin gain and injected into a fiber under test via an optical circulator. In the probe side, the Brillouin frequency-shifted probe is generated by the second MZI with a carrier suppression of 38 dB at 1550 nm by adjusting the

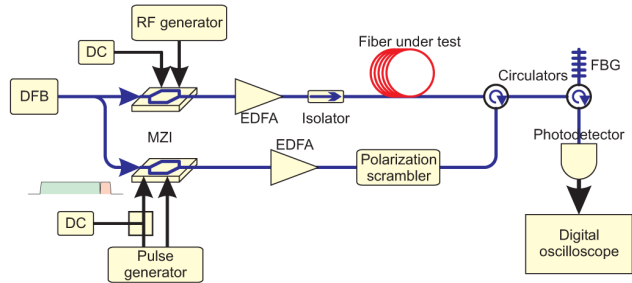


Fig. 2. Experimental setup of DPSK-BEDS system using a single Mach-Zehnder interferometer (MZI) modulator for the pump. DFB: Distributed-feedback laser. EDFA: Erbium-doped fiber amplifier. FBG: Fiber Bragg grating.

DC bias. The probe power is set to 1 mW by another EDFA. The probe is then injected into the fiber through an isolator. At the fiber output, a fiber Bragg grating (FBG) enables to select the Brillouin gain obtained by the pump at the BFS. The gain is retrieved by a photodetector and then recorded as time traces by a digital oscilloscope. By sweeping the frequency of the optical probe, the gain along the fiber is mapped as a function of frequency. In this way, all BFS variations along the fiber caused by temperature or strain can be easily detected.

IV. EXPERIMENTAL RESULTS

In order to demonstrate the performance of the concept developed in this work, a 2-m single-mode fiber (SMF) is spliced to a 1-m fiber with high numerical aperture (HNA). The splice point is protected by a heat-shrinking sleeve of 5 cm. For comparison, distributed measurements of the splice segment have been done in two BEDS systems: conventional BEDS system using a phase and an intensity modulators for pump and DPSK-BEDS system using a single intensity modulator. Fig. 3(a) shows the distributed measurement obtained in the conventional BEDS system via a π -phase shifted pulse with a pulse width of 500 ps. It clearly reveals the splice segment of 5 cm between the fibers at a frequency shift of 10.55 GHz. The BFS of the HNA and SMF are 10.67 GHz and 10.85 GHz, respectively. Fig. 3(b) displays the mapping using DPSK-BEDS developed in the work. It also manifests clearly the 5-cm splice segment and the 10.55-GHz frequency shift. Therefore, it is evident that our system manifests performances as good as the standard BEDS system. However, the contrast of the measurement in BEDS is slightly better than that in DPSK-BEDS. This is due to the peak-to-peak amplitude of 7.6 V which is only $1.23V_\pi$ in DPSK-BEDS where $2V_\pi$ is needed for the best performance. On the other hand, in BEDS a pulse amplitude of 5.1 V is applied to the phase modulator of which the V_π is 5.9 V. In this case, only V_π is required for the best operation and the amplitude meets almost this requirement ($0.87V_\pi$). Nevertheless, Fig. 3(b) shows a good margin for improvement thanks to the good signal-to-noise ratio.

We have also tested our DPSK-BEDS system with centimeter resolution for strain monitoring. For that purpose, we have set up an elongation platform and applied three different elongations over a fiber section of 5 cm in the beginning of a 260-m long SMF. Fig. 4 exhibits the elongation measurements with 5-cm spatial and 1-MHz spectral resolutions. The elongations applied

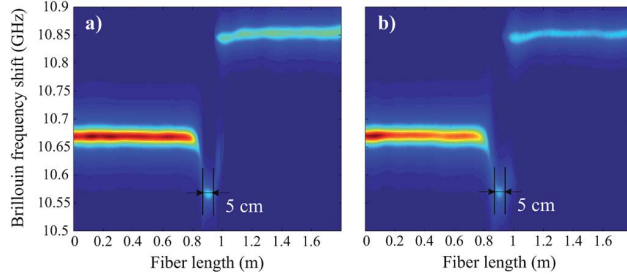


Fig. 3. Distributed measurements of HNA/SMF fibers showing a splice segment of 5 cm (a) in standard BEDS system using a phase modulator and (b) in our BEDS system based on DPSK technique.

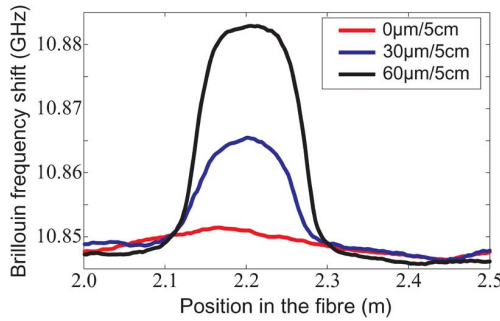


Fig. 4. Brillouin frequency shift versus the fiber length for three different elongations applied to a 5-cm fiber section.

to the section are successively 0 μm , 30 μm and 60 μm . As the elongation length increases, the BFS increases from 10.847 GHz to 10.865 GHz and 10.883 GHz. However, the figure reveals the elongation over more than 5 cm. We speculate that the pure fiber may slightly slip inside the fiber coating as a result of strain. The BFS is displaced by 18 MHz at 600 $\mu\epsilon$ and 36 MHz at 1200 $\mu\epsilon$. Thus, the strain coefficient is obtained as 3 MHz per 100 $\mu\epsilon$ with a strain accuracy of 33 $\mu\epsilon$. This accuracy can be further improved by using more frequency samples and higher pump and probe power. Since it is based on BEDS technique, our setup can potentially reach spatial resolution down to 1 cm if a faster pulse generator is used.

V. CONCLUSION

We have successfully demonstrated a new concept for Brillouin echo-distributed sensing with centimeter resolution based on differential phase-shift keying technique. A π -phase pulse with a pulse duration of 500 ps and an intensity pulse with 30 ns are generated for the pump using a single Mach-Zehnder modulator in our system. Our results clearly reveal the 5-cm splice segment between two fibers and its Brillouin frequency shift with a spatial resolution of 5 cm. The elongation test over a fiber

section of 5 cm has also been performed with good results. Our new setup enables distributed measurements with centimeter resolution and a double contrast by simply adding a negative pulse into the pump in a Brillouin optical time-domain analysis system. Therefore it simplifies conventional Brillouin echo-distributed sensing systems by using a single modulator for pump rather than two modulators, and reduces the optical loss of the pump due to the modulators. Our setup also allows an easy adjustment of the delay between two pulses as they are generated in intensity. As such, our system may offer a great potential to fiber optic sensors with centimeter resolution for structural health and geotechnical monitoring.

REFERENCES

- [1] T. Kurashima, T. Horiguchi, and M. Tateda, "Distributed-temperature sensing using stimulated Brillouin scattering in optical silica fibers," *Opt. Lett.*, vol. 15, pp. 1038–1040, 1990.
- [2] X. Bao, D. J. Webb, and D. A. Jackson, "Combined distributed temperature and strain sensor based on Brillouin loss in an optical fiber," *Opt. Lett.*, vol. 19, pp. 141–143, 1994.
- [3] K. Y. Song and H. J. Yoon, "High-resolution Brillouin optical time domain analysis based on Brillouin dynamic grating," *Opt. Lett.*, vol. 35, pp. 52–54, 2010.
- [4] K. Hotate and M. Tanaka, "Distributed fiber Brillouin strain sensing with 1-cm spatial resolution by correlation-based continuous-wave technique," *IEEE Photon. Technol. Lett.*, vol. 14, no. 2, pp. 179–181, Feb. 2002.
- [5] K. Y. Song, Z. He, and K. Hotate, "Distributed strain measurement with millimeter-order spatial resolution based on Brillouin optical correlation domain analysis," *Opt. Lett.*, vol. 31, pp. 2526–2528, 2006.
- [6] F. Rodríguez-Barrios, S. Martín-López, A. Carrasco-Sanz, P. Corredera, J. D. Ania-Castañón, L. Thévenaz, and M. González-Herráez, "Distributed Brillouin fiber sensor assisted by first-order Raman amplification," *J. Lightw. Technol.*, vol. 28, no. 15, pp. 2162–2172, Aug. 1, 2010.
- [7] M. A. Soto, G. Bolognini, and F. Di Pasquale, "Long-range simplex-coded BOTDA sensor over 120 km distance employing optical preamplification," *Opt. Lett.*, vol. 36, pp. 232–234, 2011.
- [8] M. Dossou, D. Bacquet, and P. Sriftgiser, "Vector Brillouin optical time-domain analyzer for high-order acoustic modes," *Opt. Lett.*, vol. 35, pp. 3850–3852, 2010.
- [9] M. A. Soto, G. Bolognini, F. D. Pasquale, and L. Thévenaz, "Simplex-coded BOTDA fiber sensor with 1-m spatial resolution over a 50-km range," *Opt. Lett.*, vol. 35, pp. 259–261, 2010.
- [10] A. W. Brown, B. G. Colpitts, and K. Brown, "Dark-pulse Brillouin optical time-domain sensor with 20-mm spatial resolution," *J. Lightw. Technol.*, vol. 25, no. 1, pp. 381–386, Jan. 2007.
- [11] W. Li, X. Bao, Y. Li, and L. Chen, "Differential pulse-width pair BOTDA for high spatial resolution sensing," *Opt. Express*, vol. 16, pp. 21616–21625, 2008.
- [12] L. Thévenaz, "Brillouin distributed time-domain sensing in optical fibers: State of the art and perspectives," *Frontiers Optoelectron. China*, vol. 3, pp. 13–21, 2010.
- [13] S. M. Foaleng, M. Tur, J. Beugnot, and L. Thévenaz, "High spatial and spectral resolution long-range sensing using Brillouin echoes," *J. Lightw. Technol.*, vol. 28, no. 20, pp. 2993–3003, Oct. 15, 2010.
- [14] G. Charlet, "Progress in optical modulation formats for high-bit rate WDM transmissions," *IEEE J. Quantum Electron.*, vol. 12, no. 4, pp. 469–483, Jul./Aug. 2006.
- [15] Y. J. Wen, A. Nirmalathas, and D.-S. Lee, "RZ/CSRZ-DPSK and chirped NRZ signal generation using a single-stage dual-electrode Mach-Zehnder modulator," *IEEE Photon. Technol. Lett.*, vol. 16, no. 11, pp. 2466–2468, Nov. 2004.

Distributed Brillouin Fiber Sensor With Enhanced Sensitivity Based on Anti-Stokes Single-Sideband Suppressed-Carrier Modulation

Duc Minh Nguyen, Birgit Stiller, Min Won Lee, Jean-Charles Beugnot, Herve Maillotte, Alexandre Mottet, Jerome Hauden, and Thibaut Sylvestre

Abstract—We demonstrate an alternative technique to reduce pump depletion and to improve sensitivity in the long-range Brillouin optical time-domain analysis (BOTDA) sensor. Our BOTDA system uses an anti-Stokes single-sideband suppressed-carrier modulation technique that balances the pump depletion due to fiber loss. With this technique, we show both numerically and experimentally a great improvement compared to the dual sideband standard technique.

Index Terms—Brillouin optical time domain analysis, fiber optic sensor, single-sideband modulation.

I. INTRODUCTION

BRILLOUIN Optical Time-Domain Analysis (BOTDA) sensing systems have been the subject of intense research in recent years because they offer a unique solution for continuous, real-time monitoring in civil or geotechnical engineering and petroleum industry. These fiber-optic sensors provide distributed strain or temperature measurements with meter spatial resolution over several tens of kilometers. An important factor that limits the range of BOTDA sensors however is pump depletion. This non-local effect degrades the signal-to-noise ratio (SNR) and distorts the Brillouin gain spectrum (BGS), leading to systematic errors or biases in sensors measurements [1]–[3]. Several techniques have recently been proposed to overcome these limitations and to extend the sensing range beyond 50 km. For instance, the sensing range can be extended to 100 km by using distributed Raman amplification schemes [4], or 150 km by combining frequency-division multiplexing and in-line Erbium doped fiber amplifiers (EDFAs) [5]. 120-km range has also been achieved by improving the SNR with optical pulse coding techniques and optical pre-amplification at the receiver [6]. All of these techniques rely on the use a dual sideband (DSB) probe which reduces the impact of pump depletion. Recently, Bernini et al. [7] proposed a

BOTDA system making use of an unbalanced DSB probe with a Stokes/anti-Stokes power ratio allowing a larger suppression of nonlocal effects induced by pump depletion.

In this letter, we describe and demonstrate an alternative Brillouin-loss based technique to further reduce pump depletion and to improve the sensitivity in BOTDA systems. Compared to the technique of Bernini [7], our BOTDA system uses an anti-Stokes probe generated with a single-sideband suppressed-carrier (SSB-SC) modulator to balance the pump depletion due to fiber loss [8]. With this technique, we show both numerically and experimentally enhanced performances compared to conventional DSB schemes. Distributed strain measurements over a 50-km of single-mode fiber (SMF) with 3 m spatial resolution are reported.

II. NUMERICAL SIMULATIONS

Let us consider the stimulated Brillouin scattering (SBS) between a square pump pulse and two counter-propagating continuous-wave (CW) Stokes and anti-Stokes waves. At each fiber length, the interaction time is given by the pump pulse duration if it is sufficiently longer than the phonon lifetime (~ 10 ns). During the interaction, the pump will transfer its energy to the Stokes probe (loss process) and also receive energy from the anti-Stokes beam (gain process). The gain and loss process of the pump correspond respectively to the Brillouin loss and gain for the signal. This gain/loss process is not linear since the Stokes and anti-Stokes powers change during the interaction time. This results in a non-uniform deformation of the pump that cannot be ignored in long-range measurements. To get better insight, we performed numerical simulations based on three coupled equations for the pump, Stokes and anti-Stokes waves using the finite difference method (for equations, see [9]). The input pump pulse duration is 500 ns and its peak power is 0.1 W. All other parameters are listed in the caption of Fig. 1. We also restricted the sensing length to 2.8 km in the numerics because taking into account a 50-km value as in experiment is very time-consuming and computationally intensive. Fig. 1(a) shows the computed pump pulse at the output of the sensing fiber for different input probe conditions, as indicated in the inset and in the caption. More specifically, we compare the Stokes and anti-Stokes SSB probe regimes with the balanced and unbalanced DSB ones. As it can be seen, in the Stokes SSB regime, the output pump pulse is strongly distorted and depleted (solid green curve) compared to the pump alone without input probe (dashed blue curve).

Manuscript received July 13, 2012; revised October 14, 2012; accepted November 13, 2012. Date of publication November 21, 2012; date of current version December 20, 2012. This work was supported in part by the European Program INTERREG IVA (FEDER) and in part by the Region Franche-Comté.

D. M. Nguyen, B. Stiller, M. W. Lee, J.-C. Beugnot, H. Maillotte, and T. Sylvestre are with the FEMTO-ST Institute, Université de Franche-Comté, Besançon 25030, France (e-mail: ducminh.nguyen@femto-st.fr; thibaut.sylvestre@univ-fcomte.fr).

A. Mottet and J. Hauden are with PHOTLINE Technologies, Besançon 25000, France.

Color versions of one or more of the figures in this letter are available online at <http://ieeexplore.ieee.org>.

Digital Object Identifier 10.1109/LPT.2012.2228848

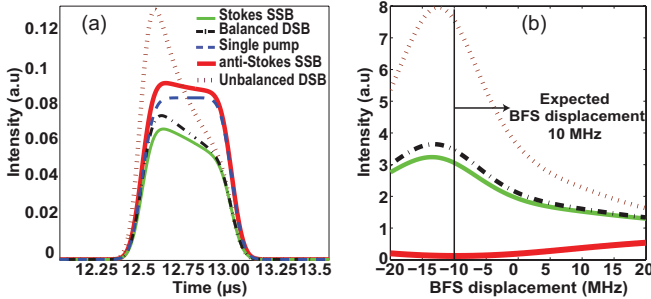


Fig. 1. Numerical simulations of (a) pump pulse depletion and (b) probe intensity versus the strain-induced BFS displacement for five different input conditions of the Stokes/anti-Stokes power ratio. Stokes power is $500 \mu\text{W}$ in Stokes SSB, balanced DSB, and unbalanced DSB regimes. Anti-Stokes power is $500 \mu\text{W}$ in the balanced DSB and the anti-Stokes SSB regimes. In the unbalanced DSB regime, the anti-Stokes power is 3.5 mW . Parameters are fiber length $L = 2.8 \text{ km}$, Brillouin gain $g = 1.66 \cdot 10^{-11} \text{ m.W}^{-1}$, loss coefficient $\alpha = 0.2 \text{ dB/km}$.

The output pump power can however be raised by using the DSB regime, as shown the dashed-dotted pulse in Fig. 1(a). In this regime, the anti-Stokes sideband strengthens the pump energy through the gain process that reduces pump depletion. Nevertheless, pump depletion still remains in the balanced DSB case. This is due to the fact that energy transfer from the pump to the Stokes probe is faster than from the anti-Stokes probe to the pump once the Stokes power exceeds that of the anti-Stokes one. In the unbalanced DSB regime (dotted red curve), the pump peak power reaches a high value but its shape and width are strongly modified by the Brillouin interaction. The solid red curve shows a direct comparison with our technique making use of a single-sideband anti-Stokes probe. As it can be seen, the pump pulse is no longer depleted and its shape is the closest to the initial one shown in blue. In such a regime, the pump power is depleted only due to the fiber loss. This leads to a great improvement of the output pump peak power and pulse shape, compared to the other probe regimes. We further compared these different probe conditions when applying strain on the fiber in order to assess the possible systematic errors induced by pump depletion for the Brillouin frequency shift (BFS). Fig. 1(b) shows the computed values of strain-induced BFS displacement. This numerical simulation was done with an assumption of an intrinsic SBS line-width of 35 MHz and a strain applied at the end of the fiber of $200 \mu\epsilon$. This strain yields a theoretical BFS displacement of 10 MHz , as indicated by the vertical black line in Fig. 1(b). Computed values of BFS displacements in the case of Stokes-SSB, balanced DSB and unbalanced DSB are 13.7 MHz , 13.3 MHz , and 12.6 MHz , respectively. These three values thus overestimate the BFS displacement of 10 MHz because of the pump depletion and pulse distortion, observed in Fig. 1(a). When using the anti-Stokes SSB probe regime, the BFS displacement was numerically calculated as 9.7 MHz (continuous bold red curve in Fig. 1(b)), which is nearest to the expected value of 10 MHz . Thus the anti-Stokes SSB regime allows for the suppression of biases in sensing measurements.

III. EXPERIMENTAL RESULTS

To verify our numerical predictions, we set up the BOTDA sensor depicted in Fig. 2. In short, a distributed feedback

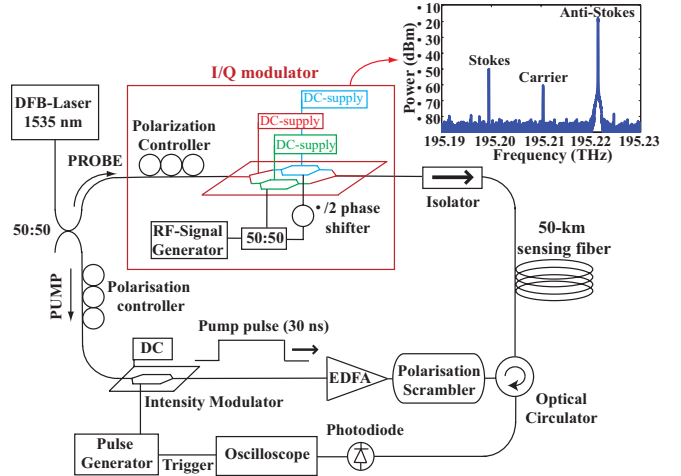


Fig. 2. Experimental setup of the Brillouin loss-based BOTDA sensor based on anti-Stokes single-sideband modulation technique.

(DFB) laser at 1535 nm is split into the pump and probe arms by a 50:50 tap coupler. In the pump side (fiber input), we insert an intensity modulator driven by a pulse generator to generate square pump pulses with a width of 30 ns , which provides a 3 m spatial resolution. These pulses are then amplified by an erbium doped-fiber amplifier (EDFA) and polarization-scrambled before being launched into a 50 km sensing fiber via an optical circulator. Our intensity modulator has a high extinction ratio of 40 dB which prevents anti-Stokes probe depletion due to the pump pulse leakage [10]. In the probe side (fiber output), we use an I/Q modulator [11] to generate an anti-Stokes probe whose frequency is swept around the BFS of the sensing fiber. More specifically, it consists in two parallel Mach-Zehnder interferometers (MZI) nested into a third combining MZI. An RF tone signal tunable around 11 GHz is injected into both RF ports of the modulator with a $\pi/2$ -phase shift. With this SSB-SC modulator, we achieved a carrier suppression of 45 dB and a side-mode suppression of 35 dB at 1535 nm , as shown in the inset of Fig. 2. The probe power is set to 1.6 mW and injected into the sensing fiber after an isolator. At the fiber output, the anti-Stokes probe is extracted by a circulator and a 10-GHz bandpass FBG filter before being analyzed by a digital oscilloscope and an optical spectral analyzer (OSA). By sweeping the optical probe frequency, the BGS along the fiber is mapped as a function of frequency. In this way, all BFS variations along the fiber due to temperature change or applied strain can be detected. For the data acquisition, we have normalized the data with the DC offset by using the DC mode of our oscilloscope with an impedance of $1 \text{ M}\Omega$ to increase the photodetector sensitivity.

First, we performed distributed measurements without applying strain to compare the anti-Stokes SSB case to standard DSB technique using the same input power conditions. Fig. 3(a) and (b) show the BOTDA traces in false color for the two regimes, respectively. From these figures, we plotted in Fig. 3(c) the Brillouin gain (blue) and loss (red) amplitudes versus the distance for a frequency value of 10.925 GHz , and in Fig. 3(d), the Brillouin gain and loss spectra measured at the fiber end. The value of 10.925 GHz

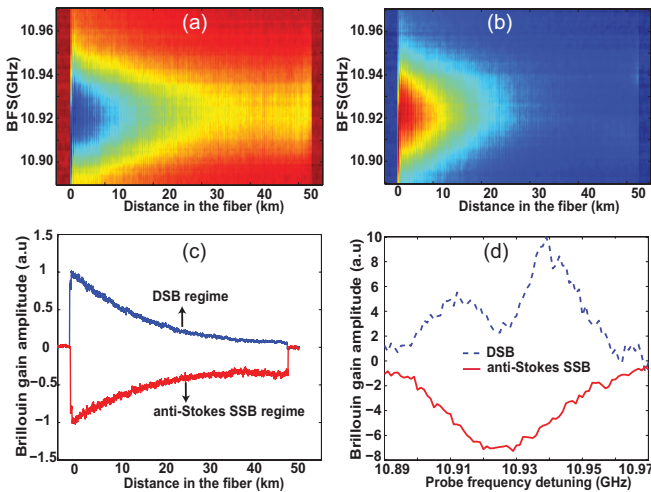


Fig. 3. Distributed measurements over a 50-km single-mode fiber using (a) anti-Stokes SSB regime and (b) balanced DSB regime. (c) Brillouin gain amplitude as a function of the fiber length for the two regimes measured at the Brillouin frequency shift of 10.925 GHz. (d) Brillouin gain amplitude as a function of the probe frequency detuning measured at the fiber end.

actually corresponds to the Brillouin frequency shift of our fiber. It has been determined from a Lorentzian fit of the Brillouin loss spectrum plotted in red in Fig. 3(d). There are several conclusions we might draw from all these figures. First, as it can be seen in Fig. 3(c), the probe amplitude at the beginning of the fiber is very similar in both cases but the contrast at the fiber end is significantly improved by using the anti-Stokes probe. A gain in sensitivity can be clearly seen at the end of the fiber with the anti-Stokes SSB case (red) compared to the DSB case (blue). We measured an improvement of the SNR of about 5 times. Second, whereas the use of the anti-Stokes probe provides a symmetric and single-hump Brillouin loss spectrum, Fig. 3(d) shows that the Brillouin gain spectrum in blue exhibits an asymmetric double-humped shape, which leads to a BFS displacement, as numerically shown in Fig. 1(b). Clearly, this direct comparison demonstrates the detrimental effect of pump depletion in long-range measurements and, in particular, how the anti-Stokes probe can help to further reduce this issue.

Our BOTDA sensor system has then been tested with different strain elongations up to 66 mm over 24 m at the fiber output. The aim is to check that no bias or error has been introduced by the pump depletion with the SSB modulator. Fig. 4(a) shows the BFS displacement at the fiber end due to applied strain. We measure a maximum frequency shift of 35 MHz that corresponds to a strain of $742 \mu\epsilon$. The BFS displacement versus applied strain is plotted in Fig. 4(b). We obtained by linear fitting a strain coefficient of $4.28 \text{ MHz}/100 \mu\epsilon$, which is in quite good agreement with the value of $5 \text{ MHz}/100 \mu\epsilon$ reported in literature [12]. This result means that errors introduced by the pump depletion in the anti-Stokes SSB regime can be ignored. Since the pump depletion effect is non-linear, the BFS displacements will also be non-linear if there are errors from the pump depletion. We also must stress here that we were not able to detect the applied strain when using the balanced DSB probe due to the very low SNR of our sensor at the end of the fiber, as shown in Fig. 3(c). This also

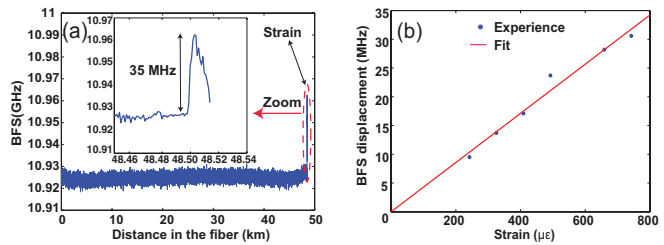


Fig. 4. (a) BFS with a strain of $742 \mu\epsilon$ over 24 m at the end of the fiber. Insets: zoom of the end of the fiber. (b) Measurement of strain coefficient at the end of the fiber versus the applied strain.

means that the SNR and thus the sensitivity has been improved with our technique compared to the balanced DSB case.

IV. CONCLUSION

We have made a long-range BOTDA sensing system that uses an anti-Stokes SSB-SC modulation technique. Enhanced sensitivity has been demonstrated both numerically and experimentally using this technique compared to the dual sideband standard one. This has been achieved by using a dual parallel Mach-Zehnder I/Q modulator in the probe path. Finally, our sensor has also been verified on a 50 km-long SMF with a measured strain coefficient of $4.28 \text{ MHz}/100 \mu\epsilon$. This letter should also contribute to a further understanding of the main limitations in BOTDA sensors.

REFERENCES

- [1] L. Thevenaz, S. F. Mafang, and J. Lin, "Depletion in a distributed Brillouin fiber sensor: Practical limitation and strategy to avoid it," in *Proc. 21st Int. Conf. Opt. Fiber Sensors*, 2011, pp. 1–4.
- [2] A. Minardo, R. Bernini, L. Zeni, L. Thevenaz, and F. Briffod, "A reconstruction technique for long-range stimulated Brillouin scattering distributed fiber-optic sensors: Experimental results," *Meas. Sci. Technol.*, vol. 16, no. 4, pp. 900–908, 2005.
- [3] M. A. Soto, G. Bolognini, and F. Di Pasquale, "Optimization of long-range BOTDA sensors with high resolution using first-order bi-directional Raman amplification," *Opt. Express*, vol. 19, no. 5, pp. 4444–4457, 2011.
- [4] X. Angulo-Vinuesa, *et al.*, "Raman-assisted Brillouin distributed temperature sensor over 100 km featuring 2 m resolution and 1.2°C uncertainty," *J. Lightw. Technol.*, vol. 30, no. 8, pp. 1060–1065, Apr. 15, 2012.
- [5] Y. Dong, L. Chen, and X. Bao, "Extending the sensing range of Brillouin optical time-domain analysis combining frequency-division multiplexing and in-line EDFAs," *J. Lightw. Technol.*, vol. 30, no. 8, pp. 1161–1167, Apr. 15, 2012.
- [6] M. A. Soto, G. Bolognini, and F. Di Pasquale, "Long-range simplex-coded BOTDA sensor over 120 km distance employing optical pre-amplification," *Opt. Lett.*, vol. 36, no. 2, pp. 232–234, 2011.
- [7] R. Bernini, A. Minardo, and L. Zeni, "Long-range distributed Brillouin fiber sensors by use of an unbalanced double sideband probe," *Opt. Express*, vol. 19, no. 24, pp. 23845–23856, 2011.
- [8] X. Bao, D. J. Webb, and D. A. Jackson, "32-km distributed temperature sensor based on Brillouin loss in an optical fiber," *Opt. Lett.*, vol. 18, no. 18, pp. 1561–1563, 1993.
- [9] M. J. Damzen, V. I. Vlad, V. Babbin, and A. Mocanescu, *Stimulated Brillouin Scattering: Fundamentals and Applications*. London, U.K.: IoP Publishing, 2003.
- [10] S. Afshar, G. A. Ferrier, X. Bao, and L. Chen, "Effect of the finite extinction ratio of an electro-optic modulator on the performance of distributed probe-pump Brillouin sensorsystems," *Opt. Lett.*, vol. 28, no. 16, pp. 1418–1420, 2003.
- [11] B. Stiller, *et al.*, "Fiber optic Brillouin distributed sensing using phase-shift keying modulation techniques," *Proc. SPIE*, vol. 8439, p. 843909, Apr. 2012.
- [12] X. Bao, D. J. Webb, and D. A. Jackson, "Very high resolution optical spectrometry by stimulated Brillouin scattering," *IEEE Photon. Technol. Lett.*, vol. 17, no. 4, pp. 855–857, Apr. 2005.

Black-light continuum generation in a silica-core photonic crystal fiber

T. Sylvestre,^{1,*} A. R. Ragueh,¹ M. W. Lee,¹ B. Stiller,¹ G. Fanjoux,¹ B. Barviau,² A. Mussot,² and A. Kudlinski²

¹Institut FEMTO-ST, Département d'Optique P. M. Duffieux, Université de Franche-Comté, CNRS, Besançon, France

²Laboratoire de Physique des Lasers, Atomes et Molécules, UMR-CNRS 8523 IRCICA, Université des Sciences et Technologies de Lille, Villeneuve d'Ascq, France

*Corresponding author: thibaut.sylvestre@univ-fcomte.fr

Received September 15, 2011; revised November 17, 2011; accepted November 17, 2011; posted November 18, 2011 (Doc. ID 154388); published January 9, 2012

We report the observation of a broadband continuum spanning from 350 to 470 nm in the black-light region of the electromagnetic spectrum as a result of picosecond pumping a solid-core silica photonic crystal fiber at 355 nm. This was achieved despite strong absorption and a large normal dispersion of silica glass in the UV. Further investigations reveal that the continuum generation results from the interplay of intermodally phase-matched four-wave mixing and cascaded Raman scattering. We also discuss the main limitations in terms of bandwidth and power due to temporal walk-off, fiber absorption, and the photo darkening effect, and we suggest simple solutions. © 2012 Optical Society of America

OCIS codes: 190.4370, 190.5650, 060.4005.

Over the last few years, there have been a number of important efforts to extend the blue and UV sides of supercontinuum (SC) generation in silica-core photonic crystal fibers (PCFs) [1–6]. These efforts are motivated by applications of broadband UV light in biomedical sciences and spectroscopy. While most of the experiments have been performed by pumping in near-IR (NIR) or visible regions, it is remarkable that the use of laser emitting in the UV as a pump for SC generation in PCF has not yet been endeavored. Generation of UV broadband light has, however, recently been reported in a single-mode high-OH fiber [7].

Herein, we demonstrate that despite both the strong absorption and large normal dispersion of silica in the UV, a broadband continuum can be efficiently generated in the black-light region of the electromagnetic spectrum by pumping a PCF with a picosecond microchip laser at 355 nm. The PCF is a standard solid-core silica PCF made by IRCICA. It is similar to those usually used for SC generation when pumping at 1064 nm in the small anomalous dispersion regime [8]. It has a triangular lattice with a pitch and hole diameter of 3.88 and 2.73 μm, respectively. Its cross-sectional image is depicted in Fig. 1(a) together with its dispersion curve for the fundamental mode around 355 nm. At this wavelength, our PCF exhibits a large normal group-velocity dispersion (GVD) dominated by material dispersion. In addition, the PCF carries several propagation modes. Three main transverse modes have been identified numerically using a finite element method. These modes are depicted in Figs. 1(b) and 1(c) together with their inverse group velocities and dispersion curves, respectively. The nonlinear coefficient is $\gamma = 34 \text{ W}^{-1} \text{ km}^{-1}$ for the fundamental mode, and its zero-dispersion wavelength (ZDW) is 1044 nm. The fiber loss at 355 nm was measured as 0.5 dBm^{-1} . As a pump laser, we used a passively Q-switched frequency-tripled Nd:YAG laser (Teemphotonics Powerchip Series) emitting 300 ps pulses (FWHM) at a repetition rate of 1 kHz and an average power of 22 mW. The output was coupled into our PCF by a 10× microscope objective. The output spectra were recorded using an optical spectrum

analyzer, and the continuum formation was analyzed by means of a variable attenuator. We also used a grating spectrometer (2400 l/mm) and a CCD color camera for modal and spectral analysis. Figure 2 shows the output spectra after 30 m of fiber for an increasing coupled pump power ranging from 0.5 to 4 mW. We can clearly see the continuum generation that starts from the pump wavelength and broadens up to the blue. The widest continuum spans 120 nm, from 350 to 470 nm, with an output power of $120 \mu\text{W}$. This corresponds to a low spectral power density of only $1 \mu\text{W}/\text{nm}$. The image in the inset shows the optical mode output of the widest continuum recorded by the color camera. The UV light appears as white, whereas the visible light is in true color. This image shows the continuum is mainly carried by the LP₃₁ mode. Figure 3 details the beginning of the continuum

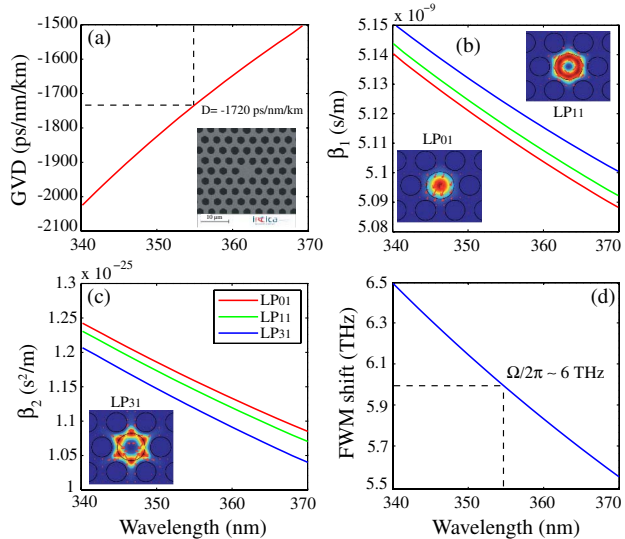


Fig. 1. (Color online) (a) Chromatic dispersion of the fundamental mode versus wavelength. Inset: SEM image of the solid-core PCF. (b), (c) The inverse group velocities and the chromatic dispersions of the three LP₀₁ (red), LP₁₁ (green), and LP₃₁ (blue) modes, respectively, shown in the insets. (d) FWM frequency shift versus wavelength. (See [Media 1](#).)

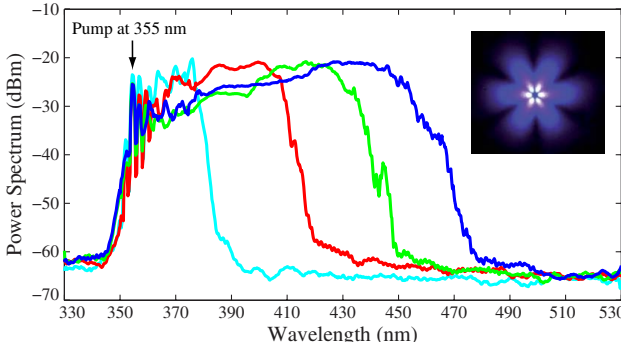


Fig. 2. (Color online) Output spectra recorded at the end of the 30 m long PCF for a variable coupled pump power from 0.5 to 4 mW. The spectral resolution is 0.5 nm. The inset shows the optical mode output of the blue continuum.

generation by cutting the fiber back to 1 and 4 m, respectively, keeping the same injection conditions. As can be seen in Fig. 3(a), we identify a preliminary intermodal four-wave mixing (FWM) process involving the pump (labeled P) in a mixed-mode distribution (see top image), an anti-Stokes sideband (AS₁) in the LP₀₁ mode, and a Stokes one (S₁) in the LP₁₁ mode. The phase-matching condition for this modal FWM process reads as $\kappa = (\beta_1^{11} - \beta_1^{01})\Omega + \beta_2\Omega^2 + 2\gamma P$ [9], where the first, second, and third terms represent the contributions of modal and chromatic dispersion and nonlinearity, respectively, to the phase mismatch. $\frac{\Omega}{2\pi}$ is the FWM frequency shift. β_1^{11} and β_1^{01} are the inverse group velocities of the LP₁₁ and LP₀₁ modes. β_2 is the GVD coefficient at pump wavelength. Figure 1(d) shows the FWM frequency shift versus the pump wavelength calculated from the above equation. At 355 nm, we found a frequency shift of 6 THz, in good agreement with the measurement of Fig. 3(a). We have also checked that all other possible FWM processes involving other modes are not phase-matched. For Fig. 3(b), the pump power exceeds the Raman threshold, which yields two strong first- and second-order Raman Stokes bands, R₁ and R₂. Simultaneously, parametric Stokes band S₁ acts as a second pump and generates both harmonic sideband S₂ and its own first-order Raman Stokes (SR₁). Surprisingly, we also observe the efficient generation of two anti-Stokes bands, AR₂ and ASR₂, far from the pump. We have checked that these waves result from FWM involving six waves, namely the pump P, the parametric band S₁, and Raman Stokes waves SR₁ and second-order R₂. In particular, AR₂ at 344 nm has been identified as being second-order Raman anti-Stokes

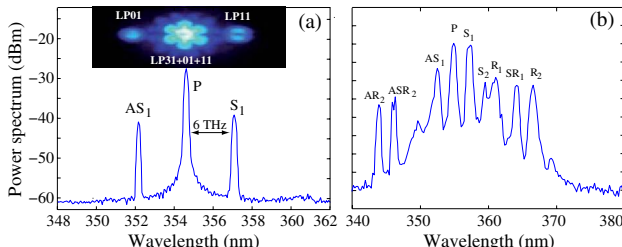


Fig. 3. (Color online) Output spectra recorded at the end of the photonic crystal fiber for shorter fiber lengths: (a) $L = 1$ m, (b) $L = 4$ m. The inset shows the modal distribution of FWM.

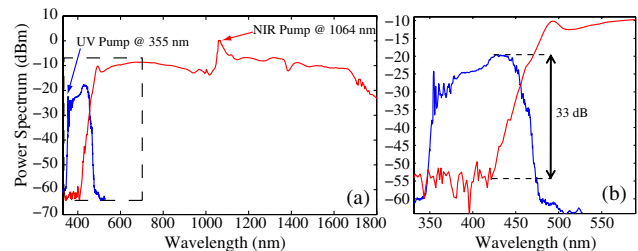


Fig. 4. (Color online) Direct comparison of spectra recorded at the output of the PCF under UV (355 nm, blue) and IR (1064 nm, red) laser pumping. Pump powers are 4 and 25 mW, respectively. (b) A zoom of the part of (a) shown in the dashed box.

upshifted by 26 THz from the pump. To our knowledge, this is the first time that second-order anti-Stokes was efficiently generated in the absence of first-order [10]. We have indeed verified that these waves are phase-matched in higher-order modes of the PCF and fall far from the Raman absorption band. At higher pump power, all Raman and parametric bands together merge and, because of the large Raman gain bandwidth, the CRS evolves toward a smooth continuum, as those shown in Fig. 2. This spectral broadening dynamics is analogous to the one previously reported using visible 532 nm pump pulses propagating in a dispersion-shifted fiber [9]. Note also that all the anti-Stokes waves reported in Fig. 3 no longer appear in Fig. 2 because of absorption. Moreover, all Raman Stokes bands are mainly carried by the LP₃₁ mode, which explains the optical mode distribution of Fig. 2.

Figure 4 compares the UV continuum generation with that generated by an IR subnanosecond microchip laser at 1064 nm, close to the ZDW of the PCF [8]. The experiments have been performed by replacing the UV laser by the IR one, keeping the same PCF, but with different coupled pump power. As can be seen, the SC generation

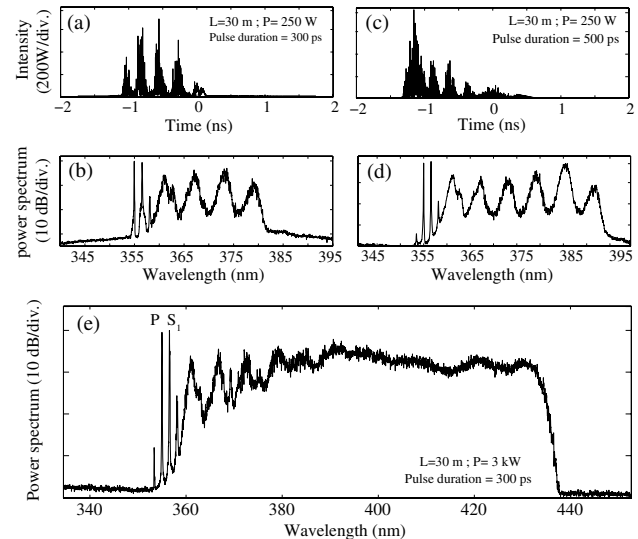


Fig. 5. Numerical simulations of cascaded Raman generation for two input pulse durations and UV continuum generation in the PCF. (a), (c) Temporal and (b),(d) spectral outputs. Parameters are indicated in the figures and text. (e) The UV-visible continuum generation for a peak power of 3kW.

using the IR pump spans more than two octaves from 450 nm to more than 1800 nm, whereas the UV continuum is limited to a third of an octave only. However, the latter covers a new UV-visible spectral window that is not accessible with the IR pump.

Let us now discuss the main limitations. The most important ones are fiber absorption and the photodarkening effect caused by UV radiation. We have indeed observed that the continuum bandwidth strongly decreases after about 20 min due to solarization. These detrimental effects could be mitigated by using specialty high-OH or solarization-resistant optical fiber, as in Ref. [7]. The third drawback is the large normal dispersion of silica that induces a strong pulse walk-off among the Raman pulses and thus limits the continuum extension toward longer wavelengths. This can be easily overcome by using longer nanosecond pulses. To verify the impact of walk-off, we performed split-step numerical simulations based on the generalized nonlinear Schrödinger equation, including the full Raman susceptibility and the wavelength-dependent absorption. As initial conditions, we consider a picosecond pump pulse at 355 nm together with the parametric band S_1 with half of the power to mimic the FWM of Fig. 3. Including the multimode behavior and the FWM intermodal coupling in the numerics is actually very time-consuming and computationally intensive. We also used the one-photon-per-mode model as an input condition. Figures 5(a)–(d) show the results of our numerical computations for 30 m of single-mode nonlinear propagation and for two pulse durations. As can be seen in Fig. 5(d), for a 500 ps pulse duration, a sixth-order Raman cascade is generated, whereas only four Raman orders occur for a 300 ps pulse duration [Fig. 5(b)]. Figures 5(a) and 5(c) show the corresponding temporal intensities. In both traces, we can clearly identify a train of noiselike Raman pulses that are optically delayed by walk-off. The temporal walk-off is about 300 ps, which is close to the pump pulse duration. Consequently, the Raman pulses do not overlap at all after 30 m of propagation, thus limiting the Raman cascade, as shown in Figs. 5(b) and 5(d). For comparison, we have analytically calculated the Raman pulse walk-off from the following expression: $T = D.L.\Delta\lambda$, where $\Delta\lambda$ is the Raman shift in wavelength. We found a pulse walk-off of 288 ps for $L = 30$ m, in good agreement with numerical simulations. Finally, the numerical simulation of Fig. 5(e)

was realized with the same conditions but at a higher peak power of 3 kW. It shows that the CRS evolves into a continuum that spans from 355 to about 430 nm, in rather good agreement with the experimental one shown in green in Fig. 2.

In conclusion, we reported the observation of a broadband black-light continuum in a solid-core silica photonic crystal fiber as a result of pumping at 355 nm. The continuum generation has been identified as resulting from the interplay between intermodal FWM and cascaded Raman generation. This fiber-format broadband IR-free black-light source could find possible applications as a Wood's lamp for multicolor excitation of fluorescent proteins in medicine, dermatology, molecular biology, or gas absorption spectroscopy [7,11]. Further progress will be pursued in the near future to improve the continuum bandwidth and spectral power density by using solarization-resistant silica optical fibers.

References

1. J. H. V. Price, T. M. Monro, K. Furusawa, W. Belardi, J. C. Baggett, S. Coyle, C. Netti, J. J. Baumberg, R. Paschotta, and D. J. Richardson, *Appl. Phys. B* **77**, 291 (2003).
2. A. Efimov, A. J. Taylor, F. J. Omenetto, J. C. Knight, W. Wadsworth, and P. S. J. Russell, *Opt. Express* **11**, 910 (2003).
3. G. Genty, M. Lehtonen, and H. Ludvigsen, *Opt. Lett.* **30**, 756 (2005).
4. A. Kudlinski, A. K. George, J. C. Knight, J. C. Travers, A. B. Rulkov, S. V. Popov, and J. R. Taylor, *Opt. Express* **14**, 5715 (2006).
5. J. M. Stone and J. C. Knight, *Opt. Express* **16**, 2670 (2008).
6. S. P. Stark, A. Podlipensky, N. Y. Joly, and P. St. J. Russell, *J. Opt. Soc. Am. B* **27**, 592 (2010).
7. R. J. Bartula, J. W. Walewski, and S. T. Sanders, *Appl. Phys. B* **84**, 395 (2006).
8. W. J. Wadsworth, N. Joly, J. C. Knight, T. A. Birks, F. Biancalana, and P. St. J. Russell, *Opt. Express* **12**, 299 (2004).
9. A. Mussot, T. Sylvestre, L. Provino, and H. Maillotte, *Opt. Lett.* **28**, 1820 (2003).
10. D. A. Akimov, E. E. Serebryannikov, A. M. Zheltikov, M. Schmitt, R. Maksimenka, W. Kiefer, K. V. Dukel'skii, V. S. Shevandin, and Yu. N. Kondrat'ev, *Opt. Lett.* **28**, 1948 (2003).
11. B.-W. Liu, M. Hu, S.-J. Wang, L. Chai, C. Wang, N. Dai, J.-Y. Li, and A. M. Zheltikov, *Opt. Lett.* **35**, 3958 (2010).

Investigation of a planar optical waveguide in 2D PPLN using Helium implantation technique

Q. Ripault,^{1,5,*} M. W. Lee,¹ F. Mériche,² T. Touam,³ B. Courtois,⁴ E. Ntsoenzok,⁴ L.-H. Peng,⁵ A. Fischer,¹ and A. Boudrioua¹

¹Laboratoire de Physique des Lasers, CNRS UMR 7538, Université de Paris 13, 93430 Villetaneuse, France

²Laboratoire d'Etudes des Matériaux, Université de Jijel, Algeria

³Laboratoire des Semi-conducteurs, Université Badji Mokhtar, BP 12 Annaba 23000, Algeria

⁴Conditions Extrême et Matériaux: Haute Température et Irradiation, CNRS UPR 3079, 45071 Orléans, France

⁵Graduate Institut of Photonics and Optoelectronics, GIPO, National Taiwan University, Taipei, 106, Taiwan

*quentin.ripault@univ-paris13.fr

Abstract: In this work, we report the investigation of a planar waveguide in a 2D periodically-poled lithium niobate (PPLN). The waveguide is fabricated by helium (He^+) implantation at 2 MeV and a fluence of 1.5×10^{16} ions/cm². Second harmonic generation (SHG) at 532 nm using a Q-switched laser and a CW laser diode at 1064 nm, was measured as a function of angular distribution and temperature. The experimental results show higher gain in SHG conversion efficiency in the waveguide than in the bulk 2D PPLN. In particular, SHGs from 2D reciprocal lattice vectors (RLV) are observed and studied.

© 2013 Optical Society of America

OCIS codes: (130.3730) Lithium niobate, (130.7405) Wavelength conversion devices; (190.4390) Nonlinear optics, integrated optics.

References and links

1. O. B. Jensen, P. E. Andersen, B. Sumpf, K.-H. Hasler, G. Erbert, and P. M. Petersen, “1.5 W green light generation by single pass second harmonic generation of a single-frequency tapered diode,” *Opt. Express* **17**(18), 6532–6539 (2009).
2. N. G. R. Broderick, G. W. Ross, H. L. Offerhaus, D. J. Richardson, and D. C. Hanna, “Hexagonally Poled lithium niobate: a two-dimensional nonlinear photonic crystal,” *Phys. Rev. Lett.* **84**(19), 4345–4348 (2000).
3. L. H. Peng, C. C. Hsu, J. Ng, and A. H. Kung, “Wavelength tunability of second-harmonic generation from two dimensional $\chi^{(2)}$ nonlinear photonic crystals with a tetragonal lattice structure,” *Appl. Phys. Lett.* **84**(17), 3250–3252 (2004).
4. V. Berger, “Nonlinear Photonic Crystals,” *Phys. Rev. Lett.* **81**(19), 4136–4139 (1998).
5. M. L. Shah, “Waveguide in LiNbO₃ by ion exchange techniques,” *Appl. Phys. Lett.* **26**(11), 652–653 (1975).
6. K. Gallo, C. Codemard, C. B. E. Gawith, J. Nilsson, P. G. R. Smith, N. G. R. Broderick, and D. J. Richardson, “Guided-wave second-harmonic generation in a LiNbO₃ nonlinear photonic crystal,” *Opt. Lett.* **31**(9), 1232–1234 (2006).
7. B. Vincent, A. Boudrioua, R. Kremer, and P. Moretti, “Second harmonic generation in helium-implanted periodically poled lithium niobate planar waveguides,” *Opt. Commun.* **247**(4-6), 461–469 (2005).
8. J. Rams, J. Olivares, P. J. Chandler, and P. D. Townsend, “Second harmonic generation capabilities of ion implanted LinbO₃ waveguides,” *J. Appl. Opt.* **84**, 5180–5183 (1998).
9. F. Chen, “Photonic guiding structures in lithium niobate crystals produced by energetic ion beams,” *J. Appl. Opt.* **106**, 081101 (2012).
10. F. Chen, “Micro- and submicrometric waveguiding structures in optical crystals produced by ion beams for photonic applications,” *Laser Photon. Rev.* **6**(5), 622–640 (2012).
11. A. M. Radojevic, M. Levy, R. M. Osgood, Jr., D. H. Jundt, A. Kumar, and H. Bakhrui, “Second-order optical nonlinearity of 10-μm -thick periodically poled LiNbO₃ films,” *Opt. Lett.* **25**(14), 1034–1036 (2000).
12. M. Yamada, N. Nada, M. Saitoh, and K. Watanabe, “First order quasi-phase matched LiNbO₃ waveguide periodically poled by applying an external field for efficient blue second-harmonic generation,” *Appl. Phys. Lett.* **62**(5), 435–436 (1993).
13. J. F. Ziegler, J. P. Biersack, and U. Littmark, *The Stopping and Range of Ions in Solids* (Pergamon, 1985), www.srim.org.
14. F. Chen, X. L. Wang, and K. M. Wang, “Development of ion implanted optical waveguides in optical materials: a review,” *Int. Optical Materials* **29**(11), 1523–1542 (2007).

15. L. Wang, K. M. Wang, F. Chen, X. L. Wang, L. L. Wang, H. Liu, and Q. M. Lu, "Optical waveguide in stoichiometric lithium niobate formed by 500 keV proton implantation," *Opt. Express* **15**(25), 16880–16885 (2007).
16. P. D. Townsend, P. J. Chandler, and L. Zhang, *Optical Effects of Ion Implantation* (Cambridge University Press, 1994).
17. J. M. White and P. F. Heidrich, "Optical waveguide refractive index profiles determined from measurement of mode indices: a simple analysis," *Appl. Opt.* **15**(1), 151–155 (1976).
18. T. Pliska, D. Fluck, P. Gunter, L. Beckers, and C. Buchal, "Mode propagation losses in He^+ ion-implanted KNbO_3 waveguides," *J. Opt. Soc. Am. B* **15**(2), 628–639 (1998).
19. S. L. Li, K. M. Wang, F. Chen, X. L. Wang, G. Fu, D. Y. Shen, H. J. Ma, and R. Nie, "Monomode optical waveguide excited at 1540 nm in LiNbO_3 formed by MeV carbon ion implantation at low doses," *Opt. Express* **12**(5), 747–752 (2004).
20. B. Vincent, R. Kremer, A. Boudrioua, P. Moretti, Y. C. Zhang, C. Hsu, and L. H. Peng, "Green light generation in a periodically poled Zn-doped LiNbO_3 planar waveguide fabricated by He^+ implantation," *Appl. Phys. B* **89**(2-3), 235–239 (2007).

1. Introduction

Nonlinear integrated optics has attracted much attention as it allows designs of new optical components for solid tunable coherent and miniature light sources [1]. In particular, integrated optics using nonlinear photonic crystals (NLPC) has been recently subject of several developments for applications in the field of light sources and optical signal processing [2, 3]. NLPCs are materials where the sign of $\chi^{(2)}$ is periodically reversed in two dimensions [4]. This produces many reciprocal lattice vectors (RLV) in the 2D reciprocal lattice, corresponding to one or more phase matching solution. Consequently, the 2D structure provides a much greater flexibility to quasi-phase matching (QPM) processes [2] than 1D structure. Despite of low QPM orders, the high flexibility of 2D structure allows multi-wavelength light generation by temperature and angular tuning. 2D-PPLN is an excellent materiel for this purpose. Moreover it offers new QPM orders which are no multiples of the fundamental QPM process. Therefore, such a structure in a waveguide configuration can provide high non-linear conversion efficiency with low power due to long interaction length and high energy density confinement within the crystal.

Up until now, the most widely-used waveguide fabrication techniques in periodically-poled crystals such as 1D PPLN are in-diffusion of metals and ionic exchange [5, 6]. However, it has been reported that these techniques not obviously affect nonlinear optical properties of the crystal. Recently, Helium ion implantation with several MeV energies has been developed and it manifests an alternative technique to fabricate optical waveguides in nonlinear crystals including 1D PPLN [7–10]. The flexibility of the implantation technique particularly comes from the fact that one can precisely control the implantation parameters. Regarding to this, the ion beam energy allows us to define accurately the waveguide thickness which is related to the implantation energy of the ions within the crystal. Furthermore, the fluence of ions gives rise to the refractive index variation, creating an optical barrier. This method also allows fabricating nonlinear crystal thin films by crystal ion slicing technique (CIS) [11]. This well-controlled method does not virtually affect linear and non-linear optical properties of PPLN after an optimized post-annealing step of the sample [8]. Besides, He^+ implantation ensures a good homogeneity of optical properties along the waveguide, and avoids out-diffusion of lithium oxide from the sample surface which may occur at high annealing temperature with other methods. Despite it induces defects and stress in the implanted region with increasing ion fluence [9, 10], this process shows high efficiency in frequency conversion [8].

In this paper, we report, for the first time to the best of our knowledge, the investigation of optical waveguides in 2D PPLN using He^+ implantation technique. The 2D PPLN with a square lattice of a period of 6.92 μm is used in our experiments. The 2D PPLN waveguide obtained by He^+ implantation is characterized by the guiding properties and non-linear optical properties. The experimental results particularly include second harmonic generation (SHG)

measurements at high power density with a Q-switched laser at 1064 nm. SHG from 2D RLV is also investigated. The characterizations on bulk and waveguides are compared.

2. Sample preparations

The 2D PPLN (z-cut) used in this work is obtained by electrical poling method [12]. An electric field density of 21 kV/mm closed to the coercive field of the material, is applied to LiNbO₃ through a titanium microelectrode lattice [8]. The poled area is 6 mm x 6 mm at the centre of the sample with a thickness of 1 mm. Figure 1 indicates both z + and z- faces of the poled region with a 2D square lattice with a period of $\Lambda = 6.92 \mu\text{m}$ and a duty cycle of 50%. This square lattice period is particularly chosen to obtain QPM for SHG at 1064 nm.

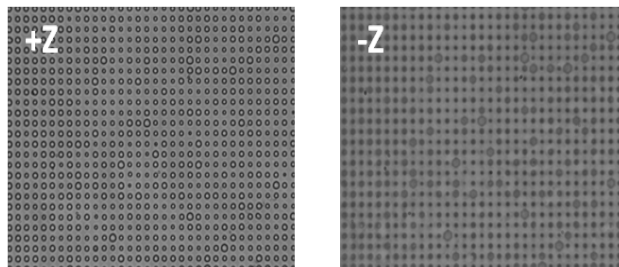


Fig. 1. z + and z- 2D-periodically-poled surfaces of LiNbO₃ with a square lattice period of 6.92 μm revealed by chemical etching.

After the poling process, helium ions are implanted with a fluence of $1.5 \times 10^{16} \text{ ions/cm}^2$ and energy of 1.5 MeV on the entire surface of the 2D-PPLN z + side by using a Van De Graaff accelerator. According to Stopping and Range of Ions in Matter (SRIM) simulations [13], the implantation energy is set to 1.5 MeV. At this energy, an optical confinement barrier is expected to be built at a depth of 3.6 μm below the surface of our samples [14, 15]. Thus, light can be confined between this barrier and the crystal-air interface. In fact, a large disordering of the crystal lattice is formed by the energy deposition, which results in the decrease of both the ordinary and extraordinary indices of the crystal, thus creating a light confinement for TE and TM guided modes. The choice of implantation energy allows low TM-multimode guiding at a wavelength of 1064 nm (quasi single-mode waveguide at this wavelength). The implantation fluence is chosen to obtain a maximum refractive index variation in the optical barrier. After the implantation, the sample is annealed at 200°C for 1 hour [8]. The annealing treatment allows the crystal to recover from the implantation-induced defects [16]. Note that the implantation should be undertaken after poling, because the quality of the poling process highly depends on the purity of substrates. In fact, it has been shown that poling process on He⁺-implanted LiNbO₃ can alter the growth of reversed domains [7].

3. Linear optical properties of the NLPC waveguide

First, we have measured the waveguiding properties of our He⁺ NLPC samples at 532 nm and 632 nm. For this purpose, we have used the well-known dark m-lines method based on prism coupling in order to excite the structure guided modes. Our results indicate that the waveguide supports both the ordinary and extraordinary guided modes (TE and TM modes, respectively). Note that, 5 TE and 3 TM modes were clearly identified.

Afterward, we have extrapolated the refractive index profile of our sample. We have used the inverse Wentzel-Kramers-Brillouin (i-WKB) method [17] to reconstruct the refractive index profiles. For instance, at 633 nm, the results indicate that the maximum index variation is obtained as 0.07 for the ordinary index and 0.019 for the extraordinary one. The obtained waveguide shows a quasi-step index profile and low-m multimode for TM-polarization which allows SHG using the optimal non-linear coefficients d_{33} at 1064 nm. Comparing these results with other samples made with lower fluences, it is seen that the implantation fluence has a

greater influence on the ordinary index than the extraordinary one. It is noted that only the extraordinary effective indices participate to fulfill QPM conditions in our work.

We have also estimated that the profile of n_o indicates a waveguide thickness of 3.6 μm which is similar to the one obtained by the damage profile simulated using SRIM code [13]. As a matter of fact, the ions are initially slowed by electronic excitation (defined as the electronic stopping region just below the surface) with the ionization of the crystal and creation of point defects along their path. At the end of the ion track, a low refractive index optical barrier is built up because of the lattice disorder produced by the nuclear collisions with damages in the crystal lattice and the creation of impurities [18].

We have also measured the optical losses by using a CCD camera in order to collect the light scattered from the waveguide surface. An end-fire coupling configuration is used to couple-in light beam through the polished waveguide face with a microscope objective. Measurements are performed at 532 nm, 633 nm and 1064 nm. We have found that our sample presents a global optical loss of 3 dB/cm. We speculate that defects and optical tunnelling might be at the origin signal attenuation along the waveguide [19]. The attenuation can be optimised by finding out a compromise between implantation and post-implantation parameters. Another study was conducted concerning multiple He⁺-implantation at lower fluences and revealed losses of about 2 dB/cm.

4. Second harmonic generation measurements

An experimental setup similar to reference [20] is used in order to measure the non-linear properties of the bulk and the He⁺-implanted 2D-PPLN waveguide. Using a Q-switched laser at 1064 nm, the beam goes through a half wave plate and a polarization splitter cube to select the TM polarization and vary the pump power. The NLPC sample is temperature-stabilized using an oven in order to achieve phase matching at the pump laser wavelength. The laser beam is coupled into the waveguide through a x20 microscope objective at a normal incidence. In order to calculate the fundamental power included into the conversion, we have considered 70% of the incident power due to the Fresnel coupling losses. Then, SHG signal at 532 nm is collected via another microscope objective and the infrared is then filtered out by a dichroic mirror in front of the power meter.

First, we have considered the angular distribution of the SHG signal obtained from a sample with a square lattice and a period of $\Lambda = 6.92 \mu\text{m}$ at different temperatures (T). By using the nonlinear Bragg's law [4], we can predict the walk-off angles of each RLV according to the temperature. Note that the nonlinear Bragg's law [4] is set by:

$$\lambda_{2\omega} = \frac{2\pi}{|\vec{G}_{mn}|} \sqrt{(n_{2\omega}(T) - n_\omega(T))^2 + 4n_{2\omega}(T)n_\omega(T) \sin^2 \frac{\theta_{wo}}{2}} \quad (1)$$

where $\theta_{wo} = (\vec{k}_{2\omega}, \vec{k}_\omega)$ is the walk-off angle, n_ω and $n_{2\omega}$ are the extraordinary refractive indices at 1064 nm and 532 nm, and $|\vec{G}_{mn}| = \frac{2\pi}{\Lambda} \sqrt{m^2 + n^2}$ with m and n integers

From Eq. (1), the observed SHG-external angles Θ_{mn} for these RLVs are calculated:

$$\Theta_{mn}(T) = \arcsin \left[n_{2\omega}(T) \sin \left[2 \arcsin \left[\frac{\left(\frac{\lambda_{2\omega}}{\Lambda} \right)^2 (m^2 + n^2) - (n_{2\omega}(T) - n_\omega(T))^2}{4n_{2\omega}(T)n_\omega(T)} \right]^{1/2} \right] \right] \quad (2)$$

From Eq. (2), the calculated angles at 53°C are 0° for \mathbf{G}_{10} , $\pm 4.6^\circ$ for $\mathbf{G}_{1\pm 1}$ and $\pm 7.8^\circ$ for $\mathbf{G}_{1\pm 2}$. As a matter of fact, Fig. 4 (a) indicates that the TM-modes can contribute to the SHG for the RLVs of \mathbf{G}_{10} , \mathbf{G}_{1-1} , \mathbf{G}_{11} , \mathbf{G}_{1-2} and \mathbf{G}_{12} .

As an example, the experimental results are reported in Fig. 2(b). At 53°C the SHG signal is only observed for \mathbf{G}_{10} . However, at 102°C, in addition to the \mathbf{G}_{10} contribution, the SHG is also observed around $\pm 5^\circ$ in both the bulk and the waveguide in Fig. 2(b), which are close to the calculated values. This is a clear evidence of the RLV contribution to SHG, which is not observed in 1D-PPLN. Moreover, the SHG intensity for \mathbf{G}_{1-1} and \mathbf{G}_{11} in the waveguide is higher than that in the bulk with a slight angular shift due to the fact that in the waveguide, one has to consider the effective refractive indices instead of the material refractive index. It is clearly seen from the figure that the SHG efficiency is improved in the waveguide. On the other hand, the SHG intensity relative to the \mathbf{G}_{1-2} and \mathbf{G}_{12} RLVs is not observed in our work.

In the second step, the SHG temperature tuning curves are measured in the 2D-PPLN bulk and the waveguide. Results are displayed in Fig. 3. The optimal crystal temperature is obtained as 53 °C for \mathbf{G}_{10} and 102 °C for $\mathbf{G}_{1\pm 1}$. In the inset of the figure, the images taken by a CCD camera clearly show the SHGs for RLV \mathbf{G}_{10} and $\mathbf{G}_{1\pm 1}$. The images confirm again the \mathbf{G}_{1-1} and \mathbf{G}_{11} contribution to SHG. The temperature tuning bandwidth at each peak is halved in the waveguide compared to the bulk case. We also notice a slight shift of the maximum peak temperature in the waveguide configuration (≈ 0.2 °C). In fact, the consideration of the effective refractive indices in the waveguide QPM conditions should slightly decrease the crystal working temperature. The experimental results are fitted with a *sinc* function [18]. From this fitting, the interaction length is obtained as 4.4 mm in the waveguide and 1.2 mm in the bulk.

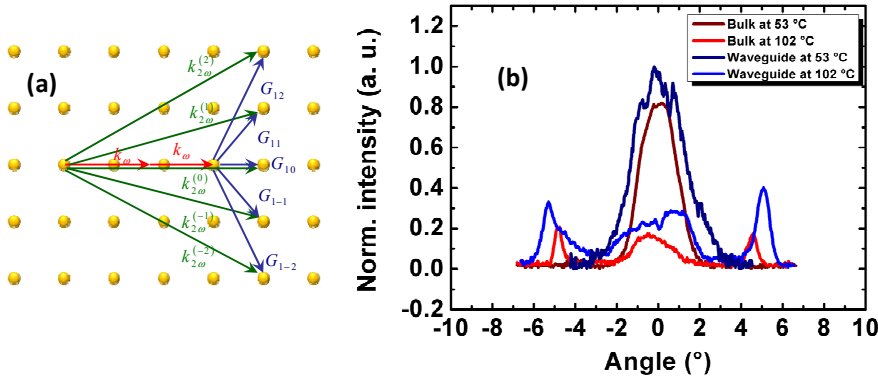


Fig. 2. (a) The schematic geometrical reciprocal lattice for SHG interaction. (b) The normalized far-field SHG intensity angular distribution from different RLVs, in bulk at 53°C (brown trace) and 102°C (red trace) and waveguide at 53°C (dark blue trace) and 102°C (blue trace).

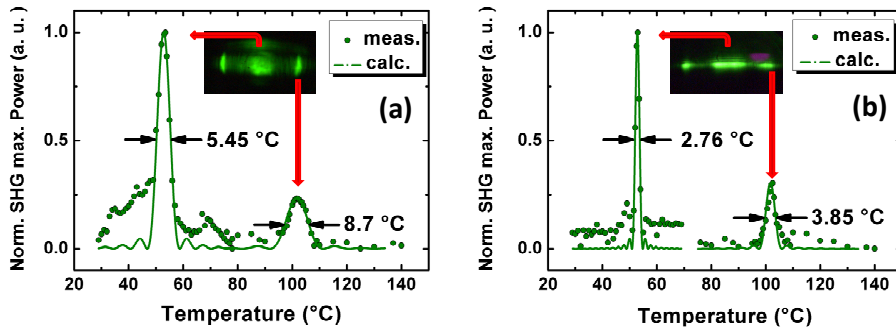


Fig. 3. Normalized optical SHG powers vs. temperature from (a) the 2D-PPLN bulk and (b) the waveguide.

Finally, we report the SHG power at 532 nm versus the pump power at 1064 nm. Initially, we have worked in pulsed regime with a Q-switched laser with a pulse width of 7 ns at a repetition rate of 15 Hz. We note that the SHG emission for G_{10} in the waveguide is almost doubled as shown in Fig. 4(a). This is very likely due to the pump beam confinement in the planar waveguide and the improved effective interaction length as the waveguide is considered.

On the other hand, the SHG is saturated at lower optical pump power in the waveguide than that in the bulk due to the higher power density in the waveguide as shown in Fig. 4(c). Furthermore, at these pump intensities, we observe few damages from photorefractive effects in the waveguide. We have also studied SHGs at much lower pump power density with a CW diode laser at 1064 nm (Fig. 4(b)). For that pump source, the injection pump power into the sample is measured as ~ 250 mW. At this power, the QPM frequency doubling output power from the waveguide reaches a maximum power of 2.9 mW whereas 1.1 mW is measured from the bulk 2D-PPLN as shown in Fig. 4(b). In Fig. 4(c), the SHG power from the waveguide is three time stronger than that from the bulk, which again clearly shows the improvement of SHG efficiency. The experimental results are fitted to the theoretical curve for second harmonic generation with a polynomial function in Fig. 4(b). The fit gives a non-linear conversion efficiency of 1.23%/W for the waveguide and 0.4%/W for the bulk case. Indeed, the improvement in SHG emission comes from the long interaction length in the waveguide.

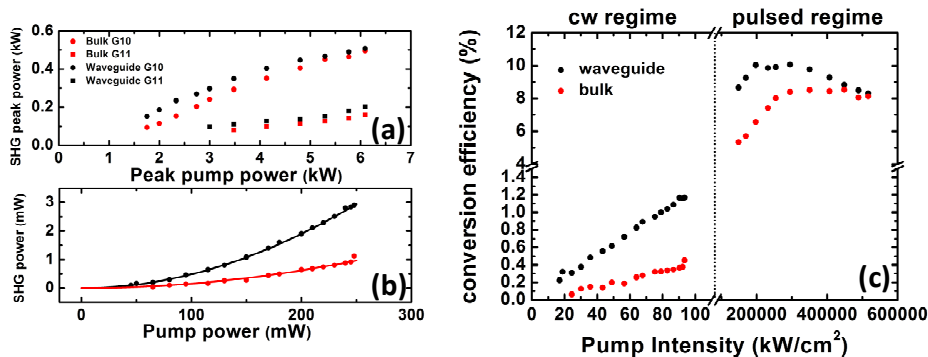


Fig. 4. SHG output power vs. input power in pulsed (a) and CW regimes (b). In (b) the numerical fit results in a nonlinear conversion efficiency of 1.23%/W for the waveguide. (c) Conversion efficiency resulting from the 2D-PPLN waveguide (black points) and the bulk (red points) in CW and pulsed regimes.

5. Conclusion

In this work, we have successfully demonstrated a waveguide in 2D-PPLN by the Helium implantation technique. The obtained experimental results clearly demonstrate that this technique does not affect the non-linear properties of our 2D-PPLN. Furthermore, under the same experimental conditions, the 2D-PPLN waveguide exhibits a three times higher conversion efficiency in SHG from infrared light to green light compared to the bulk ones. We have also observed SHGs resulting from the reciprocal vectors in the 2D lattice crystal.

Acknowledgment

The authors gratefully acknowledge the Taipei Representative Office in France (Taiwan) for support of this research.



Multiwavelength generation from multi-nonlinear optical process in a 2D PPLT

ZOHRA YELLAS,¹ MIN WON LEE,^{2,*} RÉGIS KREMER,³ KAI-HSUN CHANG,⁴ MAHMOUD R. BEGHOUL,¹ LUNG-HAN PENG⁴ AND AZZEDINE BOUDRIOUA²

¹Laboratoire d'Etudes des Matériaux (LEM), Université de Jijel, 18000 Algeria

²Laboratoire de Physique de Lasers CNRS UMR 7538, Université Paris 13, Sorbonne Paris Cité, 93430 Villetaneuse, France

³Université de Lorraine, Laboratoire Matériaux Optiques, Photoniques et Systèmes, EA 4423, Metz, France

⁴Graduate Institute of Photonics and Optoelectronics and Department of Electrical Engineering, National Taiwan University, Taipei, Taiwan

*min.lee@univ-paris13.fr

Abstract: We have demonstrated multi-wavelength generation in a nonlinear photonic crystals of lithium tantalate. The optical parametric generation leads to second harmonic generation, sum-frequency generation and other frequency conversion in a cascade process. These conversions are assisted by all the optical nonlinear process involving $\chi^{(2)}$ and achieved by satisfying the quasi-phase matching conditions.

© 2017 Optical Society of America under the terms of the OSA Open Access Publishing Agreement

OCIS codes: (190.4410) Nonlinear optics, parametric processes; (190.7220) Upconversion.

References and links

1. V. Berger, "Nonlinear Photonic Crystals," *Phys. Rev. Lett.* **81**, 4136–4139 (1998).
2. A. Arie, N. Habschoos, and A. Bahabad, "Quasi phase matching in two-dimensional nonlinear photonic crystals," *Opt. Quant. Electron.* **39**, 361–375 (2007).
3. N. G. R. Broderick, G. W. Ross, H. L. Offerhaus, D. J. Richardson, and D. C. Hanna, "Hexagonally Poled Lithium Niobate: A Two-Dimensional Nonlinear Photonic Crystal," *Phys. Rev. Lett.* **84**, 4345–4348 (2000).
4. L.-H. Peng and C.-C. Hsu, "Wavelength tunability of second-harmonic generation from two-dimensional $\chi^{(2)}$ nonlinear photonic crystals with a tetragonal lattice structure," *Appl. Phys. Lett.* **84**, 3250–3252 (2004).
5. P. Xu, J. F. Wang, C. Li, Z. D. Xie, X. J. Lv, H. Y. Leng, J. S. Zhao, and S. N. Zhu, "Simultaneous optical parametric oscillation and intracavity second-harmonic generation based on a hexagonally poled lithium tantalate," *Opt. Express* **17**, 4289–4294 (2009).
6. Q. Ripault, M. W. Lee, F. Mâlfliche, T. Touam, B. Courtois, E. Ntsoenzok, L.-H. Peng, A. Fischer, and A. Boudrioua, "Investigation of a planar optical waveguide in 2d PPLN using Helium implantation technique," *Opt. Express* **21**, 7202–7208 (2013).
7. Y. Sheng, S. M. Saltiel, and K. Koynov, "Cascaded third-harmonic generation in a single short-range-ordered nonlinear photonic crystal," *Opt. Lett.* **34**, 656–658 (2009).
8. W. Q. Zhang, F. Yang, and X. Li, "Double quasi phase matching for both optical parametric oscillator and difference frequency generation," *Opt. Commun.* **282**, 1406–1411 (2009).
9. M. Levenius, V. Pasiskevicius, and K. Gallo, "Angular degrees of freedom in twin-beam parametric down-conversion," *Appl. Phys. Lett.* **101**, 121114 (2012).
10. M. Lazoul, A. Boudrioua, L. M. Simohamed, A. Fischer, and L.-H. Peng, "Experimental study of multiwavelength parametric generation in a two-dimensional periodically poled lithium tantalate crystal," *Opt. Lett.* **38**, 3892–3894 (2013).
11. L. Chen, P. Xu, Y. F. Bai, X. W. Luo, M. L. Zhong, M. Dai, M. H. Lu, and S. N. Zhu, "Concurrent optical parametric down-conversion in $\chi^{(2)}$ nonlinear photonic crystals," *Opt. Express* **22**, 13164–13169 (2014).
12. S. Carrasco, A. V. Sergienko, B. E. A. Saleh, M. C. Teich, J. P. Torres, and L. Torner, "Spectral engineering of entangled two-photon states," *Phys. Rev. A* **73**, 063802 (2006).
13. S. Witte and K. S. E. Eikema, "Ultrafast Optical Parametric Chirped-Pulse Amplification," *IEEE J. Sel. Top. Quantum Electron.* **18**, 296–307 (2012).
14. T. Töpfer, K. P. Petrov, Y. Mine, D. Jundt, R. F. Curl, and F. K. Tittel, "Room-temperature mid-infrared laser sensor for trace gas detection," *Appl. Opt.* **36**, 8042–8049 (1997).

#307281

Journal © 2017

<https://doi.org/10.1364/OE.25.030253>

Received 15 Sep 2017; revised 9 Nov 2017; accepted 11 Nov 2017; published 17 Nov 2017

Corrected: 22 November 2017

15. X. Fang, D. Wei, D. Liu, W. Zhong, R. Ni, Z. Chen, X. Hu, Y. Zhang, S. N. Zhu, and M. Xiao, "Multiple copies of orbital angular momentum states through second-harmonic generation in a two-dimensional periodically poled LiTaO₃ crystal," *Appl. Phys. Lett.* **107**, 161102 (2015).
16. C.-Q. Xu and B. Chen, "Cascaded wavelength conversions based on sum-frequency generation and difference-frequency generation," *Opt. Lett.* **29**, 292–294 (2004).
17. C.-M. Lai, I.-N. Hu, Y.-Y. Lai, Z.-X. Huang, L.-H. Peng, A. Boudrioua, and A.-H. Kung, "Upconversion blue laser by intracavity frequency self-doubling of periodically poled lithium tantalate parametric oscillator," *Opt. Lett.* **35**, 160–162 (2010).
18. M. Levenius, V. Pasiskevicius, F. Laurell, and K. Gallo, "Ultra-broadband optical parametric generation in periodically poled stoichiometric LiTaO₃," *Opt. Express* **19**, 4121–4128 (2011).
19. M. Conforti, F. Baronio, M. Levenius, and K. Gallo, "Broadband parametric processes in $\chi^{(2)}$ nonlinear photonic crystals," *Opt. Lett.* **39**, 3457–3460 (2014).
20. M. Levenius, V. Pasiskevicius, and K. Gallo, "Cascaded up-conversion of twin-beam OPG in nonlinear photonic crystals," in "2013 Conference on Lasers Electro-Optics Europe International Quantum Electronics Conference CLEO EUROPE/IQEC," (2013), pp. 1.
21. A. Bruner, D. Eger, M. B. Oron, P. Blau, M. Katz, and S. Ruschin, "Temperature-dependent Sellmeier equation for the refractive index of stoichiometric lithium tantalate," *Opt. Lett.* **28**, 194–196 (2003).

Nonlinear photonic crystals have attracted great attention over decades for optical frequency conversion. They are nonlinear crystals with a 2 dimensional periodically-poled lattice such as periodically-poled lithium tantalite (2D-PPLT) and periodically-poled lithium niobate (2D-PPLN). They have a great flexibility of quasi-phase matching thank to the reciprocal lattice vectors [1, 2]. Such characteristics facilitates frequency conversion such as second harmonic generation (SHG) [3–6], sum-frequency generation (SFG) [7], difference frequency generation (DFG) [8] or optical parametric generation (OPG) [9–11]. The reciprocal lattice vectors also allow wavelength tuneability by changing temperature [4] or incident angle [9, 10].

In fact, optical frequency conversion is essential in a number of potential applications. Particularly, frequency conversion using quasi-phase matching (QPM) allows entangled photon-pair generation for quantum optics [12], amplification of ultra-fast pulses [13], gas detection sensing [14] and multiple copies of orbital angular momentum states [15].

However, the aforementioned nonlinear processes do not usually occur at the same time because of the different phase matching conditions for each process. It has been reported that SFG and DFG can be generated in a PPLN when facilitated by a cascaded process [16]. For nonlinear photonic crystals, a blue light can be generated from an OPG-signal in a SHG process using a PPLT with a square lattice [17] or a PPLT with a hexagonal lattice [5]. In some studies, it has been demonstrated that a broadband wavelength can be generated in a hexagonal nonlinear photonic crystal [18, 19]. Moreover, several nonlinear processes have been involved in multi-wavelength generation in a hexagonally-poled LiTaO₃ [20]. In this case, SHG and OPG were generated and SFG was then generated by a cascaded process.

In this work, we demonstrate for the first time multi-wavelength generation in a square lattice 2D PPLT exploiting multi optical nonlinear process. By pumping the crystal at 532 nm, OPG firstly occurs and OPG triggers SHG and SFG. In a single crystal, it has also been observed simultaneously three different OPG processes.

The nonlinear crystal used in this work is a lithium tantalate (LiTaO₃) with a thickness of 0.5 mm. The crystal is periodically poled to invert the polarisation in 2 directions as shown in Fig. 1(a). The average lattice period is $\Lambda_x = \Lambda_y = 8.52 \mu\text{m}$ with a filling factor of 38 % in a single set of square array. The poled area is 2 cm × 1 cm. Note that these parameters have been chosen from previous work as they allow efficient optical parametric generation with a maximum conversion efficiency [10].

Our 2D PPLT is characterised using an experimental setup illustrated in Fig. 1(b). The pump laser used in this work is a pulsed laser at 532 nm and delivers a maximum energy of 40 μJ with a pulse width of 500 ps. A half-wave plate is used to adjust the polarisation of the pump beam and a lens of 20cm focal length is positioned to inject the pump into the crystal. The peak

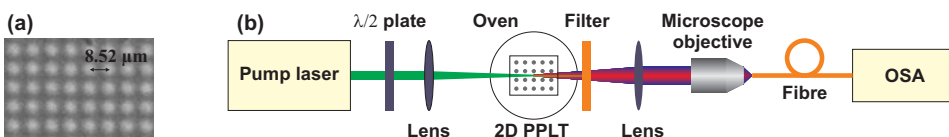


Fig. 1. (a) 2D PPLT: view on Z^+ . (b) Experimental setup. OSA: Optical Spectrum Analyser.

power can be delivered up to 80 kW which is focused to the sample with a beam waist of 95 μm , leading to a peak intensity of 282 MW/cm 2 . The crystal is put in a small oven to control the crystal temperature at 110 °C. The light generated by the nonlinear process is collimated by a lens and the pump beam is removed by a band stop filter at 532 nm. The filtered light is injected into a standard multimode fibre with a core diameter of 50 μm by a microscope objective. The spectrum of multi-wavelength light is registered by an optical spectrum analyser.

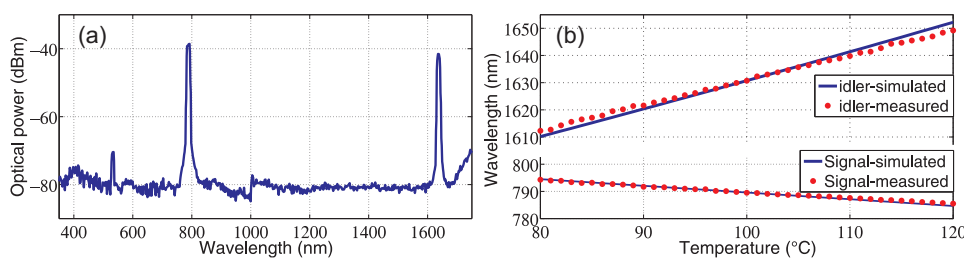


Fig. 2. (a) Spectrum with the signal (787 nm) and idler (1640 nm) measured with a peak power of 16 kW. (b) Wavelength tuneability of the signal and idler vs. temperature.

First, OPG is undertaken at a peak power of 16 kW (8 μJ) at 110 °C and an incident angle of 0 °. Figure 2(a) shows an OPG spectrum which is measured in the colinear direction with the pump source. In the figure, the peak at 532 nm is the residual pump and the peaks at 787 nm and 1640 nm are expected to be the signal and idler, respectively. These wavelengths satisfy the energy and momentum conservation laws as described in the OPG process, which are given by:

$$\frac{1}{\lambda_p} - \frac{1}{\lambda_s} - \frac{1}{\lambda_i} = 0 \quad (1)$$

$$\frac{n_p(\lambda_p, T)}{\lambda_p} - \frac{n_s(\lambda_s, T)}{\lambda_s} - \frac{n_i(\lambda_i, T)}{\lambda_i} - \frac{\sqrt{m^2 + n^2}}{\Lambda} = 0 \quad (2)$$

where $n(\lambda, T)$ is the refractive index at given wavelength λ and temperature T , m and n are the QPM orders for the reciprocal lattice vector $\mathbf{K}_{m,n}$ and Λ is the QPM period. The refractive index of Lithium Tantalate is obtained from Ref. [21]. As the measurements are undertaken in a collinear direction, 1D QPM condition can rather be considered i.e. $\mathbf{K}_{1,0}$ as a first approximation. It is found from the equations that the signal and idler occur at 787 nm and 1640 nm for a QPM period of 8.51 μm in a very good agreement with the experimental data.

This result is further emphasised by analysing the variation of the OPG interaction with the crystal temperature varied from 80 °C to 120 °C. The temperature variation results in tuning the wavelengths as shown in Fig. 2(b). The lower and upper solid lines represent the signal and idler wavelengths, respectively, obtained in simulations with a QPM period of 8.51 μm as a function of the temperature. The lower and upper circle dots indicate those measured in the experiment. It is clearly seen from the figure that the measured wavelengths for the signal and idler are again in a good agreement with those obtained in simulation. As such, this comparison confirms the assumption of 1D QPM OPG interaction with the crystal period of 8.52 μm .

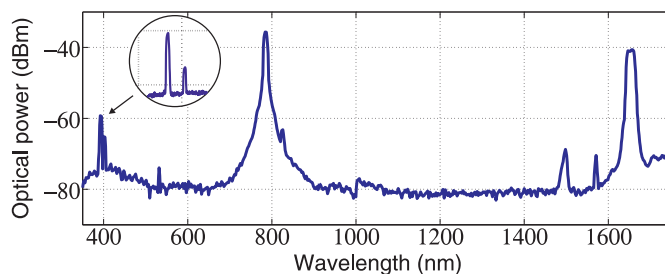


Fig. 3. Full spectrum measured at a peak power of 40 kW with a resolution of 5 nm from 350 nm to 1750 nm at 110 °C. The inset is a zoom-in spectrum around 400 nm.

In the following experiments, the peak power of the pump is increased to 40 kW (energy of 20 μ J) and the crystal temperature is set to 110 °C. Under these conditions, unexpected phenomena occur. First, a strong blue light is observed at the output of the sample. Second, as displayed in Fig. 3, the spectrum measured at this pump power from 350 nm to 1750 nm with a resolution of 5 nm shows unexpectedly another 5 peaks observed at: 393 nm, 402 nm, 820 nm, 1514 nm and 1574 nm. The signal at 787 nm and the idler at 1640 nm are present with a strong power and the other peaks are much smaller than the signal and idler. Note that these wavelengths are measured via zoom-in spectra with a resolution of 1 nm which are not presented in this paper.

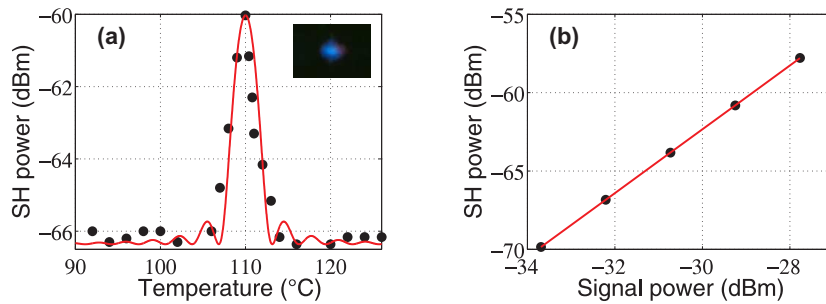


Fig. 4. (a) SH power vs sample temperature and an image of the blue light. (b) SH power vs signal power in Log scale (dBm).

Let us first study the peak generated at 393 nm. It is found that the wavelength of this peak is almost half of that of the signal. Therefore, it is suggested that the strong signal of 787 nm leads to SHG at 393 nm in a cascade process. In fact, the blue light observed in the work is due to the fluorescence of a paper screen by the ultraviolet light at 393 nm [the picture in Fig. 4(a)]. From the conservation equations [Eqs. (1), (2)] a SHG process is obtained when $m = 3$ and a grating period $\Lambda = 8.4 \mu\text{m}$ which is close to $8.52 \mu\text{m}$ of our sample period. This indicates that the third order QPM ($m = 3$) contributes to the SHG in this case.

The SH power tunability is also investigated as increasing the temperature as shown in Fig. 4(a). The obtained results are fitted by using a *sinc* function. Figure. 4(b) is the plot of the SH power versus the signal power and a linear fit in a Log scale with a slope of 2.04 which very close to 2 in theory. These results emphasise the SHG process.

The wavelength tuneability as a function of temperature is also studied. In Fig. 5, the blue solid line is obtained by dividing the simulated signal wavelengths by 2 as in a SHG process whilst the circle dots indicate the ones measured from spectra. The measurement manifests a good agreement with the SHG simulation and the line slope is negative as in Fig. 2(b). It is shown that the SHG follows the behaviour of the signal wave obtained from the OPG process. Again,

this statement confirms a cascaded SHG process to generate the peak at 393 nm.

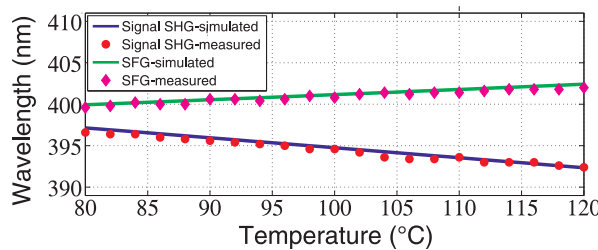


Fig. 5. Wavelength tuning as a function of the temperature for SHG and the SFG processes.

It is clearly seen from the inset of Fig. 3 that the SHG component at 393 nm is accompanied by another peak at 402 nm. It is suggested that this peak is generated by interacting the pump (532 nm) and idler (1640 nm). In this case, the two frequencies of the pump and idler are summed up in a SFG process to generate a wavelength of 402 nm. The QPM period is obtained as $\Lambda = 8.1 \mu\text{m}$ with $m = 2$. It is therefore expected that the second order QPM contributes to this SFG process. In Fig. 5, the green solid line indicates the SFG calculated from the pump and simulated idler, and the diamond dots represent the one measured in the experiment. In the figure, the peak at 402 nm follows the same temperature dependent behaviour as the idler one as the pump wavelength remains constant. This confirms the cascaded SFG process.

We will now investigate the three remained peaks: 820 nm, 1514 nm and 1574 nm. It is worth noting from Fig. 3 that at this high pump energy the signal/idler spectrum width (i.e. gain spectrum width) of the original OPG peaks widens with the increase of pump energy, indicating an increase of the parametric gain spectrum.

At first, it is suggested from Eq. (1) that the peak at 820 nm is generated from the idler (1640 nm) in a SHG process, the peak at 1514 nm from the signal (787 nm) and idler (1640 nm) in a DFG process and the peak at 1574 nm from the signal in a parametric frequency down-conversion process for wavelength doubling. However, from Eq. (2) the QPM period is obtained as around $\Lambda = 21 \mu\text{m}$ for these processes, which is much greater than the crystal period.

In another approach, it is found from Eqs. (1) and (2) that two other OPG processes can be responsible for these peaks. For instance, the sum of the frequencies of 820 nm and 1514 nm leads to that of the pump at 532 nm. For this process, the QPM is met with a period of $8.38 \mu\text{m}$, which is close to the crystal period. Therefore, it is assumed that another second OPG process is involved for these wavelengths with 820 nm for signal and 1514 nm for idler. It can be, also, suggested that the pump is involved in a third OPG process with 803 nm for signal and 1574 nm for idler. In this case, the QPM period is calculated to $8.4 \mu\text{m}$ which is very close to that of the sample. It is speculated that the peak at 803 nm is present in the spectrum, but drowned in the large signal linewidth in Fig. 3. The QPM is met in the given temperature range.

As summarized in table 1, the pair of 820 nm and 1514 nm forms the second OPG process whilst the pair of 803 nm and 1574 nm is the third OPG interaction. Note that the peak at 803 nm does not appear in Fig. 3 because of the large linewidth of the signal at 787 nm.

By using the conservation equations at 110 °C, it is demonstrated that these OPG processes are a QPM interactions with $m = 1$ ($\mathbf{K}_{1,0}$) and a grating period roughly similar to the value of $8.5 \mu\text{m}$ (see table 1). In fact, the QPM interactions have been investigated for the three OPG at different temperatures. The study reveals that the QPM is satisfied with a grating period of around $8.5 \mu\text{m}$ with a QPM order of 1 ($\mathbf{K}_{1,0}$) in the range of 80 °C – 120 °C. Note that all the nonlinear interactions previously reported fulfil the energy conservation law. However, only the three OPG processes satisfy the momentum conservation law. One possible reason for these processes with the different periods may be because of the non-uniform poling structure. It is also suggested

Table 1. QPM features of cascaded nonlinear interactions in 2D-PPLT where refractive index may change with the pump intensity, leading to effective change in the QPM periodicity and then giving rise to additional OPG processes 2 and 3.

| λ (nm) | interaction | QPM Λ (μm) | QPM order m |
|----------------|-------------|---------------------------------|---------------|
| 393 | SHG | 8.4 | 3 |
| 402 | SFG | 8.1 | 2 |
| 787, 1640 | OPG 1 | 8.51 | 1 |
| 820, 1514 | OPG 2 | 8.38 | 1 |
| 803, 1574 | OPG 3 | 8.42 | 1 |

that the unexpected two OPG-like processes may assist the SHG for 820 nm, the DFG for 1514 nm and the down-conversion for 1577 nm. Therefore, one can speculate that these non-linear interactions seem to arise simultaneously in a cascaded and even mixed processes which give the observed behaviour.

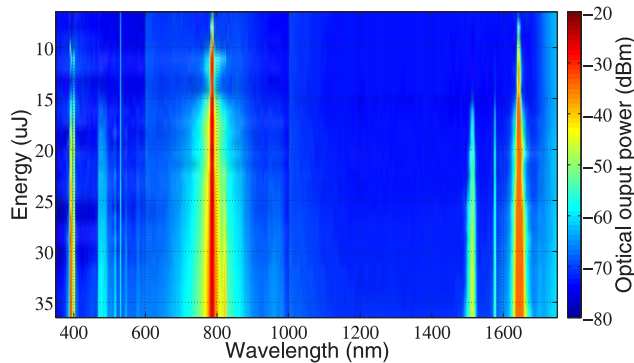


Fig. 6. Energy map from 7 μJ (49 MW/cm^2) to 37 μJ (261 MW/cm^2).

For further investigation, the pump power is varied from 7 μJ to 37 μJ at 110 °C and the spectra are measured with a step of 1 μJ as shown in Fig. 6. As seen in the figure, the SHG peak at 393 nm starts to appear clearly at 10 μJ (70 MW/cm^2). The so-called second and third OPG processes occur at 15 μJ (106 MW/cm^2).

For the first time, we have demonstrated the generation of multi-wavelength via different second order optical nonlinear process using 2D PPLT with a square lattice period of 8.52 μm . The nonlinear processes involved in the multiwavelength generation are optical parametric generation, second-harmonic generation and sum-frequency generation. The wavelengths are generated by satisfying the quasi-phase matching condition with reciprocal lattice vectors. A thorough investigation is under progress in order to completely map the nonlinear processes related to the pump parameters (angle, temperature). We are currently investigating the cause of refractive index change with the increase of pump power and the non-colinear reciprocal vectors, which results will be reported in a forthcoming publication.

Acknowledgement

This work has been supported by the PICS project from the CNRS and the BQR-2016 programme from the university.

High-resolution low-frequency fluctuation map of a multimode laser diode subject to filtered optical feedback via a fiber Bragg grating

FADWA BALADI,¹ MIN WON LEE,^{1,*} JEAN-RENÉ BURIE,² MAURO A. BETTIATI,²
AZZEDINE BOUDRIOUA,¹ AND ALEXIS P. A. FISCHER¹

¹Laboratoire de Physique des Lasers CNRS UMR 7538, Université Paris 13, Sorbonne Paris Cité, 93430 Villejuif, France

²3SP Technologies, Route de Villejust, 91625 Nozay, France

*Corresponding author: min.lee@univ-paris13.fr

Received 5 May 2016; revised 30 May 2016; accepted 30 May 2016; posted 31 May 2016 (Doc. ID 264457); published 21 June 2016

A highly detailed and extended map of low-frequency fluctuations is established for a high-power multi-mode 980 nm laser diode subject to filtered optical feedback from a fiber Bragg grating. The low-frequency fluctuations limits and substructures exhibit substantial differences with previous works. © 2016 Optical Society of America

OCIS codes: (140.3490) Lasers, distributed-feedback; (060.2420) Fibers, polarization-maintaining; (060.3735) Fiber Bragg gratings.

<http://dx.doi.org/10.1364/OL.41.002950>

Optical amplifiers such as erbium-doped fiber amplifiers (EDFA) play an important role in optical communications networks. In most cases, an EDFA is pumped by a pump module consisting of a high-power multimode laser diode (LD) emitting at 980 nm and wavelength-stabilized via a fiber Bragg grating (FBG). In fact, a pump module can be seen as an LD subject to external optical feedback from an FBG. Unlike conventional optical feedback (COF) obtained with a simple external mirror, the FBG with its pass-band profile provides, in fact, a filtered optical feedback (FOF). High-power, longitudinally multimode laser diodes can be achieved with long, low internal losses chips and anti-reflection coated facet [1,2]. However, the major drawback of such laser diodes is a high sensitivity to optical feedback from the external cavity which may result in detrimental dynamical behaviors [3]. Among the different behaviors, low-frequency fluctuations (LFF) are chaotic oscillations known as the intermittent chaos of saddle node instability, and are a typical characteristic of semiconductor lasers [4]. It has been reported that they appear close to the threshold [3]. Dynamical behaviors of LD subject to COF have been widely studied for decades [3–7]. The dynamical behaviors in pump modules have been theoretically investigated with different expressions of the FBG reflectivity [8–11]. However, LDs subject to FOF have recently been studied only in a few papers [12,13].

Some dynamical behavior maps have also been reported. However, the maps were established only in a COF configuration with a quite limited injection current range and a small number of data points [14,15]. Moreover, over the last two decades, the technology of semiconductor lasers fabrication has significantly been improved. Hence, there has been recently a renewed interest in the physics of optical feedback in semiconductor lasers [16], also for a better modeling of the multimode operation [17].

In this Letter, an LFF map using an LD subject to FOF emitting at 980 nm is built for the first time, to the best of our knowledge. The map is established as a function of laser drive current and optical feedback ratio using an LD with an FBG in a fully automated setup. In this Letter, the optical feedback ratio is defined as the ratio of the light injected into the LD over the emitted light in percentage. This Letter is undertaken by pushing the laser current up to seven times the laser threshold. This highly detailed map allows identifying the real parametric borders of the LFF region which are physically interesting and may incidentally be useful for applications.

The laser system used in this Letter is illustrated in Fig. 1(a). The LD consists of a 3.9 mm long Fabry–Perot cavity. The laser facet is anti-reflection coated, and its power is as high as 350 mW at a current of 500 mA and a temperature of 25°C. The threshold current of the solitary LD is measured as 74 mA with a slope efficiency of 0.8 mW/mA. The LD is characterized by a multimode emission and coupled to a 4 m long fiber, including an FBG. The reflectivity of the FBG is 30%, and the filter profile is centered at 974 nm with a full width at half-maximum of 0.6 nm (180 GHz). This configuration establishes a frequency-selective external cavity with a length of 4 m, leading to an FOF configuration. It is reported in [8–11] that such a configuration allows a wavelength-stabilized emission. The 3.9 mm long internal laser cavity induces an 11 GHz longitudinal mode-spaced emission which is much narrower than the linewidth of the FBG. Figure 1(b) shows an optical spectrum of the LD in an FOF configuration measured by an optical spectrum analyzer with a resolution of 0.03 nm at 250 mA and a feedback ratio of 1.5%.

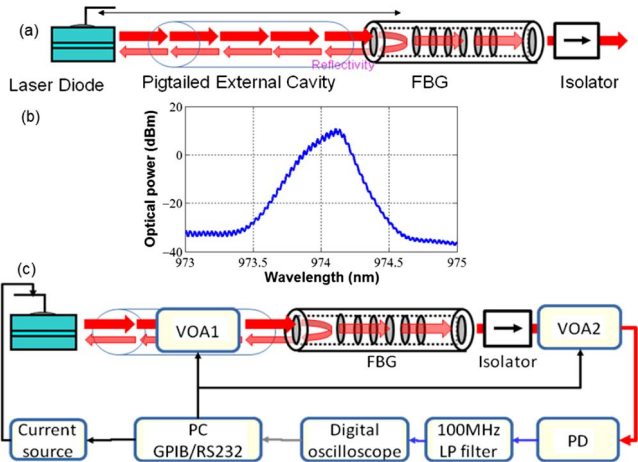


Fig. 1. (a) Schematic diagram of the laser system. (b) Laser spectrum at 250 mA. (c) Experimental setup. VOA, variable optical attenuator; PD, photodetector; FBG, fiber Bragg grating; LP filter, low-pass filter; PC, personal computer; GPIB, general purpose interface bus; RS232, serial communication.

The multimode behavior is clearly observed in this figure by a modulation on the spectrum. However, the emission is very stable, thanks to the FOF via the FBG.

The experimental setup is shown schematically in Fig. 1(c). To vary the feedback ratio, a variable optical attenuator (VOA) is inserted between the laser and the FBG. The external cavity length remains unchanged. Thus, the total feedback ratio is controlled by VOA 1. Its output is transmitted to a photodetector (PD) through an optical isolator and VOA 2. The PD signal is filtered at 100 MHz by a low-pass filter and recorded by a digital oscilloscope. The oscilloscope records time traces with 200,000 data points in a time window of 40 μ s. The whole system is fully automated with a computer via general purpose interface bus (GPIB) and serial ports. Taking into account the round-trip attenuation through VOA 1 and the 30% reflectivity of the FBG, the feedback ratio can be varied between 0.5% and 12.5%, as calibrated through the threshold current reduction.

Time traces recorded by the oscilloscope are presented in the left column of Fig. 2. They are obtained with the FBG relative feedback ratio of 3% and normalized to plot the corresponding histograms shown in the right column of Fig. 2. As the drive current is varied, three different types of distributions from the histograms can be distinguished: normal, right-skewed, and left-skewed distributions. At 83 mA in Fig. 2(a) and 124 mA in Fig. 2(b), the time series presents well-known LFF power dropouts which appear more frequently as the current increases. In fact, over the window of 40 μ s, three dropouts have been observed in the time trace of 83 mA, while 20 dropouts have been observed in that of 124 mA. Hence, the number of dropouts is significantly increased. Their corresponding histograms are skewed to the left, as shown in Figs. 2(a') and 2(b'). Eventually, Fig. 2(b') exhibits bimodal histogram because of the strong presence of dropouts. At 189 mA, in Fig. 2(c), the time series is characterized by a normal distribution [Fig. 2(c')], indicating the vanishing of power dropouts. However, the disappearance of dropouts is not necessarily related to decreasing the number of dropouts. It appears

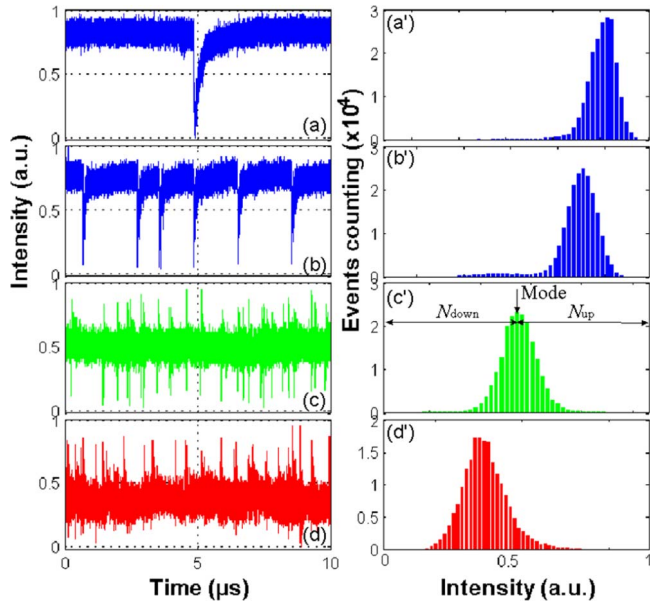


Fig. 2. Experimental time traces measured with a relative feedback ratio of 3.0% (left) and their corresponding histograms (right) at 83 mA (a), (a'), 124 mA (b), (b'), 189 mA (c), (c'), and 250 mA (d), (d').

that the amplitude of dropouts decreases and is overwhelmed by the fully developed chaos regime. At 250 mA in Fig. 2(d), the time series exhibits intensity pulses, leading to a right-skewed histogram in Fig. 2(d').

Now the distribution of the histograms is investigated. We define the left span length N_{down} and the right one N_{up} , as indicated in Fig. 2(c'). In normal distribution, the wing spans of N_{down} and N_{up} are near identical ($N_{\text{up}} \approx N_{\text{down}}$), and the mean value of the time trace corresponds to the mode. When LFF dropouts occur, as in Figs. 2(a) and 2(b), the left span N_{down} is greater than N_{up} , as shown in Figs. 2(a') and 2(b'). For intensity pulses which appear at higher currents, N_{up} is greater than N_{down} , as shown in Fig. 2(d'). This indicates power jump-ups which were first observed with strong optical feedback in [14]. With color encoding of the $N_{\text{up}} - N_{\text{down}}$ value, a dynamical behavior map is established from 11,275 time traces obtained with a current ranging from 50 to 500 mA with a 1 mA step current and feedback ratios scanned from 0.5% to 12.5% by a step of 0.5%. The current is, in fact, pushed to almost seven times the threshold current. Figure 3 shows the LFF map based on the histogram analysis from those measurements as functions of FBG reflectivity (feedback ratio) and laser current.

The color scale indicates the difference of the wing span length $N_{\text{up}} - N_{\text{down}}$. When LFF dropouts occur, the difference becomes negative ($N_{\text{down}} > N_{\text{up}}$) and encoded blue, while it becomes positive and encoded red for LFF jump-ups ($N_{\text{down}} < N_{\text{up}}$). The map shows four different behaviors: gray for currents below the threshold currents, blue for LFF dropouts, red for LFF jump-ups, and green for the absence of LFF.

It is suggested that several zones and limits in the map can be explained by two factors: the multimode operation of the laser and the presence of the FBG that filters out some longitudinal modes. It is shown from the map that the dropouts happen far

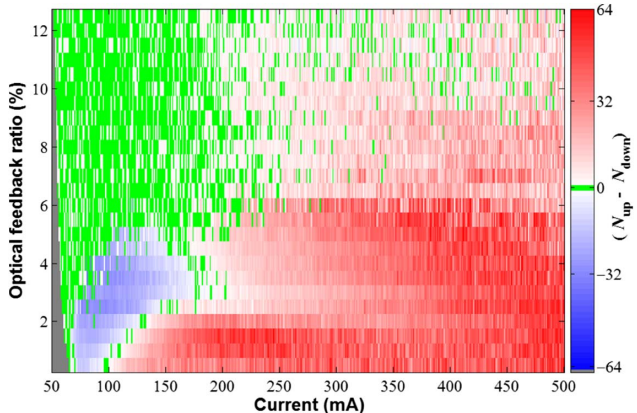


Fig. 3. LFF map as functions of FBG reflectivity (feedback ratio) and laser current.

from the threshold current (more than twice the threshold current in our case), as reported in [6,14].

Unlike the works in [14,15], the LFF exists for a larger current range and for lower values of the feedback ratio. Unexpectedly, it appears clearly that jump-ups are present on a wider area than that for dropouts. Particularly, the zone identified as Regime IV in [14] is, in our case, an LFF regime with jump-ups. As the feedback ratio is increased, the LFF dropout current zone increases as reported in [15]. However, it decreases after 3% and disappears beyond 6%. Jump-ups dominate the upper part of the map (high currents). It is clearly shown from the map that LFF appears not only near the threshold, but also at more than twice the solitary laser threshold current. The map is similar in shape to the one reported in [14]. According to the map in the reference, the green color on the top left side of the map is suggested regime V. However, the green zone between the blue and red is fully developed chaos with a normal distribution shown in Fig. 2(c'). We speculate that the difference between our map and the ones reported in the cited references should be attributed to the FOF configuration. It appears that the high power of our LD does not contribute to such a difference, as our slope efficiency is only 1.5 times greater than that reported in [14]. The same experiment has been undertaken with another LD of its kind. The results obtained are very similar to those reported in this Letter.

We now investigate the evolution of the histograms as a function of laser current. The power at each current is measured and added into the histograms obtained previously as offset. In this case, the histograms are not normalized, and they shift as the current increases. Figure 4 shows an L-I curve-like histogram image as a function of laser current at a feedback ratio of 1.5%. The histograms at each current are presented in 3D, and the number of data points is encoded in color scale. Populations greater than 500 data points are encoded dark red so that small details can be revealed. As seen in the figure, the threshold current is measured as 61 mA at 1.5%. Increasing the current, we find that both the amplitude and the dynamics increase. It is noticed from the figure that another dark red line appears just under the main curve. This line is clearly visible in the image zoomed near the threshold current (inset). The lower line in fact corresponds to the second mode of the histogram

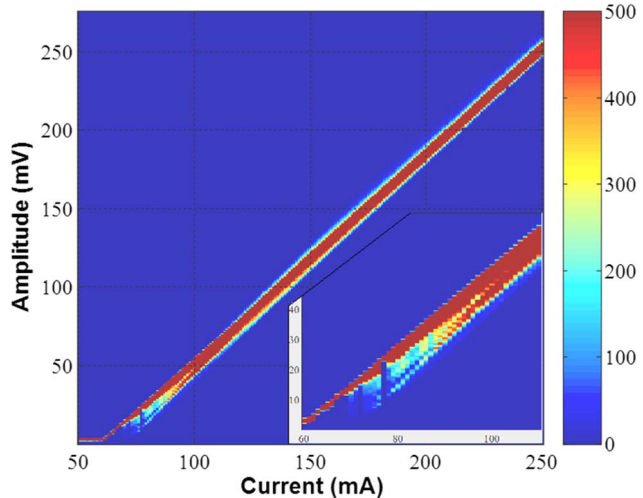


Fig. 4. L-I curve-like histogram map as a function of laser current at 1.5%. The dark red indicates high probability distribution, and the dark blue represents low probability distribution. The inset is a zoom from 60 to 110 mA and from 0 to 70 mV.

shown in Fig. 2(b') due to the strong presence of LFF dropout. Increasing the current further, the second mode merges into the main curve. On the other hand, decreasing the current, the line fades out. However, it can be estimated that the line would start at around 74 mA which is the threshold current of the solitary laser. This indicates that the dropout amplitude is defined by the solitary laser power level at a given current. This is a clear experimental demonstration of the work reported in [14] using the histogram analysis.

We have investigated the LFF of a high-power multimode LD subject to FOF via an FBG which is used as a pump module for EDFAs. For the first time, a highly detailed LFF map is established in an FOF configuration as a function of the current and the reflectivity from 11,275 time traces, thanks to a fully automated setup. The two types of LFF dynamics have clearly been identified in the map. The upper limit of existence of the LFF dropout is at 6%, and the LFF regime exists on a much wider range than previously thought. Moreover, the jump-up is the dominant LFF dynamics in our map. The LFF limits can be attributed to two factors: the multimode operation of the laser and the longitudinal filtering effect due to the FBG (FOF configuration).

Funding. OSEO-Vertical Project Funding.

REFERENCES

1. M. A. Bettati, C. Starck, F. Laruelle, V. Cargemel, P. Pagnod, P. Garabedian, D. Keller, G. Ughetto, J.-C. Bertreux, L. Raymond, G. Gelly, and R.-M. Capella, Proc. SPIE **6104**, 61040F (2006).
2. G. Yang, G. Smith, M. Davis, D. Loeber, M. Hu, C. Zah, and R. Bhat, IEEE Photon. Technol. Lett. **16**, 2403 (2004).
3. J. Ohtsubo, *Semiconductor Lasers*, Vol. **111** of Springer Series in Optical Sciences (Springer, 2008).
4. R. Tkach and A. Chraplyvy, J. Lightwave Technol. **4**, 1655 (1986).
5. G. Huyet, S. Balle, M. Giudici, C. Green, G. Giacomelli, and J. R. Tredicce, Opt. Commun. **149**, 341 (1998).

6. L. Mashal, R. M. Nguimdo, G. Van der Sande, M. C. Soriano, J. Danckaert, and G. Verschaffelt, IEEE J. Quantum Electron. **49**, 790 (2013).
7. M. Sciamanna and K. A. Shore, Nat. Photonics **9**, 151 (2015).
8. M. Achtenhagen, S. Mohrdiek, T. Pliska, N. Matuschek, C. Harder, and A. Hardy, IEEE Photon. Technol. Lett. **13**, 415 (2001).
9. A. Ferrari, G. Ghislotti, S. Balsamo, V. Spano, and F. Trezzi, J. Lightwave Technol. **20**, 515 (2002).
10. A. Naumenko, P. Besnard, N. Loiko, G. Ughetto, and J. C. Bertreux, IEEE J. Quantum Electron. **39**, 1216 (2003).
11. M. K. Davis and A. Echavarria, J. Lightwave Technol. **22**, 2816 (2004).
12. M. Yousefi and D. Lenstra, IEEE J. Quantum Electron **35**, 970 (1999).
13. A. P. A. Fischer, M. Yousefi, D. Lenstra, M. W. Carter, and G. Vemuri, Phys. Rev. Lett. **92**, 023901 (2004).
14. M.-W. Pan, B.-P. Shi, and G. R. Gray, Opt. Lett. **22**, 166 (1997).
15. T. Heil, I. Fischer, and W. Elsäßer, Phys. Rev. A **58**, R2672 (1998).
16. S. Donati and R. H. Horng, IEEE J. Sel. Top. Quantum Electron. **19**, 1500309 (2013).
17. D. Lenstra and M. Yousefi, Opt. Express **22**, 8143 (2014).

Demonstration of optical rogue waves using a laser diode emitting at 980 nm and a fiber Bragg grating

MIN WON LEE,^{1,*} FADWA BALADI,¹ JEAN-RENÉ BURIE,² MAURO A. BETTIATI,² AZZEDINE BOUDRIOUA,¹ AND ALEXIS P. A. FISCHER¹

¹Laboratoire de Physique de Lasers CNRS UMR 7538, Université Paris 13, Sorbonne Paris Cité, 93430 Villejuif, France

²3SP Technologies, Route de Villejust, 91625 Nozay, France

*Corresponding author: min.lee@univ-paris13.fr

Received 27 June 2016; revised 31 August 2016; accepted 31 August 2016; posted 1 September 2016 (Doc. ID 269192); published 21 September 2016

Rogue waves are observed for the first time, to the best of our knowledge, in a 980 nm laser diode subject to filtered optical feedback via a fiber Bragg grating. By counting the number of rogue waves in a fixed time window, a rogue wave map is established experimentally as a function of both the optical feedback ratio and the laser current. The comparison with low frequency fluctuations (LFFs) reveals that the rogue waves observed in our system are, in fact, LFF jump-ups. © 2016 Optical Society of America

OCIS codes: (140.5960) Semiconductor lasers; (060.3735) Fiber Bragg gratings; (190.3100) Instabilities and chaos.

<http://dx.doi.org/10.1364/OL.41.004476>

The rogue wave phenomena have been observed for centuries. In ocean science, they are defined as waves greater than their mean values plus four to eight times the standard deviations [1]. Such huge waves are categorized as extreme events. These extreme events are rare and result from nonlinear systems. These events have attracted attention over the decade to study the rogue waves in ocean science [1], extreme climates [2], financial crisis [3], etc.

Rogue waves have also been observed in nonlinear optical systems [4]. The first experimental observation was reported in the process of supercontinuum generation [5], followed by a numerical work to control the occurrence of such waves [6]. A Peregrine soliton is also considered as a rogue wave [7]. Optical rogue waves have also been studied in a Kerr-lens mode-locked Ti-sapphire laser [8]. These experiments have been undertaken using a pulsed laser as a seed. However, optical rogue waves have been observed during the process of supercontinuum generation using a continuous-emission pump [9]. In these works, the mechanism of the formation of optical rogue waves has been studied using the nonlinear Schrödinger equation. A theory work on controlling the appearance of rogue waves in injected laser diodes was also reported in Ref. [10].

Another approach to the formation of optical rogue waves or extreme pulses exploits the deterministic nonlinearities. This is the case of laser diodes. Recently, optical rogue waves have been observed using laser diodes such as a VCSEL with optical injection [11,12], a laser diode subject to optical phase-conjugate feedback [13], and a laser diode subject to optical feedback with a very short cavity [14].

In fact, laser diodes can be rendered chaotic when subject to optical feedback. This is quite well known and has been studied for decades [15–19]. According to the optical feedback ratio, laser diodes show different dynamical behaviors. Low-frequency fluctuation (LFF) is one of the behaviors in the coherence collapse regime with intensity dropouts and jump-ups [20]. Although dropout behavior has intensively been investigated, jump-up behavior has been the subject of only a few studies.

We report for the first time, to the best of our knowledge, the observation of rogue waves in a high-power laser diode emitting at 980 nm subject to a filtered optical feedback via a fiber Bragg grating (FBG). The main application of these systems deals with erbium-doped fiber amplifiers that are widely used in optical communications networks, where they are used as pump modules. The objective of this Letter is to determine the parameter range where such nonlinear phenomena appear. In this Letter, we will establish a rogue wave map as a function of two parameters: the laser drive current and the optical feedback ratio. We will also show how LFF behavior is related to the appearance of the rogue waves.

The experimental setup is shown schematically in Fig. 1, using fiber optical components. The laser diode (LD) emits at 974 nm, and its temperature and laser current are stabilized by a current source. It is a pigtailed multimode laser diode in a butterfly package, of which the spectrum can be referred to [21]. The laser power can reach 350 mW at a current of 500 mA and a temperature of 25°C. The threshold current of the solitary laser diode is 74 mA. The LD emission is coupled to a variable optical attenuator (VOA) and an FBG. The FBG provides two effects: reflections from the Bragg grating and the filtering. The reflected emission from the FBG is fed back to

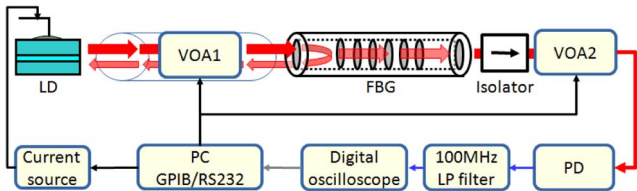


Fig. 1. Experimental setup. VOA, variable optical attenuator; PD, photodetector; FBG, fiber Bragg grating; LP filter, low-pass filter; PC, personal computer; GPIB, general purpose interface bus; RS232, serial communications.

the LD through VOA 1, forming an external cavity of 4.2 m. The reflectivity of the FBG is 30% at 974 nm with a linewidth of 0.6 nm, and the total attenuation is controlled by the automated VOA 1. Taking into account the round-trip attenuation of VOA 1 and the 30% reflectivity of FBG, the feedback ratio ranges from 0% to 12.5%. Its output is transmitted to a 5 GHz photodetector (PD) through an optical isolator and VOA 2. VOA 2 is used to ensure a constant power level to protect the PD. To investigate LFF and the rogue waves, electrical signals beyond 100 MHz bandwidth are filtered out using a low-pass filter. The PD signals are recorded by a digital real-time oscilloscope with a bandwidth of 2.5 GHz as time traces with 200,000 data points in a time window of 40 μ s.

The whole setup is fully automated by a personal computer (PC) with a general purpose interface bus (GPIB) and serial communications (RS232). The current and the optical feedback ratio can be scanned automatically from 50 to 500 mA and from 0% to 12.5%.

Figure 2 shows the rogue waves obtained from our laser system for different currents and feedback ratios. In this Letter, the

definition of the rogue wave is the wave mean value plus eight times the standard deviation as the rogue wave defined in ocean science. The red lines in the figures represent the limits of the rogue waves (the rogue wave threshold) based on this definition. With these criteria, a single intensity pulse for a 5.5% feedback ratio and a 240 mA current over 40 μ s exceeds the threshold in Fig. 2(a). It is clearly seen from the figure that a very high and short pulse arises suddenly from a noise-like signal. Hence, this pulse can be qualified as a rogue wave. It has been verified that the dynamical behavior of the rest of the time series is chaotic. At 223 mA and 2.0%, the rogue waves appear more frequently [Fig. 2(c)]. At 0.5% and 167 mA, the rogue waves occur even more frequently [Fig. 2(e)]. Thus, these cannot be considered as rare events. With the rogue wave threshold, the number of rogue waves is counted to 1 in Fig. 2(a). In Fig. 2(c), the number can be clearly counted to seven, and the number increases to 24 in Fig. 2(e).

In the right column of Fig. 2, the histograms are presented for (b) 5.5% and 240 mA, (d) 2.0% and 223 mA, and (f) 0.5% and 167 mA. The histograms are built from the corresponding time traces. Among 200,000 data points in a time trace, downward peaks are removed, and only the data points in upward peaks are used for building the histograms. As seen in the figures, the histograms are L-shaped, which is a typical characteristic of rogue waves [5]. In our case, the rogue waves occur rarely, compared to the number of data points. As the number of events is very high near the mean value of the time traces, the probability beyond the rogue wave threshold is very low. It is clearly shown in the figures that the number of events beyond the rogue wave threshold increases from the top figure to the bottom figure.

A zoom-in of the rogue wave in Fig. 2(a) is shown in Fig. 3. From the figure, the rogue wave pulse width is measured as

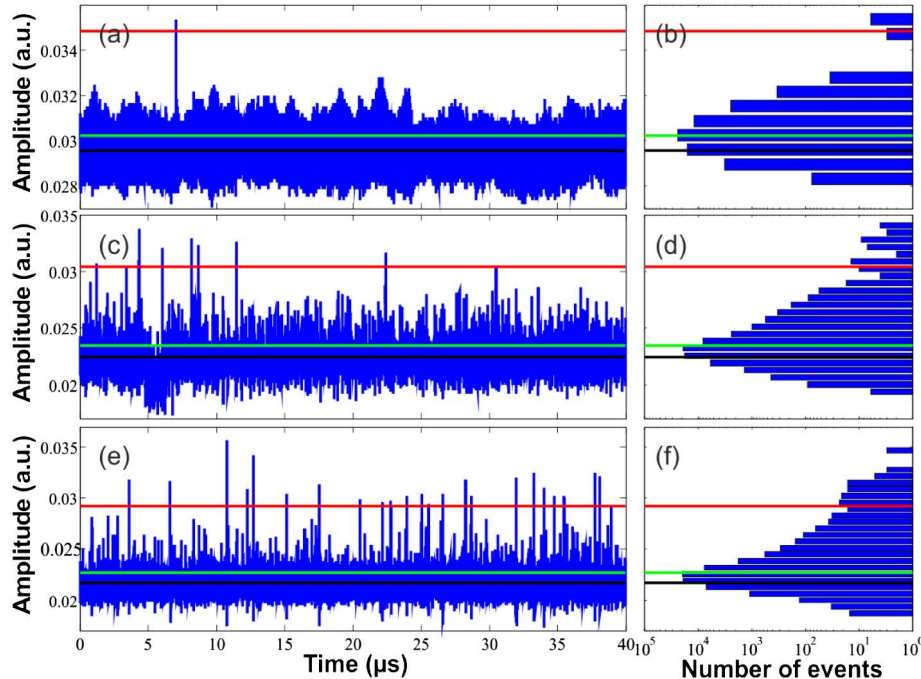


Fig. 2. Time traces at (a) 5.5% and 240 mA, (c) 2.0% and 223 mA, and (e) 0.5% and 167 mA, and the corresponding histograms (b), (d), and (f). The y-axis of the histograms is presented in log scale. The red, black, and green lines represent the rogue wave threshold, the mean value, and the standard deviation, respectively.

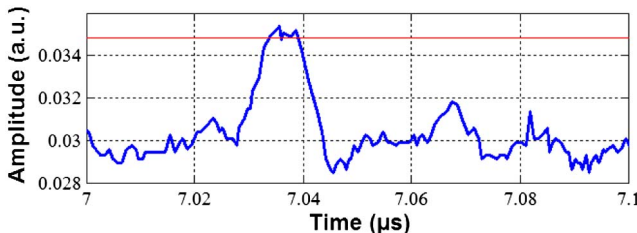


Fig. 3. Zoom-in of the rogue wave generated at 5.5% and 240 mA. The rogue wave threshold is indicated with a red line.

10 ns. This is a very short event compared to the 40 μs time window. It has been verified that the other rogue waves in this Letter have a similar pulse width. However, compared to the results reported in [11–13], it is noticed that our pulse width is one order of magnitude larger than the ones reported in the references. It is speculated that it may be attributed to the multimode high-power laser diode and the FBG for feedback. However, a further study may be needed to fully understand.

To study in more detail, the number of rogue waves is counted for each 40 μs time trace, as shown in Fig. 2, as functions of both the feedback ratio and the laser current. These numbers are used for establishing the map shown in Fig. 4. To establish the map, the laser current is swept from 50 to 500 mA which is seven times the threshold current of the solitary laser, and the feedback ratio is varied from 0.5% to 12.5% by 0.5%. Our fully automated setup allows the measurement of 11,275 time traces for such parameter range. The number of rogue waves is coded, as shown in the color code scale from blue to red for 0–30. Figure 4 exhibits two zones of appearance of the rogue waves. The first zone (from 0.5% to 2% and $100 \text{ mA} < I < 400 \text{ mA}$) exhibits a strong appearance of rogue waves, compared to the second one (from 4% to 6% above 150 mA). In this Letter, up to 27 rogue waves have been observed in a single time trace. However, it is clearly seen that the rogue waves disappear as the laser current is further increased. Apart from these zones, the rogue waves do not

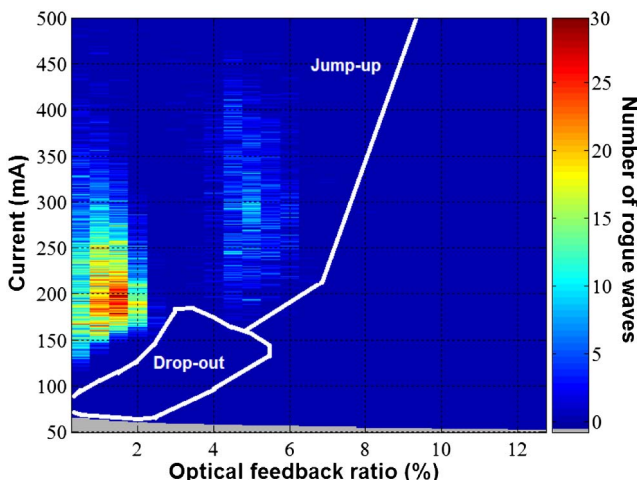


Fig. 4. Map of rogue waves as functions of the FBG reflectivity (optical feedback ratio) and the laser current. The dropout and jump-up zones are indicated.

appear in the system. A further study is needed to investigate the reason for the existence of two separate zones.

As mentioned above, our laser system is a chaotic system. Therefore, it also exhibits LFF such as dropout and jump-up. Our previous work showed the dropout and jump-up zones in a chaotic behavior map [21]. From this work, the zones of these behaviors are indicated in Fig. 4. It is clearly seen from the figure that rogue waves are part of jump-ups which can occur rarely with intense pulses. It can be assumed that the jump-ups reported in [20] may be rogue waves. At high currents, the rogue waves occur so frequently that the mean value and the standard deviation shift up. Thus, by the oceanographic definition, the rogue waves disappear as further increasing the laser current. It is shown from the figure that the rogue waves exist up to 6% of the feedback ratio which is also approximately the limit of the existence of the LFF dropouts.

For the first time, to the best of our knowledge, we have observed rogue waves in a high-power laser diode emitting at 980 nm subject to filtered optical feedback via an FBG. A map has been established experimentally as a function of the two parameters (the feedback ratio and the current). According to the map, the rogue waves exist in very specific and limited ranges of parameters. Moreover, the results show that the rogue waves observed in this Letter are part of LFF jump-up.

Funding. OSEO Vertical Project.

Acknowledgment. The authors would like to thank Prof. Cristina Masoller for helpful discussions.

REFERENCES

1. C. Kharif, E. Pelinovsky, and A. Slunyaev, *Rogue Waves in the Ocean* (Springer, 2009).
2. R. W. Katz, Clim. Change **100**, 71 (2010).
3. H. E. Roman, R. A. Siliprandi, C. Dose, and M. Porto, Phys. Rev. E **80**, 036114 (2009).
4. N. Akhmediev, B. Kibler, F. Baronio, M. Belić, W.-P. Zhong, Y. Zhang, W. Chang, J. M. Soto-Crespo, P. Vouzas, P. Grelu, C. Lecaplain, K. Hammami, S. Rica, A. Picozzi, M. Tiidi, K. Panajotov, A. Mussot, A. Bendahmane, P. Sriftgiser, G. Genty, J. Dudley, A. Kudlinski, A. Demircan, U. Morgner, S. Amiraranashvili, C. Bree, G. Steinmeyer, C. Masoller, N. G. R. Broderick, A. F. J. Runge, M. Erkintalo, S. Residori, U. Bortolozzo, F. T. Arecchi, S. Wabnitz, C. G. Tiofack, S. Coulibaly, and M. Taki, J. Opt. **18**, 063001 (2016).
5. D. R. Solli, C. Ropers, P. Koonath, and B. Jalali, Nature **450**, 1054 (2007).
6. J. M. Dudley, G. Genty, and B. J. Eggleton, Opt. Express **16**, 3644 (2008).
7. B. Kibler, J. Fatome, C. Finot, G. Millot, F. Dias, G. Genty, N. Akhmediev, and J. M. Dudley, Nat. Phys. **6**, 790 (2010).
8. M. G. Kovalsky, A. A. Hnilo, and J. R. Tredicce, Opt. Lett. **36**, 4449 (2011).
9. A. Mussot, A. Kudlinski, M. Kolobov, E. Louvergneaux, M. Douay, and M. Taki, Opt. Express **17**, 17010 (2009).
10. J. Ahuja, D. Bhiku Nalawade, J. Zamora-Munt, R. Vilaseca, and C. Masoller, Opt. Express **22**, 28377 (2014).
11. C. Bonatto, M. Feyereisen, S. Barland, M. Giudici, C. Masoller, J. R. Rios Leite, and J. R. Tredicce, Phys. Rev. Lett. **107**, 053901 (2011).
12. K. Schires, A. Hurtado, I. D. Henning, and M. J. Adams, Electron. Lett. **48**, 872 (2012).
13. A. K. Dal Bosco, D. Wolfersberger, and M. Sciamanna, Opt. Lett. **38**, 703 (2013).

14. J. A. Reinoso, J. Zamora-Munt, and C. Masoller, Phys. Rev. E **87**, 062913 (2013).
15. R. Tkach and A. Chraplyvy, J. Lightwave Technol. **4**, 1655 (1986).
16. M. K. Davis and A. Echavarria, J. Lightwave Technol. **22**, 2816 (2004).
17. A. P. A. Fischer, M. Yousefi, D. Lenstra, W. G. Carter, and G. Vemuri, Phys. Rev. Lett. **92**, 023901 (2004).
18. J. Ohtsubo, *Semiconductor Lasers*, vol. **111**, Springer Series in Optical Sciences (Springer, 2008).
19. M. Sciamanna and K. A. Shore, Nat. Photonics **9**, 151 (2015).
20. M.-W. Pan, B.-P. Shi, and G. R. Gray, Opt. Lett. **22**, 166 (1997).
21. F. Baladi, M. W. Lee, J.-R. Burie, M. A. Bettati, A. P. A. Fischer, and A. Boudrioua, Opt. Lett. **41**, 2950 (2016).



Electrical modelling and design of ultra-fast micro-OLED with coplanar wave-guided electrodes in ON-OFF regime



A.C. Chime^{a,d}, S. Bensmida^c, M. Chakaroun^a, M.W. Lee^a, H. Nkwawo^a, A.P.A. Fischer^{a,b,*}

^a Université Paris 13, Sorbonne Paris Cité, Laboratoire de Physique des Lasers, UMR CNRS 7538, 93430 Villetaneuse, France

^b Centrale de Proximité en Nanotechnologies de Paris Nord, Université Sorbonne Paris Cité, 93430 Villetaneuse, France

^c Communication Systems and Networks Group, Merchant Venturers School of Engineering, University of Bristol, MVB Bld, Woodland Rd, Bristol, BS8 1UB, UK

^d Institut Universitaire de Technologie FOTSO Victor, Université de Dschang, Cameroun

ARTICLE INFO

Keywords:

OLED

Ultra-fast OLED

OLED electrical equivalent model

Hightspeed OLED

Feeder line electrodes

Coplanar waveguide electrodes

ABSTRACT

This work proposes a new electrical model and design of ultra-fast μ-OLED devices under ON-OFF electrical pulse regime. The new model is an equivalent electrical model capable of accounting for large amplitude excitation as well as ultra-short pulse response. Moreover, coplanar wave-guided electrodes are proposed, for the first time, to maximize pulse energy delivery to the organic hetero-structure and to minimize the μ-OLED time response. An analytical expression of the time response is derived from the model which reveals the design key parameters. Moreover, preliminary experimental results presented in this work demonstrate state-of-the-art OLED current density of 2 kA/cm^2 and better than state-of-the-art optical pulse duration as short as 10 ns in the range of the radiative lifetime of singlet excitons.

1. Introduction

Organic Light Emitting Diodes (OLEDs) are mainly and largely exploited in display and lighting applications. However, in the field of organic opto-electronics, the demonstration of the organic laser diode remains one of the most important challenge. The main obstacles to achieve lasing with organic semiconductors under electrical pumping are; the low mobility in organic semiconductors, heating, several loss mechanisms due to injected charges, exciton formation, and high laser-threshold level [1,2].

High current density is one of the requirements to reach the laser threshold excitation level [3,4]. Such high excitation levels require extremely high charges densities. This leads to additional absorption losses that are the result of undesired annihilation processes (in particular singlet-polaron and singlet-triplet quenching) [1,5–7]. As triplets do not contribute to the lasing process and have long excited state lifetime, they quickly accumulate in the gain medium and become detrimental to the laser effect. This phenomenon can be avoided in the presence of very short pulsed excitation. This can be achieved by choosing a pulse duration that is short enough so that the triplet population does not become significant before the end of the pulse and by adjusting the repetition rate (or the duty cycle) such that there is sufficient time for triplet relaxation between successive pulses [7]. In other words, the pulse duration should be less than the lifetime of the singlet

states (The radiative lifetime of singlet excitons being in the range from 0.2 to 20 ns) [8], while the repetition period should be greater than the relaxation time of the triplet states. Additionally, a small active area device should lead to low sample capacitance, and hence, fast response time [9]. Short pulse duration should therefore result in avoiding exciton annihilation and, hence, could lead to better external quantum efficiency (EQE) [3,10–12]. Moreover, under these conditions of high density of excitation, better heat management may lead to higher current densities [1,9,13].

Recently, significant research efforts reported OLED responses under pulsed electrical excitation regime [1,9,14,15]. To the best of authors knowledge, the shortest pulse durations were reported in Refs. [1,15] with 50 ns pulse. Shorter pulses require a large bandwidth impedance matching circuit so that the energy of the electrical pulse is effectively transmitted to the component. This last aspect was omitted in previously reported work.

In this paper, a new OLED equivalent electrical model is proposed and developed for ON-OFF operation regime in the presence of high amplitude pulse excitation. Authors introduced an OLED electrical model that identifies key design parameters [15]. This paper builds on this previous work and proposes an OLED electrical model that is further fine-tuned to reproduce the device electrical response to faster and shorter pulses than those reported in Ref. [15]. The model takes into account the physical characteristics and topology of the OLED.

* Corresponding author. Université Paris 13, Sorbonne Paris Cité, Laboratoire de Physique des Lasers, UMR CNRS 7538, 93430 Villetaneuse, France.

E-mail address: Fischer@iutv.univ-paris13.fr (A.P.A. Fischer).

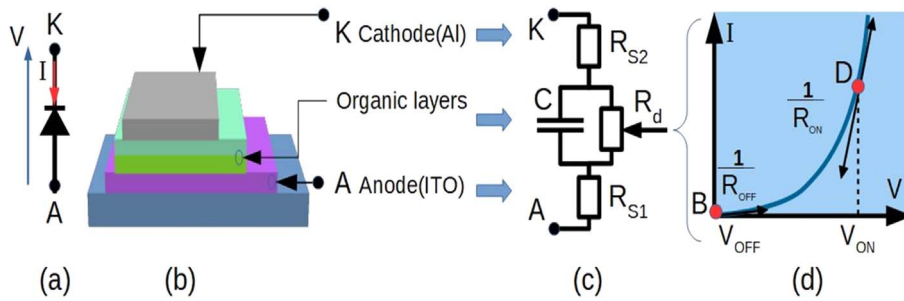


Fig. 1. Equivalent electrical model of different part of OLED device.

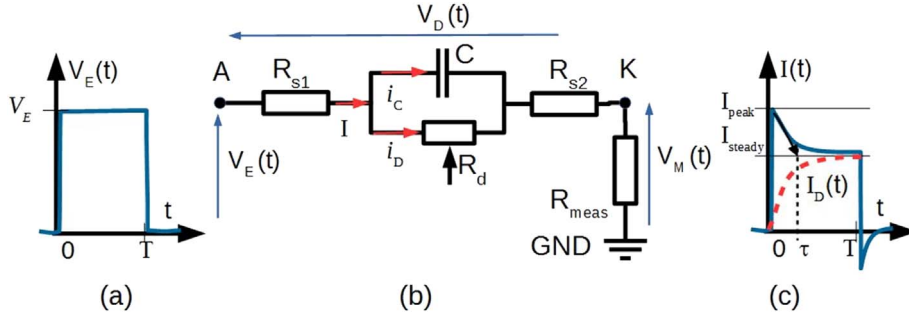


Fig. 2. Electrical circuit for pulsed excitation of OLED.

A new and original ultra-fast OLED design with a topology that is optimized from the equivalent electric model key parameters is then presented as well as a coplanar waveguide electrodes complying with radio-frequency circuits and systems design rules. To demonstrate the effectiveness of the proposed design approach, this paper presents preliminary experimental measurements of the new OLED design, in the presence of an ultra-short pulse, in terms of electrical and optical responses.

2. Equivalent electrical model

The most commonly used simple equivalent electrical model for an OLED are not optimized for ON-OFF operation scheme with high amplitude of excitation [16,17]. The proposed equivalent electrical model, shown in Fig. 1c, is established from the OLED geometry/topology, shown on Fig. 1b, and its I-V characteristic, shown in Fig. 1d. Fig. 1b depicts a typical OLED geometry with a stacked structure of thin organic layers sandwiched between an indium tin oxide (ITO) anode, and a metallic (Al) cathode. From an electrical point of view, this structure is equivalent to a combination of several resistors and a capacitor. The resistors represent ohmic losses due to; firstly, the ITO sheet resistance (contact resistance R_{S1}), secondly, the low conductivity of each of the organic layers (bulk resistance R_b), and thirdly, the cathode resistance (contact resistance R_{S2}). The capacitive behavior results from the fact that the OLED is basically made of almost dielectric materials, i.e. the organic layers sandwiched between metallic plates (the electrodes). Additionally, the energy barriers between adjacent organic layers induce a junction capacitance. For the sake of simplicity, all the capacitors are included in a single equivalent capacitor C . The proposed equivalent electrical model elements are shown on Fig. 1c.

Typical I-V OLED curve is shown Fig. 1d. In ON-OFF regime the operation points are B and D corresponding respectively to an excitation voltage $V_{OFF} = 0$ V (OFF-state) and to an excitation voltage $V_{ON} \gg 0$ (ON state). The respective slopes of the I-V curve in B and D are:

$$\frac{1}{R_{OFF}} = \frac{dI}{dV_{atV=V_{OFF}=0}} \quad \text{and} \quad \frac{1}{R_{ON}} = \frac{dI}{dV_{atV=V_{ON}}} \quad (1)$$

R_{ON} being the effective resistance in the equivalent circuit while

high excitation voltage is applied during the ON state. The higher the amplitude of excitation, the lower is R_{ON} resistance. During the OFF state a similar reasoning applies except that the effective resistance R_{OFF} is high enough to be considered as an open circuit. This is clearly shown by the slope of the I-V curve which is close to zero. In ON-OFF operation regime a dynamic resistor R_d is used that is either equal to R_{ON} or to R_{OFF} depending on which state the OLED is switched to. In order to take the ON-OFF switching into account in the equivalent electrical circuit, we introduced the dynamical resistance R_d which is the sum of the inverse of the slope of the I-V curve, and of the bulk resistor R_b such that $R_d = R_{ON} + R_b$ in ON state and $R_d = R_{OFF} + R_b$ in the OFF state.

In order to measure the current I flowing through the OLED, a measurement resistor (R_{meas}) is connected in series with the device as shown on Fig. 2b.

From the electrical excitation circuit shown in Fig. 2b, the relationship between the OLED current I and the excitation voltage V_E reads:

$$\begin{aligned} \frac{dI(t)}{dt} + \left(1 + \frac{R_d}{R_{S1} + R_{S2} + R_{meas}} \right) \frac{1}{R_d C} I(t) \\ = \frac{1}{R_{S1} + R_{S2} + R_{meas}} \left[\frac{dV_E(t)}{dt} + \frac{1}{R_d C} V_E(t) \right] \end{aligned} \quad (2)$$

The current I flowing through R_{meas} is the sum of i_D and i_C which are respectively the currents flowing through the diode and the junction capacitor C . The part of the current flowing through the dynamic resistor R_d and not through the capacitance is then:

$$i_D(t) = \frac{V_E(t) - (R_{S1} + R_{S2} + R_{meas})I(t)}{R_d} \quad (3)$$

The ON-OFF operation regime is modeled with an analytical expression of the excitation voltage $V_E(t)$ defined as a gate function with a constant amplitude V_E , between 0 to T and with zero amplitude outside as shown Fig. 2a.

The current waveform $I(t)$ flowing through the OLED, shown in Fig. 2c is then obtained by solving eq. (2) with $V_E(t)$ being replaced by its on-state value V_E and its derivative by zero. For the sake of simplification we introduced the total serial resistance $R_{ST} = R_{S1} + R_{S2} + R_{meas}$

and consider only the rising flank of the solution (step function) of the differential equation eq. (2).

$$I(t) = \frac{1}{R_d + R_{ST}} \left[1 + \frac{R_d}{R_{ST}} \exp\left(-\frac{R_d + R_{ST}}{R_{ST} R_d C} t\right) \right] V_E \quad (4)$$

Using eqs. (3) and (4), the effective current I_D flowing through R_d reads:

$$I_D(t) = \frac{1}{R_d + R_{ST}} \left[1 - \exp\left(-\frac{R_d + R_{ST}}{R_{ST} R_d C} t\right) \right] V_E \quad (5)$$

$I(t)$ starts with an initial turn-on peak current value I_{peak} given by eq. (6) calculated in the particular case $t = 0$.

$$I_{peak} = \frac{V_E}{R_{S1} + R_{S2} + R_{meas}} = \frac{V_E}{R_{ST}} \quad (6)$$

The current peak is followed by a decay toward a steady state value of $I(t)$ reached for t larger than the decay time or for $t = +\infty$ given by eq. (7);

$$I_{steady} = I(t = +\infty) = \frac{V_E}{R_d + R_{ST}} = \frac{(R_{S1} + R_{S2} + R_{meas})}{R_d + (R_{S1} + R_{S2} + R_{meas})} I_{peak} \quad (7)$$

A more physical understanding of eq. (6) is revealed if at the onset of the pulse it is assumed that C is a short circuit and R_d is infinite. Then, the equivalent electric circuit is reduced to the serial resistances $R_{ST} = R_{S1} + R_{S2} + R_{meas}$ and the current flowing through them when a voltage V_E is applied at their terminals is indeed given by Ohm's law and eq. (6).

Similar but different physical understanding holds for the expression of the steady-state current given by eq. (7); when C is fully loaded, its current stops, and C can be replaced by an open circuit in the equivalent circuit which reduces to the serial resistances $R_d + R_{ST}$. Consequently, the steady-state current is simply given by Ohm's law with voltage V_E applied to the terminals of $R_d + R_{ST}$.

Equations (6) and (7) indicate that reductions in the values of the serial resistors R_{S1} and R_{S2} as well as the dynamic resistor R_d help to maximize the μ -OLED steady-state current which is the value towards which converges $I_D(t)$ the essential and unique contributing current to the light emission by the OLED (See Fig. 2c).

The time constant τ (Eq. (6)) of the exponential decay is derived from the exponential term in eqs. (4) and (5) and reads as a function of the electrical model elements R_{S1} , R_{S2} , R_{meas} , R_d and C :

$$\tau = \frac{C}{R_d} + \frac{1}{R_{S1} + R_{S2} + R_{meas}} \quad (8)$$

The electrical time response of the device, ie. the time needed for $I(t)$ to decay from 90% to 10% of its peak value to its steady state value, (or for $I_D(t)$ to grow from 10% up to 90% of the steady state value) is simply $T_r = 2.2 \tau$. From Eq. (8), it is clear that a first route to reduce the OLED time response is to minimize the capacitance C for example by reducing the active area surface S . Another route to reduce the value of T_r is to reduce the values of resistors R_d , R_{S1} , R_{S2} , and R_{meas} . It is worth noting that to achieve T_r minimization, both R_d and ($R_{ST} = R_{S1} + R_{S2} + R_{meas}$) must be minimized. Otherwise, $\tau \sim R_d C$ if $R_d \ll (R_{S1} + R_{S2} + R_{meas})$, or $\tau \sim (R_{S1} + R_{S2} + R_{meas}) C$ if $R_d \gg (R_{S1} + R_{S2} + R_{meas})$.

Fig. 3 presents the OLED electrical time constant τ and the normalized current density as a function of the dynamic resistance R_d for four different scenarios; In the first realistic scenario the measurement resistor $R_{meas} = 50\Omega$ and the serial resistors R_{S1} and R_{S2} are large resulting a total value $R_{ST1} = R_{S1} + R_{S2} + R_{meas} = 106\Omega$ while the capacitance $C_1 = 13\text{ pF}$. The choice of these model parameters values is based on previous measurements reported in Ref. [15]. In the second more optimistic scenario, all the serial resistors R_{S1} and R_{S2} have been minimized via metallization of the ITO and the measurement resistor is set to $R_{meas} = 10\Omega$ resulting in $R_{ST2} = 16\Omega$. The capacitance remains

$C_1 = 13\text{ pF}$. The third and fourth scenarios correspond respectively to $R_{ST1} = 106\Omega$ and $C_2 = 1.3\text{ pF}$ and $R_{ST2} = 16\Omega$ with $C_2 = 1.3\text{ pF}$ which are very optimistic scenarios with a tenfold reduction of the μ -OLED capacitance.

In Fig. 3a the electrical time constant function saturates to $\tau_1 = 1.36\text{ ns}$ in the first scenario case ($R_{ST1} = 106\Omega$ -red line with circles) whereas it saturates to $\tau_2 = 206\text{ ps}$ in the second case with $R_s = 16\Omega$ (black lines with squares). In the third and fourth scenarios the electrical time constant saturates respectively to $\tau_3 = 142\text{ ps}$ and $\tau_4 = 22\text{ ps}$. In any case, decreasing R_d below R_{ST} will reduce further the time constant. With these small values of the electrical time constants, this numerical analysis provide preliminary indications on the possibility to design optoelectronic organic devices one or more order of magnitude faster than what has been reported so far in the literature. Moreover, these low values of the electrical time constants being available for a large range of the dynamic resistance R_d . This indicates that high excitation level (low R_d values) is not compulsory to achieve high-speed behavior in organic optoelectronic devices.

In Fig. 3b the current density is evaluated as a function of R_d . The maximum current density achievable with low R_d values is limited by the serial resistance ($R_{ST} = R_{S1} + R_{S2} + R_{meas}$) to 10 kA/cm^2 in the first scenario and to $\sim 50\text{ kA/cm}^2$ in the second one. Note that with $R_{ST1} = 106\Omega$ and $R_d = 300\Omega$, which constitute realistic conditions, the maximum current is to be limited by $I_D/S = 2.1\text{ kA/cm}^2$. To minimized R_d , the operating point D (Fig. 1) is to be moved up along the I-V curve by increasing V_{ON} , whereas to minimized ($R_{ST} = R_{S1} + R_{S2} + R_{meas}$) the device is to be modified physically; R_{S1} can be minimized via the metallization of the part of the ITO that is not the active area, R_{S2} can be minimized with a thicker aluminum deposition and with shorter electrical track. Finally R_{meas} can simply be set to the minimum resistance value that still allows a noise limited measurement of the $V_M(t)$ voltage taking into account the sensitivity of the measurement equipment. Note however that the turn-on peak current I_{peak} increases with the value of the total resistance R_{ST} and actually will tend to infinity if R_{ST} is to be zero. In practice this means a destruction of the OLED. Also, note that the steady current I_{steady} tends to the peak current I_{peak} when $R_d \ll (R_{S1} + R_{S2} + R_{meas})$ as illustrated from Fig. 4b. This is likely going to result to; firstly to a maximization of the expected steady state current and secondly to a beneficial mitigation of the transient effects.

The analysis of the analytical expressions can therefore be summarized into three design guidelines; 1) reducing the OLED active area, 2) minimizing the serial resistance and 3) operating with amplitude pulses high enough to obtain a dynamical resistance R_d smaller than the total of the serial resistances R_{ST} and to access operation regime with smaller difference between I_{steady} and I_{peak} .

2.1. Numerical results

The differential equation (Eq. (2)) is solved numerically using Runge-Kutta 2nd and 3rd order method using different excitation functions, different values of the capacitance C . The current $I_D(t)$ flowing through the active part of the μ -OLED is then deduced. Results are shown Fig. 4 in the case of gate excitation function (upper figures in Fig. 4) and sigmoid excitation function (lower figures in Fig. 4) with a 10 ns duration.

In the case of a gate excitation function (Fig. 4a and b), the beginning and the end of the pulse response exhibit overshoots indicating the charge and the discharge of the C capacitance. As expected, the overshoots become less pronounced in duration when the capacitance C decreases from $C_1 = 13\text{ pF}$ to $C_2 = 1.3\text{ pF}$, which corresponds to the decrease of the electrical time constant τ_e (Eq. (5)). In the case of a sigmoid excitation function (Fig. 4c and d) the overshoot is not visible for the smaller value of the time constant ($R_d = 300\Omega$, $C = 1.3\text{ pF}$). We would like to emphasize that the absence of overshoot is not an evidence of slow response. Note that whatever the excitation function is, the I_D current does reach its maximum (stationary state) before the end

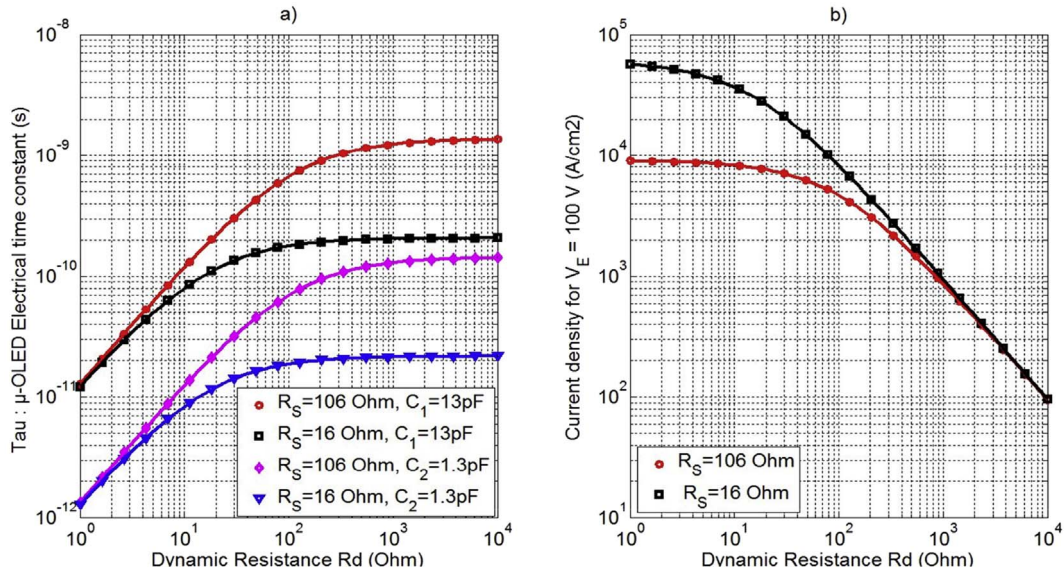


Fig. 3. (a) μ -OLED Electrical time Constant and (b) Current density $J_D = I_D/S$ ($S = 87 \times 120 \mu\text{m}^2$) for a 100 V excitation as a function of the dynamical resistance R_d for $R_{ST1} = 106\Omega$ and $R_{ST2} = 16\Omega$ with $C_1 = 13 \text{ pF}$ and $C_2 = 1.3 \text{ pF}$.

of the pulse duration. A first conclusion is that the excitation function has a large impact on the discharge and therefore the estimation of the μ -OLED time constant from the measurement of the capacitance discharge is to be considered cautiously. Moreover, the current I_D reaches its steady value faster with the gate excitation function than with the sigmoid. For this reason, it is important to preserve the integrity of the excitation signal. This can be done among other things by minimizing the parasitic reflection resulting from impedance mismatch. Here we propose to improve the impedance matching between μ -OLED electrodes and wires coming from a pulse generator with feeder line electrodes.

2.2. OLED circuit design

Operating OLEDs in ON/OFF mode means driving them with pulses. In the presence of ultra-short pulses, the driving signal contains high frequency components and issues such as impedance matching must be taken into account. Indeed, when voltage impulse of few nanoseconds is applied to an OLED, part of its energy is reflected (not absorbed by/delivered to the OLED) if there is any impedance mismatch between the feeding line and the device or anywhere in the driving circuit. The amount of reflected energy is quantified by the reflection coefficient that is defined by:

$$\Gamma = \frac{Z_D - Z_C}{Z_D + Z_C} \quad (9)$$

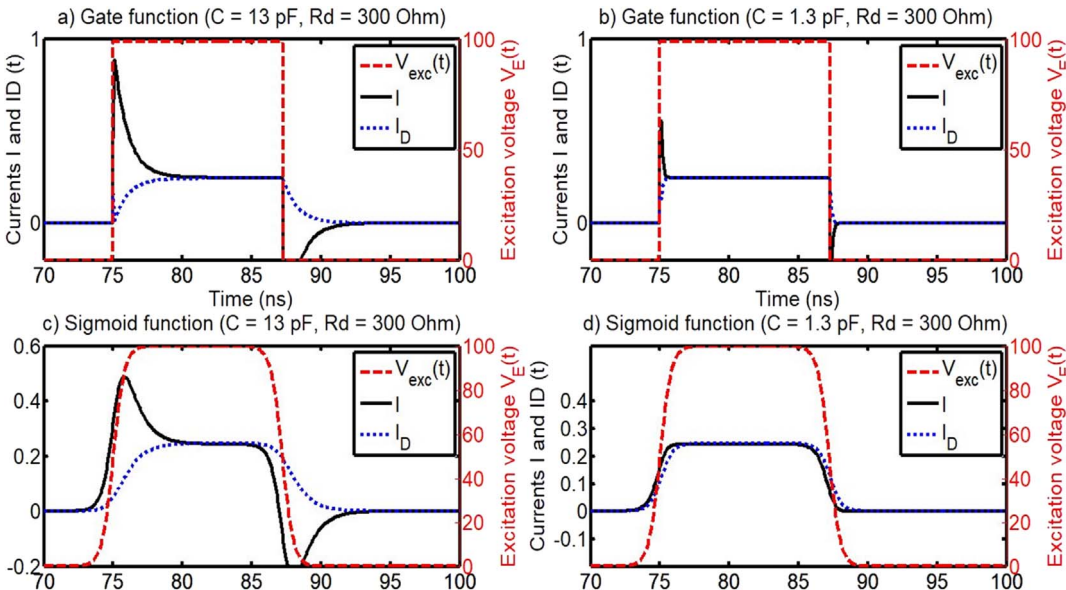


Fig. 4. Simulations showing the electrical response of a μ -OLED to a ~ 10 ns pulse excitation based on the differential equation (2) and on equation (3). The different simulations were run with $R_d = 300 \Omega$, with different capacitance values ($C = C_1 = 13 \text{ pF}$ left column and $C = C_2 = 1.3 \text{ pF}$ right column), and with different shapes of the electrical excitation signal (upper figures with gate functions, lower figures with sigmoid functions). Continuous black traces correspond to the total current I while dotted blue lines correspond to the part I_D of the current flowing through the organic hetero-structure and that produces the emission of light. In a) and b) the excitation (red stripped line) is a gate function, whereas in c) and d) the excitation function is a sigmoid. In a) and c) the time constant is $\tau_1 = 1 \text{ ns}$ ($C_1 = 13 \text{ pF}$). In b) and d) the time constant are $\tau_2 = 100 \text{ ps}$ ($C_2 = 1.3 \text{ pF}$). (For interpretation of the references to colour in this figure legend, the reader is referred to the Web version of this article.)

where Z_D is the equivalent impedance of the device and Z_C is the characteristic impedance of the line. Reflection has also the effect of distorting pulse waveforms which makes it difficult to even estimate the response time of the device has mentioned previously. To avoid as much as possible undesired effects, we applied two modifications on the ITO electrode; we propose for the first time in the OLED technology to integrate both part of the driving circuit and the matched feeding lines onto the ITO thin film coating the glass substrate [18]. More specifically, OLED electrode dimensions and shape will be modified to become coplanar waveguide feeding lines.

Coplanar waveguide (CPW) has been chosen to design the new pattern of OLED electrodes because it requires only one side of the substrate covered with conductive material contrary to micro-strip configuration. It is thus easily and quickly adaptable to current OLED substrates. The dimensions of the feeding lines are calculated to obtain a characteristic impedance Z_c equal to 50Ω at the $F_b = 1\text{ GHz}$ base frequency (knowing that 98% of the pulse spectrum energy lie in frequency range from 0 to $5F_b$).

CPW line was described for the first time by C. WEN [19], but it is applied to design ultra-fast organic optoelectronic devices for the first time. It consists of a strip of thin conductive strip on the surface of a dielectric with two ground planes running adjacent and parallel to the strip as shown on Fig. 5.

Fig. 5 illustrates the CPW structure where H and ϵ_r are respectively the thickness and the relative dielectric permittivity of the dielectric material which is a glass substrate used in this work. W and T are the width and thickness of the central strip respectively whereas G is the width of the gap on either sides between the central strip and the ground planes. With a $W = 1000\mu\text{m}$ width ITO central anode separate by a gap $G = 243\mu\text{m}$ from the ITO ground planes on a $H = 700\mu\text{m}$ thick glass substrate with relative permittivity $\epsilon_r = 7.75$ a $Z_c = 50\Omega$ characteristic impedance is obtained.

CPW is compatible with the integration of electrical elements of the driving circuit onto the substrate as close as possible to the OLED so as to reduce the effect of parasitic reflections and preserve the shape of the fast electrical excitation pulses.

In the current work, integrating the electrical driving circuit reduces to the addition of a built-in measurement resistance R_{meas} . To integrate the latter onto the substrate, two thin stripes connecting the cathode to both ground planes with $R_{\text{stripe}} = 2 \times R_{\text{meas}}$ are added as illustrated in Fig. 5. The width L of these stripes is simply calculated from the law of resistance with its length imposed by the gap G , with the section defined partially by the ITO thickness $T = 120\text{ nm}$, and with the ITO resistivity ρ_{ITO} :

$$L = \rho_{\text{ITO}} \frac{G}{2R_{\text{meas}} T} \quad (10)$$

Practical dimensions for $R_{\text{MEAS}} = 50\Omega$ are $G = 243\mu\text{m}$ and $L = 182\mu\text{m}$.

2.3. Experimental results and validation of the model

After fabrication, the samples are characterized electrically first under DC operation. The serial resistances exhibits $R_{S1} = 45\Omega$, $R_{S2} = 10\Omega$, $R_{\text{meas}} = 51\Omega$. The active area has been measured to $S = 87 \times 120\mu\text{m}^2$, and the surface capacitance value of 124nF/cm^2 at 0.5 Ghz estimated from a previous work with similar organic heterostructure has been used. The total serial resistance and the estimated capacitance $C_1 = 13\text{ pF}$ corresponds to scenario 1.

The Organic heterostructure is made with 30 nm of m-MTDA as hole injection layer (HIL), 10 nm-thick NPD as hole transport layer (HTL), 30 nm of Alq3 doped with DCM as a light emitting layer, 5 nm of BCP as hole blocking layer (HBL), and 25 nm of Alq3 as electron transporting layer respectively ended with a LiF (1 nm)/Al (120 nm) cathode layer.

In order to record the opto-electrical behavior of the device, each OLED is placed on a response time measurement system consisting of a probe station (Cascade opto-PM5), a high pulse generator (AVTECH AVL-2A-B), and a digital oscilloscope (Tektronix TDS 7254). A 100 V amplitude excitation pulse with 10 ns duration is delivered from the generator and applied to the device, while measurements are recorded with the digital oscilloscope. Current density response is measured across the built-in measurement resistance R_{meas} using a GSG probe. Simultaneously, light output is collected from the bottom of the substrate into a $\text{NA} = 0.5$ numerical aperture optical fibre connected to an avalanche photodiode with 400 MHz bandwidth (Thorlabs APD3040A2). All measurements are performed in an ambient atmosphere at room temperature.

Fig. 6 presents both experimental results and simulations for the sake of comparison and validation of the model. More specifically, Fig. 6a presents the excitation voltage $V_E(t)$ (blue striped line), the electrical response $V_M(t)$ (green line with dots) measured across the measurement resistance R_{meas} , and a simulation (red continuous line) performed with the measured excitation signal $V_E(t)$ (blue striped line).

The measured excitation voltage $V_E(t)$ exhibits smooth flanks similar than those of the sigmoid functions in Fig. 4c and d. Because of this and following the conclusions of the numerical analysis the electrical time constant can not be measured directly from the measured time trace, but rather from the parameters used for the fitting between the measurement and equation (2).

For these reasons and for the sake of comparison, the measured electrical response and electrical response simulated from equation (2) with $R_{S1} = 106\Omega$, $R_d = 312\Omega$ (extracted by fitting), and $C_5 = 1.4\text{ pF}$ (13.8nF/cm^2) are both plotted on the same figure. The electrical response $V_M(t)$ exhibits a pulse duration (FWHM) of 9.0 ns similar to that of the excitation which is a strong indication that the μ -OLED with CPW electrodes respond much faster than the pulse duration. Note that the parameters used for the fitting are very close to those involved in the third scenario since R_{S1} is the same, $R_d = 312\Omega$ differs by 4% only and $C_5 = 1.4\text{ pF}$ differs by 7% from C_2 . Clearly, the good qualitative fitting between the measurement and the simulation based on reasonable values of the electrical model validates the modelling in ON-OFF regime and demonstrates its relevancy. Based on this conclusion it appears safe to used the model to estimate the electrical time constant. From the electrical parameters values $R_{S1} = 106\Omega$, $R_d = 312\Omega$, and $C_5 = 1.4\text{ pF}$, equation (6) provides an electrical response time of $\tau_e = 110\text{ ps}$.

This the first of the two strong indications that 50Ω impedance characteristic CPW electrodes are very beneficial to very-high speed μ -

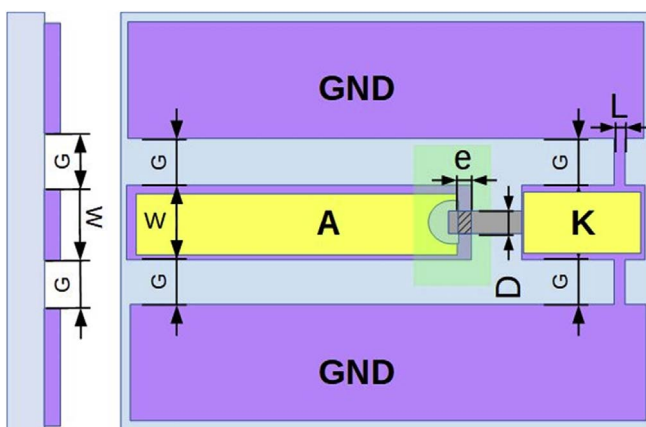
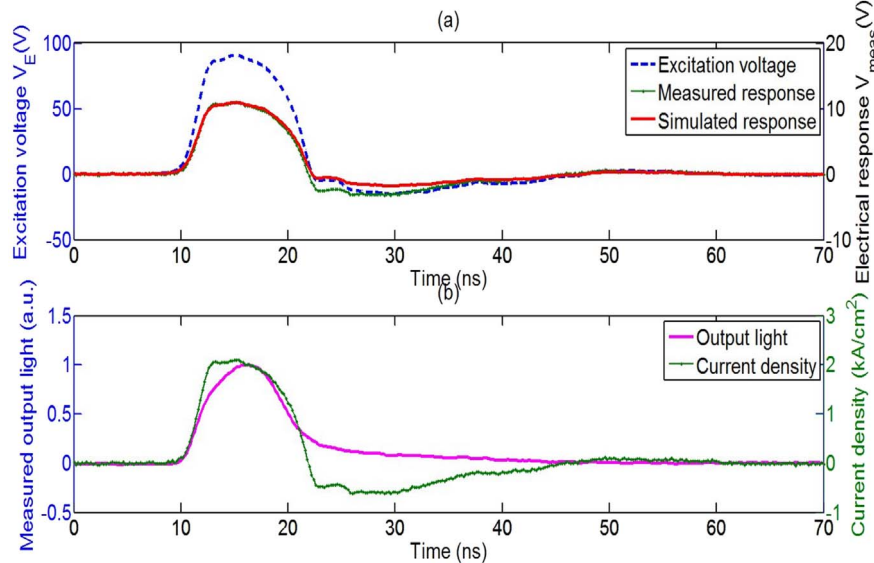


Fig. 5. Structure of a μ -OLED on ITO with coplanar waveguide electrodes as feeder line an integrated measurement resistances. (GND:Ground plane), (A: Anode K: Cathode) (ITO: Purple, Gold: Yellow, Aluminum: Grey, light blue: glass substrate). (For interpretation of the references to colour in this figure legend, the reader is referred to the Web version of this article.)



OLED.

Indeed, the electrical response to a pulse excitation of the μ -OLED with CPW electrodes $\tau_e = 110$ ps is two orders of magnitude lower than previously reported work with the same active area but without CPW electrodes ($\tau \ll 9.6$ ns \pm 3.3 ns) [15]. Such an almost adiabatic response explains why the electrical response exhibits the same pulse duration than the excitation.

A second indication of the benefit of the CPW electrodes is to compare the value of the capacitance and the surface capacitance of μ -OLED with and without CPW electrodes. The surface capacitance calculated from the ratio C_5 to S with $S = e \times D = 87 \times 120 \mu\text{m}^2$ is $C_5/S = 13.8 \text{nF/cm}^2$. It is tenfold smaller than that reported in the previous study [15], but in better agreement with other values reported in the literature in the range 20–40 nF/cm² and in the MHz range [19]. The active area S being similar in the current experiment and in the experiment reported in Ref. [15], the main difference between both types of μ -OLED being the CPW feeding line electrodes, it confirms their role in the tenfold parasitic capacitance reduction. The capacity difference can be explained by the impedance mismatch along the electrical line with different characteristic impedance of the wires, cables, distant measurement resistance and device resulting in a total parasitic capacitance ten fold larger (124 nF/cm²) when CPW is absent.

Fig. 6b presents the light output (continuous magenta trace) and the current density $J_D(t) = I_{D(t)}/S$ (green thin line with dots) calculated from eq. (3) using the measured voltage response $V_M(t)$ and the measured excitation voltage $V_E(t)$. The current density waveform exhibits a rising flank sharper than the falling flank although the pulse duration remains equal to the excitation pulse duration at 9.0 ns.

The peak value of the current density reaches 2.04 kA/cm² which is less than 3% different from the maximum current density value 2.1 kA/cm² calculated from equation (5) with $R_d = 312 \Omega$ and very similar to what is plotted in Fig. 3b. This is an indication of the relevancy and the robustness of the model. The rise time of the $I_D(t)$ current from 10% to 90% of its maximum value is 2.1 ns indicating that the device can be submitted to pulses shorter than 10 ns with a still perceptible light response. Note again that the reason why the μ -OLED electrical rise time is different from $\sim \approx 2.2\tau_e = 242$ ps is because the excitation signal is not a gate-like function.

Additionally, the current I_D flowing through the organic heterostructure is effectively converted into photons as proved by the output light emission (magenta trace in Fig. 6b). With 8.2 ns and 3.6 ns in duration and rise time respectively, the optical pulse exhibits smaller duration and slower rise time than that of the electrical pulse. A

Fig. 6. Time domain waveforms of electrical and optical response of the μ -OLED device for 9 ns pulse duration and an excitation amplitude of $V_E = 100$ V. a) Excitation $V_E(t)$ (blue stripped line), measured electrical response $V_M(t)$ (green line with dots) and simulated electrical response (red thick line) showing a good fit between the measurement and the simulation. b) Measured current density $J_D(t)$ (green thin line with dots) and the optical response (thick magenta line)). (For interpretation of the references to colour in this figure legend, the reader is referred to the Web version of this article.)

qualitative analysis of the light output shows that the optical trace increases exponentially up to the half of the duration of the current density pulse and decreases exponentially after it, confirming that the measured optical response is slower than the electrical response. Further investigation with a faster photodiode is required to check whether or not the measurement is not limited by the photodiode response time.

3. Conclusion and perspectives

The current study proposes a model for high speed μ -OLED in ON-OFF pulse excitation regime that is successfully validated with measurements. The coplanar waveguide electrodes made of ITO on glass substrates compatible with $S = 87 \times 120 \mu\text{m}^2$ μ -OLED and with 50Ω integrated measurement resistance lead to tenfold smaller capacitance values, and two orders of magnitude faster electrical response down to $\tau = 110$ ps. The combination of preliminary measurements and simulation demonstrated the interest of the proposed design for the reduction of the μ -OLED electrical time response under ultra short pulse excitation scheme. This work shows successful generation of perceptible light response under better than state-of-the-art ultra short electrical pulse duration of 9 ns, 2.1 ns rise-time. It demonstrates not only pulse duration in the range of the radiative lifetime of singlet excitons, but also that the OLED device can sustain state of the art current density up to 2 kA/cm² without heat breakdown.

As perspectives, the metallization of the electrodes can lead to a further decreases of the serial resistance and therefore to a further decrease of the electrical time response down to 20 ps and to current density up to 3 kA/cm² in the case of an excitation amplitude of 100 V. The next step will be to quantify precisely the true light intensity emitted by the OLED to investigate the optical excitation density as steps forwards towards the resolution of the electric excitation issue of the organic diode laser.

References

- [1] D. Kasemann, R. Brückner, H. Fröb, K. Leo, Organic light-emitting diodes under high currents explored by transient electroluminescence on the nanosecond scale, *Phys. Rev. B* 84 (11) (Sep. 2011).
- [2] I.D.W. Samuel, G.A. Turnbull, Organic semiconductor lasers, *Chem. Rev.* 107 (4) (Apr. 2007) 1272–1295.
- [3] H. Yamamoto, T. Oyamada, H. Sasabe, C. Adachi, Amplified spontaneous emission under optical pumping from an organic semiconductor laser structure equipped with transparent carrier injection electrodes, *Appl. Phys. Lett.* 84 (8) (Feb. 2004) 1401–1403.
- [4] H. Nakatani, N. Matsumoto, H. Uchiuzou, M. Nishiyama, M. Yahiro, C. Adachi, Very low amplified spontaneous emission threshold and electroluminescence

- characteristics of 1,1'-diphenyl substituted fluorene derivatives, *Opt. Mater.* 30 (4) (Dec. 2007) 630–636.
- [5] H. Nakanotani, H. Sasabe, C. Adachi, Singlet-singlet and singlet-heat annihilations in fluorescence-based organic light-emitting diodes under steady-state high current density, *Appl. Phys. Lett.* 86 (21) (May 2005) 213506.
- [6] M.A. Baldo, R.J. Holmes, S.R. Forrest, Prospects for electrically pumped organic lasers, *Phys. Rev. B* 66 (3) (Jul. 2002).
- [7] C. Gartner, C. Karnutsch, C. Pflumm, U. Lemmer, Numerical device simulation of double-heterostructure organic laser diodes including current-induced absorption processes, *IEEE J. Quant. Electron.* 43 (11) (Nov. 2007) 1006–1017.
- [8] A.J.C. Kuehne, M.C. Gather, Organic lasers: recent developments on materials, device geometries, and fabrication techniques, *Chem. Rev.* 116 (21) (Nov. 2016) 12823–12864.
- [9] H. Nakanotani, T. Oyamada, Y. Kawamura, H. Sasabe, C. Adachi, Injection and transport of high current density over 1000 A/cm^2 in organic light emitting diodes under pulse excitation, *Jpn. J. Appl. Phys.* 44 (6R) (2005) 3659.
- [10] S. Schols, L. Van Willigenburg, S. Steudel, J. Genoe, P. Heremans, Pulsed excitation of OLEDs with a remote metallic cathode, *IEEE J. Quant. Electron.* 46 (1) (Jan. 2010) 62–67.
- [11] N.C. Giebink, S.R. Forrest, Temporal response of optically pumped organic semiconductor lasers and its implication for reaching threshold under electrical excitation, *Phys. Rev. B* 79 (7) (Feb. 2009).
- [12] Zhang, M. Whited, M.E. Thompson, S.R. Forrest, Singlet-triplet quenching in high intensity fluorescent organic light emitting diodes, *Chem. Phys. Lett.* 495 (4–6) (Aug. 2010) 161–165.
- [13] B. Wei, M. Ichikawa, K. Furukawa, T. Koyama, Y. Taniguchi, High peak luminance of molecularly dye-doped organic light-emitting diodes under intense voltage pulses, *J. Appl. Phys.* 98 (4) (Aug. 2005) 44506.
- [14] V.G. Kozlov, et al., Structures for organic diode lasers and optical properties of organic semiconductors under intense optical and electrical excitations, *IEEE J. Quant. Electron.* 36 (1) (2000) 18–26.
- [15] L. Zeng, et al., Electrical and optical impulse response of high-speed micro-OLEDs under ultrashort pulse excitation, *IEEE Trans. Electron. Dev.* 64 (7) (Jul. 2017) 2942–2948.
- [16] S.H. Kim, et al., Impedance spectroscopy of single- and double-layer polymer light-emitting diode, *J. Appl. Phys.* 87 (2) (Jan. 2000) 882–888.
- [17] Joon-ho Ahn, Dong-Hoe Chung, Joon-Ung Lee, Equivalent-circuit analysis of organic light-emitting diodes by using the frequency-dependent response of an ITO/Alq₃/Al device, *J. Kor. Phys. Soc.* 46 (2) (Feb. 2005) 546–550.
- [18] W. Hilberg, From approximations to exact relations for characteristic impedances, *IEEE Trans. Microw. Theory Tech.* 17 (5) (1969) 259–265.
- [19] C.P. Wen, Coplanar waveguide: a surface strip transmission line suitable for non-reciprocal gyromagnetic device applications, *IEEE Trans. Microw. Theory Tech.* 17 (12) (1969) 1087–1090.

GLOSSAIRE

- ASE** Emission spontanée amplifiée
(Amplified spontaneous emission) : 36, 39
- BEDS** Brillouin echoes distributed sensing : II, 23, 40–45
- BFS** Décalage de fréquence Brillouin
(Brillouin frequency shift) : 36, 40, 42, 43, 45, 73, 74
- BGS** Spectre de gain Brillouin
(Brillouin gain spectrum) : 40–42, 73
- BOCDA** Brillouin optical correlation-domain analysis : 40, 72
- BOTDA** Brillouin optical time-domain analysis : II, 23, 40, 41, 44, 45
- BPM** Accord de phase par biréfringence
(Birefringence phase matching) : 53
- COF** Feedback optique conventionnel
(Conventional optical feedback) : 66, 67, 72–74
- CPNL** Cristal photonique non linéaire : 8, 52–58
- DFB** Distributed feedback : 33, 41
- DFG** Génération de différence-fréquence
(Difference-frequency generation) : 35, 52–54, 60, 64
- DPSK** Differential phase-shift keying : II, 23, 44, 45
- EDFA** Amplificateur à fibre dopée erbium
(Erbium-doped fibre amplifier) : 41, 66
- FBG** Réseau de Bragg fibré
(Fibre Bragg grating) : II, 51, 66, 67, 69, 72
- FOF** Feedback optique filtré
(Filtered optical feedback) : 66, 67, 70, 72
- FOPA** Amplification paramétrique optique fibrée
(Fibre optical parametric amplification) : 36–39
- FWM** Mélange à quatre ondes
(Four-wave mixing) : 35, 36
- HHG** Génération de demi-harmonique
(Half-harmonic generation) : 60, 64
- HNA** Grande ouverture numérique
(High numerical aperture) : 45
- OLD** Diode laser organique
(Organic laser diode) : 74, 75
- OLED** Diode électroluminescente organique
(Organic light-emitting diode) : 74, 75
- OPG** Génération paramétrique optique
(Optical parametric generation) : II, 1, 35, 51–54, 57–62, 64, 65, 83
- OSA** Analyseur de spectre optique
(Optical spectrum analyser) : 38, 58

PCF Fibre à cristal photonique

(Photonic crystal fibre) : II, 23, 37, 38, 42, 43, 45, 46

PPLN Niobate de Lithium périodiquement polarisé

(Periodically-polarised Lithium niobate) : II, 51, 53–55, 57, 60

PPLT Tantalat de Lithium périodiquement polarisé

(Periodically-polarised Lithium tantalate) : II, 51, 53, 54, 57–63, 65, 83

QPM Quasi-accord de phase

(quasi-phase matching) : 53, 55, 57–63, 65

RLV Vecteur de réseau réciproque

(Reciprocal lattice vector) : 53, 55, 56, 58, 59

SBS Rétrodiffusion Brillouin stimulée

(Stimulated Brillouin scattering) : II, 35, 36, 40–43, 51, 72–74

SBSOF Feedback optique par une rétrodiffusion Brillouin stimulée

(Stimulated Brillouin scattering-based optical feedback) : 72–74

SFG Génération de somme-fréquence

(Sum-frequency generation) : 35, 52–54, 60–65

SHG Génération de second-harmonique

(Second-harmonic generation) : II, 1, 35, 51–58, 60–65

SMF Fibre monomode

(Single-mode fibre) : 35–37, 40, 45

SPM Auto-modulation de phase

(Self-phase modulation) : 36

SRS Rétrodiffusion Raman stimulée

(stimulated Raman scattering) : 35, 36

THG Génération de troisième-harmonique

(Third-harmonic generation) : 63, 64

VCSEL Vertical-cavity surface-emmiting laser : I, 23, 31, 32, 70

XPM Modulation de phase croisée

(Cross-phase modulation) : 36

YDFA Amplificateur à fibre dopée ytterbium

(Ytterbium-doped fibre amplifier) : 38

ZDW Longueur d'onde à dispersion nulle

(zero-dispersion wavelength) : 36–38, 45

RÉSUMÉ

Les domaines de l'optique non linéaire et de la dynamique non linéaire trouvent plusieurs applications dans des domaines divers et variés, notamment les télécommunications optiques et les lasers. Dans ce contexte, je me suis intéressé à étudier l'interaction et la dynamique optique non linéaire. Dans un premier temps, je présenterai l'étude de la dynamique des diodes lasers soumises à un retour optique par un réseau de Bragg fibré ou par une rétrodiffusion Brillouin stimulée.

Par la suite, je présenterai particulièrement l'étude de la génération paramétrique optique dans les cristaux photoniques non linéaires qui permettent la génération multi-longueurs d'ondes allant de l'UVA au proche infrarouge à partir d'une seule pompe. Ces travaux soulignent l'importance des effets non linéaires pour développer et réaliser de nouvelles sources multi-longueurs d'ondes et abordables ainsi que de nouveaux composants photoniques pour l'optique quantique.

MOTS CLÉS

cristal photonique non linéaire, génération paramétrique optique, dynamique non linéaire, retour optique, rétrodiffusion Brillouin stimulée

ABSTRACT

Nonlinear optics and nonlinear dynamics provide number of applications in different research areas, particularly in optical telecommunications and lasers. In this context, I am interested in studying nonlinear optical dynamics and interactions. First, I will show the study of the dynamical behaviours of laser diodes subject to optical feedback via a fibre Bragg grating or stimulated Brillouin scattering.

Afterwards, I will show particularly our study of optical parametric generation in nonlinear photonic crystals which allow multi-wavelength generation from UVA to near infrared. These works address the importance of nonlinear effects for the development of new tuneable multi-wavelength sources as well as new photonic devices for quantum optics.

KEY-WORDS

nonlinear photonic crystal, optical parametric generation, nonlinear dynamics, optical feedback, stimulated Brillouin scattering